DYNAMIC SOIL-STRUCTURE INTERACTION IN BUILDINGS WITH OIL DAMPERS

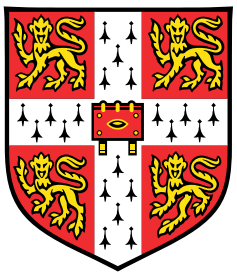

Jad I. Boksmati

Department of Engineering
University of Cambridge

This dissertation is submitted for the degree of
Doctor of Philosophy

Churchill College December 2020

I would like to dedicate this thesis to my loving parents, Ibrahim and Fida, and to my late grandfather, Saeed . . .

Declaration

I hereby declare that except where specific reference is made to the work of others, the contents of this dissertation are original and have not been submitted in whole or in part for consideration for any other degree or qualification in this, or any other university. This dissertation is my own work and contains nothing which is the outcome of work done in collaboration with others, except as specified in the text and Acknowledgements. This dissertation contains fewer than 65,000 words, and has less than 150 figures.

Jad I. Boksmati
December 2020

DYNAMIC SOIL-STRUCTURE INTERACTION IN BUILDINGS WITH OIL DAMPERS

Jad I. Boksmati

Research into the seismic performance of structures with oil dampers have so far been driven primarily by the structural engineering community, with influential experimental work on the topic originating mainly from large scale shaking table testing of fixed-base prototype frames. Despite considerable advancements over the years in building complexity and realism into these test structures, little to no experimental effort has been made to investigate dynamic soil-structure interaction in such structures. Fixed-base shaking table testing of structures fitted with oil dampers confines energy dissipation to the supplemental damping devices alone, neglecting any contributions from foundation-soil inertial interaction that may arise in the field. A considerable portion of literature on oil dampers in structures emanates from a mathematical optimisation background, proposing computational algorithms to solve for optimal damper sizes and locations in a structure. Such iterative linear analysis is conducted in the frequency domain, and offers limited physical insight into the different facets of this complex nonlinear Soil-Structure Interaction (SSI) problem. Numerical and analytical work examining the effects of SSI on buildings with oil dampers have been limited in nature, often resorting to equivalent linear procedures to simplify the modelling of geometric and soil nonlinearities at the foundation-soil interface. This research seeks to address some of these limitations by pioneering the application of high gravity geotechnical centrifuge testing as a viable research tool to experimentally investigate dynamic SSI in buildings with oil dampers.

Miniature oil dampers for use in small-scale model structures were developed for this purpose, following a series of trial-and-error experimentations. Sixteen centrifuge tests were conducted in total, each involving two similar 2-DOF linear elastic structures, one fitted with miniature oil dampers, and one left bare for comparison. Ground flexibility was varied between tests by changing frame base fixity conditions from fully rigid fixed base, to shallow embedment of raft foundations into dry dense and loose sand beds. Aspect ratios and foundation bearing pressures of the model structures were also varied to trigger different levels of SSI. Miniature accelerometers were used during the centrifuge tests to measure soil and structural accelerations, along with miniature load cells to track experimental oil damper hysteresis during shaking. The model frames were subjected to near resonant frequency sinusoidal excitations of different magnitudes to trigger different levels of SSI. The dynamic response of the structures to realistic multi-frequency component excitations was also recorded.

Inter-storey oil dampers as tested in this study have delivered consistent improvements to the seismic response of structures for all of the input motions and ground conditions investigated in the centrifuge. It was found that additional viscous damping in the superstructure came at the expense of inertial interaction at its foundation-soil interface. The damped soil-structure systems were less sensitive to changes in ground conditions and foundation bearing pressures compared to their regular bare frame counterparts. Optimal oil damper control over structural accelerations and drifts was recorded for fixed base conditions, during weak excitations that did not trigger considerable resonance in the superstructures. Upon shallow embedment of the rafts into dry sand beds, reductions in damper control were reported, reaching minimal levels for the loose sand cases during moderate to strong near resonant frequency excitations. These reductions were not the result of subpar performance of the damped structures per se, but rather a consequence of the considerable improvement in the dynamic response of the regular frames being used as comparative benchmarks. If the foundation of a regular structure is permitted to rock during strong shaking, experimental evidence points to dynamic responses that are close to those expected from a similar structure fitted with oil dampers. However, such natural seismic mitigation measure was shown to be highly variable and unreliable for weaker excitations.

Base flexibility and dynamic SSI did not have adverse consequences on the performance of structures fitted with oil dampers. While it is true that reductions in oil damper hysteresis were observed with reducing base fixity, this should not be interpreted as degradation in damper effectiveness. On the contrary, when excited close to resonance, the damped frames exhibited similar, albeit slightly lower, floor accelerations as base fixity was reduced. Estimation of the seismic input energy into a soil-structure system during near resonant frequency shaking showed both, damped and bare structures benefiting from natural rocking isolation; releasing the foundation rotational kinematic restraints lowers total energy going into the superstructures, causing the oil dampers in the frames to do less work. Even during SSI, the oil dampers continued to be the primary source of energy dissipation in the soil-structure systems.

Lastly, the promising application of using nonlinear lumped-parameter structural models, with hyperbolic foundation moment-rotation backbone curves to predict centrifuge data, was demonstrated for the damped and regular bare structures. Such simplified models, solved in the time domain, offer a more elegant solution during early stage design compared to the response spectrum procedures currently advocated by published guidelines on the analysis of damped structures.

Acknowledgements

I truly believe that every experience we encounter in life, regardless of how trivial it may be, shapes who we are in some way. The past four years of working at the Schofield Centre have without a doubt been pivotal for me at a personal, intellectual and social level. I would not be where I am today without the camaraderie of many individuals who assisted me on this journey. First and foremost, I would like to extend my utmost gratitude to my supervisor, Professor Gopal Madabhushi, for giving me this opportunity, and for his guidance, patience and support throughout this project. My sincere gratitude also extends to Dr. Thusyanthan Indrasenan for encouraging me to pursue a PhD.

It goes without saying that none of this experimental work would be possible without the support of all the technical and administrative staff at the Schofield Centre. I would like to thank John Chandler, Mark Smith, Kristian Pether, and Chris McGinnie for their invaluable contributions and input into fabricating parts for the tests, instrumenting the models, and running the centrifuge. My sincere thanks also extends to the centre administrator, Magdalena Charytoniuk, who has always been very helpful and accommodating to my requests.

I owe a huge deal of gratitude to Dr. Abdulhakim Zeybek for showing me the basics of sand pouring and centrifuge testing, and to Dr. Iason Pelekis for his insightful discussions on soil-structure interaction. I would like to thank Dr. Fiona Hughes, Andrei Dobrisan, Samy Garcia, Geoff Eichhorn, Dr. Srikanth Madabhushi, Dr. Stephan Van Eeden, Dr. Chuhan Deng to name a few. Special thanks to Dr. Thejesh Garala for being there with me from day one. Particular thanks to my dear friend Alessandro Fusco for his tremendous support during the highs and lows of this project.

The financial support provided by the Saudi Cultural Bureau in London, and the Ministry of Education in the Kingdom of Saudi Arabia was crucial for me to be able to pursue this degree. Their support is greatly appreciated.

Finally, I dedicate this work to my brother Osama. May science and engineering inspire you the same way they inspire me everyday to challenge myself and think big.

Table of contents

List of figures **xv**

List of tables **xxv**

Nomenclature **xxvii**

1 Introduction **1**
1.1 Background 1
1.2 Research Problem & Objectives 3
1.3 Thesis Outline 5

2 Literature Review **7**
2.1 Introduction 7
2.2 Passive Fluid Dampers in Structures 10
2.2.1 Description of Damping Devices 10
2.2.2 Analytical Modelling of Fluid Dampers 12
2.2.3 Simplified Analysis of Buildings With Fluid Dampers 17
2.2.4 Experimental Testing of Damped Structures 30
2.3 Dynamic Soil-Structure Interaction 33
2.3.1 Modelling Foundation-Soil Interaction 33
2.3.2 Effects on Structure Response 38
2.4 Soil-Structure Interaction in Structures With Viscous Dampers 43
2.5 Summary 47

3 Experimental Methodology & Model Structures **49**
3.1 Introduction 49
3.1.1 Centrifuge Modelling Theory 50
3.2 Equipment for High-Gravity Testing 53
3.2.1 Turner Beam Centrifuge 53

3.2.2 Automatic Sand Pourer 54
3.2.3 Equivalent Shear Beam (ESB) Box 56
3.2.4 Servo-Hydraulic Actuator 58
3.2.5 Instrumentation 59
3.2.6 Data Acquisition 62
3.3 Design of Model Structures 63
3.3.1 Construction 63
3.3.2 Dynamic Characterisation 70
3.4 Miniature Oil Dampers 79
3.4.1 Miniature Oil Damper A 79
3.4.2 Miniature Oil Damper B 86
3.5 Model Preparation 94
3.5.1 Hostun HN31 Sand 94
3.5.2 Pouring and Instrumenting Sand 95
3.5.3 Positioning of Model Structures 97
3.5.4 Static Vertical Factor of Safety for Bearing Capacity 98
3.6 Testing Procedures 99
3.7 Presentation of Data 101
3.8 Centrifuge Testing Programme 104

4 Prediction of Fixed-Base Dynamic Structural Response 109
4.1 Introduction 109
4.2 Time History Predictions for Bare Frames 109
4.3 Mathematical Modelling of Miniature Oil Dampers 118
4.4 Time History Predictions for Damped Frames 124
4.5 Response Spectrum Analysis (RSA) 132
4.6 Summary 140

5 Soil-Structure System Response 143
5.1 Introduction 143
5.2 Sand-bed Characterisation 145
5.3 System Transfer Functions 149
5.4 Absolute Floor Accelerations 152
5.5 Foundation Moment-Rotation Behaviour 165
5.6 Summary 170

6 Seismic Demand on the Superstructures 173
6.1 Introduction . . . 173
6.2 Storey Shear and Inter-storey Drifts . . . 173
6.3 Inter-storey Oil Damper Performance . . . 186
6.4 Seismic Input Energy Distribution . . . 199
6.5 Summary . . . 205

7 Prediction of Dynamic Soil-Structure System Response 207
7.1 Introduction . . . 207
7.2 Modelling of Foundation-Soil Systems . . . 208
7.2.1 Wolf Discrete-Element Model . . . 208
7.2.2 Hyperbolic Model . . . 215
7.3 Frames with Inter-storey Oil Dampers . . . 226
7.4 Summary . . . 238

8 Conclusions 241
8.1 Research Findings . . . 241
8.1.1 Performance With & Without Oil Dampers . . . 242
8.1.2 Effects of SSI on Structures With Oil Dampers . . . 247
8.2 Implications of Research to Practice . . . 251
8.3 Recommendations For Further Work . . . 253

References 257

List of figures

1.1 57-Storey Torre Mayor Tower equipped with 98 fluid dampers in Mexico City, Mexico. (Rahimian et al., 2019; Summerson, 2017; Taylor, 2007) . . 2
1.2 Seismic retrofit of 13 storey reinforced concrete tower, the Tower of Hope in Orange County, California with fluid viscous dampers. (Seamer and Wang, 2019) 3

2.1 Control system logic of passive and active dampers in structures (from Symans and Constantinou (1995)). 8
2.2 Typical internal construction of fluid dampers used in structures according to Guo et al. (2015) with (a) internal oil accumulators and (b) run-through piston rods. 10
2.3 Example application of Equation 2.1 for a random damper showing the effects of damping exponent α on damper force-velocity-displacement relationships. 11
2.4 Damping coefficients, storage stiffness, and hysteresis loops for linear dampers with internal accumulators at different driving frequencies as tested by Constantinou and Symans (1992). 13
2.5 (a) Schematic of damper component testing rig (Constantinou and Symans, 1992) (b) damper force-velocity regression from Seleemah and Constantinou (1997) (c) damper force-velocity regression from Chang et al. (2008) 14
2.6 Maxwell and Kelvin-Voigt mechanical models for visco-elastic material behaviour (Greco and Marano, 2013). 16
2.7 Response Spectrum Analysis (RSA) procedure for linear structures with viscous dampers as per FEMA-273 (1997). 18
2.8 Modifications to 5% damped pseudo-acceleration spectrum to account for higher damping as per 1997 FEMA-273 (1997) and Ramirez et al. (2001). . 19
2.9 Numerical velocity predictions compared to corrected spectral pseudo-velocities from Ramirez et al. (2001). 21

2.10 Direct 5-step procedure for dimensioning linear/nonlinear viscous dampers in structures and analysing their performance (Silvestri et al., 2010). 24
2.11 Mean displacements reduction factor (η_δ) and mean accelerations reduction factor (η_a) for increasing damping ratios according to Silvestri et al. (2010). 25
2.12 (a) Undamped structure (b) Rayleigh classical damping (c) Mass-proportional damping (d) Stiffness proportional damping (from Silvestri et al. (2010)). . 26
2.13 Approximating ratio of mass-proportional damping to stiffness-proportional damping for different N number of floors in shear-type structures from Silvestri et al. (2010). 28
2.14 Checking internal frame actions for two Equivalent Static Analysis (ESA) cases: ESA1 at peak lateral frame deformations, and ESA2 at peak inter-storey velocities (Palermo et al., 2018). 29
2.15 Evolution of experimental testing of frames equipped with viscous damping devices. 32
2.16 (a) Seismic response of structure founded on rock and on soft soil deposits (b) Bedrock acceleration transmission through soil column (c) Kinematic interaction (d) Inertial interaction (modified from Wolf (1985)). 33
2.17 (a) Wave energy radiation from foundation experiencing dynamic horizontal shear and overturning moments (Lu (2016)) (b) localised zone of soil yielding beneath shallow foundation (Anastasopoulos et al. (2010); Gajan and Kutter (2008)). 34
2.18 Simplified substructure approach to account for SSI using impedance functions (after Kramer and Stewart (2004); Lu (2016)). 35
2.19 Foundation-soil system lumped parameter model analogues to halfspace solutions (from Chuanromanee (1995)). 36
2.20 Rotational dynamic stiffness for square foundation on elastic halfspace with a Poisson's ratio of $\nu = 1/3$ and hysteretic damping of 5%. (from Chuanromanee (1995)). 36
2.21 Comparison of experimental peak pseudo-accelerations from centrifuge to theoretical peak pseudo-accelerations assuming fixed-base conditions for SDOF structures of different periods (from Kim et al. (2015)). 39
2.22 Time trace of mass displacement relative to foundation (u_r) and its horizontal component of rotation ($u_{Rocking}$) for stiff (top) and flexible (bottom) SDOF structures during a 0.2 g peak Northridge earthquake (from Kim et al. (2015)). 40

2.23 (left) Seismic over-turning moments (right) and inter-storey drift ratios for five different soil types simulated by foundation macro-element model during 0.9 g Northridge input excitation (from Grange et al. (2009)). 42
2.24 Effects of ground flexibility on overall soil-structure system damping ratio at the fundamental mode. (from Chuanromanee et al. (1995)) 44
2.25 Percentage of overall damping contributed by different system mechanisms for an 8-storey shear type structure. (from Chuanromanee et al. (1995)) . . 44

3.1 (a) Top-down view of centrifugal acceleration field generated due to circular motion of the centrifuge (b) Centrifugal forces acting at different points in the experimental package. 50
3.2 Variation of centrifugal acceleration across model soil depth in the centrifuge. 51
3.3 10 m diameter Turner Beam Centrifuge located at the Schofield Centre, University of Cambridge, UK. 53
3.4 (a) Automatic sand pourer frame, hopper and nozzle setup (b) Robotic sand pouring pattern along the longitudinal and transverse axes of the model container. 55
3.5 Equivalent Shear Beam (ESB) box, its geometry and construction. 57
3.6 Servo-hydraulic actuator loaded on the blue swing with an experimental package. 59
3.7 (left) Piezo-electric accelerometer (right) Typical calibration curve. 60
3.8 (left) MEMS accelerometer (right) Typical calibration curve. 61
3.9 (left) F255 miniature tension/compression load cell (right) Typical calibration curve. 61
3.10 Air-hammer device with sand coating around brass tube. 62
3.11 3D rendering of virtual prototype and actual centrifuge model structures. . . 65
3.12 Geometry and construction of the Squat frames (all units in mm). 66
3.13 Squat frames equipped with inclined miniature oil dampers type B. 67
3.14 Geometry and construction of tall structures (all units in mm). 69
3.15 Tall model structures with and without inter-storey dampers. 69
3.16 Mass lumping and lateral storey stiffness assumed during preliminary sizing of model structures. 72
3.17 Fast-Fourier Transform (FFT) results from hammer impact testing on second storey floor plates. 73
3.18 Fixed-base centrifuge testing at 50 g for (a) squat frames (b) tall frames. . . 75
3.19 Second storey acceleration time traces and FFT spectra for 0 to 1.2 Hz sweep base excitation. 76

3.20 MAGOM 15 mm Bore hydraulic cylinder geometry and construction. . . . 80
3.21 Hydraulic cylinder repurposed into a passive oil damper. 81
3.22 Ling-200 series shaker testing of miniature damper A. 82
3.23 Force-displacement and force-velocity traces of miniature damper A from Ling-200 series shaker tests. 83
3.24 Experimental damper force-velocity traces as measured in trial centrifuge tests. 85
3.25 Miniature damper B geometry, construction and internal mechanism. 86
3.26 Trial centrifuge tests at 50 g to test the performance of different damper configurations. 88
3.27 Oil damper B force-velocity-displacement plots for Configuration 1. 89
3.28 Oil damper B force-velocity-displacement plots for Configuration 2. 90
3.29 Working mechanism for open and sealed oil damper B. 91
3.30 Oil damper B force-velocity-displacement plots for Configuration 3. 92
3.31 Oil damper B force-velocity-displacement plots for Configuration 4. 92
3.32 Oil damper B force-velocity-displacement plots for Configuration 5. 93
3.33 De-airing of hydraulic oil for damper B assembly. 94
3.34 (a) Air hammer and first layer of intruments close to bottom of the container (b) Intermediate layer of instruments (c) Final instrumentation layer (d) Weighing of sand at foundation level. 96
3.35 (a) Top-down view of squat frames on foundation surface (b) Horizontality of frames checked with spirit level (c) Embedment of model frames to top of raft foundation. 98
3.36 (a) Servo-shaker being loaded (b) Centrifuge package ready for loading (c) Centrifuge package on blue end of the beam. 100
3.37 Typical earthquake firing sequence during a centrifuge test. 101
3.38 Integration and filtering of damper accelerations to compute damper stroke velocities and stroke displacements. 103
3.39 Centrifuge testing matrix. 104
3.40 Typical experimental package layout for a fixed base test. 105
3.41 Typical experimental package layout for dry sand tests with the ESB container for the Squat frames. 106
3.42 Typical experimental package layout for dry sand tests with the ESB container for the Tall frames. 107

4.1 Numerical integration scheme for fixed base bare structures. 111

4.2 Numerical predictions of time histories and second storey transfer function for the bare Squat frame without dampers during a scaled Imperial Valley excitation. 113
4.3 Numerical predictions of time histories and second storey transfer function for the bare Tall frame without dampers during a weak near resonant frequency excitation. 114
4.4 Numerical predictions for the bare Tall frame during strong near resonant frequency excitation with (top) constant lateral storey stiffness (bottom) varying lateral storey stiffness. 115
4.5 Fixed-base finite element simulation of the bare Tall frame during strong near resonant frequency excitation. 116
4.6 Fixed-base finite element simulation of the bare Squat frame during strong near resonant frequency excitation. 117
4.7 Experimental, theoretical, and simplified mathematical model of a damping system. 118
4.8 Deriving dashpot and spring constitutive models for first storey and second storey miniature oil dampers D2 as used in the Tall damped structure. . . . 120
4.9 First storey dashpot and spring constitutive models for oil dampers D3, D2 and D1 as used in the damped Squat frame. 122
4.10 Second storey dashpot and spring constitutive models for oil dampers D3, D2 and D1 as used in the damped Squat frame. 123
4.11 Numerical integration scheme for fixed base damped structures. 125
4.12 Numerical predictions for the Squat frame during strong near-resonant frequency input motions equipped with D3 light damping configuration. . . . 127
4.13 Numerical predictions for the Squat frame during strong near-resonant frequency input motions equipped with D2 medium damping configuration. . . 128
4.14 Numerical predictions for the Squat frame during strong near-resonant frequency input motions equipped with D1 heavy damping configuration. . . . 129
4.15 Numerical predictions for the Squat frame equipped with D2 dampers during a scaled Kobe excitation. 130
4.16 Numerical predictions for the Tall frame equipped with D2 dampers during a sine-sweep excitation. 131
4.17 5 % damped response spectral plots from experimental foundation and roof structural accelerations for the tall structures. 137

4.18 5 % damped response spectral plots from experimental foundation and roof structural accelerations for (left) Tall frames (right) Squat frames during near resonant frequency shaking. 139

5.1 Definition of positive sign convention for displacements, velocities, accelerations and inertial loading on a model frame. 144
5.2 Average densities of dense and loose sand prepared for dynamic centrifuge testing. 145
5.3 Experimental shear wave velocity and small-strain stiffness measurements from air hammer testing. 146
5.4 Bedrock acceleration transmission and amplification in dry dense and loose sand. 148
5.5 Experimental transfer functions derived from a weak sine-sweep base excitation (peak foundation input 0.09 g) for different sand densities and foundation bearing pressure cases. 150
5.6 Second storey accelerations normalised by peak foundation input during near resonant frequency base excitations for Squat frames with Light foundations and D2 dampers. 153
5.7 Second storey accelerations normalised by peak foundation input during near resonant frequency base excitations for Tall frames with Light foundations and D2 dampers. 154
5.8 Second storey accelerations normalised by peak foundation input during near resonant frequency base excitations for Tall frames with Heavy foundations and D2 dampers. 155
5.9 Foundation rotational acceleration traces during near resonant frequency excitations for Tall frames with Light foundations and D2 dampers. 157
5.10 Foundation rotational acceleration traces during near resonant frequency excitations for Tall frames with Heavy foundations and D2 dampers. 158
5.11 Second storey accelerations and foundation rotational accelerations for Squat and Tall structures during a sinusoidal base excitation close to Mode 2 of the frames. 160
5.12 Normalised second storey accelerations for the Tall structures with Heavy foundations and D2 dampers during multi-frequency component base excitations. 162
5.13 Normalised second storey accelerations for the damped Squat structure with a Light foundation embedded in dry Dense sand with different damper configurations. 164

5.14 Moment-rotation loops for the model structures during moderate near resonant frequency excitations. 166
5.15 Moments, first storey damper forces, and frame rotations for the damped structures with Light foundations during moderate near resonant frequency excitations. 168

6.1 Definition of storey shear and inter-storey drifts from experimental acceleration data. 174
6.2 Peak storey shear forces and storey displacements during sine-sweep and scaled realistic excitations for Squat frames with Light foundations and D2 dampers. 175
6.3 Peak storey shear forces and storey displacements during sine-sweep and scaled realistic excitations for Tall frames with Heavy foundations and D2 dampers. 176
6.4 Definition of equivalent viscous damping ratio for classical, irregular and asymmetrical hysteresis loops. 178
6.5 Storey shear forces and inter-storey drifts during moderate near resonant frequency excitations for the Squat frames. 180
6.6 Storey shear forces and inter-storey drifts during moderate near resonant frequency excitations for the Tall frames. 181
6.7 Storey shear forces and inter-storey drifts during strong near resonant frequency excitations for the Tall frames. 182
6.8 Equivalent viscous damping ratios computed from damped frame storey shear versus inter-storey drift loops. 183
6.9 Equivalent viscous damping ratios computed from bare frame moment-rotation loops at cycles of peak rotations. 185
6.10 Total acceleration phase delay between roofs and foundations of tested structures embedded in loose dry sands with different bearing pressures and D2 dampers. 188
6.11 Illustration of different foundation-floor phase differences for a generic one-storey structure experiencing sinusoidal horizontal foundation accelerations. 189
6.12 Floor inertial load, internal frame forces, and velocities for an idealistic one-storey structure, equipped with a linear viscous damper, responding at a 90° foundation-floor phase difference during a sinusoidal horizontal base excitation. 191
6.13 Total floor velocities and rotational acceleration traces for the frames with D2 dampers embedded in Loose sand during near resonant frequency excitations. 192

6.14 Comparison of inter-storey oil damper energy dissipation and frame recoverable strain energy for the damped Squat frame with D2 dampers at different base fixity conditions during moderate near resonant frequency excitations. 194
6.15 Comparison of inter-storey oil damper energy dissipation and frame recoverable strain energy for the damped Tall frame with D2 dampers at different base fixity conditions during moderate near resonant frequency excitations. 195
6.16 Comparison of damper inputs at different base fixity conditions for the damped structures with light foundations during moderate near resonant frequency excitations. 196
6.17 Experimental moment-rotation loops for the damped Tall frame with D2 dampers during moderate near resonant frequency excitations. 198
6.18 Illustration of horizontal ground acceleration input into a soil-structure system with the corresponding frame reaction forces during shaking. 199
6.19 Energy traces for the Tall structures with D2 dampers for different base fixity conditions during sine sweep and near resonant frequency excitations. . . . 201
6.20 Normalised energy traces for the Tall structures with D2 dampers embedded in Loose sands during near resonant frequency excitations of different intensities. 203
6.21 Energy traces for the Tall structures with D2 dampers for different base fixity conditions during scaled Imperial Valley input motions. 204

7.1 Lumped parameter model for an embedded prism foundation after Wolf (1988) inserted beneath the 2-DOF frame. 208
7.2 Numerical predictions using the Wolf (1988) lumped parameter model for the regular Squat and Tall structures embedded in Dense sand during a sine-sweep excitation. 211
7.3 Numerical predictions using the Wolf (1988) lumped parameter model for the regular Tall structure with a Heavy foundation embedded in Dense sand during near resonant frequency excitations of different magnitudes. 212
7.4 Effect of soil shear modulus variation on numerical predictions for the regular Squat structure with a Light foundation embedded in Loose sand during a strong near resonant frequency excitation. 214
7.5 Linear variation of vertical stress assumed beneath the foundation subjected to overturning moments (Heron, 2013). 216
7.6 Comparing the hyperbolic backbone curve to experimental moment-rotation loops for the regular squat and tall frames during weak near resonant frequency excitations. 218

7.7 Comparing the hyperbolic backbone curve to experimental moment-rotation loops for the regular squat and tall frames during strong near resonant frequency excitations. 219
7.8 Visualising the hyperbolic moment-rotation model as a parallel assembly of a nonlinear soil spring and a linear dashpot at the foundation. 220
7.9 Newmark solution algorithm for a regular frame with a hyperbolic foundation-soil model. 222
7.10 Numerical predictions using the Heron (2013) hyperbolic model for the regular Tall and Squat structures embedded in Dense sand during weak near resonant frequency excitations. 223
7.11 Numerical predictions using the Heron (2013) hyperbolic model for the regular Tall and Squat structures with Heavy foundations embedded in Dense sand during sine-sweep and scaled Imperial Valley excitations respectively. 224
7.12 Numerical predictions using the Heron (2013) hyperbolic model for the regular Tall and Squat structures with Light foundations embedded in Loose sand during strong near resonant frequency excitations. 225
7.13 Visualising the damped structures as 2-DOF systems with nonlinear dashpots, and a hyperbolic foundation-soil model inserted at the centre of the foundation. 226
7.14 Numerical predictions for the damped Squat structure with a Light foundation and D2 dampers (medium damping), embedded in Loose sand during a strong near resonant frequency excitation. 228
7.15 Numerical predictions for the damped Squat structure with a Heavy foundation and D2 dampers (medium damping), embedded in Loose sand during a sine-sweep excitation. 229
7.16 Numerical predictions for the damped Tall structure with a Heavy foundation and D2 dampers (medium damping), embedded in Dense sand during a strong near resonant frequency excitation. 230
7.17 Numerical predictions for the damped Tall structure with a Light foundation and D2 dampers (medium damping), embedded in Dense sand during a strong near resonant frequency excitation. 231
7.18 Numerical predictions for the damped Squat structure with a Light foundation and D3 dampers (light damping), embedded in Dense sand during a strong near resonant frequency excitation. 232
7.19 Time history predictions from lumped-parameter models for the Tall structures during a theoretical scaled Kobe excitation with fixed-base conditions, and embedment of Heavy foundations into dry Loose sand. 234

7.20 Time history predictions from lumped-parameter models for the Squat structures during theoretical scaled Imperial Valley and Kocaeli excitations, for the case of Heavy foundations embedded in dry Loose sand. 235
7.21 Investigating the effects of foundation input motion intensity and soil small-strain shear modulus of soil on normalised peak inter-storey drifts during embedment in loose sand. 236
7.22 Investigating the effects of foundation input motion intensity and different damper properties on normalised peak inter-storey drifts during embedment in loose sand. 237

8.1 Percentage drop in peak total floor accelerations after D2 oil damper installation for different ground conditions and base excitations. 244
8.2 Peak inter-storey drifts for the Tall and Squat structures with D2 dampers measured during weak and strong near resonant frequency excitations. . . . 246

List of tables

3.1 Dynamic centrifuge and shaking-table similitude scaling laws. (Madabhushi, 2015; Seleemah and Constantinou, 1997) . . . 52
3.2 Aluminium alloy grade 6082-T6 properties. . . . 66
3.3 Theoretical lumped mass and lateral storey stiffness compared to MATLAB solutions for the Squat model frame. . . . 77
3.4 Summary of centrifuge model structures used in this study. . . . 78
3.5 Damper setup configurations for fixed base trial centrifuge tests. . . . 87
3.6 Soil properties of Hostun HN31 sand. (Shepley, 2013) . . . 95
3.7 Peak and critical-state friction angles for Hostun HN31 sand. (Heron, 2013) 95
3.8 Static vertical factor of safety against bearing capacity failure. . . . 99

4.1 Tall damped structure peak response as computed by simplified procedure, numerical integration, and as measured experimentally during scaled Kobe excitation. . . . 136
4.2 Tall damped structure peak response as computed by simplified procedure, numerical integration, and as measured experimentally during scaled Imperial Valley. . . . 136
4.3 Tall damped structure peak response as computed by simplified procedure, numerical integration, and as measured experimentally during sine-sweep excitation. . . . 138
4.4 Squat damped structure peak response as computed by simplified procedure, numerical integration, and as measured experimentally during strong near resonant frequency excitation. . . . 139

7.1 Soil shear modulus degradation parameters. . . . 216
7.2 Selected model parameters from Heron (2013) . . . 217

Nomenclature

Other Symbols

$[\hat{k}]$	modified stiffness matrix from Newmark nonlinear integration in Chopra (2012)
$[C]$	classical damping matrix
$[K]$	stiffness matrix
$[M]$	mass matrix
α	damping exponent
$\ddot{\theta}$	foundation rotational acceleration
$\ddot{u}_g$	foundation acceleration
$\ddot{u}_t$	total floor accelerations
$\ddot{u}_{net,i}$	i^{th} floor structural acceleration relative to the base
$\dot{u}_{drift,i}$	i^{th} floor inter-storey velocity
γ	shear strain in soil
γ_e	strain parameter from Oztoprak and Bolton (2013)
γ_r	strain parameter from Oztoprak and Bolton (2013)
γ_{rep}	representative shear strain from Heron (2013)
ω_i	i^{th} natural frequency of system
τ_{rep}	representative shear stress from Heron (2013)
θ	foundation rotation

ζ structure damping ratio

ζ_{fnd} damping ratio of foundation moment-rotation loop

$\{\hat{R}\}$ array of residual forces from Newmark nonlinear integration in Chopra (2012)

$\{du\}$ incremental array of system degrees of freedom from Newmark nonlinear integration in Chopra (2012)

$\{F_d\}$ array of nonlinear dashpot forces

$\{F_s\}$ array of system stiffness forces

$\{p\}$ base excitation vector

$\{u\}$ array of system degrees of freedom

a hyperbolic degradation parameter from Oztoprak and Bolton (2013)

$A(\gamma)$ strain dependant parameter from Oztoprak and Bolton (2013)

a_1, a_2, a_3 Newmark integration constants

c damping coefficient

E_{input} total seismic input energy due to horizontal ground excitation

E_{rot} work done by seismic overturning moments on foundation rotations

E_{str} work done by seismic inertial loads on internal shear deformation in structure

FS_v vertical factor of safety of foundation

G shear stiffness of soil

G_{max} small-strain shear stiffness

h_i distance from i^{th} floor centre of gravity to base of foundation

I_d relative density of sand

I_f mass moment of inertia of the foundation about its centre of gravity

I_{0r} and I_{1r} fictitious mass moments of inertia from Wolf (1988)

k_i lateral storey stiffness of ith floor

K_r nonlinear hyperbolic rotational spring from Heron (2013)

K_{ry} rotational spring stiffness from Wolf (1988)

M foundation seismic overturning moments

$m(\gamma)$ strain dependant parameter from Oztoprak and Bolton (2013)

m_f mass of foundation

m_i lumped mass of ith floor

N centrifuge scaling factor

q bearing pressure

R shear stress to foundation moments correlation factor from Heron (2013)

r vertical displacement to vertical stress correlation factor from Heron (2013)

S shear strain to foundation rotations correlation factor from Heron (2013)

$u_{drift,i}$ i^{th} floor inter-storey drift

V_i i^{th} storey shear force

v_s shear wave velocity

Acronyms / Abbreviations

D1 Heavy damping

D2 Medium damping

D3 Light damping

MDOF Multiple-degrees-of-freedom

MEMS micro-electro-mechanical system accelerometer

PFI peak foundation input

RSA Response Spectrum Analysis

SDOF Single-degree-of-freedom

SRSS square-root-sum-of-all-squares

SSI soil-structure interaction

Chapter 1

Introduction

1.1 Background

In an interview with The New York Times, Yasuhisa Itakura, a Japanese architect based in Kobe, Japan recalls events of the 1995 earthquake that struck his city (Fuller et al., 2019). As his office building swayed during shaking, none of his furniture items or books fell to the ground. Mr. Itakura is quoted saying:

"I thought to myself, this earthquake is not that big"

This event would be later known as the Great Hanshin earthquake of 1995, killing more than 6,000 people, leaving aroung 45,000 residents homeless, and causing over $ 100 billion in damages (Caryl, 2020). The office building which Mr. Itakura was working in at that time was an early version of a base isolated structure (Fuller et al., 2019).

Close to that time in history, damage left by the 1989 Loma Prieta earthquake in Northern California was already driving interest and demand in the United States for passive seismic control of structures (Symans et al., 2008). Fast forward to today, there are over 6,400 commercial and residential structures in Japan that use seismic isolation technologies, and over 950 buildings that incorporate supplemental damping systems into their frames (Kasai et al., 2012). The U.S. has also seen more than 600 projects and bridges utilise supplemental dampers for seismic protection (Taylor Devices Inc., 2019).

Resilience and Business Continuity Plans (BCPs) have become popular terminology in the field of disaster prevention (Nakamura and Okada, 2019). In the context of earthquakes and infrastructure, these concepts imply the need for structural designs that not only survive seismic shaking, but also allow for a quick return to normal operations with minimal damages. This increasingly popular trend is inline with the current push to replace limit-state designs with performance-based designs of structures against earthquake loading.

Base isolation and supplemental damping are two popular, albeit different, strategies for achieving seismic resilience in structures. While seismic isolation controls the interface between a structure and its foundations to limit the transfer of energy during ground shaking, supplemental dampers add resilience by enhancing energy dissipation within the structural frame itself (Christopoulos and Filiatrault, 2006). The latter, specifically velocity-dependant oil dampers incorporated into structural frames, will be the main focus of this study.

The Torre Mayor Tower in Figure 1.1 is one example of a new building design in Mexico City, that incorporates a total of 98 fluid dampers distributed between the building's core-truss, moment-frame perimeter columns, and mega-braces. The added damping in the structure increased the fundamental mode damping ratios to 8.5 % and 12 % in the North-South and East-West directions respectively (Rahimian and Romero, 2003). While seismic protection of the tower was the original intent behind the oil dampers, the devices also play a role at limiting sway during high wind (Rahimian and Romero, 2003).

During preliminary sizing of Torre Mayor, given a limit on the allowable bearing pressures on the soft soil deposits of Mexico City, engineers were only able to come up with structural configurations for a maximum of 35 to 38 floors for a caisson/mat foundation system. Increasing damping of the tower to approximately 10 % of critical allowed for reductions in gross steel weight, which permitted the possibility of adding additional floors to the overall tower design (Taylor, 2007).

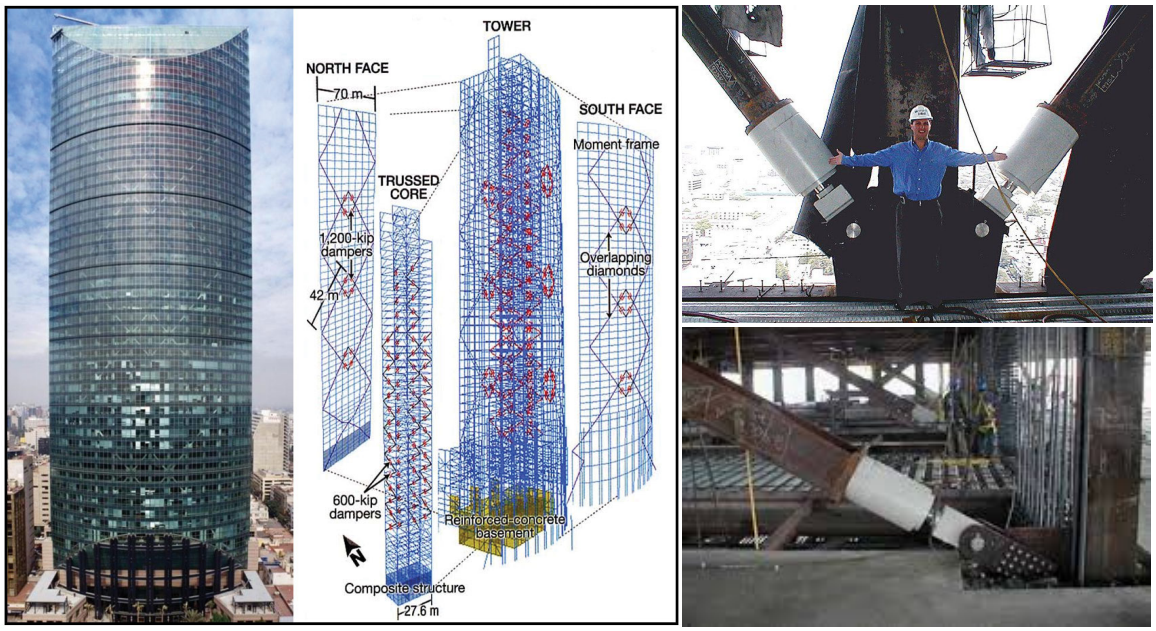

Fig. 1.1 57-Storey Torre Mayor Tower equipped with 98 fluid dampers in Mexico City, Mexico. (Rahimian et al., 2019; Summerson, 2017; Taylor, 2007)

The Tower of Hope in Orange County, California is a seismic retrofit example of a 13-storey reinforced concrete structure built in the late 1960s. The lateral force resisting system of the tower consisted of reinforced concrete moment frames that did not possess sufficient ductility in accordance to modern-day seismic standards (Seamer and Wang, 2019). The retrofit strategy chosen for the structure included fibre-reiforced polymer (FRP) strengthening of selected concrete columns and shear walls, coupled with 32 fluid viscous dampers (Seamer and Wang, 2019). The intent was to have minimal disturbance to the open-space interior architecture of the tower as shown in Figure 1.2.

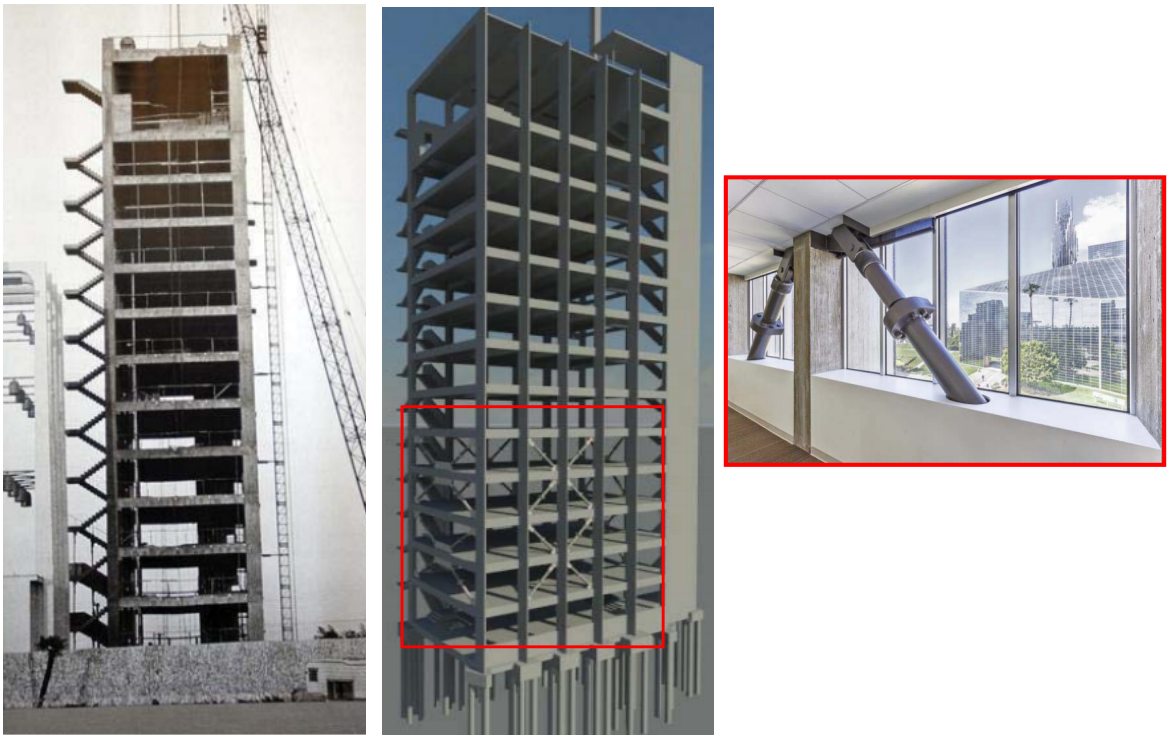

Fig. 1.2 Seismic retrofit of 13 storey reinforced concrete tower, the Tower of Hope in Orange County, California with fluid viscous dampers. (Seamer and Wang, 2019)

1.2 Research Problem & Objectives

The early 1990s saw the golden-age of experimental testing of structures with passive dampers. At that time, extensive programmes (introduced in section 2.2.4 of Chapter 2) were commissioned at renowned institutes to gather experimental data about the performance of damped structures. The process was both laborious and costly, as prototype test structures would have to be erected inside sizeable testing facilities constructed with powerful shaking tables.

To this day, fixed base shaking table testing continues to be the prevalent experimental method, albeit with greater intricacies and realism built into the test frames. Literature on the design and analysis of structures with supplemental dampers advocate the use of Response Spectrum techniques (i.e. modal analysis) based on data from these fixed base tests. They offer engineers limited insight into how dynamic soil-structure interaction might affect the damper or structure response.

During base excitations in the field, the finite stiffness of the foundation-soil system beneath a structure implies a release in the rotational kinematic restraint of the frame, which can reduce deformations in the structure. In fact, Elghazouli (2017) classifies rocking isolation as a form of seismic base isolation, citing examples of structures engineered to rock about their foundations to limit input energy during shaking. Contrary to current seismic design practice, shifting plasticity from the superstructure and foundations down into the supporting soil can allow designers to utilise soil as a natural base isolator; this is known as natural rocking isolation.

Engineered rocking isolation about the foundation, and natural rocking isolation by soil deformation, were experimentally compared by Pelekis et al. (2018) using a geotechnical centrifuge. The reduced scale of the experimental packages, coupled with the realistic recreation of dynamic soil-structure interaction allowed for a faster, cheaper and more comprehensive experimental assessment of the overall soil-structure system response compared to fixed base shaking table tests. This is not the first time seismically protected structures were tested in a geotechnical centrifuge. Jabary and Madabhushi (2015) investigated the dynamic soil-structure interaction of structures fitted with tuned-mass dampers.

Capitalising on dynamic geotechnical centrifuge testing as a primary research tool, this study seeks to achieve the following objectives:

1. Develop miniature oil dampers that can be instrumented and incorporated into model structures for dynamic testing in a geotechnical centrifuge.

2. Recreate the dynamic response of MDOF structures fitted with inter-storey oil dampers at a reduced model scale.

3. Understand how the performance of structures fitted with inter-storey oil dampers is affected by inertial interaction at the foundation-soil interface during shaking.

4. Compare the dynamic response of shallow founded regular structures to that of equivalent frames fitted with inter-storey oil dampers.

1.3 Thesis Outline

The content of this investigation is organised into the following chapters:

Chapter 2 Literature Review

Introduces fluid damping technology in structures, followed by a review of previous research in this field, and in dynamic soil-structure interaction.

Chapter 3 Experimental Methodology & Model Structures

Presents an outline of centrifuge testing theory, equipment and model preparation, followed by the development of miniature oil dampers for use in model structures.

Chapter 4 Prediction of Fixed Base Dynamic Structural Response

Derives mathematical models for the miniature oil dampers as tested in the centrifuge, along with time-history predictions of fixed base centrifuge tests using simplified discrete models for the structures. Compares results from code-based Response Spectrum Analysis to numerical and experimental time-history data.

Chapter 5 Soil-Structure System Response

Examines the soil-structure system response of regular frames and damped frames for different base fixity conditions and excitations, including a brief investigation into how different damping levels in the damped structure affect inertial interaction at the foundation-soil interface.

Chapter 6 Seismic Demand on The Superstructures

Compares storey shear forces and inter-storey drifts between regular frames and their damped counterparts for different excitations and ground conditions. The effects of global frame rotations during soil-structure interaction on oil damper performance in the superstructure are quantified. The dissipation of seismic input energy during soil-structure interaction is estimated and tracked for the regular structures, and for the structures fitted with inter-storey oil dampers.

Chapter 7 Prediction of Dynamic Soil-Structure System Response

Compares numerical predictions obtained from simplified mathematical models of the soil-structure systems to experimental traces recorded in the centrifuge for both, the regular frames, and the damped frames fitted with oil dampers.

Chapter 8 Conclusions

Provides a summary of the findings reported in this thesis, followed by a discussion on the implications of this research, and potential for further work.

Chapter 2

Literature Review

2.1 Introduction

The conventional approach to seismic design of structures aims to prevent total collapse and loss of life for pre-defined design earthquake intensities. The procedure relies on the strength and ductility of lateral force resisting frames in a structure to provide the capacity required to resist inertial floor loads during shaking. Unfortunately, a design strategy based on utilising material ductility implies that permanent damage is inherently permitted at specific locations within the structure. Whilst this might be deemed acceptable in some structures, critical assets and prominent buildings often require immediate occupancy and operation post earthquake. This is especially true for high probability, weak to moderate seismic events. Engineering such structures to respond within the elastic range during shaking can lead to uneconomical member designs and may become impractical.

It is not uncommon for design engineers in these instances to resort to supplemental vibration control measures in the superstructure. These devices reduce seismic demand on a frame either through base-isolation techniques that physically separate the superstructure from the substructure and its associated ground motions, or through energy dissipative components incorporated directly into the lateral force resisting frames of a structure. The focus of this study will be on the latter.

Inter-storey supplemental damping devices in structures can be classified primarily into two categories: Active and Passive devices. The operation of active dampers in a structure requires an integrated assembly of sensors, control systems, and external power to generate the damping forces required for vibration control. Passive dampers on the other hand offer a cheaper, more reliable and durable alternative requiring no external power source and no control-loop feedback for their operation (Constantinou and Symans, 1993). These devices are activated by storey shear deformations which induce relative motion between the points of attachment of the dampers to the structural frame.

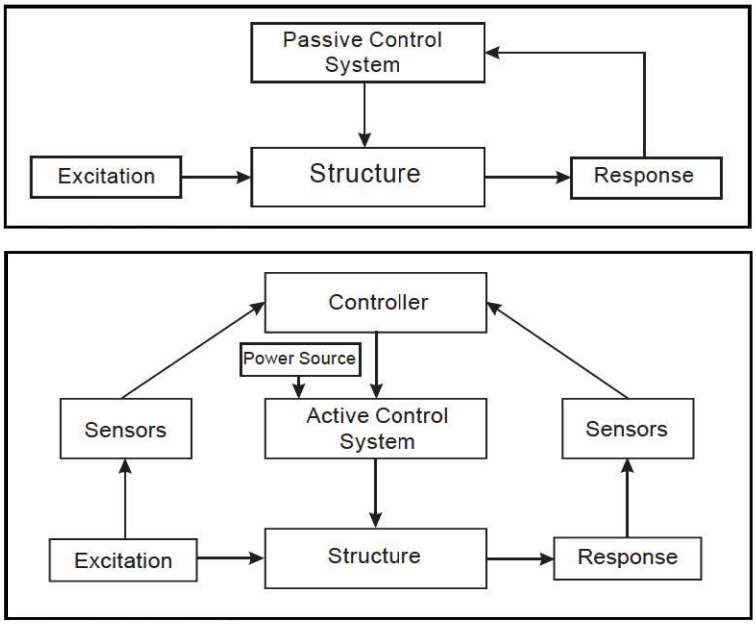

Fig. 2.1 Control system logic of passive and active dampers in structures (from Symans and Constantinou (1995)).

Figure 2.1 illustrates the operational logic for each of these control systems as visualised by Symans and Constantinou (1995). Passive structural dampers can be broadly classified into two categories, "hysteretic" and "visco-elastic" devices, depending on how they generate their resistive forces. Hysteretic dampers, such as friction dampers, buckling-restrained braces (BRBs), and yielding metal fuses, are "displacement-dependant" devices that develop forces proportional to frame deformations. By adding stiffness to the overall frame, these devices alter the dynamic characteristics of a structure and change its natural frequencies which may not always be desirable at specific sites.

Visco-elastic devices, such as visco-elastic solid materials, viscous walls, and fluid orificing dampers, are "velocity-dependant" devices producing forces that are primarily out-of-phase with peak frame deformations. These devices contribute to energy dissipation

within a frame with minimal alterations to structural stiffness and natural frequencies. The dependency of damping forces on velocity allows these devices to dissipate energy even at small elastic deformations, making them attractive solutions for mitigating both, wind loads and seismic loads, when compared to their displacement-dependant counterparts (Constantinou et al., 1998).

The focus of this study will be on the application of inter-storey oil dampers in structures as means of mitigating earthquake loads. The devices internally operate on the principle of forcing oil through orifices during damper activation, making them primarily viscous devices. Nevertheless, nonlinearities in the oil dampers, coupled with a structural connection to each floor in the frame, will also induce some "displacement-dependency, thus adding a stiffness component to the overall damper-brace assembly (Dong et al., 2016). Categorically, the dampers used in this study can be classified as visco-elastic passive devices once incorporated within the structural frames.

Civil applications of oil dampers in structures can be traced back to the early 1990's following a long successful history in military applications (Taylor, 2010). Since then, a plethora of structural engineering driven experimental and theoretical work has been undertaken to validate and optimise the performance of buildings fitted with fluid dampers. There remains however a gap in experimental verification of how these damped structures actually perform in the field when considering ground compliance beneath a building's foundations. Replicating such an experiment within the confinements of a shaking table prototype testing facility can prove to be expensive, labour-intensive, and impractical. Jabary and Madabhushi (2015) addressed this challenge by pioneering the application of dynamic geotechnical centrifuge testing to investigate the performance of model frames fitted with tuned-mass dampers. The reduced size of the model structures in the centrifuge, coupled with stress-strain similitude between the model soil column at "g" and its equivalent prototype, allow realistic dynamic soil-structure interaction behaviour to be replicated at a reduced scale.

This chapter aims to first introduce the concept of fluid damping technology in structures, followed by an overview of influential experimental shaking table research conducted in this field. Relevant literature on soil-foundation-structure interaction is then examined to understand how geometrical and material nonlinearities at the foundation-soil interface alter the dynamic response of structures. Mathematical modelling of foundation-soil systems for preliminary soil-structure interaction analysis is also reviewed. Lastly, results from coupled soil-structure numerical analysis of damped frames on compliant ground will be examined to shed light on how soil-structure interaction impacts damped frame performance.

2.2 Passive Fluid Dampers in Structures

2.2.1 Description of Damping Devices

Fluid damping devices operate on the principle of converting kinetic energy of the piston rod into thermal energy in the fluid by forcing it through small orifices machined into the damper piston head (Constantinou and Symans, 1992). Figure 2.2 visually illustrates the internal construction of two types of fluid dampers used in structural damping applications: (a) dampers with internal accumulators (b) dampers with run-through piston rods.

Once the dampers are activated, and assuming the piston rods in Figure 2.2 move to the right, the piston heads compress the damping fluid (silicone compound or oil) in chamber 2 and expand the volume of chamber 1. This pressure differential forces fluid to flow through carefully configured orifices in the piston heads, generating a force that is out-of-phase with damper displacements (Housner et al., 1997).

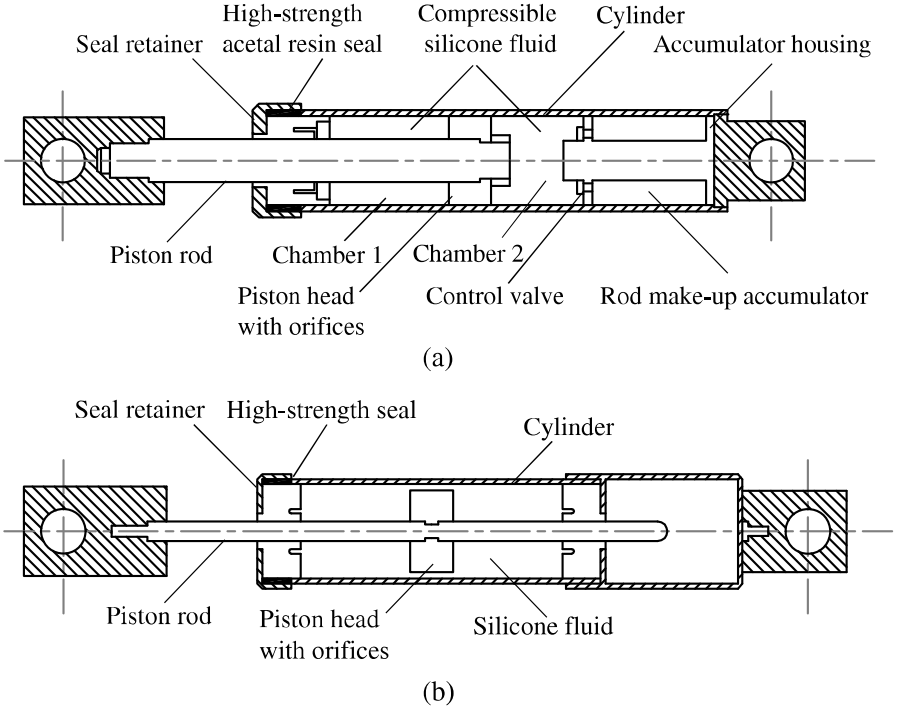

Fig. 2.2 Typical internal construction of fluid dampers used in structures according to Guo et al. (2015) with (a) internal oil accumulators and (b) run-through piston rods.

Given the compressibility of damping fluids, a restoring spring force would also arise if the volume of the piston rod going into the sealed damping chamber is not compensated for internally within the damper (Constantinou and Symans, 1993). For this reason, some manufacturers resort to internal rod make-up accumulators as shown in Figure 2.2 (a). In this

option, the volume of the piston rod going in (piston rod cross-sectional area $\times$ damper stroke) will displace an equal volume of damping fluid into the accumulator chamber through the control valves (Constantinou and Symans, 1993). Another option to replace the accumulator is a run-through piston rod design, as shown in Figure 2.2 (b). The volume of the piston rod going into the sealed chamber in this instance is simply equal to the volume of the rod going out, thus negating the effects of damper fluid compressibility.

Damper force-velocity relationships for these fluidic devices takes the generic form of:

$$F_d = C_0 \, |\dot{u}|^{\alpha} \, sgn(\dot{u}) \tag{2.1}$$

where F_d is the force, C_0 is the damping coefficient, $\dot{u}$ is velocity, $sgn(\dot{u})$ is the sign of velocity, and α is an exponent ranging from 0.25 to 2 depending on the piston head orifice design (Constantinou et al., 1998). Figure 2.3 illustrates the effects of α on damper force-velocity-displacement characteristics.

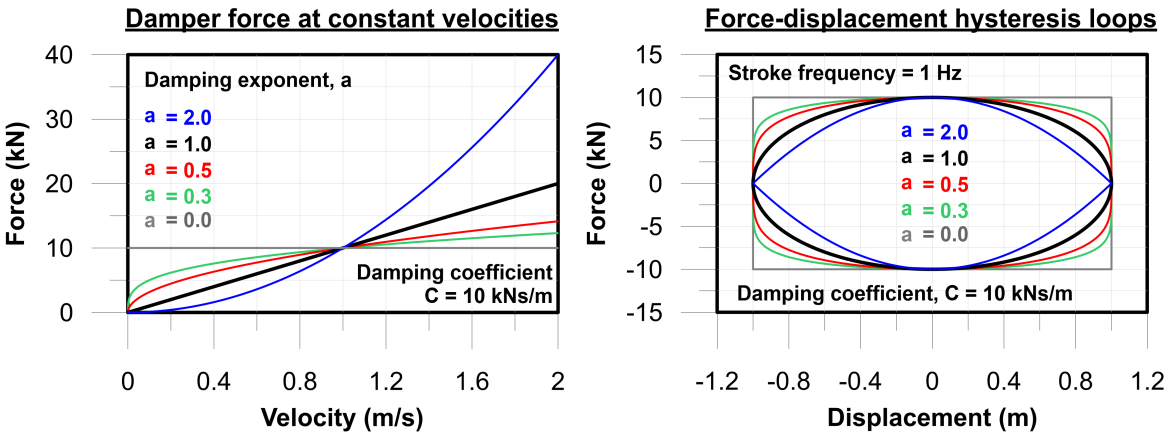

Fig. 2.3 Example application of Equation 2.1 for a random damper showing the effects of damping exponent α on damper force-velocity-displacement relationships.

For $\alpha = 0$, the device is effectively a friction damper with a distinctive rectangular hysteretic loop. Fluid dampers with cylindrical orifices machined through the piston head, also known as Bernoullian orifices, will exhibit an α exponent of 2. Such devices are not suitable for structural applications due to their ever increasing force-velocity relationship (Symans and Constantinou, 1998) as shown in Figure 2.3. This can be detrimental to structural connections and supporting members during strong excitations and high velocity inputs.

An α value of 1 is effectively a linear viscous damper with an elliptical force-displacement loop. These devices were among the first dampers to be tested experimentally in prototype frames (Constantinou and Symans, 1992; Reinhorn et al., 1995), and later on incorporated into early FEMA-273 (1997) design guidelines due to their simplicity in mathematical modelling and analysis. The linear force-velocity relationship of these dampers also makes them prone to developing high forces at high velocities which can damage supporting members (Lin and Chopra, 2002). Such devices nowadays see more damping applications in wind loading than in earthquake mitigation of structures (Taylor Devices Inc., 2019).

In the mid to late 1990's, preference was shifted to nonlinear dampers with α exponents less than 1 (Pekcan et al., 1999b; Seleemah and Constantinou, 1997; Taylor Devices Inc., 2019). The softening force-velocity relationship shown in Figure 2.3 for such devices helps limit peak damper forces at very high velocities making them more suitable for near-fault type ground excitations (Symans and Constantinou, 1998). Lin and Chopra (2002) showed that nonlinear dampers in elastic structures are capable of contributing similar levels of supplemental damping ratios as linear dampers would, with the added benefit of lower peak damper forces in the frames. Nevertheless, as shown in Figure 2.3, hysteresis loops for these nonlinear dampers take a more rectangular shape relative to the elliptical loops of linear dampers. Despite resulting in greater energy dissipation for the same displacement and force as a linear damper (Symans and Constantinou, 1998), the shape of the loop implies that higher damper forces will exist towards the end of the damper strokes (i.e. close to peak displacements). This can result in greater superposition of damper forces with restoring stiffness forces in frames, thus imposing additional stress demands on structural members that are already close to peak deformation (Lee and Taylor, 2001).

2.2.2 Analytical Modelling of Fluid Dampers

Equation 2.1 is a mathematical representation of only the viscous component of damping force. Depending on its internal construction and operation, a fluid device may also exhibit stiffness, and generate restoring forces if forced at high enough frequencies. Linear fluid dampers tested by Constantinou and Symans (1992), as well as nonlinear fluid devices tested by Seleemah and Constantinou (1997), all exhibited stiffness for driving frequencies higher than 4 Hz. Figure 2.4 presents results from damper component testing by Constantinou and Symans (1992), showing linear dampers with accumulators behaving more as viscoelastic devices above a cut-off frequency of 4 Hz.

Both linear and nonlinear dampers in the aforementioned studies used an internal accumulator to negate the effects of silicone oil compressibility. However, at high frequencies, control valves (refer to Figure 2.2) allowing oil into the accumulator may not respond as fast

as the piston rod going in/out of the sealed chamber, invoking damping fluid compressibility effects (Constantinou et al., 1998). Modern structural damper construction avoids these effects by using run-through piston rod designs to keep damper response as viscous as possible (Constantinou et al., 1998; Taylor Devices Inc., 2019). Nevertheless, once installed in-series with structural braces of finite stiffness in-between floors, the overall damper-brace system (even for ideal viscous devices) will exhibit a visco-elastic response (Dong et al., 2016; Fu and Kasai, 1998; Guo et al., 2015; Singh et al., 2003; Taylor Devices Inc., 2019).

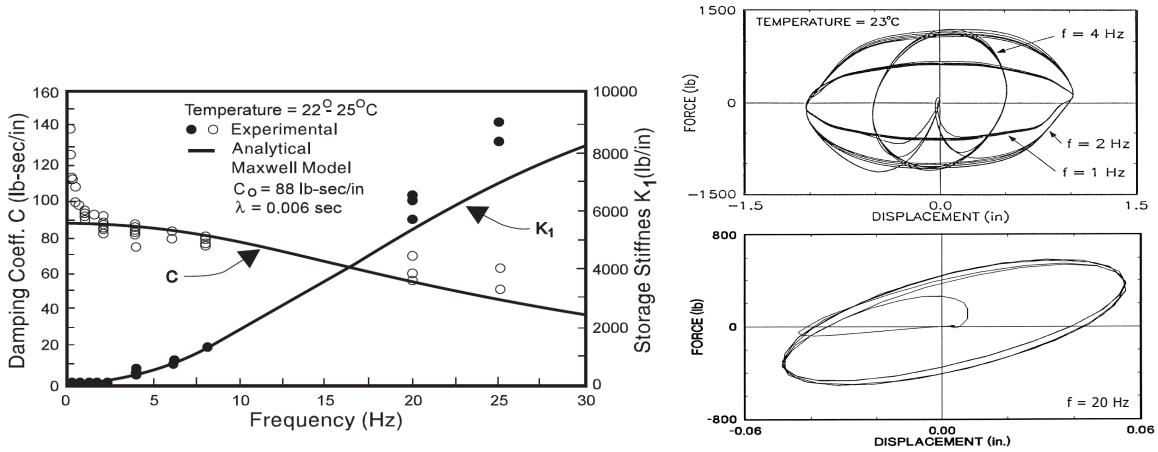

Fig. 2.4 Damping coefficients, storage stiffness, and hysteresis loops for linear dampers with internal accumulators at different driving frequencies as tested by Constantinou and Symans (1992).

Mathematical modelling of fluid dampers is mainly phenomenological in nature, derived from empirical data rather than from first principles. Different models have been proposed in literature for different devices. These are reviewed below.

Linear / Non-linear viscous dampers This approach models dampers as classical linear or nonlinear dashpots following Equation 2.1 only, thus neglecting internal damper stiffness and frequency dependency of the overall response. This was successfully implemented in time domain analysis by Constantinou and Symans (1992), Seleemah and Constantinou (1997), who adequately simulated experimental response of their test structures ignoring damper stiffening at higher structural modes.

Damper coefficients (C) and exponents (α) in this instance are obtained by curve-fitting through experimental force-velocity data extracted from sinusoidal dynamic testing of the devices. A typical schematic of a damper component testing rig, with example regressions from literature are shown in Figure 2.5.

At a component level, such a mathematical model would only be adequate if device component testing reveals limited stiffness in the dampers for the typical range of frequencies expected within a structure. At a damper-brace system level, Singh et al. (2003) showed that the effects of damper-brace flexibility on damper effectiveness can be minimised (i.e. modelling viscous component of damper force is sufficient) if brace stiffness is assigned to be at least five times that of the lateral storey stiffness.

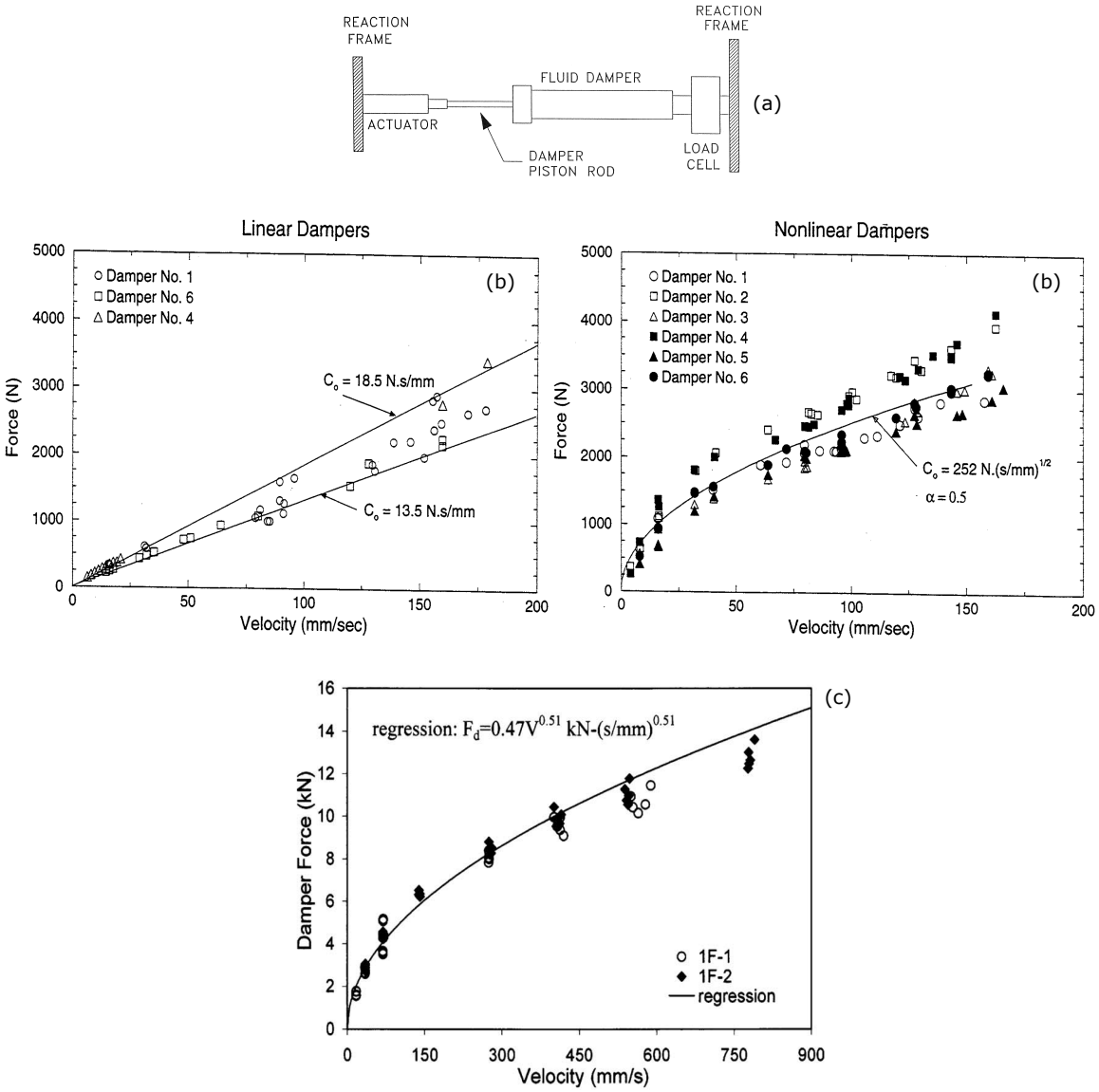

Fig. 2.5 (a) Schematic of damper component testing rig (Constantinou and Symans, 1992) (b) damper force-velocity regression from Seleemah and Constantinou (1997) (c) damper force-velocity regression from Chang et al. (2008)

Maxwell Model Fluid dampers exhibiting considerable stiffening with increasing driving frequencies are often modelled using an in-series arrangement of a linear spring and a linear dashpot (Constantinou and Symans, 1993; Greco and Marano, 2013; Reinhorn et al., 1995; Taylor Devices Inc., 2019) referred to as a Maxwell model. Damper force is given by:

$$F_d(t) + \lambda \dot{F}_d(t) = C_0 \, \dot{u}(t) \tag{2.2}$$

where $F_d(t)$ is the damper force, λ is the relaxation time ($\lambda = C_0/K_b$), K_b is brace stiffness, C_0 is damping coefficient at zero frequency, and $\dot{u}$ is velocity. The in-series spring in this model gives it the ability to capture the visco-elastic damper response across a wide range of frequencies. In the frequency domain, damper force can be written in terms of a dynamic modulus $K^*(\omega)$ (Reinhorn et al., 1995):

$$F_d(\omega) = K^*(\omega) \, u(\omega) \tag{2.3}$$

$$K^*(\omega) = K_1(\omega) + i \, K_2(\omega) \tag{2.4}$$

$$K_1(\omega) = K_b \left(\frac{(\lambda \ \omega)^2}{1 + (\lambda \ \omega)^2} \right) \tag{2.5}$$

$$K_2(\omega) = C(\omega) \ \omega \tag{2.6}$$

$$C(\omega) = C_0 \left(\frac{\omega}{1 + (\lambda \ \omega)^2} \right) \tag{2.7}$$

where K_1 is the storage modulus, K_2 is the loss modulus, $C(\omega)$ is damping coefficient at frequency ω. The solid black lines in Figure 2.4 demonstrate typical variation of K_1 and $C(\omega)$ with frequency. Defining damper characteristics in full in the frequency-domain makes the Maxwell model very attractive for use in Fourier transform methods of solving linear dynamic systems. The classical Maxwell model has been expanded by Makris and Constantinou (1991) to simulate a nonlinear spring in-series with a non-linear dashpot by employing fractional derivative calculus. Equation 2.2 now becomes:

$$F_d(t) + \lambda \frac{d^r \, F_d(t)}{dt^r} = C_0 \, \frac{d^q \, u(t)}{dt^q} \tag{2.8}$$

where r and q are the orders of the fractional derivates of the time dependant functions. In this instance, there are four parameters (λ,C_0,r, and q) which need to be fitted from experimental data. This is often achieved through parameter identification algorithms that try to match mathematical model results to experimental data from damper component testing (Greco and Marano, 2013).

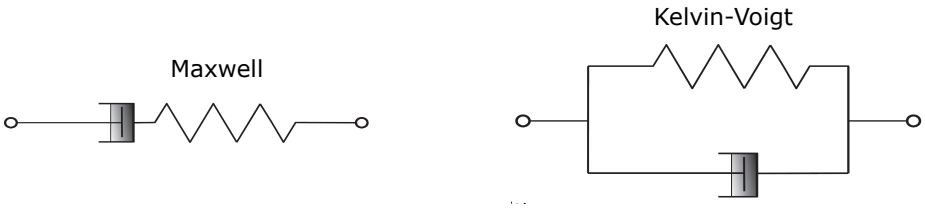

Fig. 2.6 Maxwell and Kelvin-Voigt mechanical models for visco-elastic material behaviour (Greco and Marano, 2013).

Kelvin-Voigt Model In this mathematical model, a linear spring is connected in parallel to a linear dashpot as shown in Figure 2.6 to simulate a visco-elastic response. Damper force is given by:

$$F_d(t) = K\ u(t) + C\ \dot{u}(t) \tag{2.9}$$

where K is spring stiffness, and C is damping coefficient. In the frequency domain, damping force can be written in the same form as Equation 2.3, but now the storage modulus for the linear spring is constant with frequency:

$$K_1(\omega) = K \tag{2.10}$$

and the loss modulus varies linearly with frequency:

$$K_2(\omega) = C\ \omega = \frac{W_d}{\pi\ {u_0}^2} \tag{2.11}$$

where W_d is the energy dissipated by the dashpot in one cycle of amplitude u_0 at a frequency of w. This linear mathematical model is able to capture the correct damper behaviour at one specific frequency, but does not accurately represent the viscoelastic behaviour at a range of frequencies (Greco and Marano, 2013; Shukla and Datta, 1999).

The Kelvin-Voigt model has also been expanded in literature to include a nonlinear spring in parallel combination with a nonlinear dashpot (Greco and Marano, 2013; Jozwiak et al., 2015; Terenzi, 1999). Equation 2.9 becomes:

$$F_d(t) = K\ u(t)^{\beta} + C\ \dot{u}(t)^{\alpha} \tag{2.12}$$

where β is the order of the spring polynomial, and α is the fractional power exponent of the dashpot. This higher order model allows for variation of storage and loss moduli with frequency, thus increasing the flexibility of its applications.

2.2.3 Simplified Analysis of Buildings With Fluid Dampers

Response Spectrum Analysis (RSA)

Following the 1989 Loma Prieta and 1994 Northridge earthquakes, a measurable increase in market demand for fluid-orificing structural dampers prompted SEAONC (Structural Engineers Association of Northern California) to issue a force-based design documentation specifying procedures and requirements for damped systems (Ramirez et al., 2001). At the early stages of the technology, engineers were required to design and detail frames for the full base-shear of a regular bare frame, but rely on dampers to achieve drift requirements (Ramirez et al., 2001). This then evolved to NEHRP - National Earthquake Hazard Reduction Program (1994), in which base shear calculated from 5 % damped elastic response spectrum is reduced using factors derived by Wu and Hanson (1989) to reflect the desired damping ratio. These reduction coefficients were independent of the structural natural frequency, which was a gross approximation given that studies close to that time by Newmark and Hall (1982), as well as Ashour and Hanson (1987), showed different regions of the response spectrum exhibiting different magnitudes of reduction for increasing damping ratios (Ramirez et al., 2001).

The procedures currently available for analysing the response of damped structures are primarily based on guidelines published in FEMA-273 (1997). The document introduced four simplified displacement-based procedures that superseded the seismic force-based approaches used before. The analysis procedures were: (1) linear static (also known as Equivalent Lateral Force-ELF) (2) linear dynamic (also known as Response Spectrum Analysis-RSA) (3) nonlinear static and (4) nonlinear dynamic. For linear elastic structures with viscous dampers, RSA is often implemented during preliminary analysis. Figure 2.7 summarises the fundamentals of the RSA procedure according to FEMA-273 (1997).

In Step 2 of the procedure detailed in Figure 2.7, the 5 % damped pseudo-acceleration spectrum is modified by reduction factors to reflect the added damping. These factors vary for different regions of the response spectrum following coefficients modified from Newmark and Hall (1982). This is graphically illustrated in Figure 2.8. The proposed reduction factors in FEMA-273 (1997) can be misleading as they show greater reductions in response for short-period structures than for long-period frames, hence mistakenly implying that dampers are more effective in stiff than in flexible structures (Ramirez et al., 2001).

This was the subject of study and refinement by Ramirez et al. (2001), who mathematically regressed new reduction factors shown in Figure 2.8. The coefficients were further simplified and adopted in Chapter 18 of ASCE 7-16 (2016), which now represents the latest guideline on the design of structures with supplemental dampers.

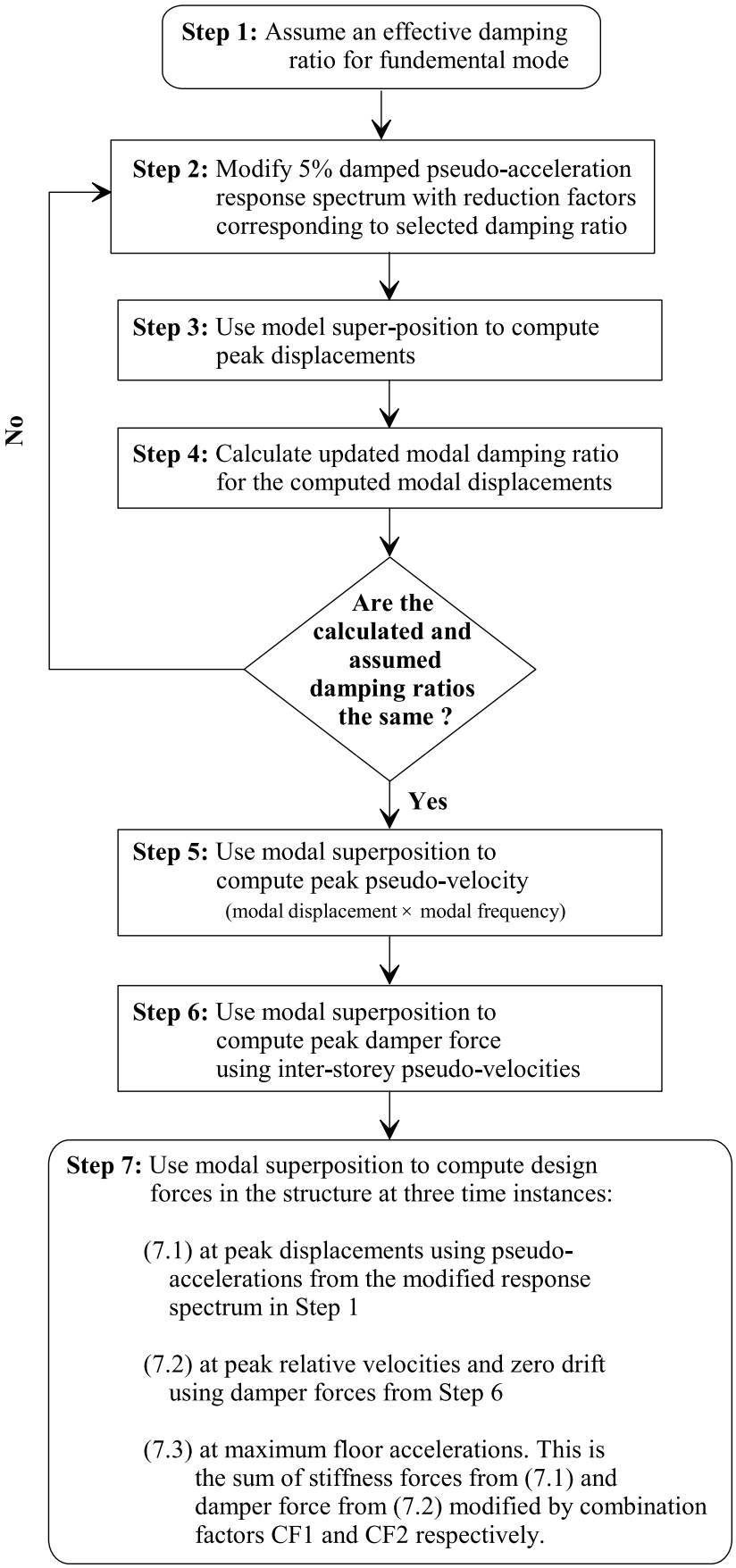

Fig. 2.7 Response Spectrum Analysis (RSA) procedure for linear structures with viscous dampers as per FEMA-273 (1997).

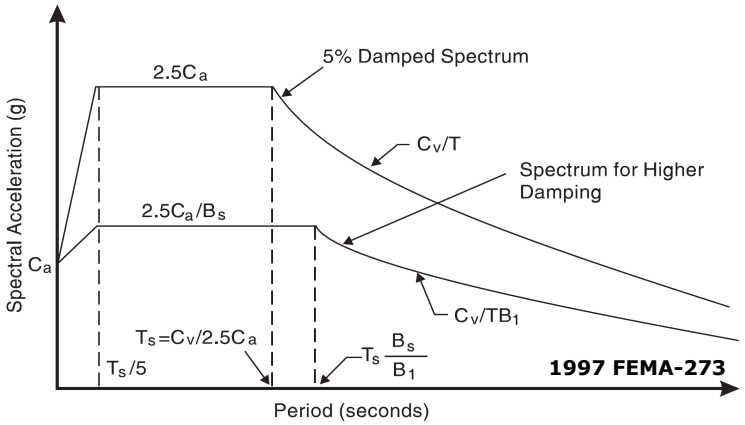

B_s : Reduction Factor in Short-Period Range
B_1 : Reduction Factor in Long-Period Range
C_a : effective peak acceleration coefficient
Cv : effective peak velocity coefficient

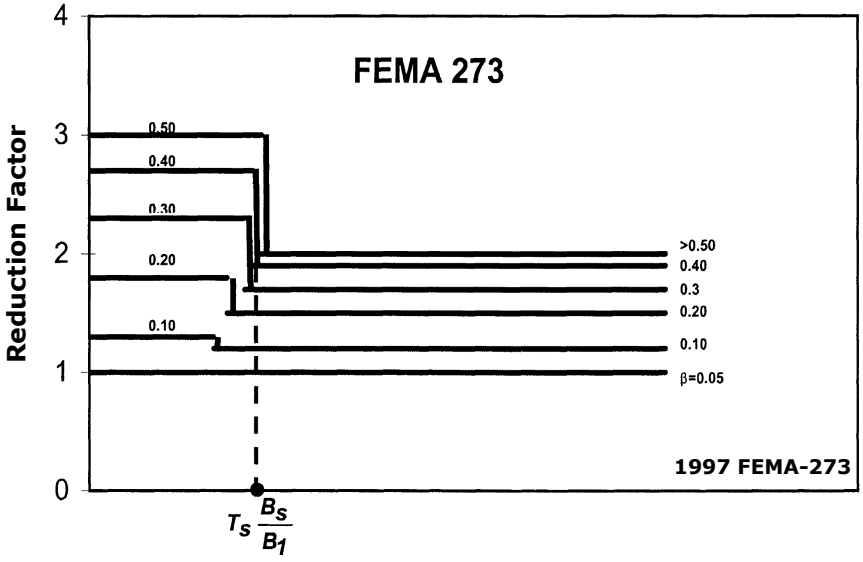

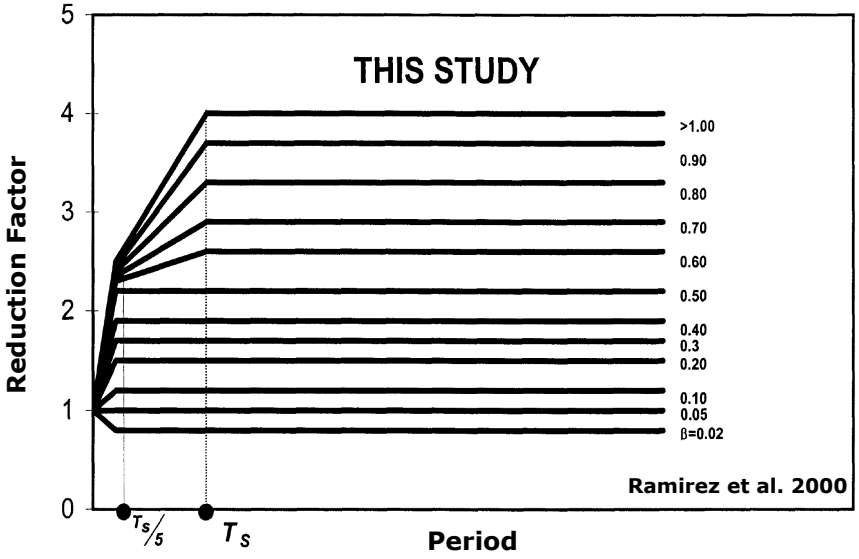

Fig. 2.8 Modifications to 5% damped pseudo-acceleration spectrum to account for higher damping as per 1997 FEMA-273 (1997) and Ramirez et al. (2001).

Step 4 of the procedure in Figure 2.7 requires a mathematical relationship between modal damping ratio, damping coefficient of the added viscous devices, and modal displacements. Constantinou and Symans (1992) derived an equation for modal damping ratio using basic energy considerations applicable only to linear viscous dampers. This was expanded by Soong and Constantinou (1994) to account for nonlinear viscous dampers by introducing a dependency of damping ratio on damping exponent α, and on modal displacements. Soong and Constantinou (1994) effectively linearised the nonlinear damper by computing an equivalent viscous damper that would dissipate equal levels of energy in one cycle at the modal frequency. This approaches underpins what FEMA-273 (1997) recommends. Pekcan et al. (1999b) proposed a refined equivalent power consumption approach in which power of a nonlinear damper in one cycle (i.e. area under force-velocity plot) is equated to that of an equivalent linear viscous damper at a specific modal velocity and frequency. Although the resulting damping ratio estimates were closer to numerical results than the conventional energy approach, the method is yet to be incorporated into design guidelines.

With modal damping ratios estimated, and peak displacements computed from superposition of modal displacements, an estimate of the expected viscous damper forces in Step 6 of the RSA procedure can be made using inter-storey velocities. Design guidelines conveniently use spectral pseudo-velocities for this purpose despite its inaccuracies for systems with non-classical high damping. To address discrepancy between actual velocities and pseudo-velocities, Pekcan et al. (1999b); Ramirez et al. (2001); Sadek et al. (1999) proposed velocity correction factors using empirically derived transformations to approximate actual modal velocities from spectral pseudo-velocities for different structural periods at high damping ratios. The effects of pseudo velocity-correction are neatly illustrated in Figure 2.9.

The last step of the RSA procedure is critical as it evaluates maximum storey shear forces to be used in member sectional design. For conventional structures with low damping, spectral pseudo-accelerations (i.e. accelerations at peak spectral displacements) can be used to evaluate storey forces. However, for heavily damped systems, peak absolute accelerations do not coincide with peak displacements in the frame; maximum storey shear forces (i.e. absolute accelerations) occur ahead in time as a result of super-imposing velocity-dependant damper forces over displacement-dependant stiffness forces in the structure. Step 7.3 addresses this by taking the sum of peak stiffness forces and peak damper forces, each multiplied by a combination factor CF1 and CF2 respectively. FEMA-273 (1997) proposes equations for these factors for linear viscous devices, which were expanded by Ramirez et al. (2001) to account for nonlinear viscous devices.

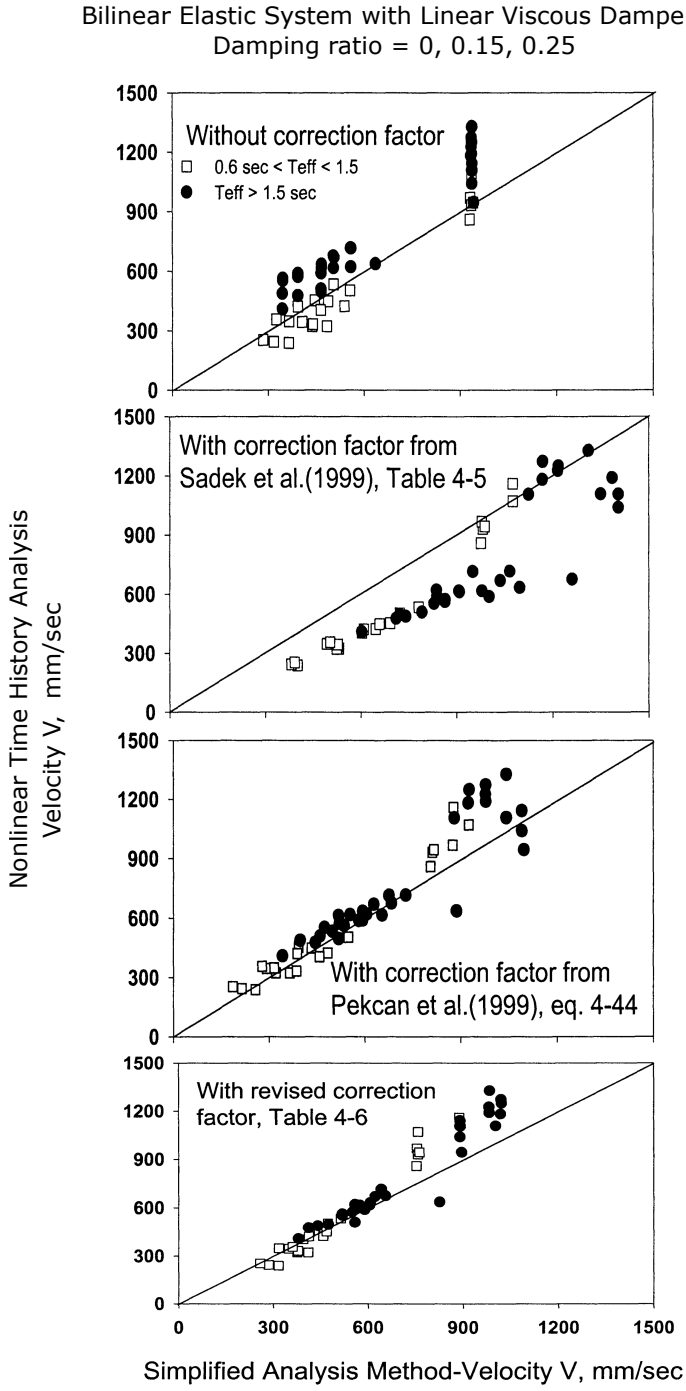

Fig. 2.9 Numerical velocity predictions compared to corrected spectral pseudo-velocities from Ramirez et al. (2001).

Application of RSA, and the equations involved in every step of the procedure will be examined further in section 4.5 of Chapter 4 of this study. The appeal of RSA in ASCE 7-16 (2016) is its utilisation of design spectra, a very common tool amongst design engineers for rapid preliminary design estimates. Central to this process is the modal superposition method, based primarily on the assumption of a classically damped system with real-valued natural frequencies and orthogonal modes. Damped structures are often non-classically damped. Solution of a generalised eigenvalue problem is required in this instance to compute natural frequencies and complex-valued mode shapes of the system.

Constantinou and Symans (1992) compared estimates of modal damping ratios obtained from a complex eigenvalue analysis to those obtained using frequencies and mode shapes assuming an undamped system. The structure examined was a 3-DOF prototype test frame equipped with linear viscous dampers. The assumption that frequencies and mode shapes of the non-classical damped structures can be approximated by those of an equivalent undamped system was found to be acceptable for the fundamental mode, and adequate for higher modes. The initial assumption of using undamped natural frequencies and mode shapes in simplified analysis procedures has become commonplace for preliminary design.

Procedures For Dimensioning Viscous Dampers

Whilst RSA provides a simple analysis tool for assessing the response of damped structures, it does not provide structured guidance to engineers on how to size dampers to achieve a specific target performance. Literature on this subject is dominated by computer-based algorithms that attempt to identify optimal damper sizing and placement in a structure by solving a constrained optimisation problem; the constraint imposed is typically on the sum of the added damping coefficients in the structure, a parameter closely associated with total damper cost. Optimisation procedures adapted in literature for this purpose typically include the genetic algorithm method (Mitchell, 1996), the sequential search algorithm (Zhang and Soong, 1992), and the more analytical gradient-based search method. Domenico et al. (2019) offers a more comprehensive description of each of these optimisation procedures.

Grounded in the theory of natural selection and evolution, the genetic algorithm method refines a random population of possible solutions, over multiple iterations, until the best solution to an optimisation problem is attained. The fitment of each solution is assessed based on an objective function, in this case, on minimising a specific performance index (inter-storey drift, acceleration, storey shear) in the damped structure. Applications of this method can be found in Liu et al. (2005); Silverstri and Trombetti (2007); Singh and Moreschi (2002); Zhao et al. (2017). Another popular optimisation technique is the inverse-problem approach developed by Takewaki (1997), as an example of a gradient-based search method.

This is an incremental procedure that identifies the damping coefficients and distribution of dampers in a structure so as to minimise the sum of amplitudes of the inter-storey drifts transfer functions (Domenico et al., 2019). Details of the mathematical steps involved in the procedure, along with numerical applications for different types of structures and support conditions can be found in Takewaki (2009).

These complex computer-based algorithms, while common in literature, are often not accessible to all engineers who would rather have a damper sizing and placement procedure grounded in established engineering principles. To that extent, placement strategies such as the uniform distribution of dampers along a building's height, a stiffness proportional distribution of damping coefficients in a structure, or one that is proportional to storey shear force (Pekcan et al., 1999a) and storey shear strain energy (Hwang et al., 2013) remain popular in practice due to their simplicity. Domenico et al. (2019) provides a comparison of these damper placement strategies for the case of a six storey shear frame structure.

Christopoulos and Filiatrault (2006) proposed a trial-and-error approach which utilises an equivalent fictitious braced structure to identify the damping coefficients required in the original frame to achieve a specific damping ratio. The stiffness of the virtual braces is distributed over the height of the fictitious structure following the distribution of inter-storey lateral stiffness of the original frame (i.e. Stiffness Proportional Damping). This distribution pattern is essential to ensure the fictitious braced structure has similar mode shapes to the original bare frame. Stiffness coefficients of these virtual braces are varied through iteration until the undamped fundamental frequency of the fictitious braced frame is equal to the damped fundamental frequency of the original structure. The brace stiffness coefficients are then mathematically correlated to damping coefficients of linear dampers, which can then be transformed into equivalent nonlinear dampers following the energy-equivalency approach discussed earlier in the RSA procedure.

Silvestri et al. (2010) proposed a simpler more direct method of computing damper properties for a specific damping ratio in a shear-type structure, without resorting to trial-and-error, without fictitious braces, and gives the designer more options on how to distribute the dampers across the height of the structure; damper placement is not limited to a stiffness proportional distribution as in Christopoulos and Filiatrault (2006). The process is summarised in Figure 2.10. Palermo et al. (2016, 2018) streamlined this procedure even further by proposing analytical equations that approximate inter-storey velocities for shear-type frames without having to conduct the numerical time-history analysis in Step 3.

Regardless of what procedure is selected from the literature highlighted above, it appears that the exercise of initial sizing of oil dampers in literature is confined to modal analysis in the frequency domain. The issues associated with this will be highlighted next, as the procedure summarised in Figure 2.10 is explored.

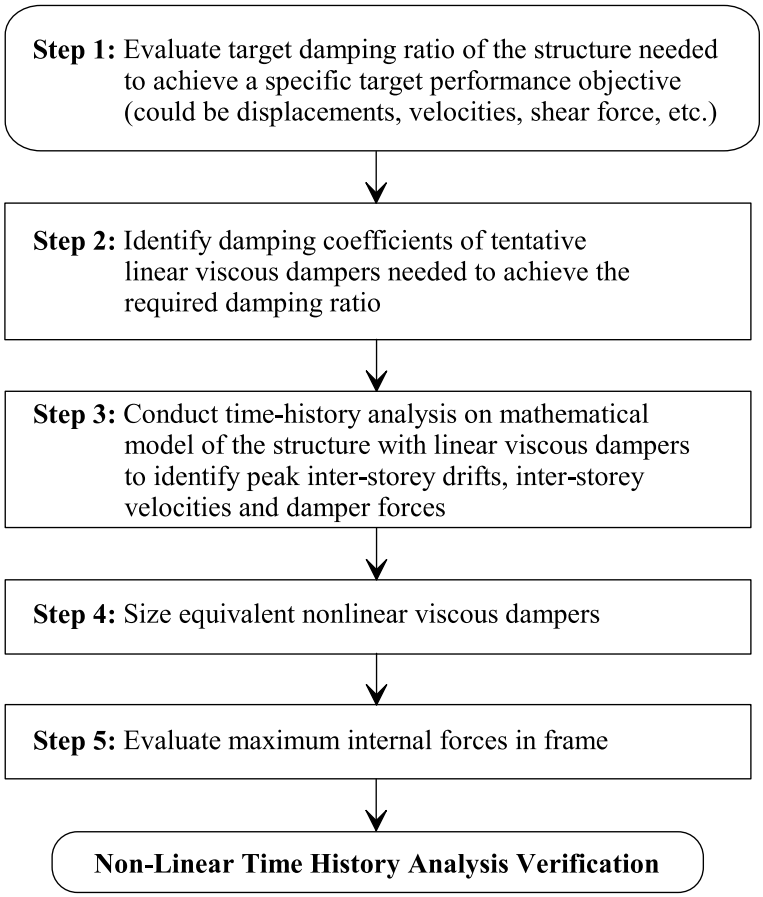

Fig. 2.10 Direct 5-step procedure for dimensioning linear/nonlinear viscous dampers in structures and analysing their performance (Silvestri et al., 2010).

Step 1: Selecting damping ratio The benefits of added viscous damping in a structure vary depending on the structure fundamental period. Any attempt at deriving response reduction factors for different damping ratios over a wide range of structural frequencies will be statistical in nature, only as good as the size and characteristics of the database used in the derivation. Silvestri et al. (2010) solved equations of motion for numerous SDOF systems, of various periods and damping ratios, for 40 input acceleration records of different intensities, in order to produce the statistical relationship shown in Figure 2.11.

Spectral parameters for a 5 % damped elastic system would be computed first, then the reduction factor needed to satisfy performance targets is identified, and the corresponding damping ratio is read off the mean curve in Figure 2.11.

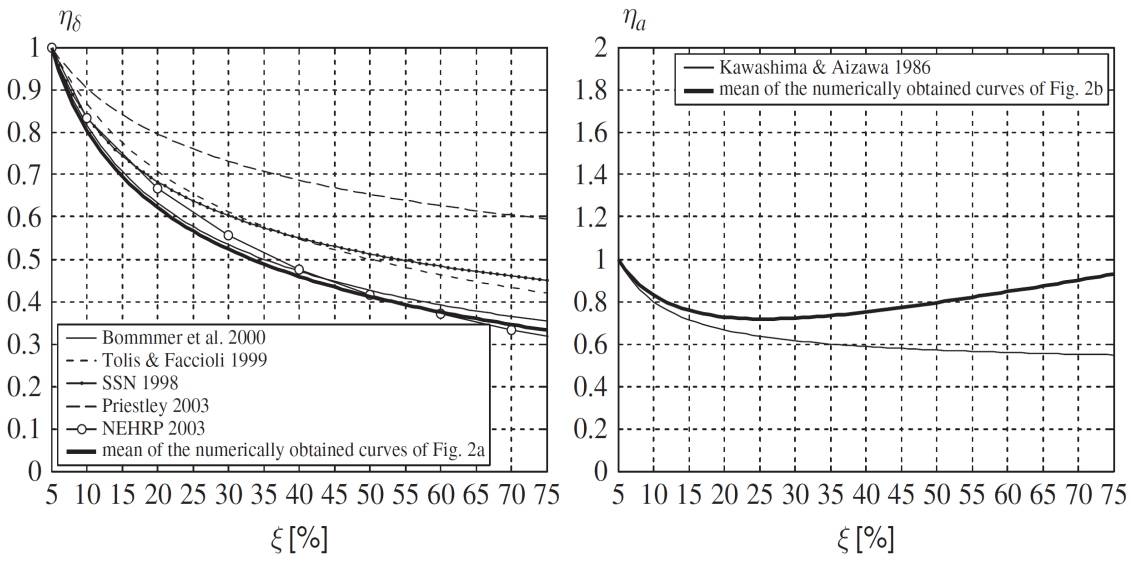

Fig. 2.11 Mean displacements reduction factor (η_δ) and mean accelerations reduction factor (η_a) for increasing damping ratios according to Silvestri et al. (2010).

Step 2: Identifying tentative linear viscous damper coefficients Working in the frequency domain while assuming orthogonal modes for the structure implies that the system damping matrix is restricted to a classical one. This is incorrect, especially for nonlinear oil dampers that tend to be prevalent in seismic protection applications in structures. The available classical damping matrix options are visualised in Figure 2.12.

Given that viscous dampers are most likely to be installed in between floors of a frame, the resulting damping effects are more akin to stiffness-proportional damping as depicted in Figure 2.12 (d). For this layout, the damping coefficient of each single damper at the j-th storey, and the damping matrix, are computed by (Silvestri et al., 2010):

$$c_j = \left(\frac{2\,\zeta_1}{\omega_1}\right)\frac{k_j}{n_j}$$

$$[C] = \frac{2\,\zeta_1}{\omega_1}\,[K] \tag{2.13}$$

where ζ_1 is the damping ratio at the first mode, ω_1 is the fundamental circular frequency, k_j is the lateral storey stiffness of the j-th floor, and n_j is the number of dampers at the jth storey.

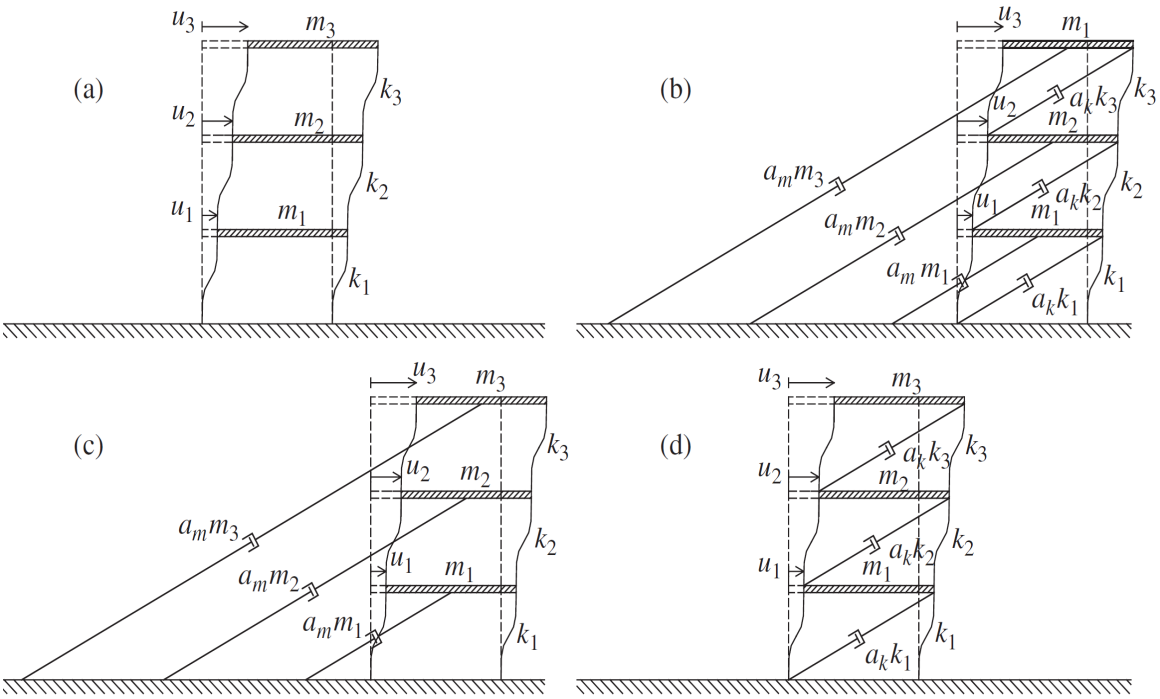

Fig. 2.12 (a) Undamped structure (b) Rayleigh classical damping (c) Mass-proportional damping (d) Stiffness proportional damping (from Silvestri et al. (2010)).

The problem is that during preliminary damper sizing for a MDOF structure, evaluating accurate storey stiffness, hence a stiffness-proportional damping matrix can be difficult, particularly for large structural systems (Silvestri et al., 2010). Lumping of mass m_j at each storey of the MDOF is a more straight forward process. For mass-proportional damping, the damping coefficient of each single damper at the j-th storey, and the damping matrix are computed by (Silvestri et al., 2010):

$$c_j = (2\ \zeta_1\ \omega_1)\ \frac{m_j}{n_j}$$

$$[C] = 2\ \zeta_1\ \omega_1\ [M] \tag{2.14}$$

where m_j is the floor mass, and n_j is the number of dampers at the jth storey. The ease at which the mass matrix can be constructed prompted Silvestri et al. (2010) to develop a

correlation factor that relates mass-proportional damping to stiffness-proportional damping:

$$\zeta_1^{SPD} = \Lambda_1 \, \zeta_1^{MPD} \tag{2.15}$$

$$\Lambda_1 = \frac{m \, \omega_1^2}{k}$$

where ζ_1^{SPD} is stiffness-proportional damping ratio and ζ_1^{MPD} is mass-proportional damping ratio, m and k are storey mass and storey stiffness respectively. The equation was derived mainly for shear-type buildings with uniform mass and uniform stiffness distribution along their height. Trombetti and Silvestri (2006) have another relationship to approximate $\frac{1}{\Lambda_1}$:

$$\frac{1}{\Lambda_1} = \frac{k}{m \, \omega_1^2} \approx \frac{N(N+1)}{2} \tag{2.16}$$

where N refers to the total number of storeys in the shear-type structure. The approximation is visually illustrated in Figure 2.13. From this relationship, the sum of all linear damping coefficients in a structure with stiffness-proportional damping can be estimated without evaluation of storey stiffness (Silvestri et al., 2010):

$$c_{total} = \zeta_1^{SPD} \, \omega_1 \, m_{total} \, N(N+1) \tag{2.17}$$

where m_{total} is the total mass of the building, and N is the number of storeys in the shear-type structure. The total damping coefficient in Equation 2.17 can be distributed in different ways across the height of the structure. For uniform dampers at all floors, damping coefficient for each damper at the j-th storey becomes:

$$c_j = \zeta_1^{SPD} \, \omega_1 \, m_{total} \left(\frac{N+1}{n_j} \right) \tag{2.18}$$

Step 3: Evaluating peak inter-storey velocities and drifts for linear dampers At this stage, with the initial damping coefficients set, Silvestri et al. (2010) calls for a numerical analysis to estimate inter-storey drifts, velocities, and verify structural response. Palermo et al. (2016, 2018), on the other hand, suggests solving further analytical equations to approximate peak inter-storey velocities and drifts; the authors allow for two deformation shapes: (1) shear profile [typical of stiff beam-flexible column arrangements] (2) linear profile [typical of moment-resisting frames]. Further correction factors applied to the estimated velocities and drifts would be required to account for higher structural modes.

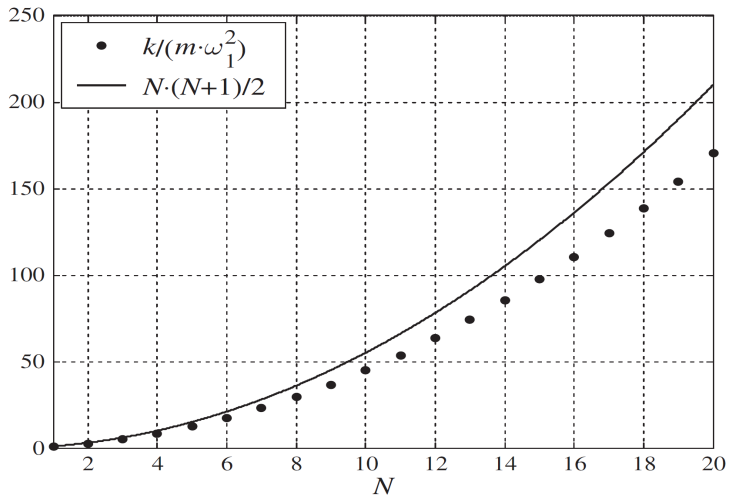

Fig. 2.13 Approximating ratio of mass-proportional damping to stiffness-proportional damping for different N number of floors in shear-type structures from Silvestri et al. (2010).

Step 4: Sizing equivalent nonlinear dampers The equivalent energy approach is used to size equivalent nonlinear dampers; nonlinear devices should dissipate the same amount of energy as the tentative linear dampers for the peak inter-storey drifts, inter-storey velocities and fundamental structural frequency estimated from Step 3. Silvestri et al. (2010) derives the following equation to estimate the nonlinear damping coefficient, c_{NL}:

$$c_{NL} \approx c_L \, (0.8 \, v_{max})^{1-\alpha} \tag{2.19}$$

where c_L is the linear damping coefficient from Step 2, v_{max} is peak inter-storey velocity from Step 3, and α is the damping exponent as available from the damper manufacturer. Of course this transition from linear to nonlinear damper is only correct at the fundamental frequency of the structure; the nonlinear dampers will be dissipating different energy levels at other frequency inputs during shaking.

Step 5: Equivalent Static Analysis (ESA) This step is similar to Step 7 in the RSA procedure in which internal actions in the frame are evaluated assuming equivalent static forces applied at different stages of the response: (1) ESA1 at peak lateral frame deformations (2) ESA2 at peak inter-storey velocities, by replacing viscous dampers with rigid diagonal stressed braces reflecting damper forces. This is visually illustrated in Figure 2.14.

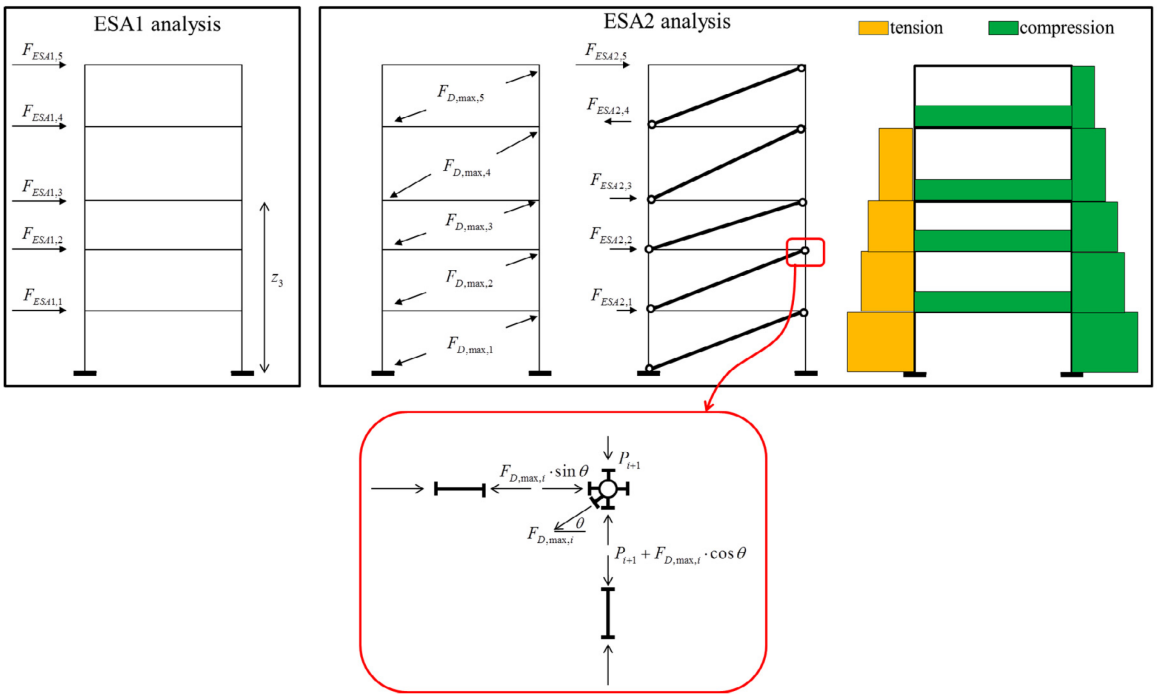

Fig. 2.14 Checking internal frame actions for two Equivalent Static Analysis (ESA) cases: ESA1 at peak lateral frame deformations, and ESA2 at peak inter-storey velocities (Palermo et al., 2018).

Rather than aiming to reduce complexity for engineers looking to size dampers during early stage design, the procedure suggested above immerses the designer into statistically derived factors, approximate correlations, crude assumptions about the system damping matrix, and linearisation of nonlinear dampers. Chapters 4 and 7 of this study seek to demonstrate the ease within which parametric damper sizing can be accomplished in the time domain using lumped-parameter models that can incorporate different nonlinear force-velocity relationships for the dampers (i.e. dashpots) being considered in design.

2.2.4 Experimental Testing of Damped Structures

Experimental investigations into the performance of viscous damped structures in literature have so far been restricted to large scale shaking table testing of prototype frames equipped with inter-storey viscous dampers. These damped frames are either scaled down from real prototype structures following laws of similitude (Chang et al., 2008; Constantinou and Symans, 1992; Reinhorn et al., 1995; Seleemah and Constantinou, 1997), or are actual full-scale prototypes erected on massive shaking-tables (Dong et al., 2016; Kasai and Matsuda, 2014).

Figure 2.15 lists key experimental studies, showing the evolution of shaking table testing of viscous damped frames with time. The list is by no means comprehensive, but demonstrates a trend of increasing complexity in replicating the in-field performance of damped structures within a controlled testing environment. A review of the experimental work highlighted in Figure 2.15 revealed the following prevalent observations :

1. Installing inter-storey velocity-dependant devices into structural frames results in small changes to the modal properties of the bare structure, with minor stiffening effects induced by the elasticity of the damper-brace assembly.

2. Uniform distribution of oil dampers across the height of a structure suppresses its higher modes, thus restricting response primarily to the fundamental frequency.

3. Experimentally derived transfer functions of damped structures show a wider frequency band-width at the fundamental mode compared to regular frames. Supplemental damping reduces transfer function peaks considerably making identification of modal frequencies challenging.

4. For base excitations that keep bare frames within limits of elasticity, installation of viscous dampers result in significant simultaneous reductions in storey drifts, storey accelerations, and storey shear forces; such simultaneous reductions in drift and forces were not possible for friction dampers, yielding metal fuses and other hysteretic dampers. This level of damper control is reduced when comparing a damped frame to a regular frame undergoing plastic deformation.

5. Nonlinear fluid dampers provide greater control over inter-storey drifts than their linear counterparts. This comes at a cost of higher storey shear forces as nonlinear dampers generate higher forces at low velocities.

6. Elasticity in the load path from the dampers to the lateral force resisting frame can void the the concept of zero fluid damping force occurring at peak frame deformations. The super-positioning of a component of the velocity-dependant damper force over stiffness forces in the frame stiffens up the overall response slightly, and imposes additional axial load demands on the columns. During plastic deformation of the columns, axial demands from the nonlinear dampers can exacerbate $P-\Delta$ effects in the frame.

In all of the aforementioned studies, test frames are bolted down to rigid shaking tables, thereby neglecting any subsoil flexibility or inertial interaction that may occur in the field. By doing so, energy dissipation is confined to the superstructure. An increasingly popular trend among researchers these days is to permit foundation rocking during seismic shaking as means of natural base isolation and energy dissipation (Anastasopoulos et al., 2010; Gelagoti et al., 2012; Grange et al., 2009; Kim et al., 2015; Kourkoulis et al., 2012; Pelekis et al., 2018). Investigating this experimentally using large-scale shaking table tests quickly becomes unfeasible and impractical. Dynamic geotechnical centrifuge testing offers a promising alternative. Recently, researchers have been successful at testing intricate reduced-scale structural models under the high gravity field of the centrifuge. Some model structures were designed to mimic beam-column nonlinearities (Mason et al., 2013; Trombetta et al., 2013), others were equipped with tuned-mass dampers for vibration control (Jabary and Madabhushi, 2015), and some structures were even fitted with metal-fuses to compare structural rocking to traditional foundation rocking (Pelekis et al., 2018), all whilst considering the effects of foundation-soil impedance.

This study aims to pioneer the application of miniature oil dampers for use in vibration control of model structures in the centrifuge. Concurrent dynamic testing of damped and bare frames allow for an interesting comparison to be made between the dynamic performance of bare frames invoking natural energy dissipation at the foundation-soil interface, to the performance of damped structures equipped with costly supplemental dampers.

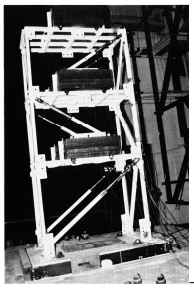

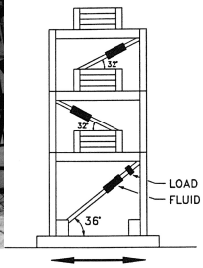

1992 Constantinou and Symans
State University of New York at Buffalo
1:4 scaled steel frame, 3 storeys
1.23 m wide × 2.54 m tall
Elastic structure
Linear viscous dampers
8 - 18 % added damping

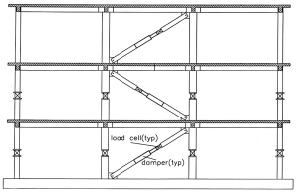

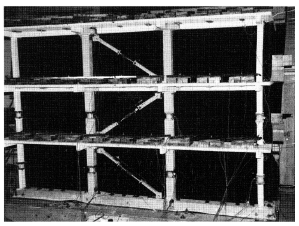

1995 Reinhorn, Li and Constantinou
State University of New York at Buffalo
1:3 scaled reinforced concrete frame, 3 storeys
5.59 m wide × 3.66 m tall
Inelastic structure
Linear viscous dampers
13 - 22 % added damping

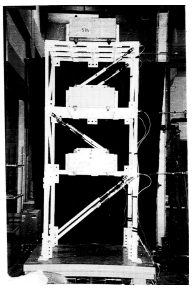

1997 Seleemah and Constantinou
State University of New York at Buffalo
1:4 scaled steel frame, 3 storeys
1.23 m wide × 2.54 m tall
Elastic structure
Linear / Nonlinear viscous dampers
10 - 19 % added damping

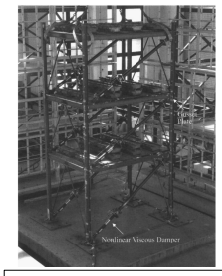

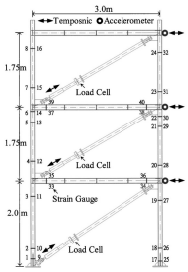

2008 Chang, Lin and Chen
National Center for Research on Earthquake Engineering
1:1.5 scaled steel frame, 3 storeys
3.0 m wide × 5.5 m tall
Elastic structure
Nonlinear viscous dampers
14 % added damping

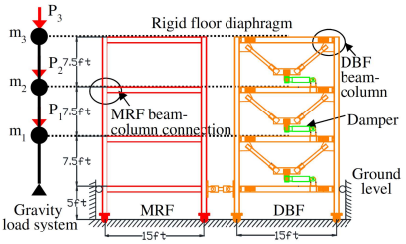

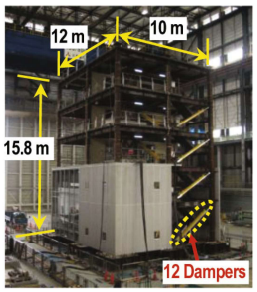

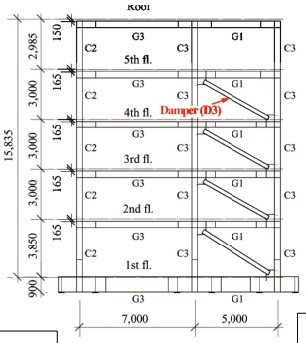

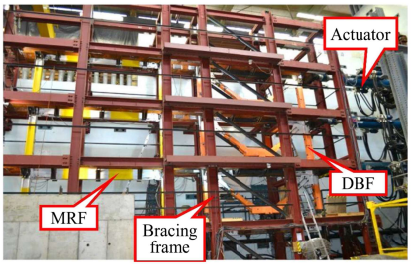

2014 Kasai, Matsuda
E-Defense, Miki, Japan
5 storey full-scale prototype
12.0 m wide × 15.8 m tall
Nonlinear viscous dampers
~ 17 % added damping

2016 Dong, Sause and Ricles
ATLSS Engineering Research Center, Lehigh University
1:1.7 scaled steel frame, 3 storeys
9.1 m wide × 8.4 m tall
Nonlinear viscous dampers
30 - 41 % added damping

Fig. 2.15 Evolution of experimental testing of frames equipped with viscous damping devices.

2.3 Dynamic Soil-Structure Interaction

2.3.1 Modelling Foundation-Soil Interaction

The complexity of the dynamic soil-structure interaction (SSI) problem has been neatly visualised by Wolf (1985) in Figure 2.16 for the case of a shallow founded rigid structure. When comparing accelerations from incident seismic waves (in this case horizontally polarised vertically propagating waves), input into the foundation and structural accelerations for a rigid rock ground condition are different from those recorded on compliant soil (Wolf, 1985). The latter represents a coupled structure-soil problem which is typically divided into three main components: (1) dynamic response of the free-field soil column, which changes characteristics of the seismic waves propagating up to the surface (2) kinematic interaction at the foundation-soil interface due to stiffness contrasts between a massless foundation and its surrounding medium (3) inertial interaction due to overturning moments and shear from the superstructure locally deforming the supporting soil. These are visually illustrated in Figure 2.16 (b,c,and d).

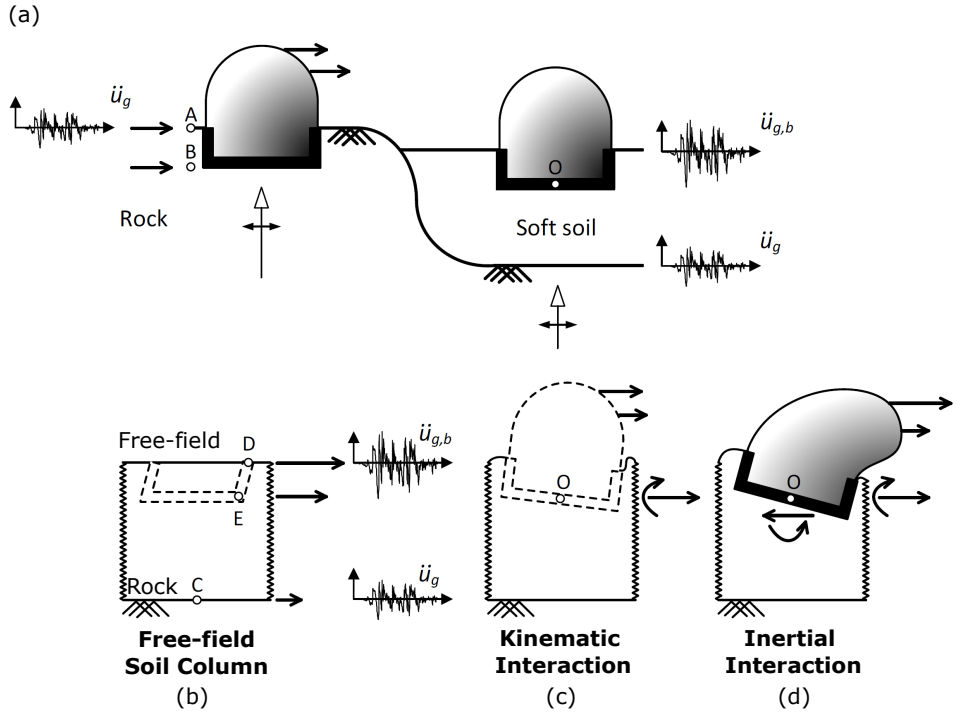

Fig. 2.16 (a) Seismic response of structure founded on rock and on soft soil deposits (b) Bedrock acceleration transmission through soil column (c) Kinematic interaction (d) Inertial interaction (modified from Wolf (1985)).

Of particular interest is the energy dissipation that occurs at the foundation-soil interface during inertial interaction. Figure 2.17 (a) shows shear (S) waves and compression (P) waves emitting out of the vibrating foundation as it responds to dynamic actions from the superstructure. These waves carry a portion of the energy back into the subsoil domain due to "radiation damping".

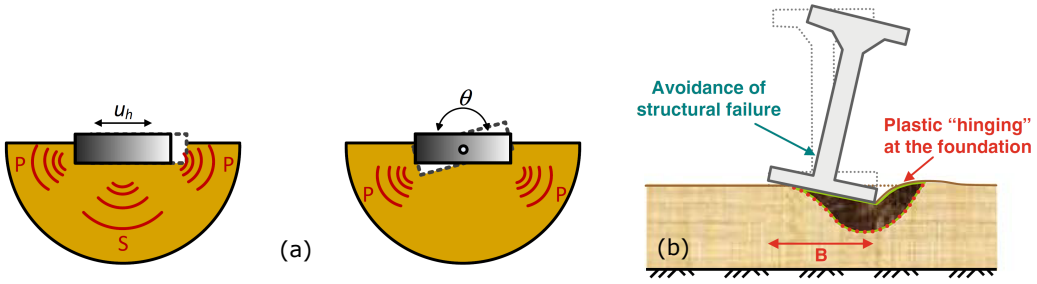

Fig. 2.17 (a) Wave energy radiation from foundation experiencing dynamic horizontal shear and overturning moments (Lu (2016)) (b) localised zone of soil yielding beneath shallow foundation (Anastasopoulos et al. (2010); Gajan and Kutter (2008)).

Simultaneously, the translation and rotation of the foundation locally deforms the surrounding subsoil, provoking soil nonlinearity and material "hysteretic damping". This is illustrated in Figure 2.17 (b). Wolf (1988), Borja et al. (1994) and Gelagoti et al. (2012) write that the formation of localised soft zones of soil beneath a foundation reduces the effects of radiation damping as it causes waves emitting out of the footing to reflect off the soft zone boundaries. In this instance, hysteretic damping would be the main source of energy dissipation.

Rigorous analysis of dynamic SSI problems is often carried out in the time-domain using discrete methods such as the Finite-Element Method (FEM). These are computationally intensive approaches that discretize both the superstructure and the soil domain into individual nodes, and solves the equations of motion at each node. By working at incremental time-steps, FE is able to utilise complex (experimentally-calibrated) constitutive soil models to simulate the nonlinear response of soil, and any accompanying volumetric changes during shaking. Special interface elements are required at the foundation-soil interface to permit uplift of the foundation (i.e. gapping) and possible sliding. Concurrently, there are specific rules to follow when deciding on the size of the soil domain to consider, choosing a mesh element size appropriate for the maximum considered earthquake frequency and soil shear wave velocity, and modelling energy absorbent boundaries. These make the application of FEM too onerous for preliminary engineering analysis.

Inline with the methods discussed in Section 2.2.3, engineers are more likely to resort to simplified procedures especially during early stage design. One common procedure to simplify the effects of SSI is the "substructure approach" shown in Figure 2.18. Central to this procedure is the evaluation of foundation impedance functions that simulate the response of a massless foundation to dynamic actions at various frequencies along different degrees of freedom (vertical, translational, and rotational). These functions are grounded on the "elastodynamic" theory of wave propagation through a homogeneous elastic (or viscoelastic) continuum (Gazetas, 1983).

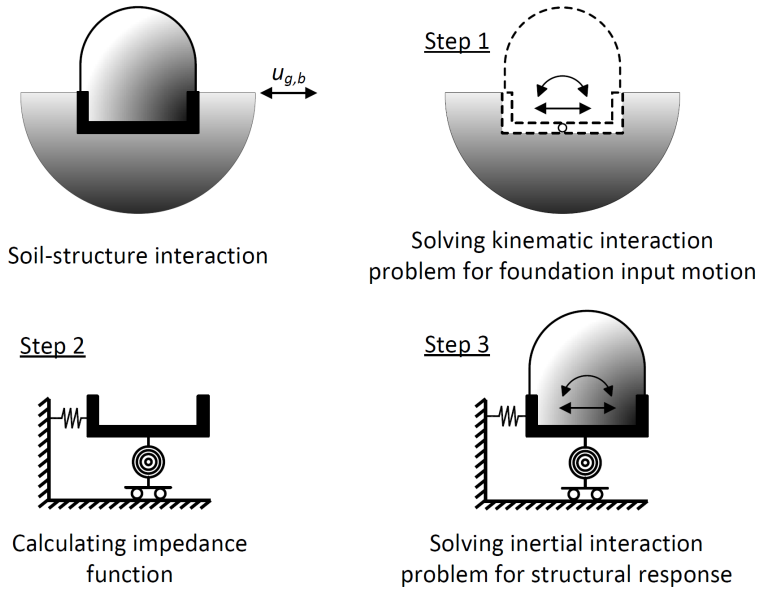

Fig. 2.18 Simplified substructure approach to account for SSI using impedance functions (after Kramer and Stewart (2004); Lu (2016)).

Research on impedance functions for different foundation configurations on elastic halfspace thrived in the late 20th century as analytical wave equation solutions and FE were implemented to generate graphical charts of subsoil stiffness and damping variation with loading frequencies. Gazetas (1983) provides a summary of this history, and presents foundation impedance charts for different degrees of freedom, geometry, embedment depths, and elastic halfspace properties. Whilst hysteretic damping in the subsoil can be incorporated in this approach, impedance functions fail to account for the effects of soil yielding and geometric nonlinearities at the foundation-soil interface (i.e. foundation uplift is not allowed).

Despite that, this method continues to remain popular amongst structural engineers as it allows the foundation-soil system to be idealised by a lumped parameter model (series of masses, springs and dashpots). The discrete models shown in Figure 2.19 are analogues of

the foundation on elastic halfspace problem, with parameters calibrated to match stiffness and damping of impedance functions.

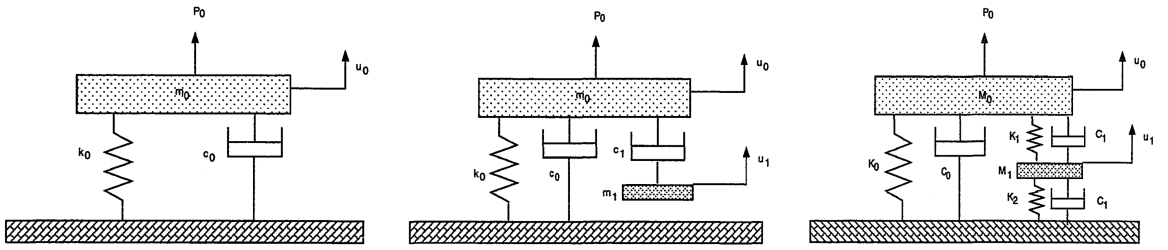

Fig. 2.19 Foundation-soil system lumped parameter model analogues to halfspace solutions (from Chuanromanee (1995)).

The three-parameter model is an early version proposed by Richart et al. (Richart and Whitman, 1966; Richart et al., 1970) calibrated to attain good agreement with halfspace solutions at specific loading frequencies. A five-parameter model was later introduced by Veletsos and Wei (1971), and Meek and Veletsos (1974) which introduced another fictitious mass to achieve better agreement with halfspace solutions over a wider range of loading frequencies. In 1995, Chuanromanee (1995) introduced a seven-parameter model that is calibrated to accurately fit dynamic stiffnesses over a wider range of frequencies for a surface square/rectangular foundation-soil system. Figure 2.20 compares the lumped-parameter model results to exact impedance functions developed by Wolf (1985).

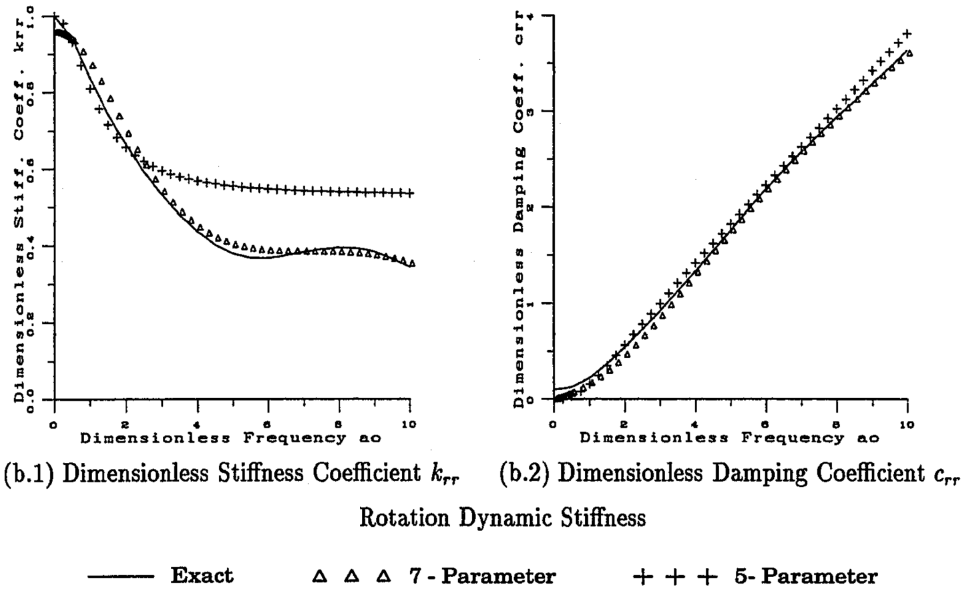

Fig. 2.20 Rotational dynamic stiffness for square foundation on elastic halfspace with a Poisson's ratio of $\nu = 1/3$ and hysteretic damping of 5%. (from Chuanromanee (1995)).

Despite the increasing complexity of the aforementioned models, they all represent mechanical analogues calibrated by curve-fitting techniques to match theoretical elastic halfspace solutions. This, as mentioned earlier, does not replicate nonlinearities in the soil and at the foundation-soil interface.

Macro-element modelling of the foundation-soil system addresses this limitation by capturing the full far-field elastic and near-field plastic nonlinearities of the problem into the constitutive model of a single element inserted at the centre of the foundation. This replaces the need to include a discretised soil domain and foundation-soil interface elements when using FEM to solve the inertial interaction problem.

Using experimental data from 1g shaking table tests, Paolucci et al. (2008) and Grange et al. (2009) calibrated macro-element models to predict the response of model raft foundations on dry sand during dynamic shaking. Both macro-element models are grounded on the concept of calibrating the shape of a multi-dimensional failure surface from 1g shaking table results, defining a plasticity flow rule, and then defining a foundation uplift model. Grange et al. (2009) and Chatzigogos et al. (2011) go through the rigorous mathematics involved in developing the constitutive relationships required for such elements.

Despite resulting in reasonably acceptable predictions of experimental dynamic foundation rotations, there are uncertainties in expanding the aforementioned model predictions to real seismic scenarios due to invalid soil stress-states during the 1g shaking table tests that were used to calibrate model parameters. Furthermore, programming such ambitious models can prove to be as demanding as coding a user-defined nonlinear soil constitutive model in FE. This deters engineers in practice from incorporating such code with their idealised structural models for preliminary assessment of SSI effects.

Recently, Heron et al. (2015) proposed a macro-element model for predicting foundation dynamic rotations grounded on fundamental principles that are familiar to practising engineers. The model is built on a moment-rotation backbone curve that uses a mobilised strength design framework (Osman and Bolton, 2005) to correlate foundation moments and rotations with representative shear stresses and shear strains in the deformation mechanism within the soil (Heron et al., 2015). Strain-dependant stiffness degradation of soil, following established relationships such as the one proposed by Oztoprak and Bolton (2013) based on confining pressures and coefficient of soil uniformity, can then be used to generate the hyperbolic moment-rotation backbone curve of the foundation. The macro-element model takes into account foundation lift-off, and accounts for energy dissipation via a set of modified Masing rules applied to the backbone curve during cyclic loading.

General parameters for this model have been statistically determined from dynamic centrifuge tests involving flexible structures on raft foundations. Therefore, soil stress-state is less of a concern compared to previous macro-element models. However, the statistical origin of the model parameters implies a certain percentage of error is expected when predicting peak moments, small-strain stiffness and energy dissipation. Heron et al. (2015) also made simplifications in the assumed pressure distribution and deformation mechanism in the sand beneath the rigid foundations. Nevertheless, the simplicity of the model makes it a good candidate for preliminary assessment of nonlinear SSI effects.

2.3.2 Effects on Structure Response

Investigations by Merritt and Housner (1954), Veletsos and Meek (1974), and Veletsos and Nair (1975) are a few among many early publications that examined the effects of soil-structure coupling analytically, assuming MDOF systems resting on elastic halfspace. It is these early studies that helped shed light on structural period elongation effects caused by SSI, the importance of radiation damping for squat stiff structures, and the need to include material hysteretic damping in the halfspace model to correctly capture response reductions for tall slender structures responding in rocking.

These studies also highlighted the importance of evaluating intensity of an earthquake excitation in the frequency domain, to appreciate the beneficial (or detrimental) effects that structural period elongation may induce if the flexible-base structural frequency moves away from (or towards) frequencies of excitation with higher energy intensities.

Even though these findings have been well established for a while now in literature, traditional seismic design continues to see practising engineers opting to analyse the dynamic response of the superstructure alone, often assuming fixed-base boundary conditions, mainly due to uncertainties in predicting foundation-soil nonlinearity (Heron et al., 2015). With an increasing push towards performance-based design, modern SSI literature examines the possibility of shifting plasticity and deformations from the superstructure into the subsoil and the foundation-soil interface. This push stems from numerical and experimental evidence of considerable rocking damping ratios and reductions in structural seismic demands when foundations are permitted to rotate during shaking. This phenomenon is called natural rocking isolation.

Gajan and Kutter (2008) conducted a series of slow cyclic and dynamic base shaking centrifuge tests of rigid shear wall models on shallow foundations in sand and clay. From experimental moment-rotation hysteresis loops, the authors reported foundation rocking damping ratios within the range of 10 % to 30 %, depending on the soil type, static vertical factor of safety of the foundation, and magnitude of rotations (i.e. intensity of input motion).

The rigid nature of the superstructure in these tests prevented the authors from making any observations regarding the impact these damping ratios had on the superstructure response.

Kim et al. (2015) conducted dynamic centrifuge tests for SDOF flexible structural models on raft foundations resting on dry dense sand. The study involved testing 7 different SDOF models, covering a range of fixed-base structural periods from 0.09 s up to 2.0 s. Two real motions were applied during testing: (1) 1994 Northridge earthquake (2) 1995 Kobe earthquake, both fired at incremental intensities up to 0.49 g.

Figure 2.21 shows peak experimental accelerations (with SSI) starting to converge to a specific peak acceleration value that is much lower than fixed-base predictions, as intensity of the input excitations increases. Deviation from fixed-base response is more prominent for the stiffer frames than it is for flexible frames. The latter needed stronger base shaking for the foundation moment-reaction and rotations to become a limiting factor on peak mass accelerations.

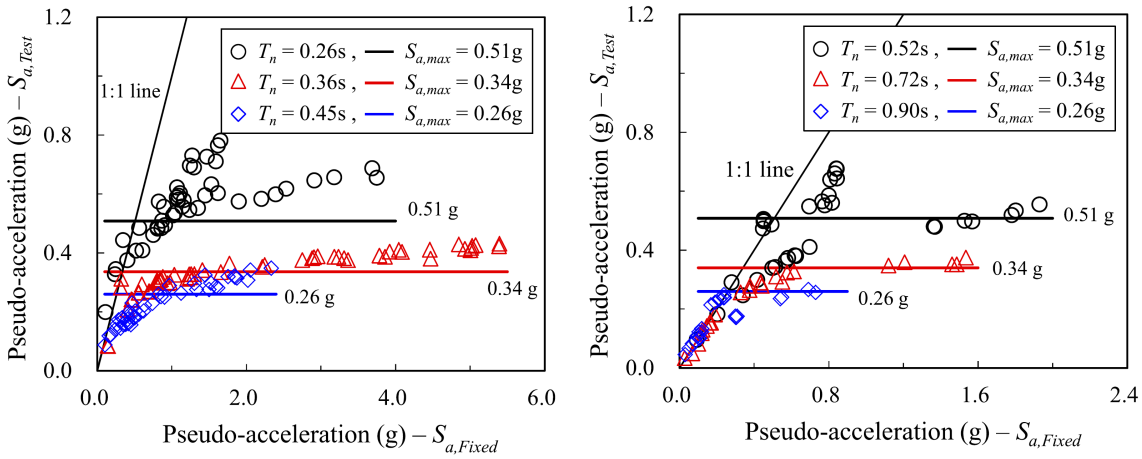

* $S_{a,max}$ = Maximum acceleration permited by ultimate moment capacity of foundation as computed by FEMA 356

Fig. 2.21 Comparison of experimental peak pseudo-accelerations from centrifuge to theoretical peak pseudo-accelerations assuming fixed-base conditions for SDOF structures of different periods (from Kim et al. (2015)).

This is better illustrated in the displacement time traces shown in Figure 2.22; the horizontal component of rocking at the mass level ($u_{Rocking}$) is almost 55 % of the structural drift (u_r) for the stiff SDOF structure, and only 16 % for the flexible model, both recorded during a 0.2 g peak Northridge earthquake. Foundation rocking damping ratios for the short period SDOF structures on dense sand were in the range of 26 % to 30 %, inline with what was reported by Gajan and Kutter (2008).

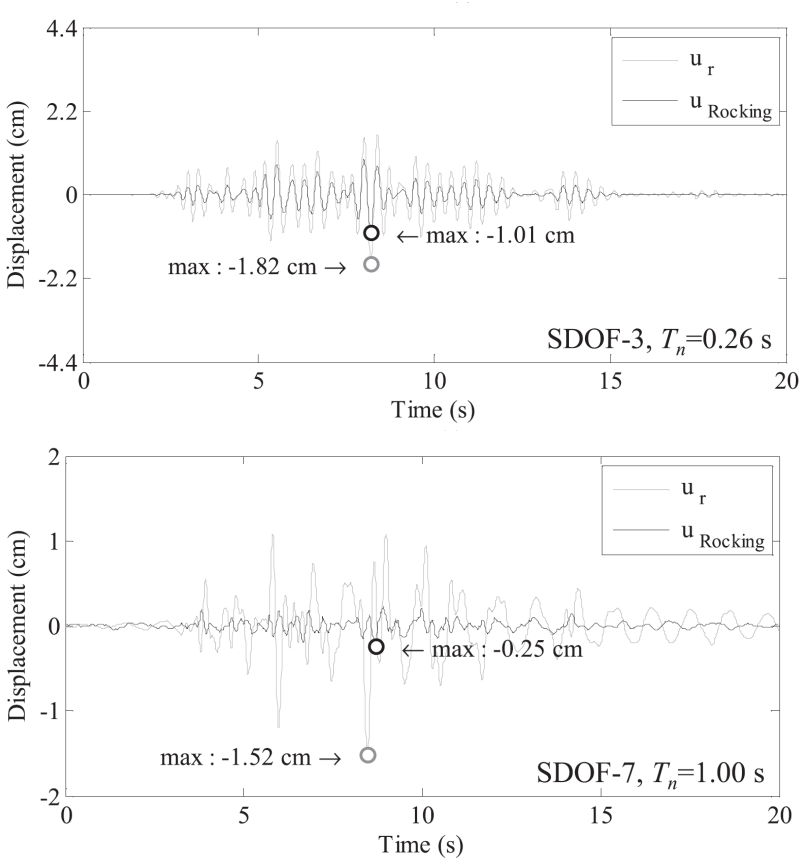

Fig. 2.22 Time trace of mass displacement relative to foundation (u_r) and its horizontal component of rotation ($u_{Rocking}$) for stiff (top) and flexible (bottom) SDOF structures during a 0.2 g peak Northridge earthquake (from Kim et al. (2015)).

According to the authors, inertial interaction for SDOF models with periods greater than 1 second was not significant. This of course should not be generalised. The choice to use Kobe and Northridge excitations implies that the input motions fired in the investigation had energy levels concentrated at the short period range of the response spectrum, with limited energy levels at periods greater than 1 second. As a result, the short structures responded with considerable accelerations, while the flexible structures did not. Testing the SDOF models at frequencies close to their respective resonant frequencies may have resulted in more valuable insights into the effects of SSI.

Numerically, Gelagoti et al. (2012) investigated the concept of natural rocking isolation for a two-storey reinforced concrete frame supported on under-designed isolated spread footings; i.e. the moment capacity of each foundation-soil system is lower than the sectional moment capacity of the column supported on the footing. The study used a kinematic hardening model, with a von Mises failure criterion and an associated flow rule, validated against centrifuge and 1g lab tests of foundations on sands and clays as summarised in

Anastasopoulos et al. (2011). The associated plasticity flow rule and pressure-independent failure surface make the constitutive model better suited for cohesive soils rather than sands. Anastasopoulos et al. (2011) does allow for modification of the von Mises surface to become pressure dependant, but acknowledges the model limitations in capturing volumetric changes of sands during cyclic loading.

Compared to conventional foundation design that uses an over-strength factor to enforce nonlinearity in the superstructure, Gelagoti et al. (2012) only observed the benefits of natural rocking isolation (i.e. under-designed spread footings) during large seismic events. For such intensity of shakes, the frame on conventional isolated spread footings collapsed, developing significant hinging at the column bases. The frame on the under-sized footings remained elastic, diverting most soil-structure system deformations to global rotations of the structure rather than destructive flexural drift in the frame. Very limited settlements were reported for the under-designed spread footings.

The mechanism of mobilising moment reaction for a vibrating structure on isolated spread footings is different from that founded on a raft foundation. Gelagoti et al. (2012) reported significant axial load changes on the spread footings during shaking, depicting the axial tension-compression couple that governs the seismic demand on the isolated footings. For lower intensity shakes, Gelagoti et al. (2012) reported elastic superstructure response for both, conventional and under-designed isolated footings, concluding that natural rocking isolation is best implemented for strong excitations.

In a related study by Anastasopoulos et al. (2010) for the case of a bridge pier (i.e. SDOF oscillator) on a raft foundation, the benefits of having an under-designed raft were observed even at moderate intensity shakes. For such a system, seismic over-turning moments from the superstructure are not resisted by vertical force-couples at the foundation, but rather by changes in soil pressure distribution beneath the raft. As rafts rotate, the geometry of the contact area with the subsoil decreases, which can potentially induce settlement of the foundation and large plastic shearing in the subsoil towards the edges of the raft, thereby degrading foundation stiffness. This was experimentally observed by Paolucci et al. (2008) and Heron (2013) during 1g shaking table and dynamic centrifuge tests. Indeed, greater permanent settlements and tilt have been reported by Anastasopoulos et al. (2010) for the under-designed raft foundation compared to the results for the under-sized footings in Gelagoti et al. (2012). It would be of interest to have a centrifuge-based (or numerical) comparison of the same superstructure founded on these two different foundation types to better understand the characteristics of natural rocking isolation of each system.

Grange et al. (2009) used a macro-element model (calibrated based on 1g shaking table tests of a frame in a shallow sand-box) to simulate the effects of SSI on a 7-storey reinforced concrete test frame founded on a raft foundation. Fixed-base response of the test structure was experimentally obtained from a rigid-base shaking table experiment. Macro-element model parameters for five different soil types were computed, varying from very soft cohesive soil ($V_s = 70m/s, G_0 = 9MPa$), to stiff cohesive soil ($V_s = 180m/s, G_0 = 61.5MPa$), to granular material ($V_s = 360m/s, G_0 = 246MPa$), and stiff ground. Results for a strong 0.9 g Northridge excitation are shown Figure 2.23.

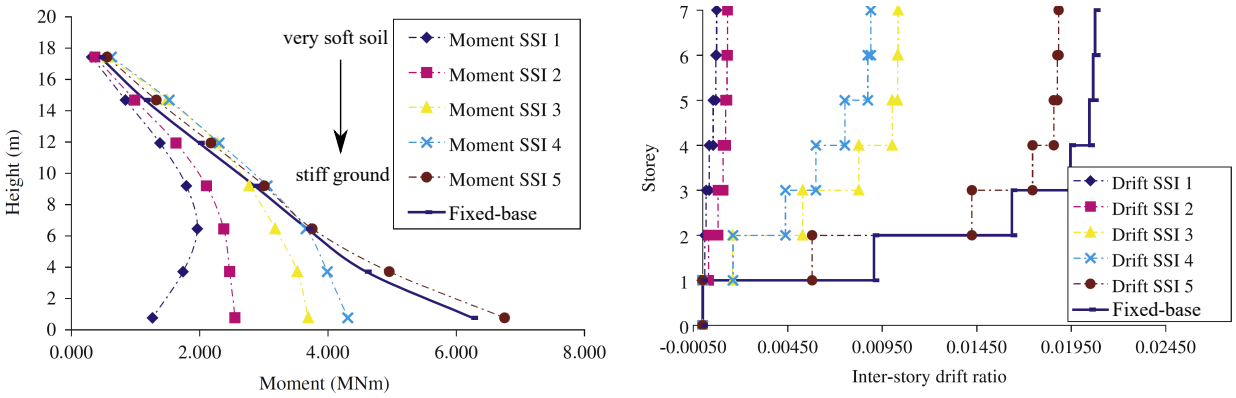

Fig. 2.23 (left) Seismic over-turning moments (right) and inter-storey drift ratios for five different soil types simulated by foundation macro-element model during 0.9 g Northridge input excitation (from Grange et al. (2009)).

Despite the invalidity of soil-stress states during calibration, the foundation-soil macro-element model captured the effects of geometric and material nonlinearities, by virtue of the reductions in seismic over-turning moments and inter-storey drifts shown in Figure 2.23. For stiff cohesive (yellow lines) and granular (light blue lines) soils, the beneficial reductions induced by SSI appear to be focused primarily at the lower stories; this is true for both moments and inter-storey drifts. In fact, for these two soil cases, inter-storey drifts higher up in the frame reported minor increases relative to the fixed-base case. If this was a damped structure, this change in drift distribution relative to the fixed-base condition is bound to change the energy dissipation patterns of dampers distributed along the height of the structure.

For very soft soils (dark blue and red lines), the nature of the strong excitation provoked a clear case of natural rocking isolation as demonstrated by the very small inter-storey drift distributions. This reinforces the idea of using natural rocking isolation as a cost-effective seismic mitigation alternative for protecting structures from strong seismic events.

2.4 Soil-Structure Interaction in Structures With Viscous Dampers

A review of current literature into the effects of SSI on the performance of viscously-damped structures has proven to be limited in nature, often lacking the depth and detail required to properly account for all problem parameters, specifically soil nonlinearity. Predominant contributions to this field continue to be grounded in structural engineering, with emphasis on damper sizing and placement optimisation. Domenico et al. (2019) reviews the main optimisation strategies developed thus far, and compares the effectiveness of each methodology at controlling the seismic response of a theoretical six-storey shear-type structure.

Within the topic of optimisation, Takewaki and Uetani (1999) developed an algorithm that allows for optimal damper placement in structures, taking into account soil flexibility, hysteretic and radiation damping. The iterative nature of the optimisation problem dictates a numerical solution in the frequency-domain, which limits the work to linear analysis. The authors addressed soil nonlinearity by an equivalent linear model similar to that adopted in the program "SHAKE" (Schnabel et al., 1972). Whilst accounting for soil hysteretic damping, the optimisation procedure by Takewaki and Uetani (1999) ignores the isolation benefits of foundation gapping, and the dissipative nature of localised subsoil yielding beneath a foundation, both of which can help refine the choice of optimal damping coefficients even further by contributing to energy dissipation in the overall system. Optimal damper sizing and distribution algorithms are not within the scope of this research. For more details on optimisation, readers can refer to Takewaki (2009).

Chuanromanee (1995) used generalised modal analysis (in the frequency domain) to solve the problem of simplified shear type structures, equipped with viscoelastic dampers, on shallow rigid foundations, in an elastic halfspace. Soil was taken to be elastic, undamped, homogeneous, and assumed to be medium dense to dense sand. Damping in the foundation-soil system is restricted to radiation damping only, with no soil hysteresis. The halfspace was mechanically modelled following the 7-parameter model introduced in section 2.3.1. Results from free-vibration analysis of an 8-storey damped structure founded on an elastic halfspace of varying stiffness are presented in Figures 2.24 and 2.25.

The highly idealised treatment of soil has led to misleading and unrealistic system damping ratios as base fixity is reduced. As shown in Figure 2.24, a moderately damped system with 10 % damping ratio (during fixed base) only achieves 6 % damping even for the case of the damped structure founded on stiff ground ($V_s = 300$ m/s). A regular frame without dampers, characterised with 5 % inherent damping at fixed base, achieves only 3.8 % damping when placed on flexible ground.

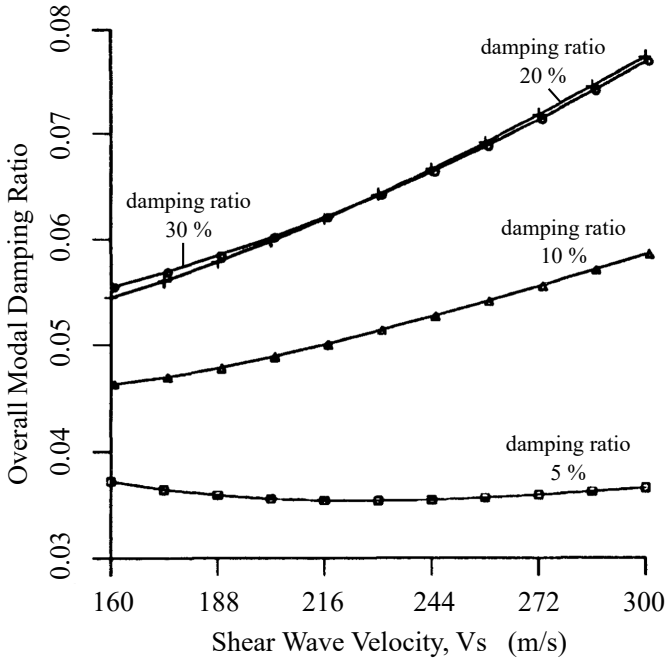

Fig. 2.24 Effects of ground flexibility on overall soil-structure system damping ratio at the fundamental mode. (from Chuanromanee et al. (1995))

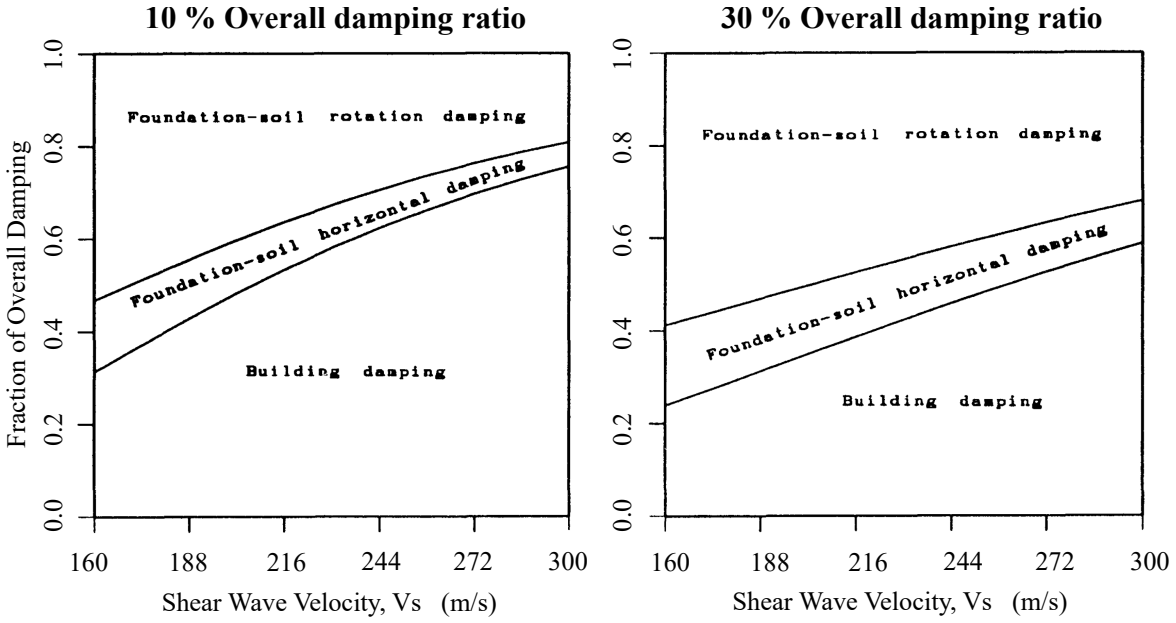

Fig. 2.25 Percentage of overall damping contributed by different system mechanisms for an 8-storey shear type structure. (from Chuanromanee et al. (1995))

In a similar analytical study of regular MDOF structures founded in an undamped elastic halfspace continuum, Rainer (1975) reported similar drops in modal damping ratios as base fixity conditions of the structures were changed from fixed base to flexible ground. In both studies, Rainer (1975) and Chuanromanee (1995) treat the modal damping ratio of a structure on compliant ground as a term encompassing three separate components of energy dissipation: work done by foundation damping forces against horizontal foundation motion, work done by foundation damping forces against foundation rocking, and work done by frame damping forces against inter-storey drifts.

As internal deformations in a structure decrease with increasing ground flexibility, results from Chuanromanee (1995) in Figure 2.25 point to a drop in the contribution of structural damping to the overall modal damping ratio of the system. Similar observations were made by Novak and Hifnawy (1983); Rainer (1975); Veletsos and Meek (1974). If the increase in foundation radiation damping during SSI does not compensate for this drop in structural damping, a reduction in the overall modal damping ratio would be reported for the SSI system compared to its fixed base counterpart (Rainer, 1975). Examples of this can be seen in Figure 2.24. Such a misleading finding of a lower modal damping ratio goes against the observations made earlier in section 2.3.2 about the beneficial role of SSI at limiting structure response during shaking. Rainer (1975) attributes this to the improper consideration of foundation hysteretic damping in the analysis, or its lack thereof, in the case of the work presented by Chuanromanee (1995).

In more recent publications, Zhao et al. (2017) used a similar linear-elastic lumped model for a MDOF structure on halfspace. Analysis was again conducted in the frequency domain using foundation-soil impedance functions, this time with hysteretic damping. Zhou et al. (2012) approached the problem numerically, using FEM to simulate the seismic response of an elastic 7-storey, shallow founded, reinforced concrete frame fitted with linear viscous dampers, on ground of varying stiffness. The fully coupled FE model used contact and gapping elements at the raft-soil interface to allow sliding and uplift. However, the authors opted for an equivalent-linear soil constitutive relationship, setting damping in the soil at 15 %. Detailed comparisons of how linear, equivalent-linear and nonlinear soil constitutive models affect SSI simulation can be found in Pitilakis et al. (2006), and Bolisetti et al. (2018). The main effects are an over-prediction of ultimate moment capacity before raft lift-off (Kourkoulis et al., 2012), and under-prediction of energy-dissipative yielding of soil beneath the foundation (Pitilakis et al., 2006).

Performance of the damped frame in Zhou et al. (2012) was tracked for different soil conditions using a "control effectiveness ratio" that compared peak response parameters for the damped structure, to those obtained for the same frame without dampers. Contrary to

the trend in Figure 2.24, peak displacements and inter-storey drifts in the damped frame decreased as base fixity was reduced from rigid to stiff and medium-stiff soil cases; i.e. damping ratio did not drop. On soft soil, higher peak displacements were recorded in the damped frame relative to the stiff, and medium-stiff ground cases. While Zhou et al. (2012) argues that this shows the importance of considering SSI, the choice of equivalent-linear soil model probably failed to capture the actual dissipative characteristics of the foundation-soil interface for the soft-soil case.

Li et al. (2015) also used FE modelling to compare the seismic response of a 10-storey reinforced concrete structure on raft foundations embedded in soft Shanghai clay, with and without viscous dampers. No details of any interface elements at the raft-soil interface have been provided, however, the authors again used an equivalent-linear approach to model soil. Li et al. (2015) observed inter-storey drifts and storey shear force values converging between the damped and undamped structures as base fixity was numerically changed from fixed base to embedment into soft clay. The authors also noted drops in inter-storey drifts and storey shear forces for the damped structure as base fixity was reduced.

Both studies, Zhou et al. (2012) and Li et al. (2015), show that the performance of a structure equipped with viscous dampers is always better than that of a regular frame, irrespective of ground conditions. However, in almost all of the aforementioned studies in this section, there is a general perception of "reduced control efficiency" of the dampers as base flexibility of the damped structure increases. Literature mostly attributes this to fundamental period elongation effects, that tend to reduce the frequencies at which the inter-storey dampers operate, and thus reduce damper energy dissipation. This, in-part, is true but can be misleading. The drive behind the apparent reduction in damper control with increasing degrees of SSI is not because the damped frame is under-performing, but rather because the bare regular frame being used as a comparative bench-mark is itself benefiting from SSI.

In addition to the expected reductions in work done by the dampers, there are also concerns on whether instantaneous foundation moment reactions during SSI can play a role at limiting peak damper forces in the frames. To overcome the numerical limitations of the aforementioned studies, this investigation aims to use high-gravity dynamic centrifuge testing to help address these concerns.

2.5 Summary

Influential literature examining the performance of structures with viscous dampers stems primarily from structural engineering research, with emphasis on experimental frame prototype testing in shaking table facilities. By fixing the base of these prototype frames to rigid shaking tables, energy dissipation during seismic excitation is confined only to the superstructure and its supplemental damping devices. This fixed-base assumption, along with classical modal analysis, underpin the current design guidelines available to engineers when estimating the dynamic response of structures with viscous damping.

Recent literature on soil-structure interaction advocates the use of soil and geometric nonlinearities at the foundation-soil interface as viable sources of energy dissipation capable of controlling structural vibrations. The concept has been validated experimentally, and approximated numerically using nonlinear FEM.

In order to make quantification of SSI effects more appealing to practising engineers at early stage design, macro-element models of foundation-soil systems have been developed in literature. These models are a significant improvement over traditional impedance functions, but lack their simplicity. With an adequate foundation-soil macro-element model, the response of a regular structure including the natural energy-dissipative processes at the foundation-soil interface can be assessed prior to deciding on the need for supplemental damping.

A review of literature revealed that the effects of SSI on the performance of structures with viscous dampers was not sufficiently explored. There is very limited experimental data as to how foundation-soil inertial interaction affects the performance of viscous dampers and the overall damped frame response. Efforts thus far have been restricted to either linear-elastic studies in the frequency domain, or coupled soil-structure FE analysis using equivalent linear soil models. Both approaches do not properly capture the dissipative and isolation characteristics of inertial interaction at the foundation.

Acknowledging the cost and complexity of investigating this problem within the confinements of a large shaking table facility, this study aims to establish the application of dynamic geotechnical centrifuge testing to experimentally observe the performance of reduced-scale damped structures considering SSI effects. The seismic performance of these frames can also be compared to that of regular structures invoking natural energy dissipation at the foundation.

Chapter 3

Experimental Methodology & Model Structures

3.1 Introduction

Experimental dynamic testing of structures, both regular and equipped with supplemental dampers, has so far been confined to medium-to-large scale shaking table tests. The shaking table facility at the EQUALS (Earthquake and Large Structures) laboratory at the University of Bristol is one example of a comparatively small 3 m $\times$ 3 m six degree-of-freedom shaking table, onto which scaled model frames can be erected. Another example is the much larger E-Defense 20 m $\times$ 15 m shaking-table facility in Japan, capable of shaking real prototype structures along six axes.

The majority of shaking table facilities around the world are not able to simulate inertial interaction at the foundation-soil interface; it is often the case that the testing frames are either founded on rigid concrete beams built into the shaker, or the base of the structural columns are bolted down onto the shaking table.

Recent experimental and numerical work into performance-based seismic design indicate that there are considerable seismic demand reductions to be gained if geometric and material nonlinearity at the foundation-soil interface are considered in the analysis. In this regard, dynamic centrifuge testing offers a unique opportunity to collect experimental data that encapsulates the complete soil-structure interaction behaviour, rather than assess the structural response alone for an unrealistic base fixity condition.

3.1.1 Centrifuge Modelling Theory

The constitutive behaviour of an element of soil subjected to external loading is highly dependent on the stress state within the soil domain. High-gravity geotechnical centrifuge testing has proven over the years to be a powerful tool in geomechanics; the centrifuge permits a one-to-one scaling of stress and strain between homologous points in a reduced-scale soil model and its equivalent prototype soil column.

This similitude in stresses and strains can be exploited in dynamic tests to recreate realistic soil impedances (stiffness and damping) beneath centrifuge model structures as they respond to in-flight base excitations. During a centrifuge test, the experimental package is accelerated in circular motion in order to subject the soil model to a predefined value of centrifugal acceleration. Figure 3.1 (a) offers a plan view of a centrifuge spinning an experimental package similar to the one tested in this study, at a constant angular velocity (ω), creating a centrifugal acceleration field (a_{cent}).

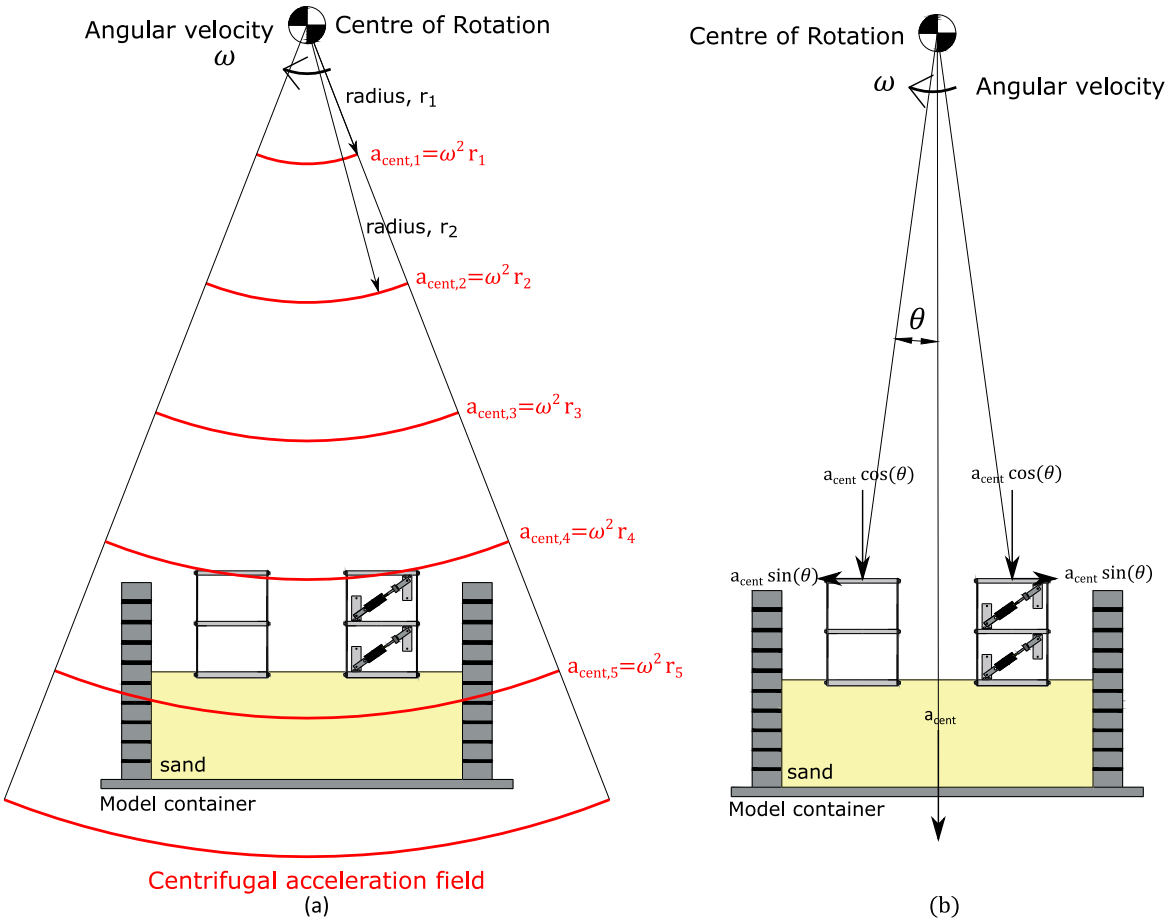

Fig. 3.1 (a) Top-down view of centrifugal acceleration field generated due to circular motion of the centrifuge (b) Centrifugal forces acting at different points in the experimental package.

The magnitude of the centrifugal acceleration varies linearly with distance from the centre of the rotation, and varies as a square of the angular velocity. As illustrated by the curvature of the red contour lines of constant centrifugal acceleration, not all points along the same horizontal plane in the experimental package are subjected to the same centrifugal accelerations. Figure 3.1 (b) shows the radial centrifugal forces acting at the centre of the soil surface, and the forces acting on the top of the centrifuge model structures positioned to either sides of the container.

The centrifugal forces acting on the model frames are inline with the centre of rotation and inclined at an angle θ to the vertical as illustrated in Figure 3.1 (b); this implies that the model frames are not only subjected to vertical centrifugal forces, but also to a small horizontal component as well. The greater the distance between the experimental package and centre of rotation (i.e. the larger the centrifuge diameter), the smaller the horizontal component of this centrifugal force.

The linear variation of centrifugal acceleration with radius of rotation creates a varying gravitational field within the reduced-scale soil model (i.e. gravity is not constant across the depth of the soil in the model container). In fact, the designated g-level in a centrifuge test can only be attained at one specific point in the soil model; soil above this point is at an under-stress state (less than nominal g), while soil below this is at an over-stress state (more than designated g-level). This is graphically illustrated in Figure 3.2.

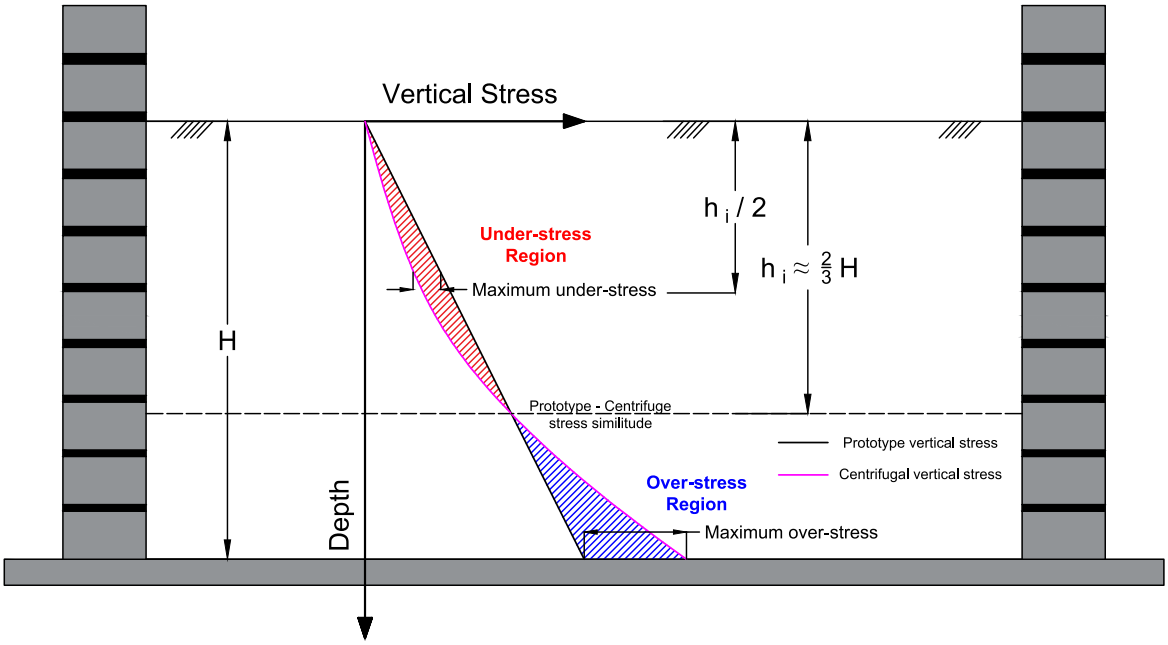

Fig. 3.2 Variation of centrifugal acceleration across model soil depth in the centrifuge.

The vertical stress applied onto the soil model in-flight varies as a quadratic function of depth, as opposed to a linear variation in the prototype case. Maximum deviation between the two gravity fields occurs at $h_i/2$ and H as illustrated graphically in Figure 3.2. Such a variation in the gravity field can induce errors in estimating vertical and horizontal stresses acting on the soil in the centrifuge. Madabhushi (2015) minimises this error by computing the depth at which the ratio of maximum under-stress (centrifugal vertical stress to prototype vertical stress at $h_i/2$) is equal to the ratio of maximum over-stress (centrifugal vertical stress to prototype vertical stress at H). The point of stress similitude between the prototype and the centrifuge soil model is mathematically shown to be at two-thirds of the total depth of the soil in the container.

Similar to the concept of similitude scaling laws in reduced-scale shaking table testing of structures, geotechnical centrifuge testing is also based on a well established set of scaling laws that link model parameters at g-level to their equivalent counterparts at 1 g prototype. Derivation and discussion of centrifuge scaling laws for key testing parameters are given in Schofield (1980) and Schofield (1981), for slow and dynamic events respectively. They are summarised in Madabhushi (2015) and compared against similitude scaling laws in Table 3.1 for completion.

Table 3.1 Dynamic centrifuge and shaking-table similitude scaling laws. (Madabhushi, 2015; Seleemah and Constantinou, 1997)

		Dynamic Centrifuge Scaling Laws at N g	Similitude Scaling Laws for N^{th} Scale Structural Models at 1 g
Parameter	SI Base Units	Scale (Model / Prototype)	Scale (Model / Prototype)
Stress	$kg \cdot m^{-1} \cdot s^{-2}$	1	1
Strain	-	1	1
Young's Modulus	$kg \cdot m^{-1} \cdot s^{-2}$	1	1
Acceleration	$m \cdot s^{-2}$	N	1
Time	s	1/N	$1/\sqrt{N}$
Frequency	s^{-1}	N	$\sqrt{N}$
Velocity	$m \cdot s^{-1}$	1	$1/\sqrt{N}$
Length	m	1/N	1/N
Mass	kg	$1/N^3$	$1/N^2$
Moment of Inertia	$kg \cdot m^2$	$1/N^5$	$1/N^4$
Force	$kg \cdot m \cdot s^{-2}$	$1/N^2$	$1/N^2$

3.2 Equipment for High-Gravity Testing

3.2.1 Turner Beam Centrifuge

The Turner Beam Centrifuge at the Schofield Centre, University of Cambridge is an underground 10 m diameter facility, designed and built by Philip Tuner in the late 1960s, for geotechnical testing applications. The machine is classified as a 150 g-ton centrifuge, indicating its capability of accelerating a 1 ton payload up to an operational g-level of 150 times earth's gravity.

The centrifuge is a balanced-beam centrifuge where one end of the beam carries a swing with the secured experimental package, while the other end carries a swing with an equivalent counterweight of steel plates; a maximum out-of-balance mass of 2 kg is permitted between the two swings to limit the stresses applied to the roller bearings of the centrifuge during spinning.

Design and construction of the Tuner beam centrifuge are described in greater detail in Schofield (1980). An image of the facility for a typical dynamic test is shown in Figure 3.3. The ends of the beam are colour coded "red" and "blue"; static tests often have the package on the red swing and the counterweight on the blue swing. This is reversed for dynamic centrifuge tests where the blue end would carry the earthquake actuator and the experimental package, while the counterweight is secured to the red end swing of the beam.

The centrifuge usually starts with the red and blue swings close to horizontal (slight outwards tilt) as shown in Figure 3.3. As the beam accelerates to about 8 g, the red and blue swings rotate 90^0 and become vertical, lining up the experimental package and the counterweight with the radial acceleration of the centrifuge.



Fig. 3.3 10 m diameter Turner Beam Centrifuge located at the Schofield Centre, University of Cambridge, UK.

With the experimental package vertical relative to the ground, the centrifuge has a working radius of 4.125 m; this is the effective radius from the centre of rotation of the beam to the top of swing platform. During dynamic tests, the reaction force required by the earthquake actuator to accelerate the heavy experimental packages is provided by inertia of the beam centrifuge itself. This implies that the bolt connections and welds on the beam structure are subjected to the vibrations transmitted during shaking. Therefore, an operational limit of around 80 g is applied to most dynamic centrifuge tests to prolong the serviceability of the beam frame and the earthquake actuator.

All dynamic high-gravity tests in this investigation were conducted at 106 rpm (rounds per minute) which exerts 50 g at a radius of 4 m away from the centre of the rotation. Following on from the equation of centrifugal acceleration presented in section 3.1.1, the centres of gravity of the model structures, and soil at half a foundation width beneath the rafts, are experiencing around 41 g and 42.5 g respectively. All centrifuge data presented in the following chapters of this thesis use a scale factor $N = 50$ (see Table 3.1), unless otherwise stated. Even though the precise prototype measurements may be slightly different due to g-level variations, the fact that all data is scaled by the same factor deems the cross-test quantitative comparisons viable and accurate.

3.2.2 Automatic Sand Pourer

Historically, sand pouring at the Schofield Centre was carried out manually with user-controlled adjustments to the hopper and nozzle hose positions to cover the entire geometry of the model container. The consistency of sand beds produced this way over multiple centrifuge tests for a specific study was solely a function of the skill and patience of the research worker.

In 2006, a robotic sand pourer shown in Figure 3.4 (a) was developed for this purpose. Details of the machine construction are provided in Madabhushi et al. (2006). The machine utilises three linear servo-motors and belts, with proximity limit switches, that allow users to precisely manoeuvre the hopper in planar 2D space, and adjust the vertical drop height of the nozzle over the container within axis limits.

Prior to commencing automatic pouring, users go through an axis setup exercise in which the coordinates of the four corner points of the model container are identified relative to the machine coordinate system. Users then input the number of pouring step increments that the machine will execute along each axis; the flow pattern and pouring step increments of the nozzle along the longitudinal and transverse axes are sketched in Figure 3.4 (b).

With these input parameters set, automatic pouring can start. Every time the machine completes one pass over the container, the nozzle is automatically raised by a distance equivalent to the depth of the sand layer poured. This ensures a consistent drop height of sand between the nozzle and the sand surface as pouring progresses. The robotic pourer can also be paused at specific sand depths for the placement of instruments. For this experimental study, calibration pours were carried out prior to centrifuge testing to identify the required machine input parameters and nozzle setup to produce dry dense and loose sand beds. Zhao et al. (2006) and Chian et al. (2010) provide initial pourer configurations to produce different sand bed densities. Details of the input variables used in this study are provided in section 3.5.2.

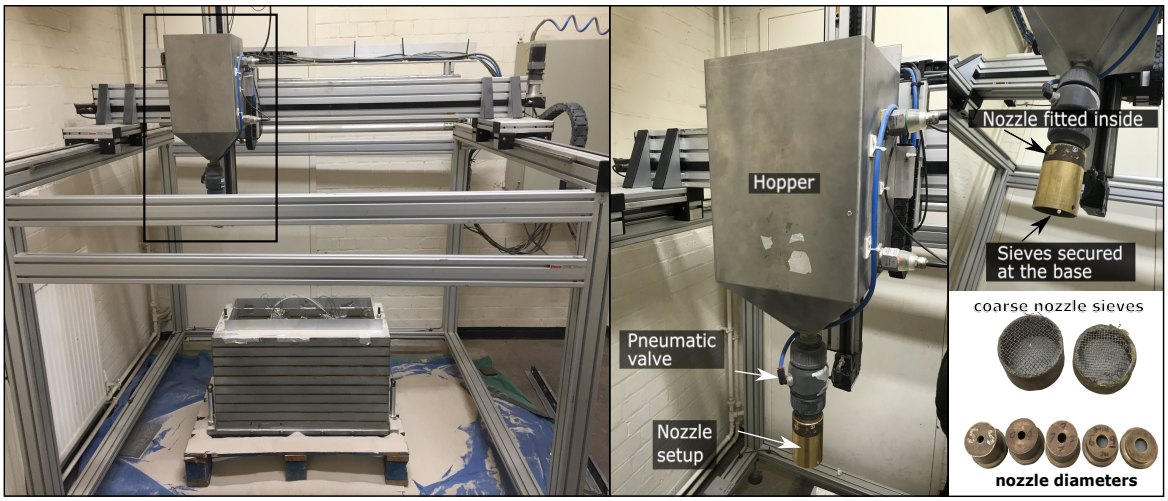

(a)

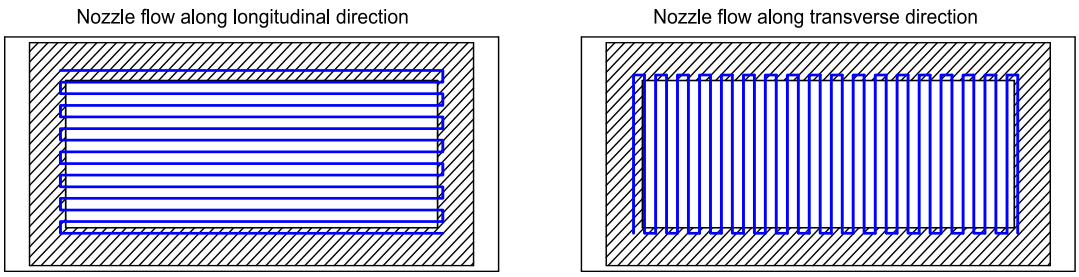

Plan view of Equivalent Shear Beam (ESB) container

(b)

Fig. 3.4 (a) Automatic sand pourer frame, hopper and nozzle setup (b) Robotic sand pouring pattern along the longitudinal and transverse axes of the model container.

3.2.3 Equivalent Shear Beam (ESB) Box

Geotechnical centrifuge testing aims to utilise high gravitational fields to mimic soil stress states at homologous points between a reduced scale soil model and its equivalent prototype soil column. Ideally, soil layers in the ground are treated as semi-infinite strata. However, in a centrifuge package, the dimensions of the reduced scale soil model are often limited.

For dynamic tests specifically, the geometry of the shaking table, and the payload capacity of the servo-hydraulic actuator, set constraints on the dimensions of the package that can be tested. The confinement of soil in a rigid wall container for high gravity testing causes material stress and strain dissimilarities to exist between the soil closest to the boundaries and its homologous counterpart in the field; this discrepancy is greatest near the rigid walls of the container, and reduces for the soil fabric further away from the boundaries.

Boundary effects are greatly exacerbated for earthquake tests. During base excitation, a model container with rigid walls would restrict the soil from deforming in shear as it would typically do in the field, thus preventing the formation of realistic strain fields in the soil model. In fact, the stiffness contrast between the deforming soil column and the container end walls can cause physical de-coupling to occur between the soil and the boundaries of the container; on re-impact, P-waves would be generated which can propagate from the end walls to the centre of the package and influence soil accelerations. According to Zeng & Schofield (1996), dynamic model containers ideally should:

1. Maintain K_0 (at-rest) soil stress states by having boundary walls that are stiff enough to resist bulging under the lateral earth pressures of soil once at g-level.

2. Have boundary walls with the same natural frequency as the soil column to minimise boundary effects and the reflection of energies back into the soil mass.

3. End wall-soil interfaces that can mobilise complementary shear stresses during horizontal base shaking of the soil to maintain stress field similitude between model and prototype.

While the first and third points can be enforced in design, the second point is not very realistic. Different experiments will use different soil models with varying stiffnesses and natural frequencies; the frequency of the model container cannot be varied to match that of soil for every test. One solution to this problem is the Equivalent Shear Beam (ESB) container shown in Figure 3.5.

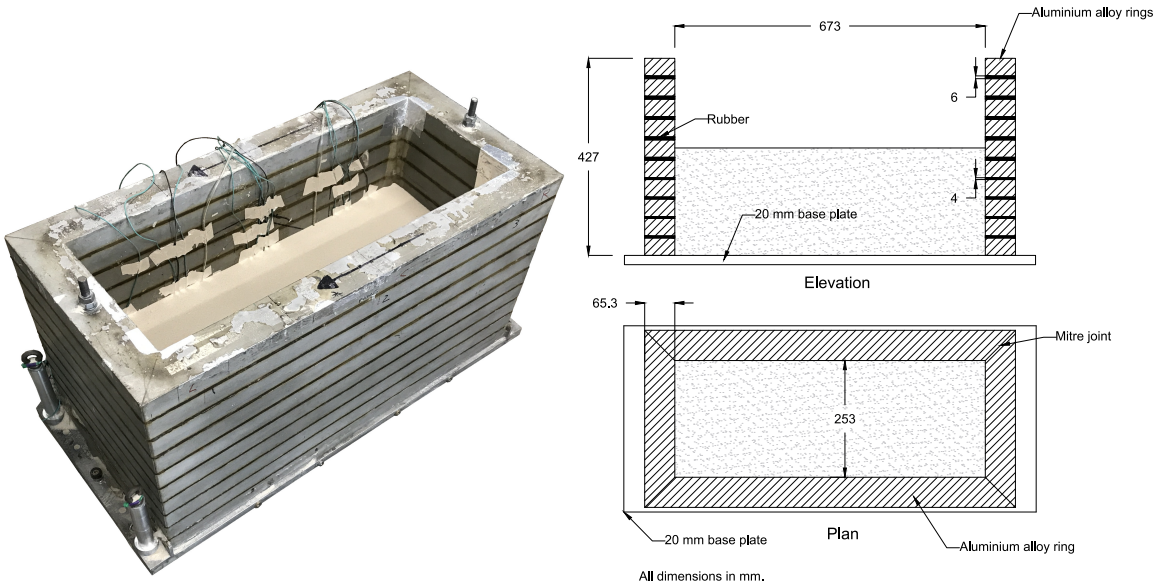

Fig. 3.5 Equivalent Shear Beam (ESB) box, its geometry and construction.

The container consists of box-sectioned aluminium alloy rings with alternate rubber membranes of different thicknesses along the height of the box. The shear stiffness of the aluminium alloy ring stack forming the end walls is controlled by the thickness of the rubber; close to the base, the rubber is 4 mm thick to mimic the large stiffness of soil under confining stress. Towards the top of the box, thicker rubber is used to account for the reducing shear stiffness profile towards the surface of the sand. Design and construction of this box are described in detail in Brennan and Madabhushi (2002).

As mentioned earlier, the shear stiffness of the ESB box cannot match the stiffness of all possible soils that will be tested in the centrifuge, hence a design compromise is required. The rubber membranes between the aluminium alloy rings were sized to match the shear stiffness profile and deformation mode of a medium dense sand with voids ratio of 0.77, K_0 of 0.55, and an internal angle of friction of 33°.

The stiffness contrast between soil masses of different densities and the flexible end walls of an ESB box was investigated by Teymur and Madabhushi (2003). Even though a smaller ESB box was used for these tests, the design philosophy and construction are very similar to the container used in this study. Soil accelerometer data from these tests noted minor amplification of accelerations as the shear waves propagate from base of the box to the sand surface; this was for dense sand profiles that matched the end wall stiffness of the ESB box.

For loose sand profiles, soil accelerations amplified towards the top of the sand surface hinting to more boundary interaction and possible formation of pressure waves reflecting back into the soil mass; this phenomenon appears to become less critical for the centre soil column compared to the near end wall section of the model. Coelho et al. (2003) observed that the central 300 mm wide soil column is the least likely to by affected by the soil-boundary interaction during dynamic tests.

3.2.4 Servo-Hydraulic Actuator

Once an experimental centrifuge package is accelerated to the designated g-level for a test, an external power source is needed to trigger horizontal dynamic excitations of the model container. Early version of dynamic centrifuge tests in Cambridge involved detonating small controlled charges positioned on top of centrifuge model structures to induce structural vibrations and investigate soil-structure interaction (Morris, 1979).

Within the same time frame, a leaf-spring actuator was developed to shake model containers in-flight; energy would be stored elastically in the leaf-spring, and released on demand in-flight. Kutter (1982) worked on constructing a Bumpy Road earthquake actuator whereby a wheel would deploy out of the base of the model container in-flight and run over a track along the walls of the centrifuge pit to provide base excitations; the vertical motions of the wheel would be translated into horizontal shaking of the model container.

In the late 1990's, Madabhushi et al. (1998) worked on developing the Stored Angular Momentum (SAM) earthquake actuator which stores energy in-flight in a fly-wheel and releases it on demand to mechanically drive a shaking table to which the experimental package would be bolted. This actuator presented a significant improvement over the previous versions as it gave refined control over shaking amplitude, frequency and duration.

Unfortunately, for all of the previous actuators, only sinusoidal motions could be triggered. An upgrade to the hydraulic slip rings of the Cambridge beam centrifuge in 2008 prompted the development of a new actuator called the servo-hydraulic actuator. The design intent was to have a machine that is capable of firing sinusoidal, and any displacement time history trace desired, to within operational limits. The actuator is shown in Figure 3.6 after loading onto the blue end of the beam centrifuge.

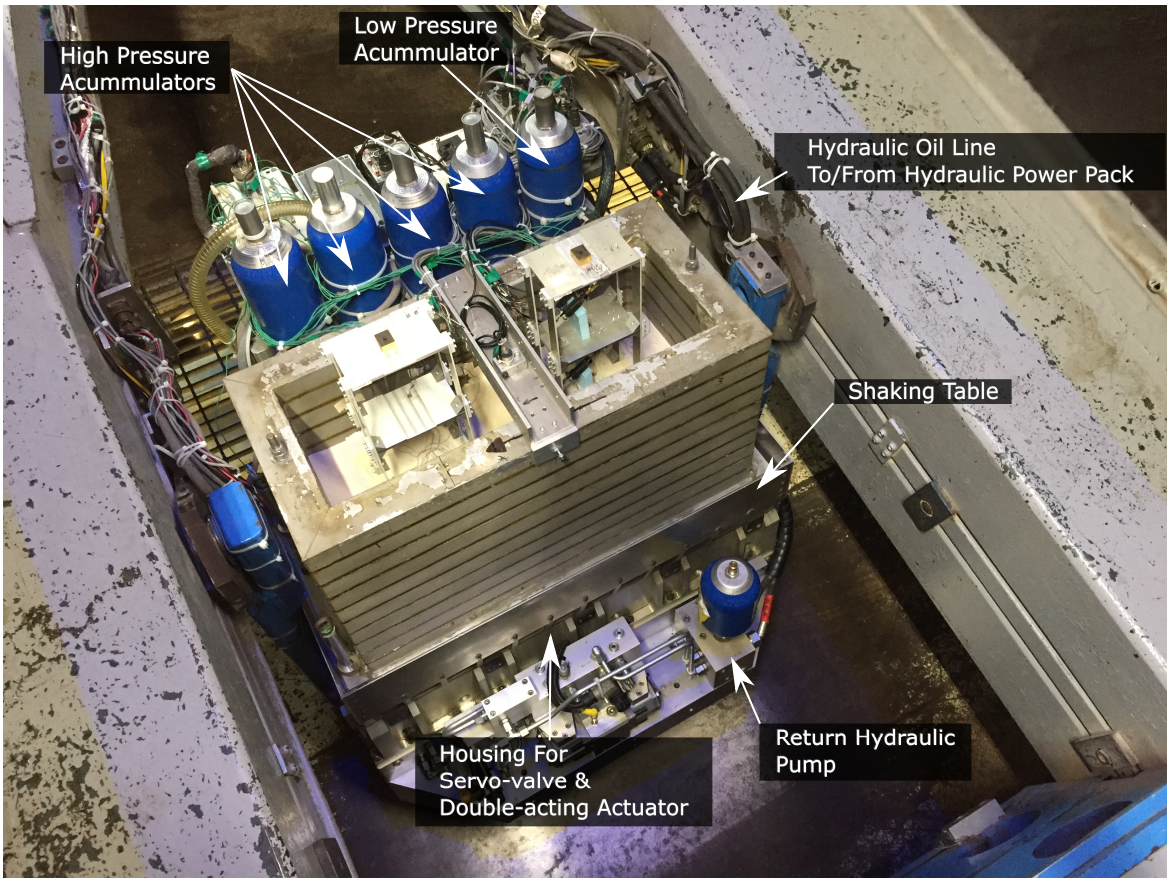

Fig. 3.6 Servo-hydraulic actuator loaded on the blue swing with an experimental package.

3.2.5 Instrumentation

The process of preparation and building of experimental model packages for centrifuge testing provides researchers with full control over the type and layout of instrumentation to be deployed to monitor the problem at hand. The reduced scale of centrifuge models has prompted a new market for miniaturised versions of instruments specifically built for high gravity testing. The instruments deployed for this investigation are described in this section.

Piezo-electric Accelerometers

Piezoelectric accelerometers, shown in Figure 3.7, were used in this study to record soil model accelerations in dynamic centrifuge tests. When an incident wave reaches one of these devices, a piezo crystal inside the head of the piezoelectric accelerometer is mechanically stressed and releases an electric charge. The charge is then converted to a voltage output using a charge amplifier. The instrument itself has an in-built filter (due to charge leakage) limiting its ability to measure frequencies lower than 5 Hz.

As a result, piezo-electric accelerometers are not able to measure constant earth acceleration or centrifugal acceleration, however they respond well to time-varying accelerations between 5 Hz to 2 kHz. This well covers the range of frequencies fired in dynamic centrifuge tests. For this study, Type A/23 piezo-electric accelerometers from DJB instruments were used. Calibration of these devices is done using a Bruel and Kjaer rig that subjects the instruments to a $\pm$ 1 g sinusoidal excitation. Maximum positive and minimum negative voltages for these accelerations are recorded. A typical calibration curve is shown in Figure 3.7.

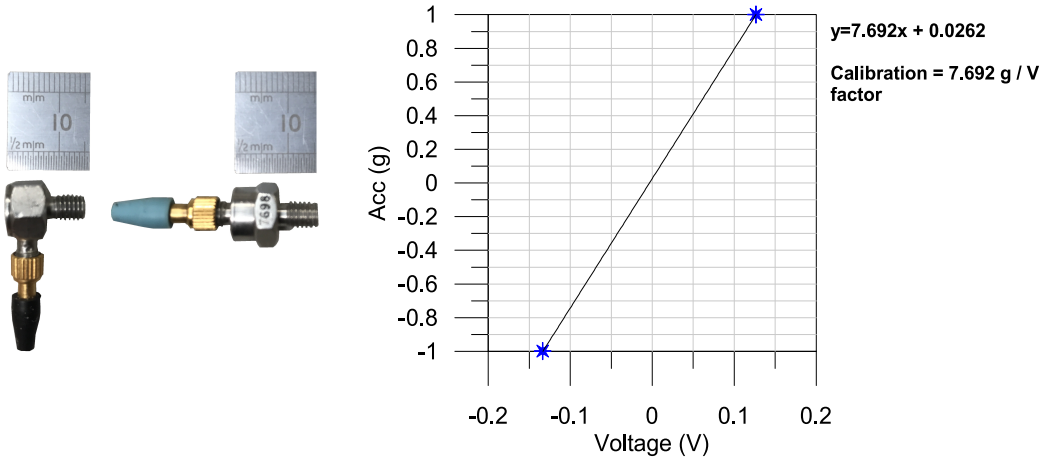

Fig. 3.7 (left) Piezo-electric accelerometer (right) Typical calibration curve.

Micro-Electro-Mechanical System (MEMS) Accelerometers

Micro-electro-mechanical-system (MEMS) accelerometers were made popular due to their widespread application in smart phones. These accelerometers are often integrated in mobile chips and are very small in size. Inside the head of a MEMS accelerometer is a small inertial mass suspended from a tiny spring. As the head is displaced, the inertial mass deforms the spring by a specific amount depending on the acceleration applied to the MEMS accelerometer head. This working principle allows the MEMS accelerometers to record constant acceleration as well as time-varying accelerations.

For this study, Type ADXL78 MEMS accelerometers made by Analog Devices were used to monitor structural and damper accelerations. Calibration of these devices was carried out by recording voltage output at different degrees of tilt. An image of the MEMS accelerometer and its typical calibration curve are presented in Figure 3.8.

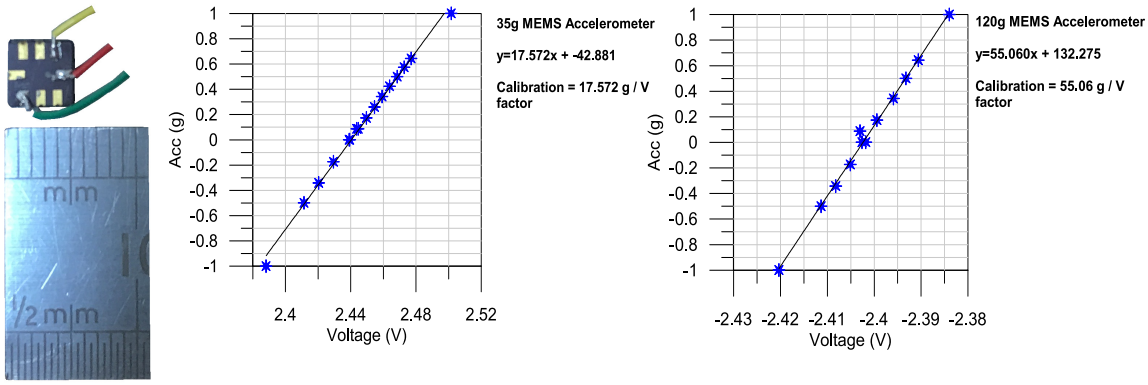

Fig. 3.8 (left) MEMS accelerometer (right) Typical calibration curve.

Load Cell

Miniature tension-compression load cells were used in this study to record in-flight forces generated by the miniature oil dampers in the damped frames during shaking. Inside such a load cell, strain gauges are used to measure the deformation of a diaphragm that is mechanically connected to studs protruding out of the load cell body. For this study, F255 Miniature Diaphragm load cells from Novatech were used. These devices were calibrated outside the centrifuge in tension by applying known weights and measuring the output voltage. A typical load cell and its calibration curve are presented in Figure 3.9.

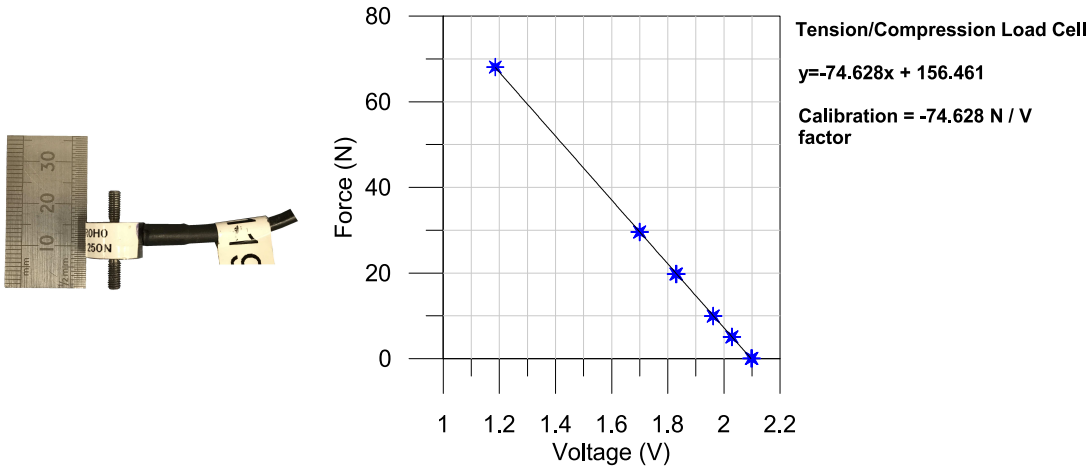

Fig. 3.9 (left) F255 miniature tension/compression load cell (right) Typical calibration curve.

Air-hammer

An air-hammer device was used to characterise the shear wave velocity and small-strain stiffness profiles of the different sand beds prepared in this investigation. An air-hammer is a simple brass tube with smooth inner walls equipped with a metallic pellet inside. Application of compressed air on one end of the brass tube accelerates the pellet inside and causes it to strike one side of the air-hammer; sending compressed air through the other end of the air hammer propels the pellet in the other opposite direction causing an impact to occur on the other side of the brass tube.

On impact of the horizontal projectile with the ends of the brass tube, horizontally polarised shear waves are created. The propagation of these shear waves upwards to the sand surface can be monitored using an array of piezo-electric accelerometers positioned at known locations above the air-hammer. Shear wave velocity for a specific soil layer is computed by dividing the distance between the two closest piezo-electric accelerometers by the time interval it takes for the shear wave to travel between the two instruments. An assessment of the small-strain stiffness of the soil layer can be made once the shear wave velocity is computed.

The air-hammer device is shown in Figure 3.10 with two air lines connected to either ends of the device. The outer surface of the brass tube is coated with sand particles to improve coupling of the device with the surrounding soil. Air-hammer data and sand bed characterisation for this study will be presented in Chapter 5.



Fig. 3.10 Air-hammer device with sand coating around brass tube.

3.2.6 Data Acquisition

Instrument data from dynamic centrifuge tests presented in this thesis have been acquired in-flight using Measurement Computing's high-speed data acquisition card (mccdaq), USB-2633, and DASYLAB software. The acquisition card features 64 single-ended analog inputs, with a maximum sampling rate of 1 MHz distributed over the 64 channels. During

data acquisition, analog voltage signals from the instruments in the centrifuge package are continuously acquired, converted into digital values and saved in .ASC form on a hard drive located in a computer at the centre of the centrifuge. A sampling frequency of 6 kHz was set in DASYLAB for all instruments during earthquakes. A higher sampling rate of 50 kHz was set for specific piezo-electric accelerometers during air-hammer tests.

3.3 Design of Model Structures

3.3.1 Construction

Selection and fabrication of small-scale model frames for use in the enhanced gravity field of a centrifuge requires careful engineering judgement. It is often the case that replicating the full characteristics of a real structure at a reduced model scale is not feasible, and a decision will have to be made on what key prototype frame features should be replicated at model scale to ensure realistic dynamic soil-structure interaction in the centrifuge.

These structural traits include system natural frequencies, building aspect ratios and foundation bearing pressures. As introduced in Chapter 1, inter-storey oil dampers are commonly incorporated into structural frames that would otherwise experience unacceptable storey drifts in the events of wind-loading or base excitations.

For this study, it was decided to focus on the seismic response of shear frames that resist lateral inertial forces through shear and bending in the columns. Two degrees of freedom frames were chosen for this investigation over the more traditional SDOF models often tested in the centrifuge. This permits the inclusion of the first and second lateral deformation modes of a multi-storey structure. A 2-DOF model would also permit the investigation of how inter-storey dampers higher up in the frame are affected by dynamic soil-structure interaction.

In this experimental study, a total of four model frames were fabricated. The structures are classified into two groups; the first category is short and wide frames which will be referred to as “Squat” structures, the second category includes slender frames referred to as “Tall” structures.

For each group, two similar 2-DOF frames were fabricated, one frame would be left bare without dampers to be used as control, while the other frame would be fitted with miniature oil dampers. During fabrication of the model structures, the floor plates were deliberately sized to be thicker and stiffer than the connecting column sections in the direction of shaking. This fabrication detail ensures that shear sway dominates the seismic response of the frames, with the floors simulating a rigid slab, and the columns having substantially smaller bending stiffness in the direction of shaking compared to their axial stiffness.

Promoting shear deformation as opposed to column axial shortening and global frame bending ensures optimal inter-storey damper activation in the structures during base excitation. It is important to highlight that no specific building prototypes were being replicated in this study when the model frames were designed and fabricated; the overall frames were sized to fit around the smallest miniature oil dampers that could be acquired at the time of the study, as well as fit the necessary damper instrumentation needed to conduct the experiments.

Notwithstanding this, the fundamental frequencies and the selected aspect ratios of the two categories of model frames were chosen to resemble that of flexible multi-storey, multi-bay structures. A target fundamental frequency of 0.8 Hz was set as a design objective for both categories of model frames during the preliminary sizing of the floor and column plates. The intention was to maintain comparable fundamental frequencies between the squat and tall frame categories, whilst possessing different aspect ratios to provoke different levels of soil-structure interaction during shaking.

Aspect ratios (structure height / 0.5 $\times$ foundation width) of 3.1 and 4.6 were selected for the squat and tall model frames respectively. All frames in this study are founded on rigid shallow raft foundations embedded into dry Hostun sand beds of varying densities. Foundation bearing pressure was also varied in this investigation by manipulating the self-weight of the raft through the attachment of brass weights to the foundation plate.

Conventional structural dynamics dictates an inherent relationship between a building's fundamental frequency and its height; the higher the building, the more flexible is its structural frame laterally, thus the longer is its fundamental period. For buildings less than 40 m high, Eurocode 8 (BSI, 2005) proposes the following equation to approximate the fundamental period of a structure (T_0) from its height (H) and type of lateral force resisting frame:

$$T_0 = C_t H^{0.75} \tag{3.1}$$

where C_t is an empirical coefficient depending on the type of frame used; for steel moment resisting frames, C_t = 0.085.

Based on Equation 3.1, a steel moment-resisting frame with a fundamental natural frequency of 0.8 Hz would be close to 36 m high. For the two aspect ratios reported earlier, and using this overall building height, an elementary sketch of two theoretical prototype frames can be envisaged. This is shown in Figure 3.11, along with a three-dimensional rendering of the 2-DOF centrifuge model frames used in this study.

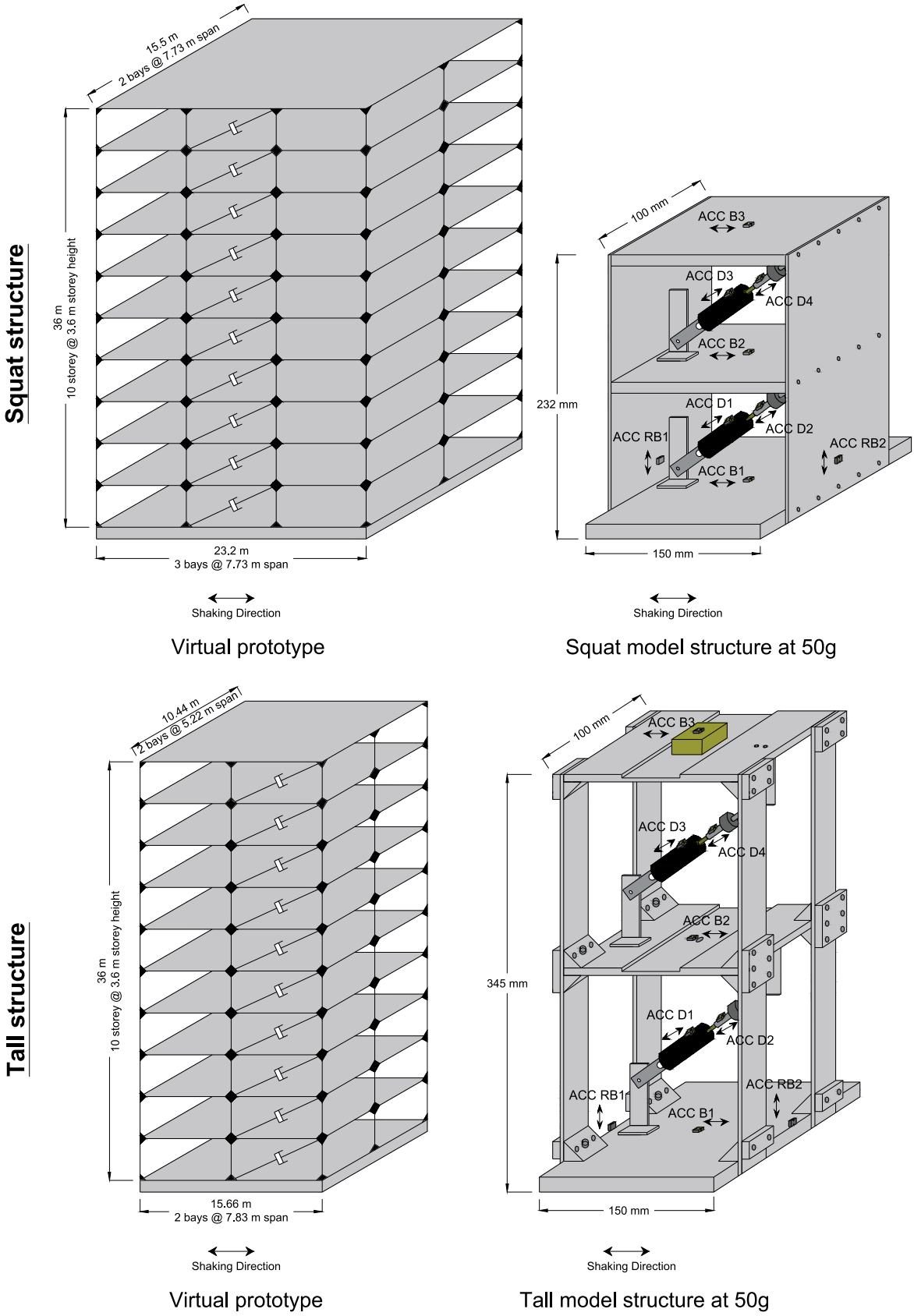

Fig. 3.11 3D rendering of virtual prototype and actual centrifuge model structures.

Both categories of centrifuge model frames were fabricated entirely from Aluminium alloy grade 6082-T6, the properties of which are summarised in Table 3.2. For the squat model frames, the vertical column plates are connected to the horizontal floor plates via a series of five M3 bolts which thread into the sides of each floor plate. Lock washers with external teeth were used in between the M3 bolts and the connecting aluminium alloy plates to minimise the possibility of the bolts turning and coming loose during shaking. The implementation of a single row of bolts to connect vertical and horizontal plates makes the stiffness of the connection very sensitive to the bolt torquing levels, which can affect experimental natural frequencies. To ensure all M3 bolts are torqued to the same level, a hand-drill with a uniform torque-setting was used to fasten all M3 bolts in the model structure. Figure 3.12 shows the overall geometry and construction of the squat frames, both with and without miniature dampers.

Table 3.2 Aluminium alloy grade 6082-T6 properties.

Property	Units	Value
Density	kg/m^3	2700
Young's Modulus (E)	GPa	70
Yield Strength σ_y	MPa	255

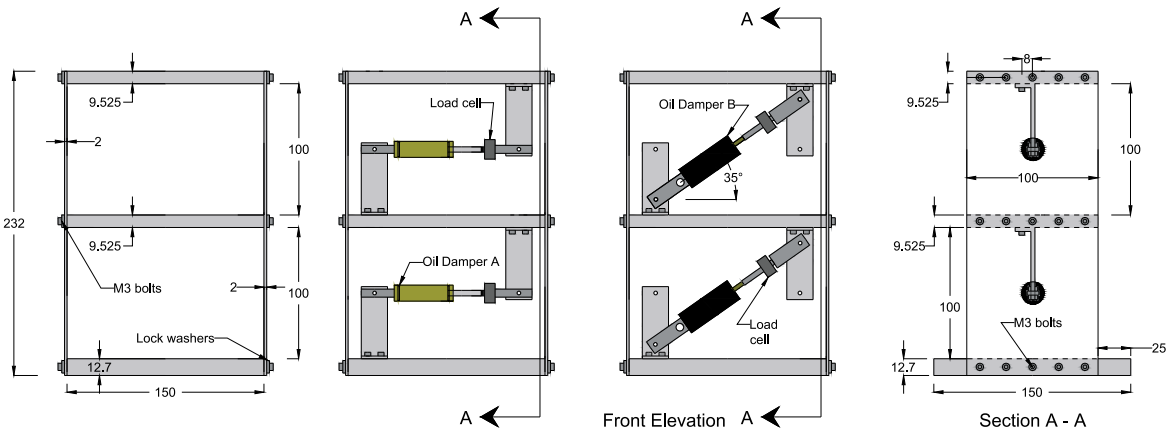

Fig. 3.12 Geometry and construction of the Squat frames (all units in mm).

Two different types of miniature oil dampers were tested with the squat structures, Dampers A and Dampers B. Description of both devices, their internal construction, development and testing will be discussed in Section 3.4. The inter-storey oil dampers are connected to each floor via L-shaped support brackets bolted down into each floor plate through two M3 bolts.

Miniature dampers B are inclined dampers fitted in between floors at an angle of 35° to the horizontal. At one end of the dampers, the damper bodies are connected to the L-shaped support brackets via pivot connections as shown in Figure 3.13. At the other end of the damper piston rods, the devices are threaded in-line with tension/compression load cells, which in turn connect to the other support brackets on the other side. A piece of blue foam is placed beneath the damper body in the damped structure to control sagging of the damper setup and avoid permanently damaging the load cells by bending; the deformable foam piece helps support the damper body whilst allowing it to move during inter-storey drift.

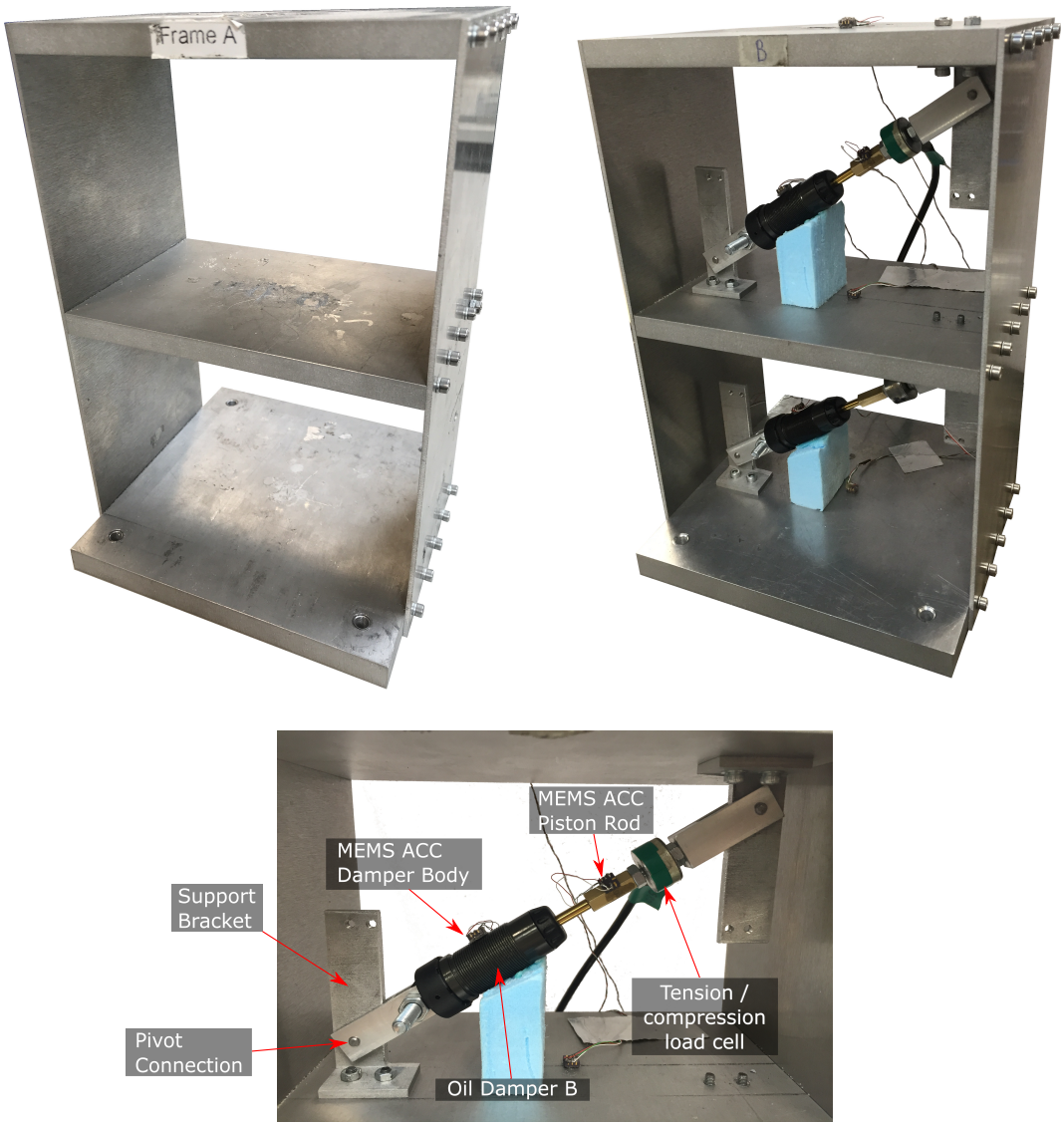

Fig. 3.13 Squat frames equipped with inclined miniature oil dampers type B.

The pivot connections at the extreme ends of the damper-load cell setup allow for small rotations to occur as the two storeys drift relative to each other during shaking. While great care was taken during fabrication to ensure the damper-support bracket connection is able to pivot with no axial play, the reduced scale of the model frames made that impossible to completely eliminate. Constantinou and Symans (1992) reported similar slipping of damper-structure connections, despite their much larger test structure and oil dampers. Any slip at the damper-frame connections would result in reduced damper input strokes relative to the actual inter-storey drift. Such fitment issues, if significant at prototype scale, can limit the effectiveness of oil dampers in a frame.

The 3D renders in Figure 3.11 show the MEMS accelerometer instrumentation layout for both the squat and tall model structures. Three horizontal MEMS accelerometers were installed horizontally at each floor to record absolute storey accelerations in the direction of shaking. As discussed earlier in section 3.1.3, the servo-hydraulic actuator applies base excitations primarily in the longitudinal direction of the shaking table, with minor secondary accelerations arising in the transverse direction. This, coupled with the stiff frame response of both squat and tall frames in the short transverse direction (major axis of bending of the vertical column plates), makes the contribution of such secondary accelerations to the overall frame response negligible, and thus did not warrant measurement.

Two vertical MEMS accelerometers were installed on both sides of the raft foundations to record vertical accelerations. By computing relative vertical accelerations between these two instruments then dividing by the foundation width, data from the vertical MEMS accelerometers can be used to compute foundation rotational accelerations during shaking.

The "Tall" model structures were designed to have a more slender aspect ratio than the squat structures, but maintain a comparable fundamental frequency. In order to achieve this, the model frame was designed to be taller than the squat structures. However, for damper-load cell fitting purposes, it was decided to maintain the same 150 mm width and 100 mm depth of the horizontal floor plates. Figure 3.14 shows the construction and schematics of the tall frames. Inclination of type B miniature oil dampers was kept at 35° by moving the entire damper setup upwards on the L-shaped supporting brackets.

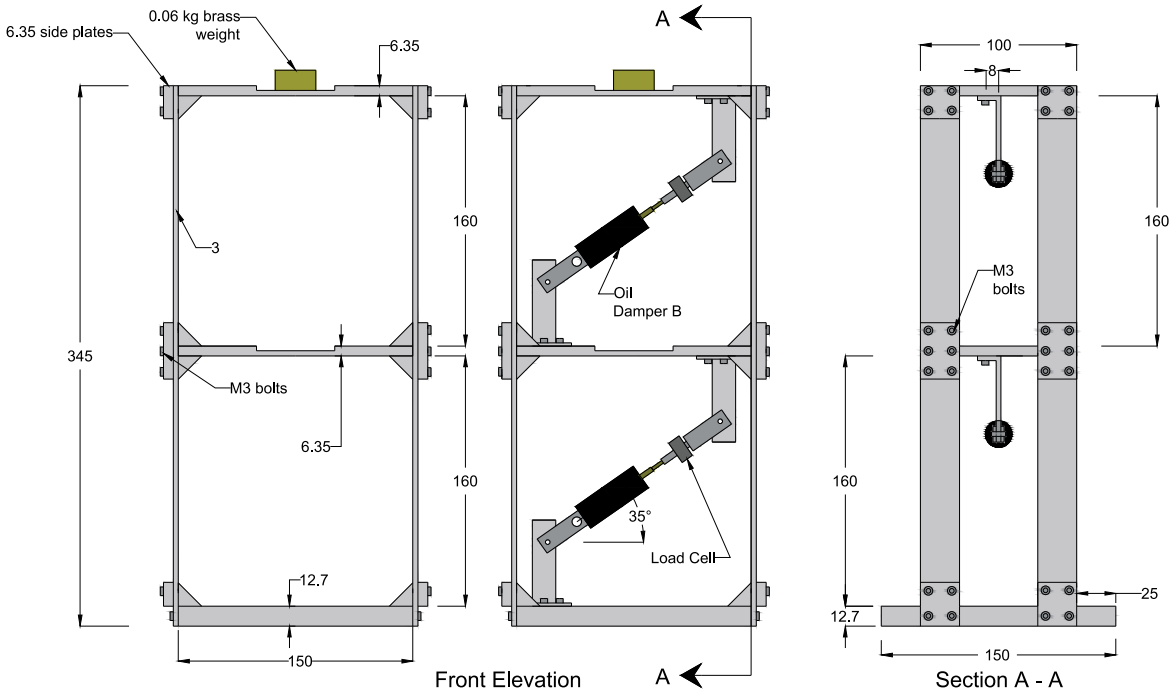

Fig. 3.14 Geometry and construction of tall structures (all units in mm).

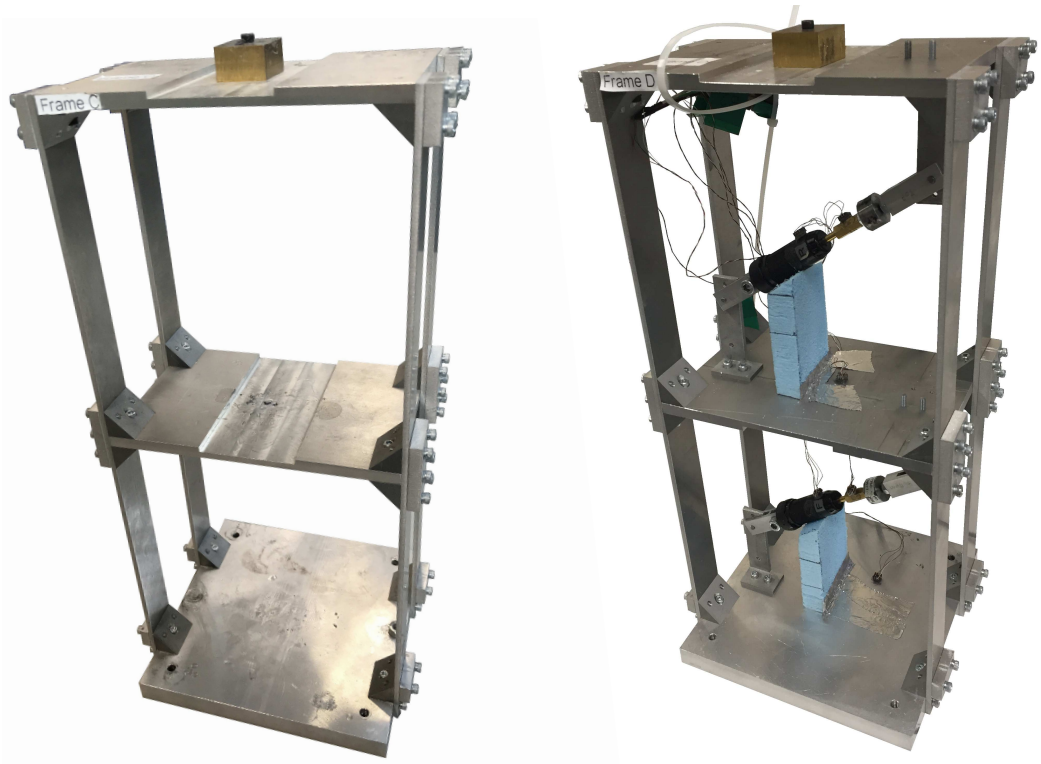

Fig. 3.15 Tall model structures with and without inter-storey dampers.

Fundamental frequency matching between the tall and squat model frames dictated the need to remove 40.5 g of mass from the first floor plate of the tall structures; this explains the 3 x 50 x 100 mm groove machined into the first floor. On the roof, a 60 g block of brass was attached via a single M3 bolt as shown in Figure 3.15. Unlike the column-floor connection detail in the squat model frames, the tall structures have two rows of M3 bolts (three rows for the first floor plate) to allow greater force-couple reactions to occur at the column-floor connections during shaking. Increasing the stiffness of these connections was deemed necessary to compensate for the longer effective lengths of the storey columns. Again, all bolts were tightened using a hand-drill with a predefined torque setting to ensure that they are torqued to the same level. The final construction of the damped and undamped tall structures is presented in Figure 3.15.

3.3.2 Dynamic Characterisation

Both categories of model structures, the squat and the tall frames, can be mathematically represented by means of a lumped parameter model. In this simplification, the continuous mass of one frame would be lumped into three masses, m_f, m_1 and m_2 at the foundation, first and second storeys respectively. The vertical side plates of the model structures provide the lateral stiffness of each floor, k_1 and k_2. For a fixed base frame, the equations governing the undamped free vibration response are given by:

$$\begin{bmatrix} m_1 & 0 \\ 0 & m_2 \end{bmatrix} \begin{Bmatrix} \ddot{u_1} \\ \ddot{u_2} \end{Bmatrix} + \begin{bmatrix} k_1+k_2 & -k_2 \\ -k_2 & k_2 \end{bmatrix} \begin{Bmatrix} u_1 \\ u_2 \end{Bmatrix} = \begin{Bmatrix} 0 \\ 0 \end{Bmatrix} \tag{3.2}$$

In single matrix form:

$$[M]\{\ddot{u}\} + [K]\{u\} = \{0\} \tag{3.3}$$

where m_1, k_1, m_2, and k_2 are the lumped masses and lateral storey stiffness values of the first and second floors respectively, u and $\ddot{u}$ are the displacements and accelerations of the two lumped masses relative to their equilibrium position at rest. Equation 3.3 is a homogeneous linear second order differential equation; the non-trivial solution of such an equation is likely to take the form of:

$$\{u\} = \{U\} sin\omega t \tag{3.4}$$

where $\{U\}$ is a spatial vector of floor displacement amplitudes in space, the magnitude of which varies sinusoidally with time (t) at a frequency of (ω). Taking the second derivative of Equation 3.4 gives:

$$\{\ddot{u}\} = -\omega^2\{U\}sin\omega t \tag{3.5}$$

substitution of Equation 3.4 and 3.5 into 3.3 gives:

$$[K]\{U\} - \omega^2[M]\{U\} = \{0\}$$

$$([K] - \omega^2[M])\{U\} = \{0\} \tag{3.6}$$

Equation 3.6 is an eigenvalue problem. By equating the determinant of the transformation matrix $([k] - \omega^2[m])$ to zero, eigenvalues ω^2 and their corresponding eigenvectors can be computed for this undamped system:

$$|[K] - \omega^2[M]| = 0$$

$$\begin{vmatrix} k_1 + k_2 - \omega^2 m_1 & -k_2 \\ -k_2 & k_2 - \omega^2 m_2 \end{vmatrix} = 0 \tag{3.7}$$

The result of Equation 3.7 is a characteristic equation in terms of ω^2 with two possible solutions, ${\omega_1}^2$ and ${\omega_2}^2$, representing the square of the natural frequencies of each mode of the structure.

During the preliminary stages of selecting the mass and geometry of the aluminium alloy plates to give the desired fundamental frequency of the model frames, an equivalent lumped model would be produced following the mass lumping assumptions highlighted in Figure 3.16; this results in a 2×2 lumped mass matrix. The stiffness matrix is then computed using a fixed-fixed assumption for the vertical plates spanning in between the floors; Figure 3.16 shows the vertical column fixity assumption and the lateral storey stiffness value used for a unit horizontal floor displacement.

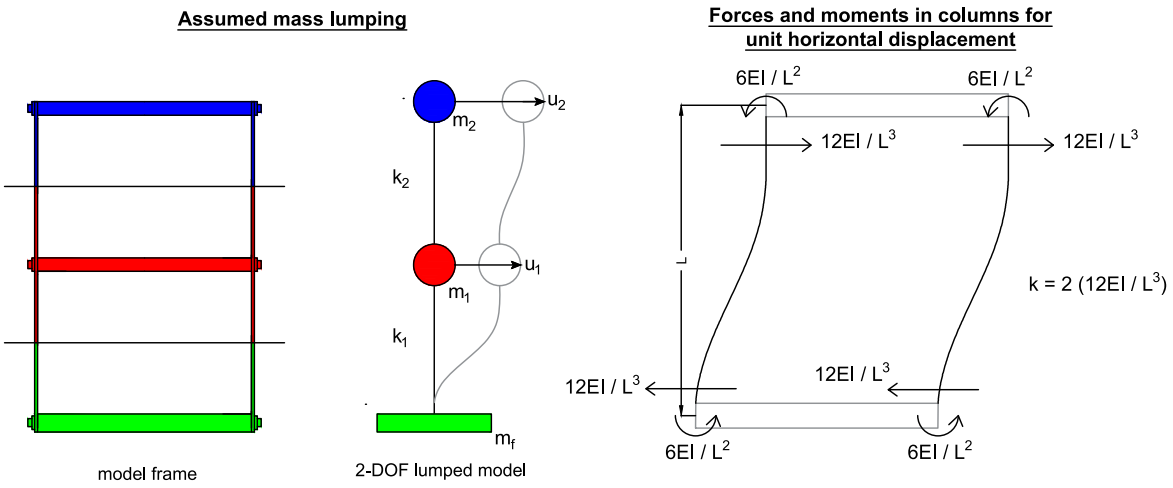

Fig. 3.16 Mass lumping and lateral storey stiffness assumed during preliminary sizing of model structures.

With the mass and stiffness matrices defined for the selected plate geometries, the eigenvalue problem would then be solved as described above to obtain the fundamental frequency of the model structure. This process is repeated multiple times with different combinations of horizontal and vertical plate geometries until an acceptable fundamental frequency is computed (i.e. close to the target objective of 40 Hz model scale / 0.8 Hz prototype scale).

Unfortunately, the model frame stiffness after fabrication, and the actual dynamic mass distribution within the structure, will be different from the theoretical values assumed. There needs to be a procedure for obtaining refined estimates of the mass and stiffness matrices that are more representative of the dynamic experimental behaviour of the model frames post fabrication. The simplest approach would be to conduct 1 g laboratory impact tests on the constructed frames to identify their experimental natural frequencies. In such a test, the model frame would be clamped down to a rigid surface, and the floors would be instrumented with horizontal MEMS accelerometers in the direction of impact. A hammer is then used to lightly strike the roof of the model frame in the same direction of shaking as the model would experience on the servo-shaker. This abrupt perturbation puts the structure into a state of decaying free vibration, provoking mainly a response at the natural frequencies of the system. Fast-Fourier-Transform (FFT) is applied to the acceleration traces recorded by the MEMS accelerometers on the floors to detect these governing frequencies. FFT results from such impact tests are presented in Figure 3.17.

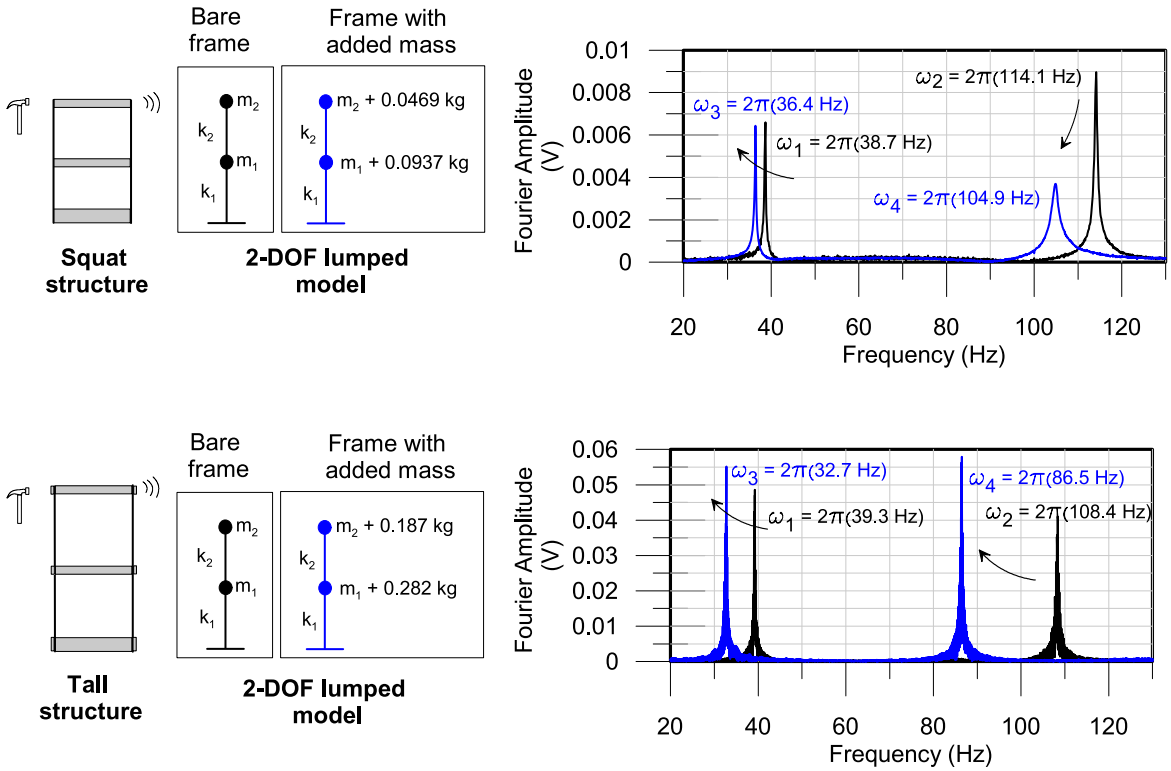

Fig. 3.17 Fast-Fourier Transform (FFT) results from hammer impact testing on second storey floor plates.

The natural frequencies of the as-built bare model frames are illustrated by the black FFT plots in Figure 3.17. Two distinctive peaks can be observed for the Squat and Tall model frames, indicating the experimental frequencies of mode 1 and mode 2 respectively. Kim et al. (2015) proposed a simple method of identifying the experimental mass and stiffness properties of a SDOF frame using what they refer to as the "added mass" concept. Impact testing would be first conducted on the frame to obtain its natural frequency ω_1. The undamped natural frequency of a SDOF system is given by:

$$\omega_1 = \sqrt{\frac{k}{m}} \tag{3.8}$$

where k is the lateral stiffness, m is the lumped mass. After impact testing ω_1 becomes known. However, there are still two unknowns in Equation 3.8, m and k.

By adding a known added mass (m_{add}) to the SDOF structure, and conducting another impact test, a new undamped natural frequency is measured:

$$\omega_2 = \sqrt{\frac{k}{m+m_{add}}} \tag{3.9}$$

The end-result of this procedure is two expressions, Equations 3.8 and 3.9, with two unknowns, k and m, which can now be solved for mathematically. This approach is believed to have a more solid basis than making rudimentary assumptions on mass lumping and column end-fixity conditions.

Applying this approach to a 2-DOF structure is possible, but mathematically more onerous. Writing the characteristic equation of the transformation matrix in Equation 3.6 gives the following:

$$(k_1+k_2-\omega^2 m_1)(k_2-\omega^2 m_2)-(k_2)^2=0 \tag{3.10}$$

with four unknowns, m_1, m_2, k_1 and k_2. Four simultaneous equations are needed, with four experimentally identified values of ω, in order to solve for the unknowns.

Figure 3.17 shows roof impact testing done on the same model frames with known masses added to each floor; the value of each added mass is shown in the blue schematic to the left of the FFT plot. In addition to the two natural frequencies of the bare frame, the addition of known mass to each floor results in two new lower natural frequencies. Four simultaneous equations can now be formulated:

$$(k_1+k_2-\omega_1^2 m_1)(k_2-\omega_1^2 m_2)-(k_2)^2=0 \tag{3.11}$$

$$(k_1+k_2-\omega_2^2 m_1)(k_2-\omega_2^2 m_2)-(k_2)^2=0 \tag{3.12}$$

$$(k_1+k_2-\omega_3^2 (m_1+m_{add,1})(k_2-\omega_3^2 (m_2+m_{add,2})-(k_2)^2=0 \tag{3.13}$$

$$(k_1+k_2-\omega_4^2 (m_1+m_{add,1})(k_2-\omega_4^2 (m_2+m_{add,2})-(k_2)^2=0 \tag{3.14}$$

To solve for the unknowns, the system of equations defined in 3.11 to 3.14 can be setup in MATLAB in terms of the four unknown variables. The “solve” function in MATLAB can then be used to solve the four simultaneous nonlinear equations; MATLAB will compute

several possible solutions for each unknown variable. The most sensible combination of lumped masses and lateral storey stiffness values would then have to be selected out of all the solutions.

Given that clamping of a structure base at 1g on the lab floor during impact testing does not result in the same fixity as bolting the frames onto the servo-shaker directly during fixed base centrifuge tests, it was decided to use frequency data from the latter for this characterisation. Images of the model frames bolted to the servo-shaker in the centrifuge as presented in Figure 3.18. Fourier components of the second floor acceleration traces are plotted in Figure 3.19 as recorded in the centrifuge during a weak sine-sweep excitation.

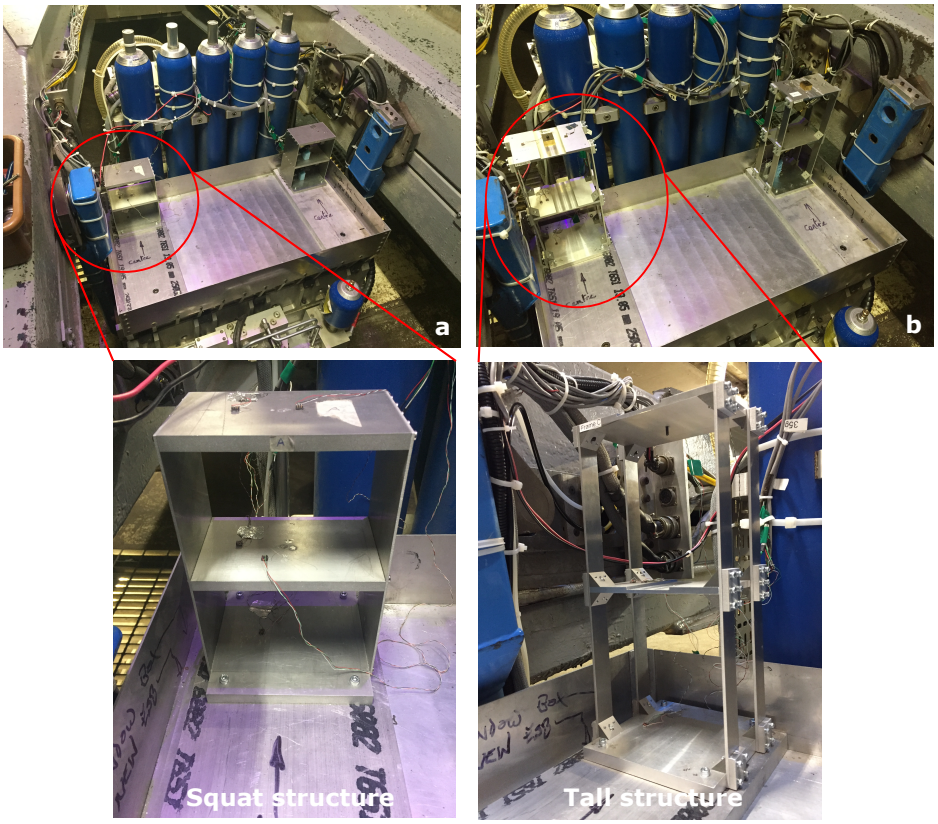

Fig. 3.18 Fixed-base centrifuge testing at 50 g for (a) squat frames (b) tall frames.

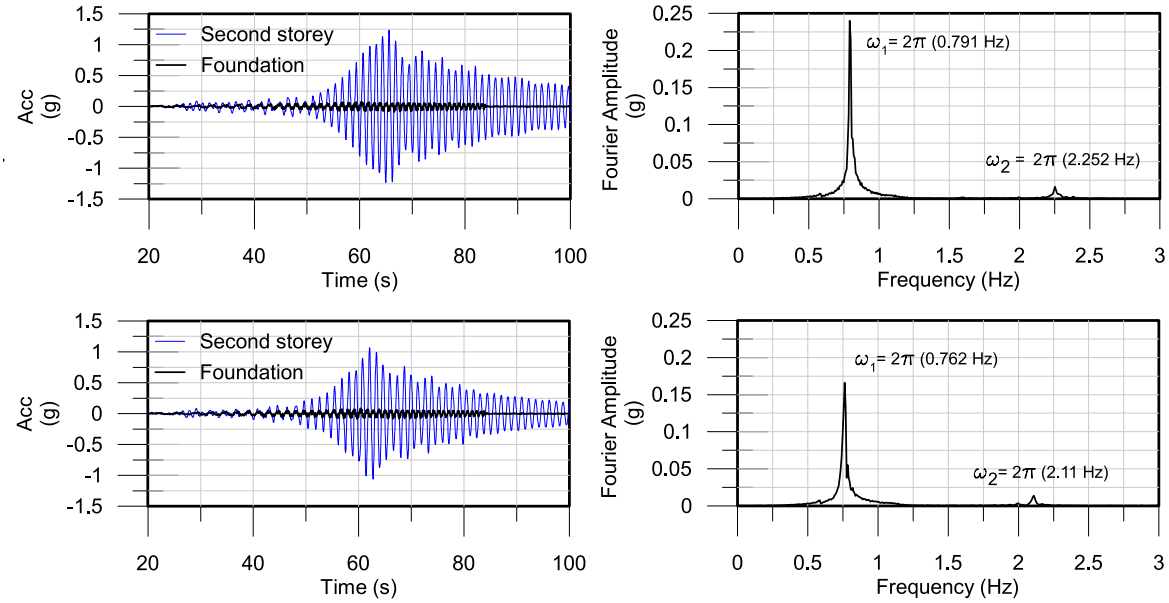

Fig. 3.19 Second storey acceleration time traces and FFT spectra for 0 to 1.2 Hz sweep base excitation.

Unfortunately, the "added mass" procedure was not conducted in the centrifuge. However, for the same added mass on each floor, the same percentage reductions in natural frequencies as the ones observed in Figure 3.17 can be used to compute two new natural frequencies; for 1 g impact testing on the squat frame, the addition of 93.7 grams and 46.9 grams to the first and second storeys reduced the first and second natural frequencies by 6 % and 8 % respectively. Applying this drop to the first natural frequency reported from the fixed base centrifuge test would reduce it to 0.74 Hz. The second natural frequency would drop to 2.07 Hz. The same can be implemented for the tall structure. Equations 3.11 to 3.14 can now be solved in MATLAB with four natural frequencies.

Example outputs from MATLAB for the squat model frame are presented in Table 3.3. Due to nonlinearity of the four simultaneous equations, MATLAB outputs seven possible combinations of lumped masses and effective lateral stiffness values. The first six solution combinations are not feasible either due to near zero masses, or negative stiffness, or unrealistic lumped mass and stiffness parameters.

Table 3.3 Theoretical lumped mass and lateral storey stiffness compared to MATLAB solutions for the Squat model frame.

(All results in model scale)		Lumped Mass		Lateral Storey Stiffness	
Traditional mass lumping and storey stiffness		m_1 (kg)	m_2 (kg)	k_1 (kN/m)	k_2 (kN/m)
		0.531	0.458	89.465	89.465
7 combinations of proposed	Solution 1	0	-0.0469	0	0
solutions from MATLAB nonlinear	Solution 2	-0.0937	0	0	0
simultaneous Equation solver	Solution 3	0.0062	-0.0512	5.15	-1.89
	Solution 4	-0.1034	0.0035	-6.09	1.83
	Solution 5	0.5113	0.3589	226.01	24.78
	Solution 6	0.9058	0.2208	71.56	85.29
	Solution 7	0.4259	0.4854	70.68	89.28

The final solution provides a plausible combination of lumped masses and storey stiffness, and will be used in the duration of this study for the Squat structures. The same logic is applied to the tall structure. A summary of the lumped masses and effective storey stiffness values for both categories of model frames are presented in Table 3.4.

Table 3.4 Summary of centrifuge model structures used in this study.

Structure Type	SQ-UN-L	SQ-UN-H	SQ-DX-L	SQ-DX-H	TL-UN-L	TL-UN-H	TL-DX-L	TL-DX-H
Model Height (m)	11.6				17.25			
Model Width (m)	7.5				7.5			
Aspect Ratio (Height / 0.5 × width)	3.1				4.6			
Centre of Gravity (m)	4.68	2.94	4.79	3.1	6.04	3.38	6.30	3.67
Bearing Pressure (kPa)	40	73.2	42.9	76.2	40.4	73.7	43.4	76.6
Fixed Base 1st Mode (Hz)	0.79		≈ 0.805		0.76		≈ 0.77	
Fixed Base 2nd Mode (Hz)	2.25		N/A		2.17		N/A	
	Lumped Mass							
m_1 (kg)	53238		62863		53962		63587	
m_2 (kg)	60675		65488		64375		67500	
m_f (kg)	115250	305875	120000	310625	107250	112000	297875	302750
	Effective Lateral Stiffness							
k_1 (kN/m)	3534				3593			
k_2 (kN/m)	4464				3869			

SQ: Squat structure / TL: Tall structure

UN: bare frame (undamped)

DX: damped frame

D1: heavy damping / Oil damper B configuration 3

D2: medium damping / Oil damper B configuration 4

D3: light damping / Oil damper B configuration 5

D4: Oil dampers A

L: light foundation / H: heavy foundation

3.4 Miniature Oil Dampers

3.4.1 Miniature Oil Damper A

Procurement and development of small-scale oil dampers that can fit into centrifuge model frames is indeed a challenge of its own. The difficulty does not lie in the damper size per se, but rather in the remarkably different operating conditions that the miniature dampers experience in the centrifuge compared to their real counterparts.

For real structures, it is not common to have inter-storey oil dampers installed in stiff frames due to the limited motion of the damper ends during seismic shaking. As such, prototype dampers fitted into structural frames are less likely to operate at frequencies higher than around 4 Hz, which is the typical fundamental frequency of stiff structures (Constantinou and Symans, 1993). Prototype damper strokes permitted during shaking also vary between $\pm$ 75 mm to $\pm$ 125 mm (Taylor Devices Inc., 2019). In the high gravitational field of a centrifuge, and in accordance with the scaling laws of frequency for dynamic centrifuge tests, the miniature oil dampers fitted into the model frames are subjected to frequencies 50 times greater than those experienced by their real counterparts.

As discussed earlier in section 3.1.1, length also scales in the centrifuge by a factor of N, where N is the corresponding g-level of the test. Therefore, prototype damper strokes of $\pm$ 75 mm to $\pm$ 125 mm will be equivalent to around $\pm$ 1.5 mm to $\pm$ 2.5 mm model scale at 50 g. In fact, the inter-storey drift values of the centrifuge frames at model scale are in the order of only a few millimetres since the frames are intended to remain elastic during shaking. The scaling laws for frequency and stroke would therefore dictate that any miniature dampers to be used in the centrifuge must be capable of dissipating energy under small-stroke high frequency motions.

The first experimental miniature dampers to be developed for this purpose were oil dampers A. These devices were originally acquired from MAGOM HRC, as hydraulic cylinders, which were modified in-house to mimic passive oil dampers for the purposes of this study. MAGOM HRC is a small company specialising mainly in the development and manufacturing of radio-controlled hydraulic products for use in scaled construction machines and radio-controlled trucks. Figure 3.20 shows the geometry and internal construction of these procured hydraulic cylinders.

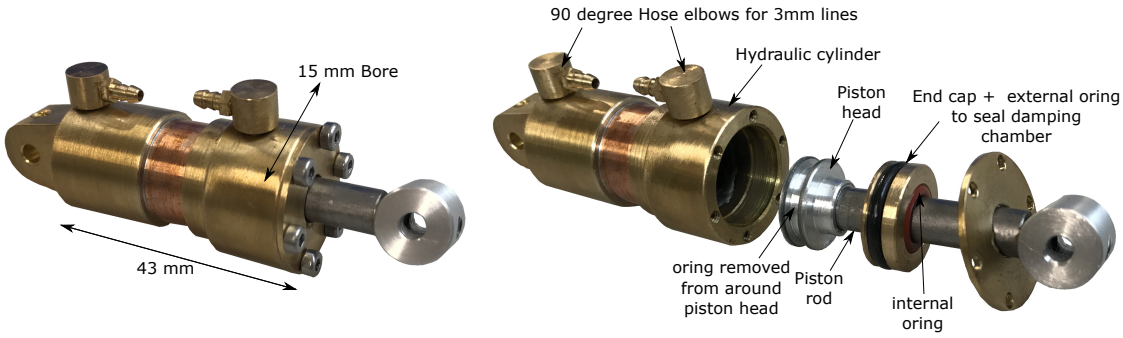

Fig. 3.20 MAGOM 15 mm Bore hydraulic cylinder geometry and construction.

Mechanically, hydraulic cylinders operate differently to passive oil dampers; a hydraulic cylinder uses an oil pressure gradient to induce motion of the piston rod, while an oil damper utilises oil pressure gradients to slow down the motion of the piston rods as it is driven externally. The key difference between these two devices is whether the oil filled chambers to either side of the piston head are sealed or interconnected. The 15 mm bore hydraulic cylinders acquired from MAGOM HRC are originally fitted with an o-ring around the piston head to ensure compartment isolation between the two chambers in front and behind the piston head; this o-ring has been removed from the piston head in Figure 3.20, but the indentation and position of the o-ring on the head remains clear. Each chamber has a nozzle that allows oil flow in and out of the cylinder; pumping pressurised oil through one nozzle would cause the piston rod to move in one direction, while pumping oil through the other nozzle would reverse that direction.

To re-purpose the hydraulic cylinders into passive oil dampers, the o-ring seal around the piston head is removed to create a 1 mm wide annular gap between the piston head and the inner chamber of the hydraulic cylinder. The two compartments, in front of and to the back of the piston head, are now linked through an annular orifice. External forcing of the piston rod would cause oil to flow from one chamber to the other, around the piston head, through the annular orifice. Oil to the forward side of the progressing piston head will build up positive pressures, while oil behind the moving piston head will be under lower pressures as this chamber expands in volume; this pressure gradient induces rapid flow of viscous oil through the annular orifice, generating a resistive damping force that is proportional to the velocity of the piston head (i.e. at rest, oil pressures in both chambers to either side of the piston head are in equilibrium, and thus, no force is generated).

As the piston rod moves in/out of the enclose cylinder, the volume of the rod itself needs to displace an equal volume of oil in/out of the chamber to avoid hydraulic lock-up of the damper. The nozzles to either side of the piston head allow the movement of displaced oil in/out of the miniature devices to external accumulator tanks. Figure 3.21 is a vertical cut along the longitudinal axis of one of the re-purposed hydraulic cylinders to show the internal components and working mechanism of miniature oil damper A.

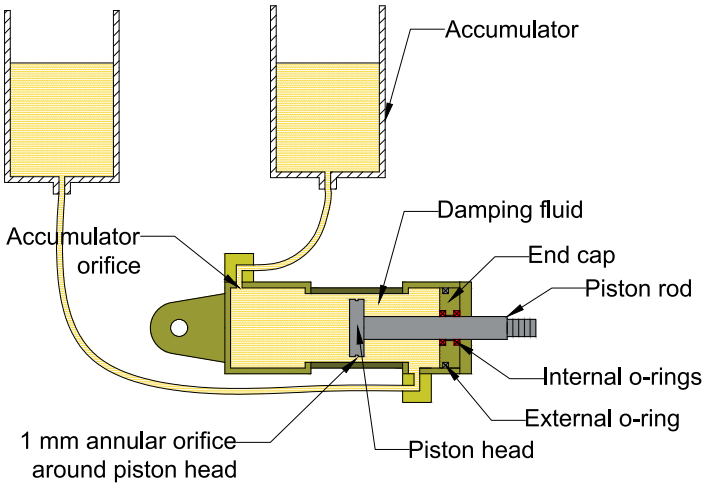

Fig. 3.21 Hydraulic cylinder repurposed into a passive oil damper.

Prior to application in the centrifuge, it was deemed important to make sure that miniature oil dampers A were indeed able to dissipate energy for small-stroke high frequency motions. In this regard, a brief experimental investigation was conducted at 1 g on the lab floor using a compact Ling 200 series electromagnetic shaker. Figure 3.22 shows the schematic layout of the experimental setup, and an image from one of the test runs.

A signal generator is first used to produce a sinusoidal voltage trace of specific amplitude and frequency. The signal is then passed through a power amplifier, which in turn drives the Ling shaker. The vibrating tip of the shaker is attached to a tension / compression load cell, which is threaded inline with the damper piston rod; the damper body is restrained by a clamp stand. Piston rod acceleration data is obtained from MEMS accelerometers by computing the relative acceleration between the damper piston rod and the damper body. The force output of the damper is also recorded experimentally by the load cell. The ease with which these dampers can be assembled/dismantled permit the investigation of multiple damping fluids. Damper force-displacement and force-velocity plots are presented in Figure 3.23 for two different damping fluids, H32 hydraulic oil (32 cSt at 40^0C) and H68 hydraulic oil (68 cSt at 40^0C).

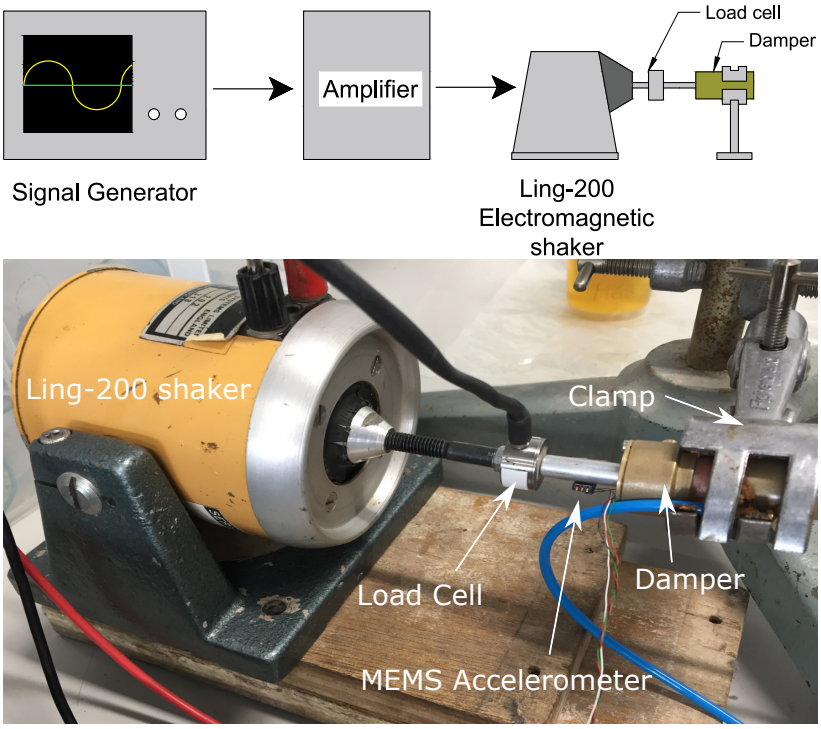

Fig. 3.22 Ling-200 series shaker testing of miniature damper A.

Results in Figure 3.23 revealed positive indications regarding the energy dissipative characteristics of miniature dampers A for small-stroke high frequency input motions; force-displacement traces take the shape of clockwise loops implying hysteresis, and the force-velocity plots indicate some relationship between damper force and stroke velocity, albeit not a linear one.

As expected, the more viscous H68 hydraulic oil generated greater damping forces than the thinner H32 oil for a given velocity, as depicted by the steeper gradients of the force-velocity traces at almost all frequencies. A very clear degradation in the damper performance is observed for both damping fluids as frequency increases from 10 Hz to 50 Hz. Force-velocity plots from these shaker tests show visible lag between damper forces and stroke velocities, indicating energy is being stored elastically due to system compliance.

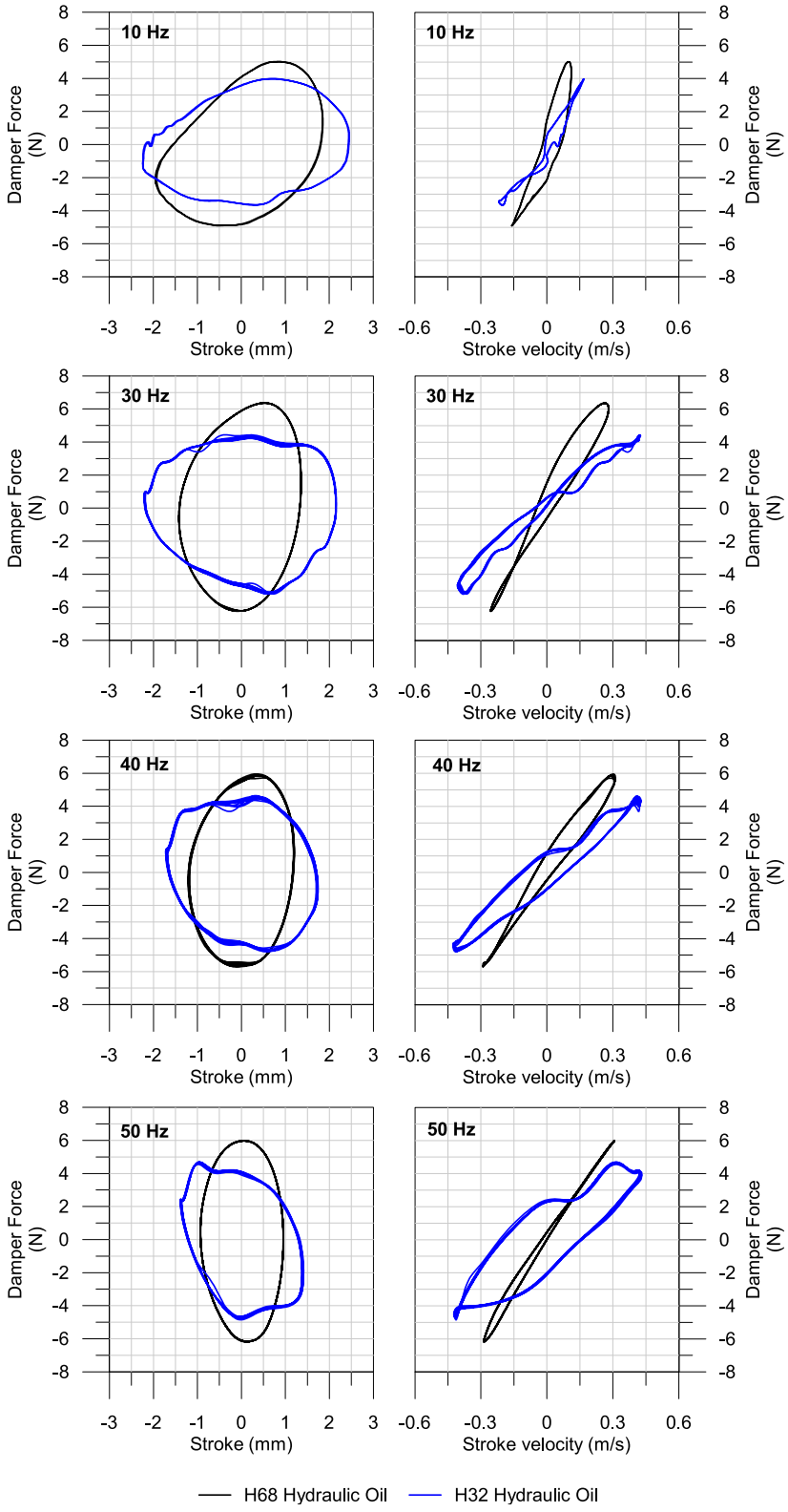

Fig. 3.23 Force-displacement and force-velocity traces of miniature damper A from Ling-200 series shaker tests.

As discussed in Boksmati et al. (2018), three possible sources of flexibility in the dampers could be envisaged:

1. The entrapment of air during assembly of the dampers and filling with oil.

2. The compressibility of hydraulic oil itself due to dissolved air. The high frequency motion of the piston head immersed in oil aggravates air bubble formation in the damping fluid, specifically if the pressures behind the piston head get too low. This is a common problem in dampers if the viscosity of the oil being compressed is too high to flow through the orifice restriction, and cannot catch up with the rapid motions of the piston. This can lead to local cavitation and foaming of the oil which degrades damper performance.

3. The displacement of oil in and out of the accumulator tanks as shown in Figure 3.21, also involves forcing oil through two restriction nozzles; again, if oil is too thick, the flow cannot match the speed of the piston motion, aggravating fluid compressibility effects and oil foaming.

Notwithstanding these limitations, the 1 g shaker tests confirm that these dampers do indeed exhibit a velocity-dependant dissipative behaviour for high frequency small stroke excitations, albeit with an additional dependency on displacements due to their inherent flexibility.

Two trial tests were conducted at 50 g in the centrifuge by fitting these dampers into a Squat model frame. The damped frame, a sketch of which is shown earlier in Figure 3.12, was tested twice, once on dry dense sand, and another on dry loose sand, using the damper instrumentation scheme described in section 3.3.1. Miniature oil dampers A were filled with H68 hydraulic oil for these tests. Examples of damper force-velocity traces recorded during these high-gravity trials are plotted in Figure 3.24 for a 15-cycle, weak and a strong, 0.8 Hz sinusoidal input motion.

Data from Figure 3.24 reveals an interesting, yet slightly discouraging, response from Miniature oil dampers A. During the weak excitation of the damped structure, the light grey plots in the figure show the dampers exhibiting severe degradation in damping coefficients as stroke velocity increased; this was not a transient phenomenon as it continued to occur for around 10 cycles. Only during the last 4 force-velocity cycles shown in black in Figure 3.24 did both dampers begin to approach, but never actually reach, a steady-state response.

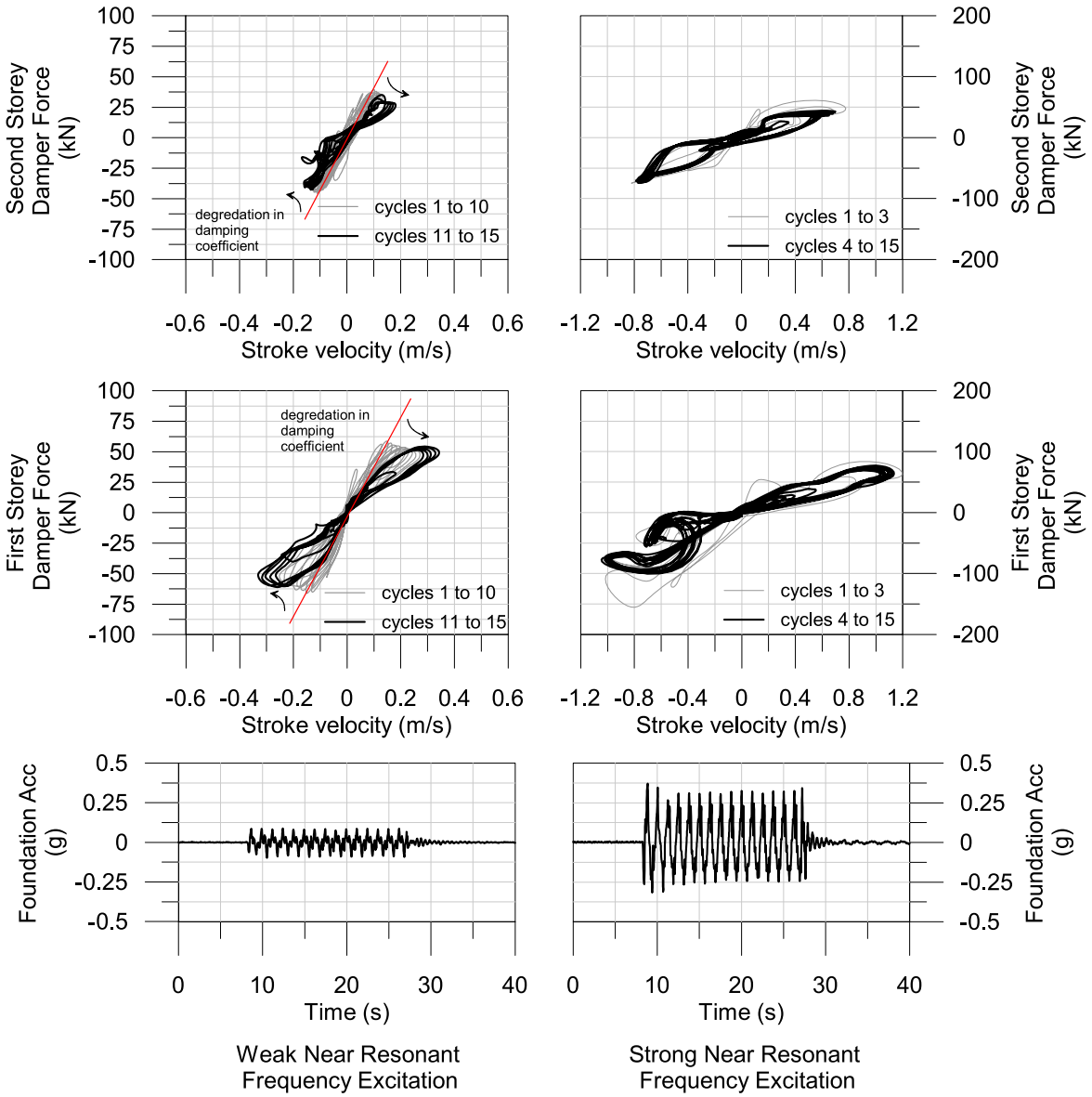

Fig. 3.24 Experimental damper force-velocity traces as measured in trial centrifuge tests.

For the strong input motion, both miniature dampers exhibit rough, yet consistent, force-velocity relationships over the entirety of the 15 input motion cycles fired. It is strongly believed that oil cavitation and foaming are responsible for the degradation trend observed in Figure 3.24 during the weak input motion. Once the damping fluid has cavitated and become foamy, damper force outputs for a sinusoidal input motion become consistent, yet very irregular.

3.4.2 Miniature Oil Damper B

The previous section introduced the first type of miniature oil dampers to be tested in this study. Boksmati et al. (2019) showed that oil dampers A are indeed successful at dissipating energy, primarily by velocity-dependant damping forces, in the centrifuge. However, cavitation and foaming of the damping fluid with increasing stroke velocities can cause considerable degradation in damping coefficients during shaking, complicating the problem of dynamic soil-structure interaction even further. Moreover, the movement of a damper piston through foamed oil is shown to result in rough and irregular force-velocity relationships, which can make analytical modelling of such devices very challenging.

To this extent, a decision was made early on in the research to pursue another type of miniature oil damper, referred to in this study as oil damper B. Geometry, construction and the internal components of miniature oil damper B are presented in Figure 3.25.

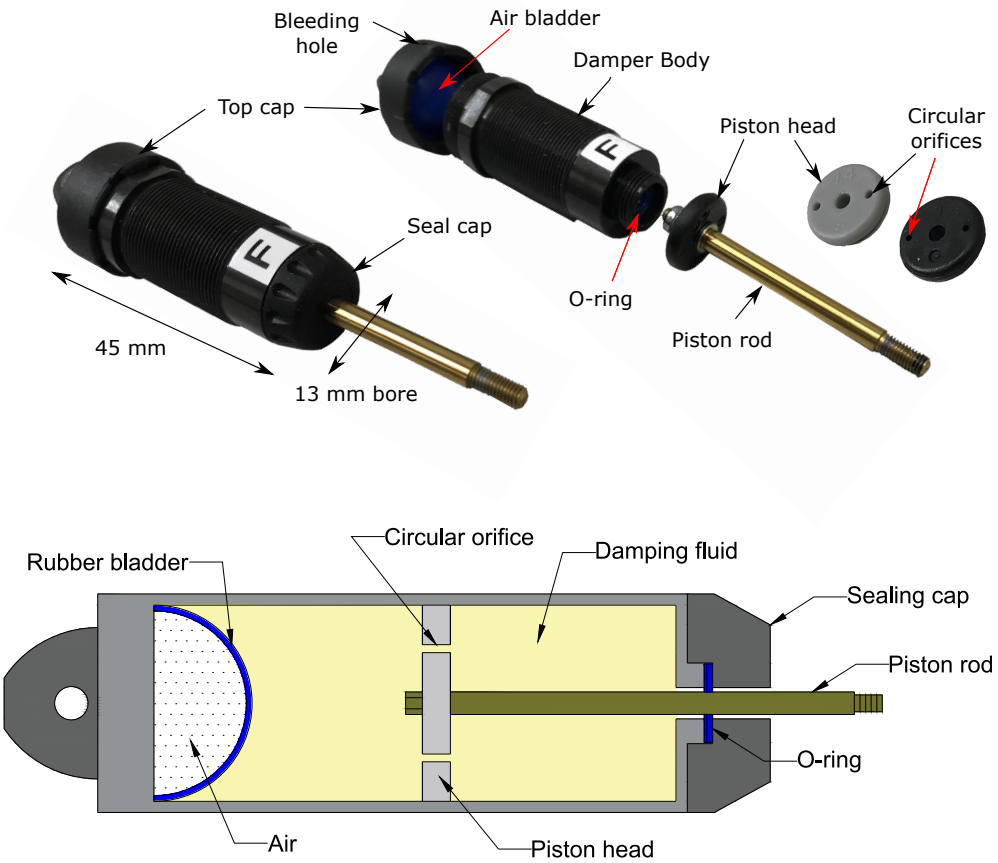

Fig. 3.25 Miniature damper B geometry, construction and internal mechanism.

These dampers, originally named GTR shocks by the manufacturer, have been acquired from Traxxas, a company specialised in engineering and building nitro and radio-controlled (RC) performance vehicles. The devices form part of a linkage-based suspension system fitted into 1/10th scale nitro RC cars to improve handling and absorb road vibrations.

The internal working mechanism and components of dampers B are different from the re-purposed hydraulic cylinders discussed in the previous section. Rather than using external accumulators to accommodate displaced oil, these new dampers use an air bladder to compensate for the volume of piston rod going in/out of the damper body. Instead of an annular orifice around the piston head, dampers B use piston heads which are flush with the inside of the Teflon-coated damper body, with two circular restrictions to allow passage of oil. There is also a substantial reduction in weight of these new dampers (15 grams) relative to the re-purposed hydraulic cylinders (57 grams). Therefore, the deviation in the structural mass participating in the dynamic response of the damped structure will be closer to that of its bare frame counterpart.

These new devices, like oil dampers A, are easy to assemble/dismantle which facilitates varying the damping output not only by changing the viscosity of the damping fluid, but also by using piston heads with different orifice sizes. Figure 3.25 shows two examples of piston heads, grey and black, with orifice diameters of 1.4 mm and 1.0 mm respectively; other orifice diameters are also available.

Preliminary testing of these devices was carried out directly in the centrifuge by fitting them into the squat model frame, and conducting multiple trials at 50 g with different damper-oil configurations. During the tests, the damped frame was bolted to the shaking table of the servo-shaker to simulate a fixed base condition as shown in Figure 3.26. Table 3.5 lists the details of each of the five trial tests conducted. Damper force-velocity and force-displacement plots are presented in Figures 3.27 to 3.32 for each damper configuration.

Table 3.5 Damper setup configurations for fixed base trial centrifuge tests.

Configuration #	Damping Fluid	Orifice Diameter	O-ring and Seal Cap	Air Bladder
1	Silicon oil / 350 cSt	1 mm dia.	No	No
2	Hydraulic oil H68 / 68 cSt	1 mm dia.	No	No
3	Hydraulic oil H68 / 68 cSt	1 mm dia.	Yes	Yes
4	Hydraulic oil H68 / 68 cSt	1.4 mm dia.	Yes	Yes
5	Hydraulic oil H32 / 32 cSt	1.6 mm dia.	Yes	Yes

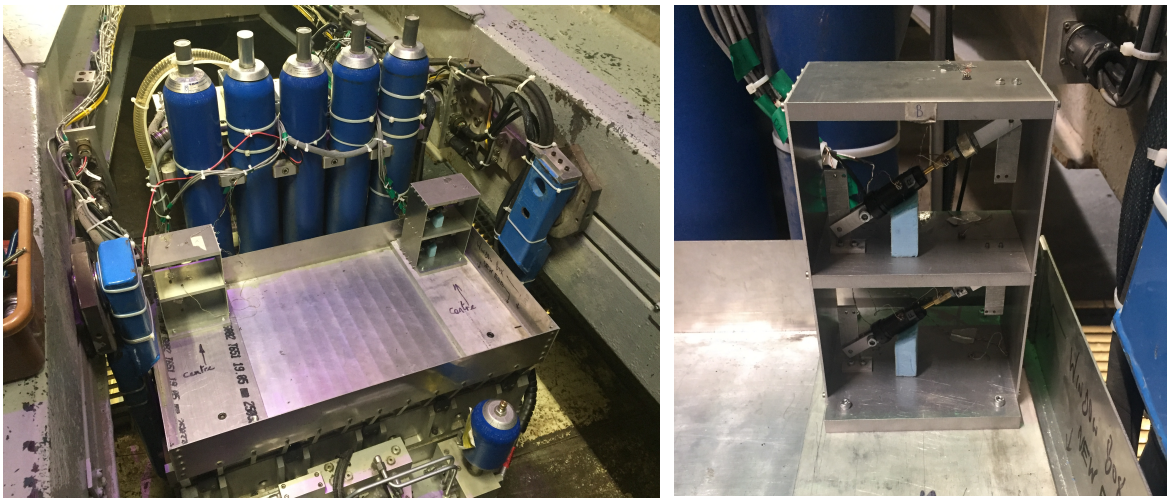

Fig. 3.26 Trial centrifuge tests at 50 g to test the performance of different damper configurations.

The first damper configuration uses 350 cSt silicon oil as a damping medium for both inter-storey dampers. The air bladder, o-ring and seal cap for both damping devices (refer to Figure 3.25) were removed in this trial to test the basic configuration of a piston moving through oil; the damper bodies are no longer sealed chambers as originally intended by Traxxas.

As evident by the second storey floor accelerations in Figure 3.27, the damped frame comes to an immediate halt at the end of the earthquake, with very little traces of free vibration. In fact, the very similar magnitudes and the minor phase difference between the floor accelerations and the foundation accelerations imply that the damped frame was very close to responding as a rigid body to the base excitation. This is typical of an overdamped system and rarely applies to damped prototype structures in the field. As such, this configuration was deemed not suitable for this study.

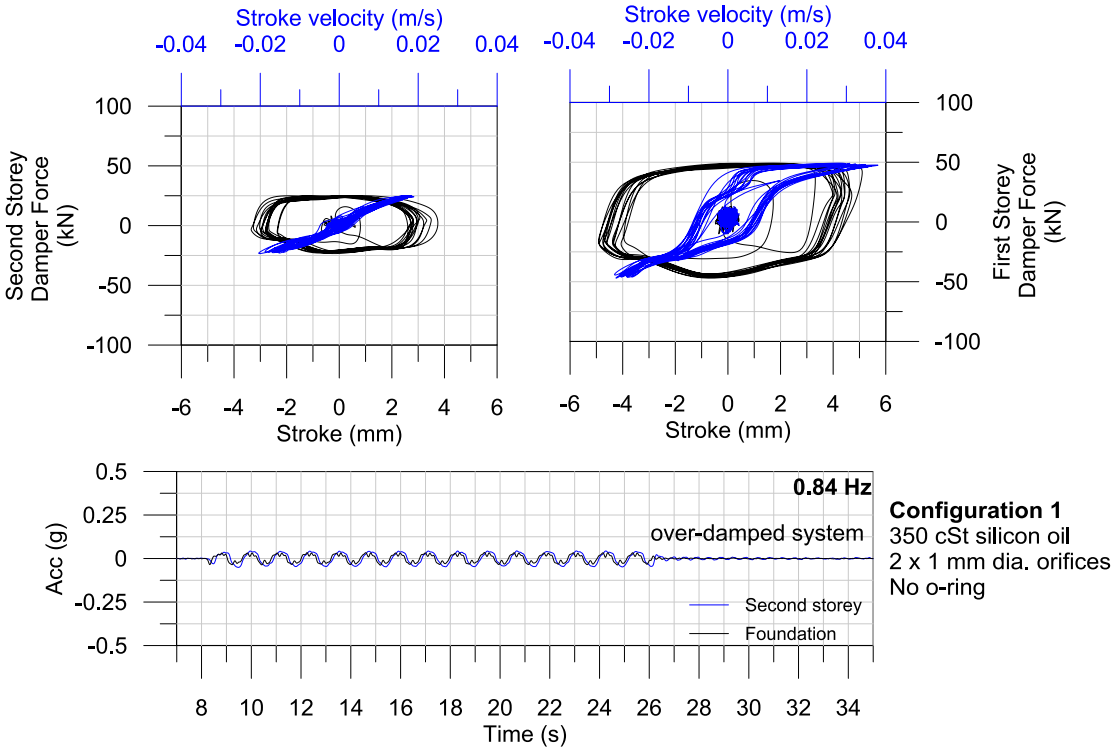

Fig. 3.27 Oil damper B force-velocity-displacement plots for Configuration 1.

The second damper configuration in Figure 3.28 uses thinner H68 hydraulic oil, with the damping fluid also exposed to the surrounding atmosphere as the bladder, o-rings and seal caps were removed for both devices. The damped structure is no longer an over-damped system as evident by the single, albeit non-symmetrical cycle of free vibration recorded after the motion has ceased. This asymmetry in peaks applies to the entire second storey acceleration trace, and is the result of heavily irregular damper force-velocity and force-displacement responses for this damper setup. The flatness in damper force-velocity is believed to be the result of the damper chamber not being air-tight.

A typical extension and compression cycle is highlighted in Figure 3.28 using magenta and cyan traces respectively. During the extension cycle of a regular sealed damper, negative pressures build up behind the moving piston while positive pressures build up ahead of the piston as the sealed oil chambers change volume. The net pressure difference creates a suction force that forces oil to flow through the orifices into the expanding chamber. Once open to air, the majority of the pressure gradient squeezing oil through the restrictions comes from the negative pressures behind the piston. If the damping fluid is too viscous to catch up with the high frequency motions of the piston, a suction force is generated as the piston moves out of the damper. This explains the flatness observed in force for both, first storey and second storey dampers in Figure 3.28.

For a sealed damper, the fluid chambers to either side of a moving piston can generate higher pressure gradients that have a better chance at squeezing oil through the orifices during high frequency motions of the piston. This is visually illustrated in Figure 3.29.

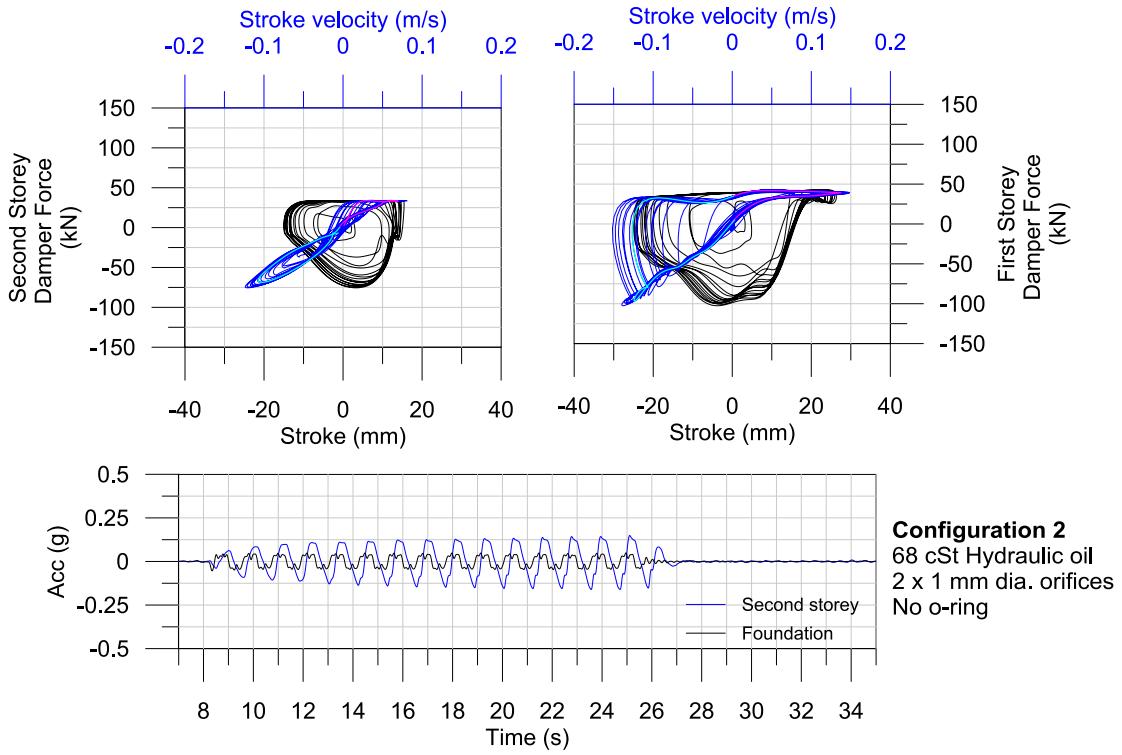

Fig. 3.28 Oil damper B force-velocity-displacement plots for Configuration 2.

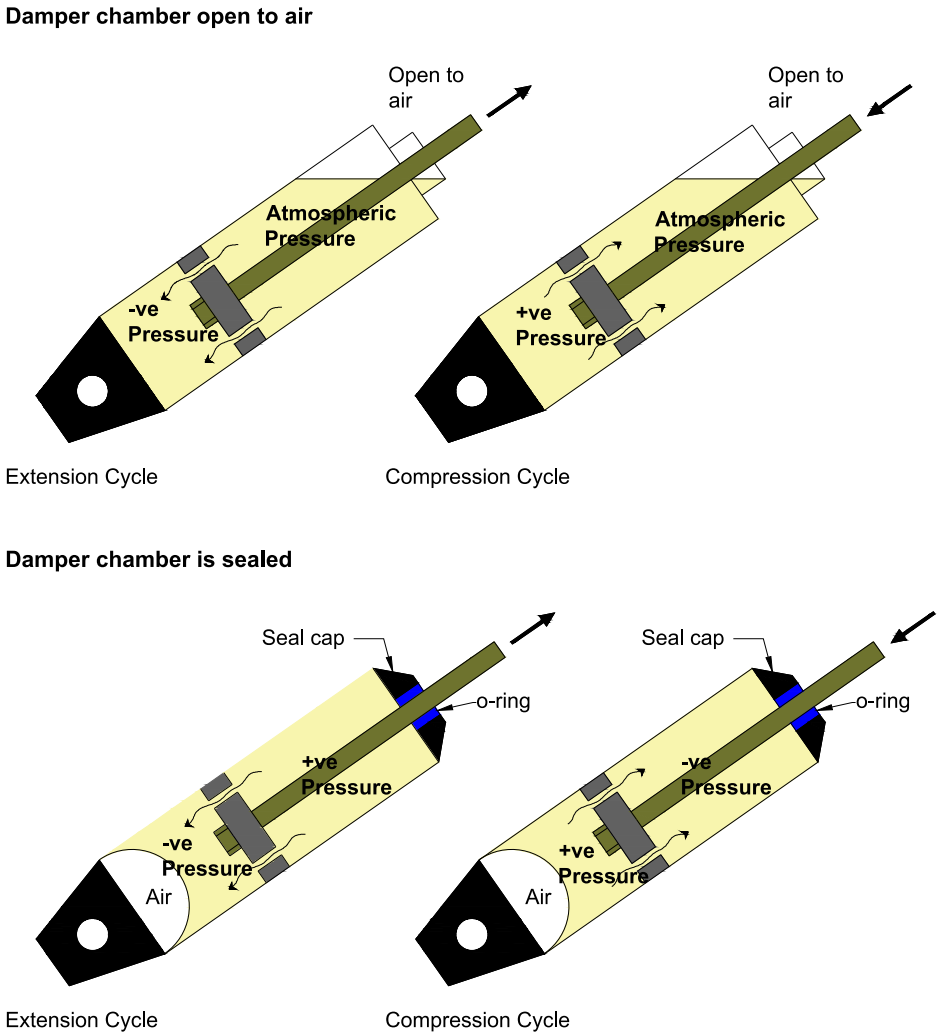

Fig. 3.29 Working mechanism for open and sealed oil damper B.

For the three remaining trial centrifuge tests, the dampers were fitted again with o-rings, seal caps and volume-compensating bladders, whilst varying hydraulic oil viscosity and piston orifice diameters. An attempt was made to approximate the damping ratio of the squat structure for each damper setup using Equation 3.15 derived from logarithmic decrement:

$$\zeta \approx \frac{1}{2\pi j} \ln \frac{u_1}{u_{1+j}} \tag{3.15}$$

where ζ is the damping ratio, j is the number of free vibration decay cycles, u_1 and u_{1+j} are the response peak values at the first cycle of free vibration, peak 1, and at peak $j+1$ respectively. This was done to the second storey acceleration traces; damping ratios are included with the plots in Figures 3.30 to 3.32. As expected, with thicker oil and smaller orifice diameters, the damping ratio of the damped structure increases.

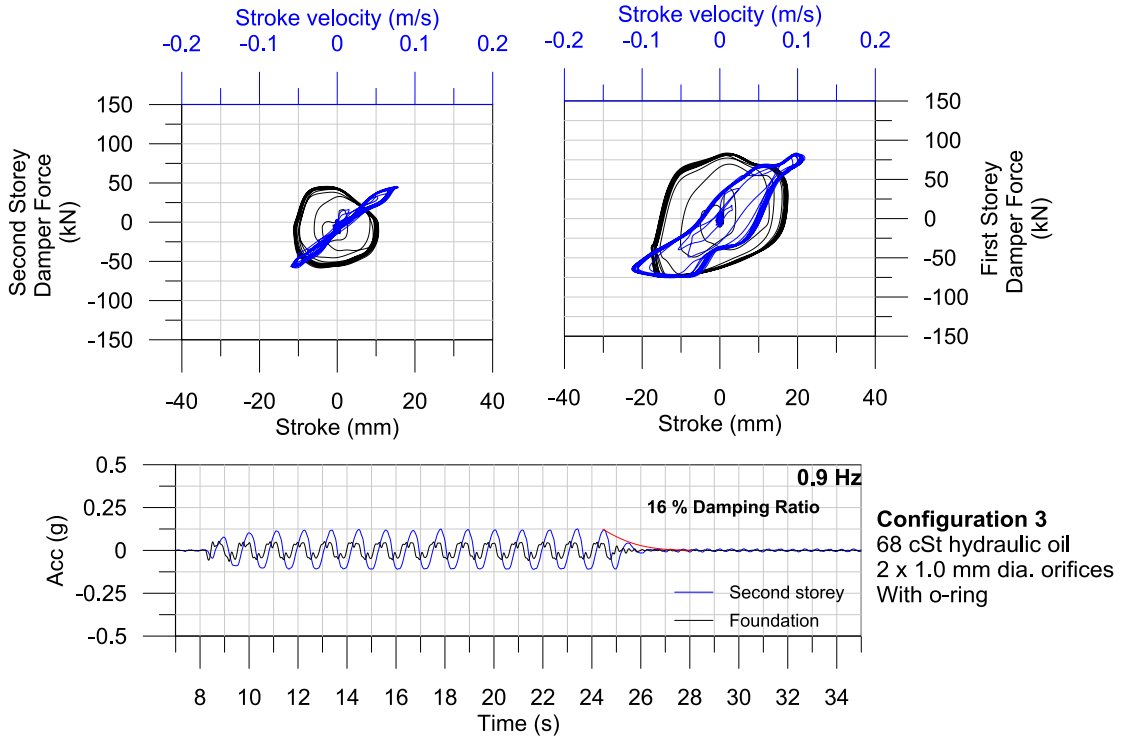

Fig. 3.30 Oil damper B force-velocity-displacement plots for Configuration 3.

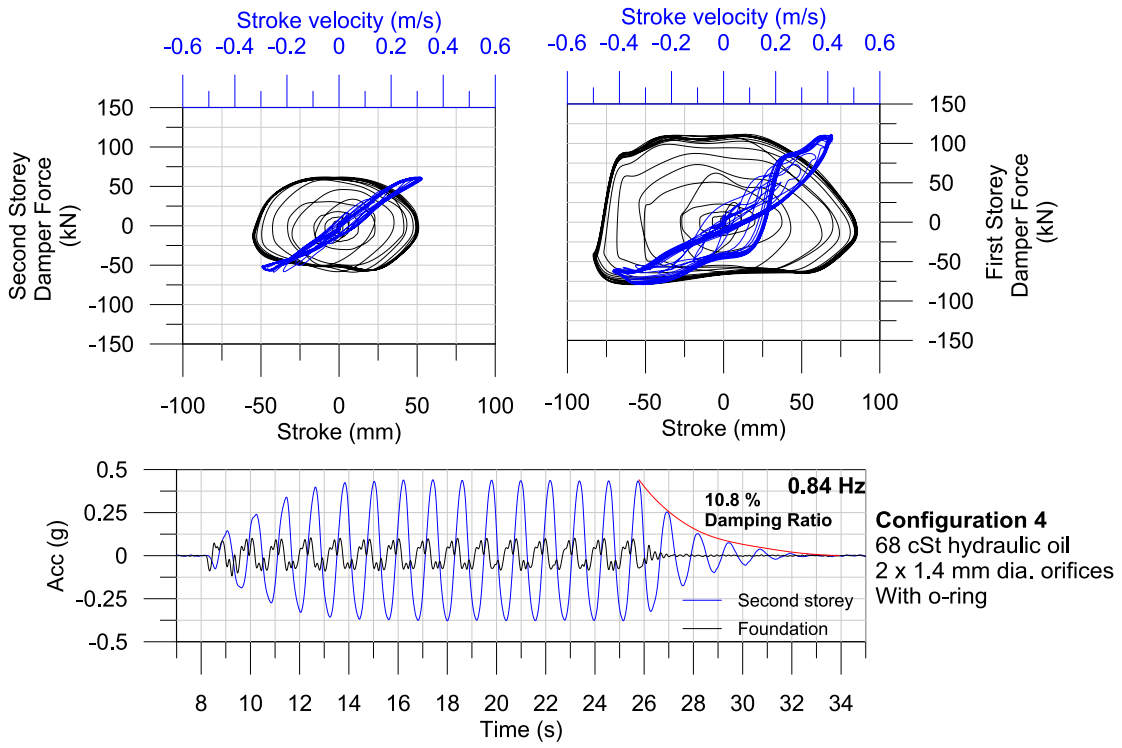

Fig. 3.31 Oil damper B force-velocity-displacement plots for Configuration 4.

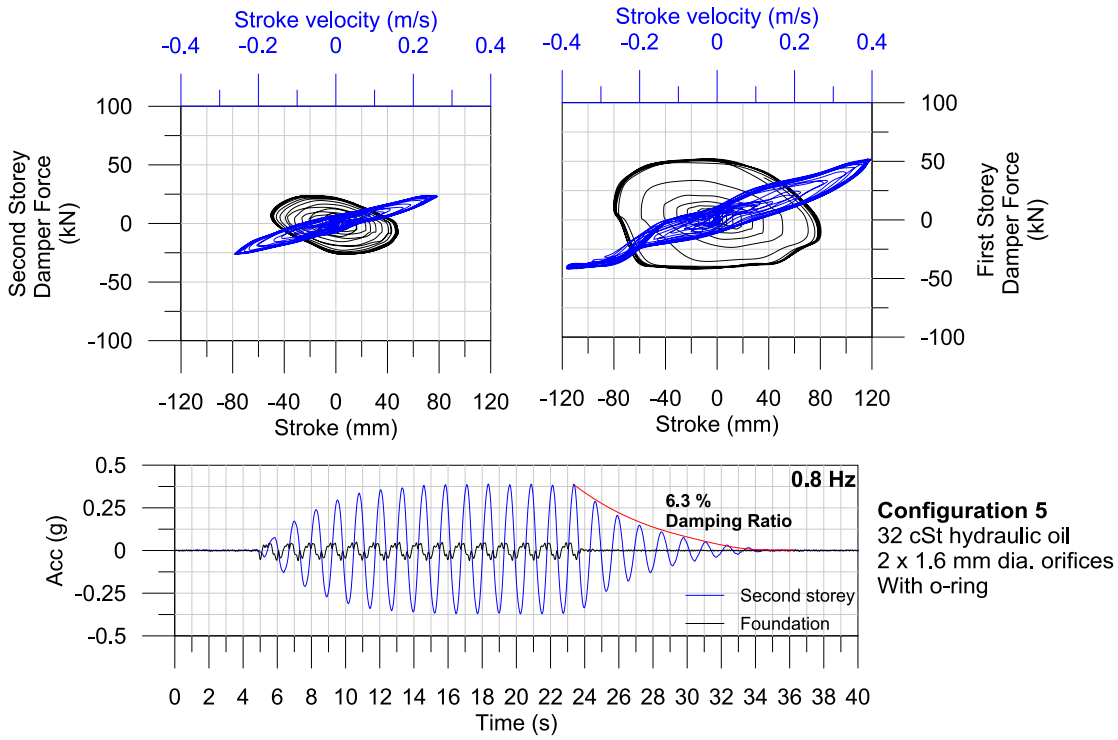

Fig. 3.32 Oil damper B force-velocity-displacement plots for Configuration 5.

The damper force-velocity plots, though not ideal, are an improvement over those plotted in Figure 3.24 for oil dampers A; they do not exhibit the same damping coefficient degradation trend with increasing number of cycles. There is, however, clear asymmetry in the force output of the dampers for compression and extension cycles. When an RC vehicle goes over a bump, the suspension shocks are intended by design to provide less damping forces in compression than in tension. This diverts more of the impact energy to the elastic springs of the vehicle, and keeps the tires in contact with the ground.

The drawback of damper compliance still exists in these dampers, with a clear lag between damper forces and stroke velocities in the force-velocity plots. The compliance in these devices mainly arises from the flexibility of the air-filled rubber bladder. In fact, when comparing first storey damper force-velocity plots for configurations 3 and 4 to that for configuration 5, it is clear that this lag between force and velocity increases with thicker oils and smaller orifice diameters; the harder it is for the damping fluid to squeeze through the orifices in the piston head, the more the damper force output will be affected by the flexibility of the air bladder.

For the purposes of this study, a total of six miniature oil dampers B were prepared; one pair of each configuration 3,4 and 5, referred to as Dampers D1, D2, and D3 respectively, in order of highest to lowest damping level.

Prior to assembly, the damping devices would be dismantled and immersed fully into a container filled with the same hydraulic oil that will be used for damping. The entire container is then subjected to -90 kPa suction, and left to de-air for at least 12 hours as shown in Figure 3.33. The dampers are then assembled in oil to reduce the possibility of air entrapment in the final assembly. Once the dampers are sealed, they are kept intact for the duration of this study to ensure damper consistency in between centrifuge tests.

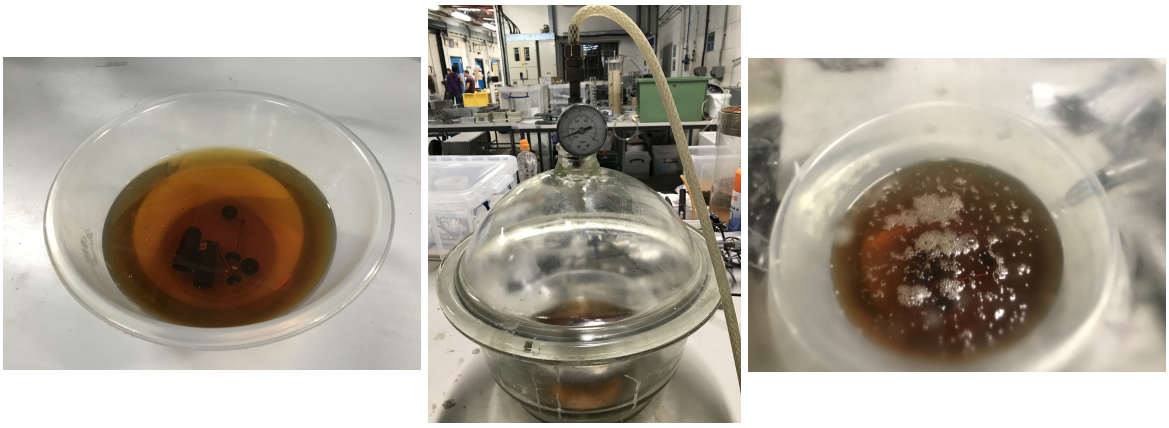

Fig. 3.33 De-airing of hydraulic oil for damper B assembly.

3.5 Model Preparation

3.5.1 Hostun HN31 Sand

Dry silica Hostun HN31 sand (Flavigny et al., 1990) was used for the dynamic centrifuge tests presented in this study. This sand, originally sourced from the Rhone-Alpes region of France, has a quartz grain mineralogy characterised typically by angular sand particles varying in diameter from 0.1 mm to 1.0 mm. Hostun HN31 sand is typically uniform in terms of particle size grading, with a D50 equal to 338 µm. Soil properties of this sand are summarised in Table 3.6, following the work of Shepley (2013).

Given that the centrifuge tests will all be conducted on dry sand, it was decided that the same "used" Hostun sand will be used for each test. Heron (2013) demonstrated that the particle size distribution (PSD) of used Hostun sand varies only slightly when compared to the PSD obtained from a new batch of Hostun sand, albeit with a slight reduction in particle size diameters. The difference between the two distributions is marginal, and any accompanying increase in stiffness due to the presence of finer grains in the soil fabric would be overshadowed by the experimental accuracies to which soil density and stiffness are measured.

Table 3.6 Soil properties of Hostun HN31 sand. (Shepley, 2013)

Properties	Value	Units
Maximum voids ratio, e_{max}	1.01	-
Minimum voids ratio, e_{min}	0.555	-
Maximum density, ρ_{max}	1620	kg/m^3
Minimum density, ρ_{min}	1318	kg/m^3
Minimum density, ρ_{min}	1318	kg/m^3
Specific Gravity, G_s	2.65	
D_{10}	0.315	mm
D_{60}	0.525	mm

In the same study, Heron (2013) reports key soil parameters from drained triaxial tests conducted on Hostun sand specimens in collaboration with the University of Coimbra, Portugal. These have been listed in Table 3.7 for completeness.

Table 3.7 Peak and critical-state friction angles for Hostun HN31 sand. (Heron, 2013)

Confining Pressure	Relative Density	ϕ_{peak}	ϕ_{crit}
80 *kPa*	51 %	37.9°	35.4°
	65 %	40.7°	35.4°
135 *kPa*	49 %	37.1°	-
	64 %	40.7°	-

3.5.2 Pouring and Instrumenting Sand

All centrifuge packages presented in this study have been prepared by air-pluviating Hostun sand into the ESB model container. The sand pouring process was completed using the automatic sand pourer described earlier in section 3.2.2. For loose sand pours, a 9 mm nozzle was fitted at the base of the sand hopper and positioned at a drop height of 530 mm above the container. For this nozzle diameter and without fitting sieves, a continuous stream of sand flows out of the hopper. Setting the stepping increments (with reference to pouring patterns in Figure 3.4) to 8 mm results in approximately 15 mm of sand being poured every time the machine completes one pass over the container. This pourer configuration results in relative densities of sand beds ranging between 30 % to 40 %.

For dense sand pours, the nozzle size is reduced to 5 mm diameter, with two coarse sieves installed within the nozzle setup. The smaller nozzle diameter and the two sieves reduce the flow rate of sand out of the hopper, resulting in a more dispersed flow of sand rather than a

constant stream. The drop height is also increased to 680 mm to densify the sand on impact with the surface. At stepping increments of 20 mm along both axes of travel, the resulting relative density of the sand bed for this configuration varies between 80 % to 90 %.

The sand beds in this study are instrumented with arrays of piezo-electric accelerometers to monitor the vertical propagation of horizontally polarised shear waves from the base of the container up into the model frame foundations during shaking. These instruments are placed at pre-defined layers in the soil profile during pouring as shown in Figure 3.34.

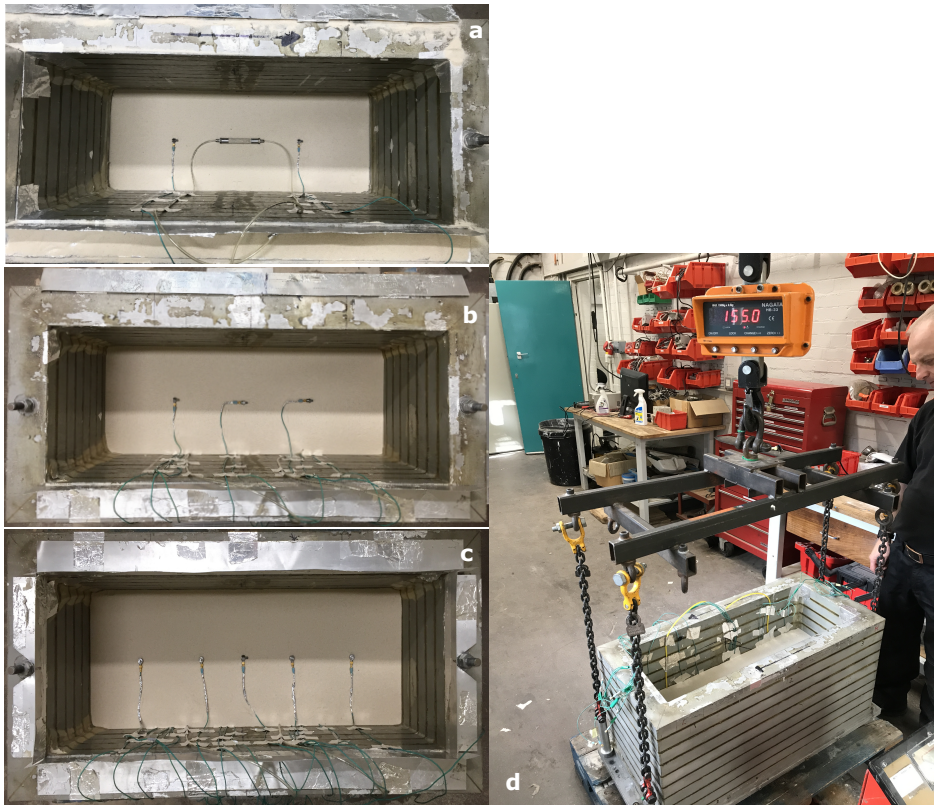

Fig. 3.34 (a) Air hammer and first layer of intruments close to bottom of the container (b) Intermediate layer of instruments (c) Final instrumentation layer (d) Weighing of sand at foundation level.

For horizontal soil accelerations, the piezo-electric accelerometers are carefully placed on the sand surface, with their threads pointing in the same direction of shaking as the box. The cables are routed to the back of the ESB container, and up the rear wall of the box to the outside. In some locations, the piezo-electric accelerometers were positioned with the thread pointing vertically upwards to record vertical accelerations in the soil. At every instrument layer, multiple depth measurements were taken at the sand surface using a metre rule to track the poured depth of sand and approximate its volume.

For each test, an air hammer device is placed on the first few millimetres of poured sand close to the bottom of the container as shown in Figure 3.34 (a). The device is positioned beneath a vertical array of piezo-electric accelerometers to help characterise the small-strain shear stiffness profile of the sand beds.

Once foundation level is reached, the poured sand inside the ESB container is weighed to compute the approximate relative density of the pour. It is important to highlight that instrument positions and surface depth measurements recorded using a ruler are measured to within $\pm$ 2 mm accuracy, which makes any sand volume computation only an approximation and is by no means accurate. Nevertheless, it is still believed that a valuable estimate of sand bed density can be obtained.

3.5.3 Positioning of Model Structures

Coelho et al. (2003) observed that the central 300 mm soil column in an ESB container is the least likely zone to be influenced by boundary effects arising from the dynamic property mismatch between the soil and the flexible end walls. This implies that the ideal positioning of a model frame is at the centre of the ESB container. For the purposes of this study, it was deemed more valuable to obtain a direct cross comparison between the seismic response of a bare frame and its damped counterpart in the same experimental package, founded on the same ground conditions, and experiencing the same input motions.

At foundation level, the two instrumented model frames are carefully placed on the sand surface at pre-defined locations. In order to minimise exposure to boundary effects during shaking, each frame is positioned 100 mm away (i.e. 5 m in prototype scale) from the end walls of the ESB container, and 51 mm away (i.e. 2.55 m in prototype scale) from the front and rear walls of the box as shown in Figure 3.35 (a).

Due to the limited size of the ESB container, a clear distance of around 160 mm (i.e. 8.0 m in prototype) is what remains between the foundations of the two model frames (edge-to-edge). According to Jiang and Yan (1998), there needs to be clearance of around 2.5 times the foundation width to completely diminish the effects of structure-soil-structure interaction. Therefore, a certain degree of structure-soil-structure interaction can be expected.

Alignment and horizontality of each frame, in both directions, were checked using a small spirit level as shown in Figure 3.35 (b). The raft foundations of the frames were then manually embedded by 12 mm of sand as shown in Figure 3.35 (c).

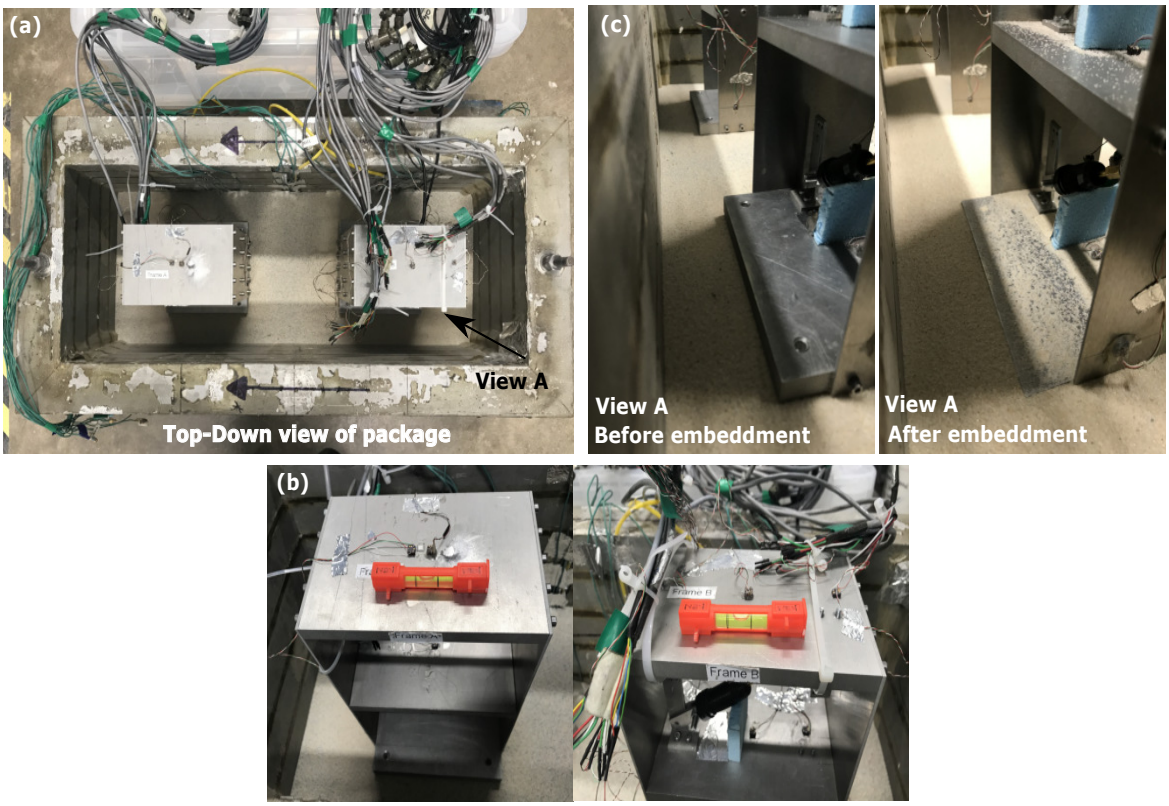

Fig. 3.35 (a) Top-down view of squat frames on foundation surface (b) Horizontality of frames checked with spirit level (c) Embedment of model frames to top of raft foundation.

3.5.4 Static Vertical Factor of Safety for Bearing Capacity

Two different relative densities (I_d) of uniform dry sand beds were investigated in this study. Dense sand was air-pluviated using the automatic sand pourer to a relative density of around 83 %; the loose sand bed was in turn poured to a relative density of approximately 34 %.

As discussed earlier in section 3.3.1, the foundation bearing pressures were varied for each category of model frame to investigate the effect of increased soil-straining on the dynamic response of the soil-structure systems. In this regard, a theoretical assessment of the static vertical factor of safety of the foundations (FS_v) against bearing capacity failure was calculated using:

$$FS_v = \frac{q_0 N_q s_q + 0.5\gamma B N_\gamma s_\gamma}{q} \tag{3.16}$$

where q_0 is the surcharge acting at the foundation level, γ is the unit weight of the sand, B is the foundation width, N_q, N_γ, s_q and s_γ are the bearing capacity factors and foundation

shape factors for surcharge and self-weight respectively. These factors have been computed following Salgado (2006) and Lyamin et al. (2007) using the following equations:

$$N_q = \frac{1+sin\phi}{1-sin\phi} e^{\pi tan\phi} \tag{3.17}$$

$$N_\gamma = 1.5(N_q - 1)tan\phi \tag{3.18}$$

$$s_q = 1 + (0.0952\phi - 1.6)\frac{D}{B}^{0.583-0.0079\phi}\frac{B}{L}^{1-0.15(D/B)} \tag{3.19}$$

$$s_\gamma = 1 + (0.0345\phi - 1.061)\frac{B}{L} \tag{3.20}$$

where ϕ is friction angle in degrees, D is the depth of soil from ground surface to foundation level, B is foundation width and L is foundation breadth.

Using critical-state and peak friction angles reported in Heron (2013) at 80 kPa, the static vertical factor of safety was estimated for each category of model frame. Results for the squat bare frame are summarised in Tables 3.8. Foundation geometry and bearing pressures for the tall model frames are similar to those for the squat structures; thus, the factors of safety reported in Table 3.8 are applicable to both, squat and tall model frames.

Table 3.8 Static vertical factor of safety against bearing capacity failure.

	Light		Heavy	
Bearing Pressure (kPa)	40		73.2	
Relative Density (I_d)	84 %	39 %	84 %	39 %
Friction angle (ϕ_{crit} / ϕ_{peak})	35.4° / 40.7°	35.4° / 37.9°	35.4° / 40.7°	35.4° / 37.9°
$FS_{v,crit}/FS_{v,peak}$	7 / 15	6 / 8	4 / 8	3 / 5

3.6 Testing Procedures

Once the instrumented model frames are placed on the sand surface and embedded, the final placement of any gantries and accompanying LVDT instruments becomes possible. Instrument cables at this stage remain unplugged protruding from the ESB container. Once the ESB box is bolted down to the shaker, the instruments are plugged into two junction

boxes positioned behind the accumulator tanks on the servo-shaker. The junction boxes relay instrument signals to a data acquisition module located at the centre of the centrifuge, where data is saved locally. The loading process is illustrated in Figure 3.36.

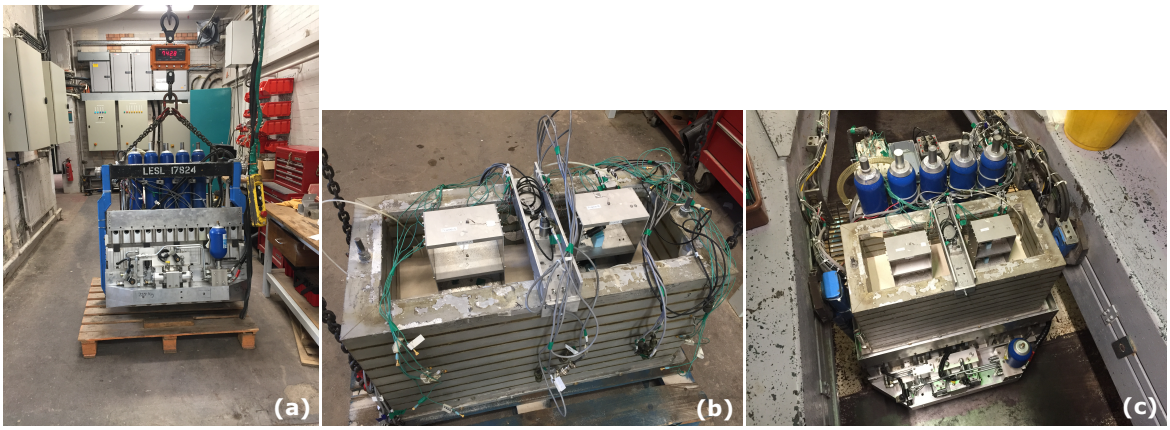

Fig. 3.36 (a) Servo-shaker being loaded (b) Centrifuge package ready for loading (c) Centrifuge package on blue end of the beam.

A centrifuge test would normally start by conducting an air hammer test at 1 g. The centrifuge is then accelerated to "swing-up" phase, followed by an air hammer test at 10 g to track the stiffness increase of the sand bed with increasing confining pressures. As the centrifuge is accelerated to 50 g, air hammer tests are conducted at 20g intervals prior to triggering any earthquakes.

During spin-up, sand surface settlement is tracked via an LVDT positioned in between the two model frames. Load cell data from the two load cells in the damped structure are also monitored; as the centrifugal force increases on the experimental package, the inclined damper-load cell setup in between floors of the model structure experience increased sagging due to their rising self-weight. This sagging puts the load cell into tension as the centrifuge spins to high g-levels. At 50 g, and for a constant centrifuge rotational speed, the load cells show stable readings. Therefore, the loads measured during shaking of the damped structure are analysed relative to this new offset.

A typical earthquake firing sequence for the centrifuge tests is shown in Figure 3.37. The first earthquake is a weak near-resonant frequency sinusoidal excitation (E1), followed by a weak 0 Hz to 60 Hz sine sweep motion (E2) to help detect fundamental frequency of the soil-structure system. The sweep is followed by a strong near-resonant frequency sinusoidal motion (E3), and a similar intensity far-from-resonant frequency sinusoidal excitation (E4). The last two motions, scaled Kobe (E4) and scaled Imperial valley records (E5), are mainly to study the frame response to a near-fault excitation, and a long-duration broad frequency motion, respectively. For tests with different sand bed densities, similar amplitude and shaking frequencies were dialled, where possible, to facilitate comparisons.

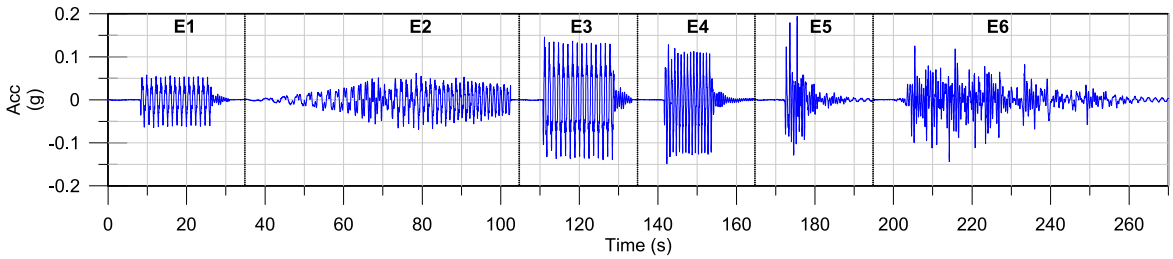

Fig. 3.37 Typical earthquake firing sequence during a centrifuge test.

During an earthquake, all instruments in the package are sampled at 6 kHz, setting the Nyquist frequency at 3 kHz, well above the frequency components of the input motions fired in this study. This ensures that higher frequency harmonics in the signal are captured without the risk of aliasing. For an air hammer test, the sampling rate is increased to 50 kHz for the accelerometer array above the air hammer. This is to ensure that sufficient data points are available in the acceleration signals to capture first arrival of the vertically propagating weak shear waves.

3.7 Presentation of Data

Instrument data from each centrifuge test is saved locally on a hard drive in raw voltage (i.e. uncalibrated) form. Post-processing of the data, and subsequent calibration of voltage to equivalent physical quantities, is done digitally after a test using MATLAB.

A standard approach to post-processing would be to first digitally filter all instrumentation data using an 8th order low-pass Butterworth filter, with a cut-off frequency set at 500 Hz. The “filtfilt” function in MATLAB is utilised to eliminate any phase differences that the digital filter might introduce into the filtered signals.

Earthquake acceleration data recorded from piezo-electric accelerometers and MEMS accelerometers are de-trended using the MATLAB "detrend" command to remove any DC offset that may exist in the signal. This is not applied to load cell and LVDT data where real experimental processes may cause a drift in the instrument signal away from its DC offset; this can include soil settling or lock-in of forces in the load cells during shaking.

The typical range of excitation frequencies fired in this study varies between 0 Hz up to 200 Hz (model scale), with the possibility of higher frequencies appearing due to higher order harmonics of the sinusoidal input motions. A low-pass filter cut-off frequency of 500 Hz is enough to include frequencies up to the 7th harmonic of the highest sinusoidal frequency fired in this study (60 Hz). Real motions like Kobe and Imperial Valley have predominant frequency components in the range of 0 Hz to 200 Hz, thus no loss of valuable information should occur with the 500 Hz cut-off.

In the following chapters, results relating to structural displacements, damper velocities, damper strokes and global frame rotations have been computed from MEMS accelerometer data by a systematic routine of integration and digital "band-pass" filtering. Figure 3.38 shows an example of this process being applied to MEMS accelerometers located on the damper bodies and damper piston rods.

The need to zero the DC offsets of the damper stroke acceleration traces becomes clear from Figure 3.38. Once the offset is zeroed, "cumtrapz" function in MATLAB is utilised to numerically integrate the filtered acceleration signal over a finite increment of time equal to the sampling period of the trace. This process amplifies low frequency components and reduces the intensity of high frequencies in the signal.

The resulting stroke velocity traces are shown in magenta in Figure 3.38, with a clear low frequency drift impacting the whole trace. "Band-pass" filtering with a frequency band of 20 Hz to 500 Hz removes the low frequency drifts in velocity as shown by the solid black velocity traces. The second integration step is then carried out to numerically integrate filtered velocity into displacements using the same "cumtrapz" command. Filtering away low frequencies in velocity result in acceptable damper stroke traces after integration as shown in Figure 3.38.

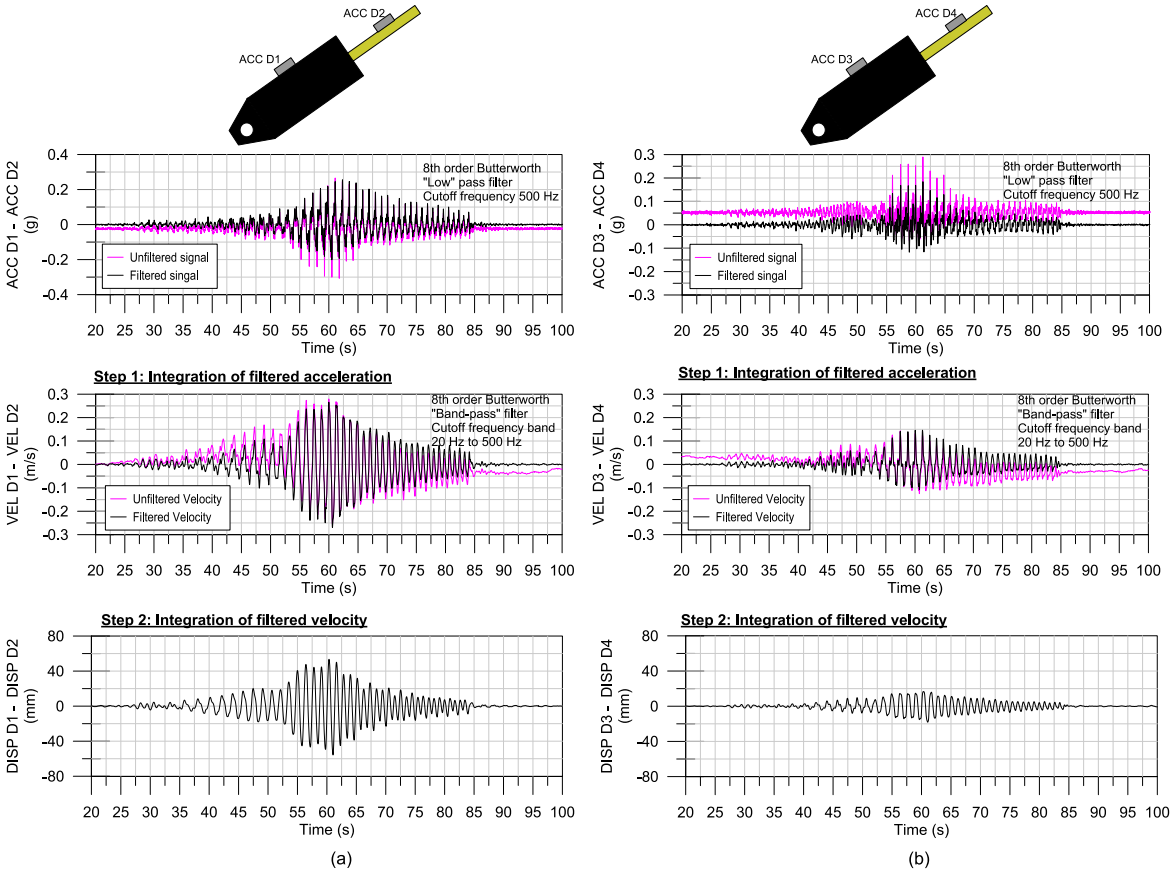

Fig. 3.38 Integration and filtering of damper accelerations to compute damper stroke velocities and stroke displacements.

Often, this process of double integration and high pass filtering can result in loss of real experimental data, specifically information pertaining to co-seismic drifts in the signal, and permanent translations of instruments due to irrecoverable deformation or settlements. Given that the model frames in this study remain elastic, MEMS accelerometers on the structure floors and dampers should return to their initial positions at the end of shaking. It is acknowledged however that global frame rotations computed from the vertical MEMS accelerometers on each side of the model frames only show dynamic rotations; successive structural tilt is removed by the band-pass filter.

3.8 Centrifuge Testing Programme

A total of 16 dynamic centrifuge tests were conducted in this study. The testing programme aimed to investigate three main parameters:

1. Effect of structure aspect ratio by testing squat and tall model frames with similar fundamental frequencies.

2. Effect of ground flexibility by testing model structures embedded in dry dense and loose sand beds, and rigidly fixed to the shaking table without soil.

3. Effects of foundation bearing pressure by testing light and heavy raft foundations.

Figure 3.39 describes the centrifuge testing programme. Figures 3.40 to 3.42 illustrate typical experimental package layouts with instrument positions and earthquake firing sequences for fixed base tests, tests involving the squat frames, and tests involving the tall model structures respectively.

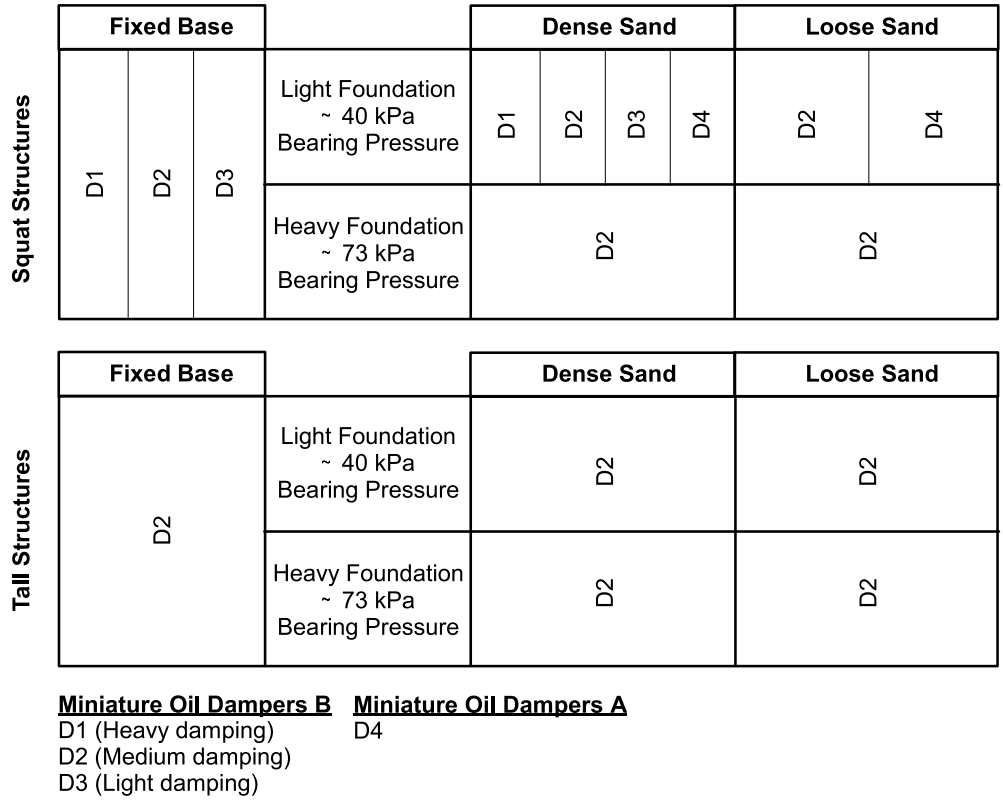

Fig. 3.39 Centrifuge testing matrix.

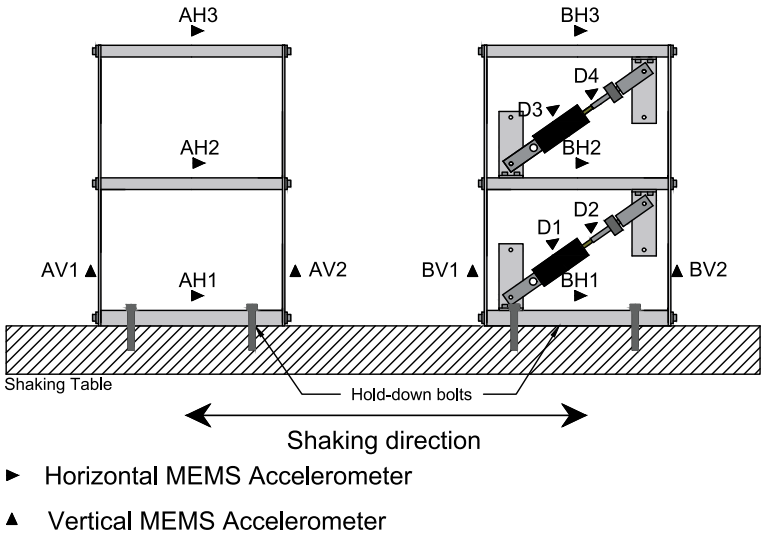

Fig. 3.40 Typical experimental package layout for a fixed base test.

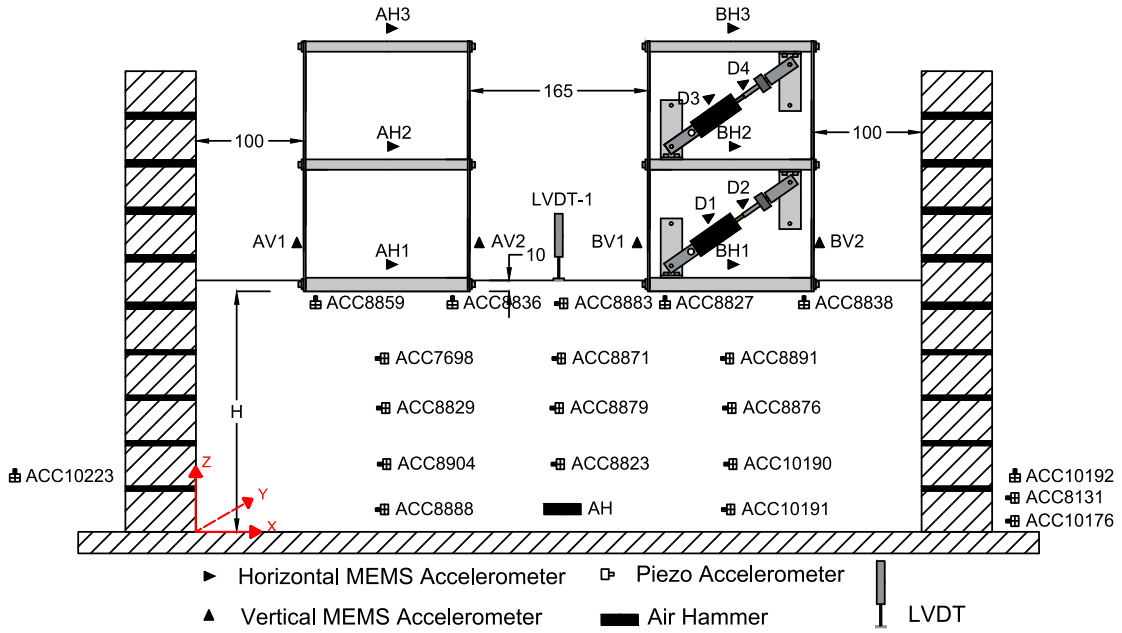

Squat-Light-Dense-D1			
H	223 mm	**I_d**	80 %
Instrument	Z (mm)	X (mm)	Y (mm)
AH	16	337	125
ACC8888	16	175	127
ACC10191	16	496	127
ACC8904	58	177	126
ACC8823	58	338	127
ACC10190	58	498	127
ACC8876	110	497	126
ACC8879	110	337	127
ACC8829	110	176	127
ACC8891	156	495	128
ACC8871	156	339	126
ACC7698	156	175	127
ACC8838	207	564	125
ACC8827	207	435	125
ACC8883	207	341	125
ACC8836	207	238	125
ACC8859	207	111	126

Base Excitation Sequence

E1: 42 Hz , 15 cycles , 1.0 V (peak input acc 0.07 g)
E2: 0 Hz to 60 Hz Sweep, 1.0 V (peak input acc 0.08 g)
E3: 42 Hz, 15 cycles , 2.0 V (peak input acc 0.18 g)
E4: 62 Hz, 15 cycles, 1.0 V (peak input acc 0.12 g)
E5: Kobe boost, 0.25 V (peak input acc 0.17 g)
E6: Kobe boost, 0.35 V (peak input acc 0.26 g)
E7: Imperial Valley, 4.0 V (peak input acc 0.12 g)

Fig. 3.41 Typical experimental package layout for dry sand tests with the ESB container for the Squat frames.

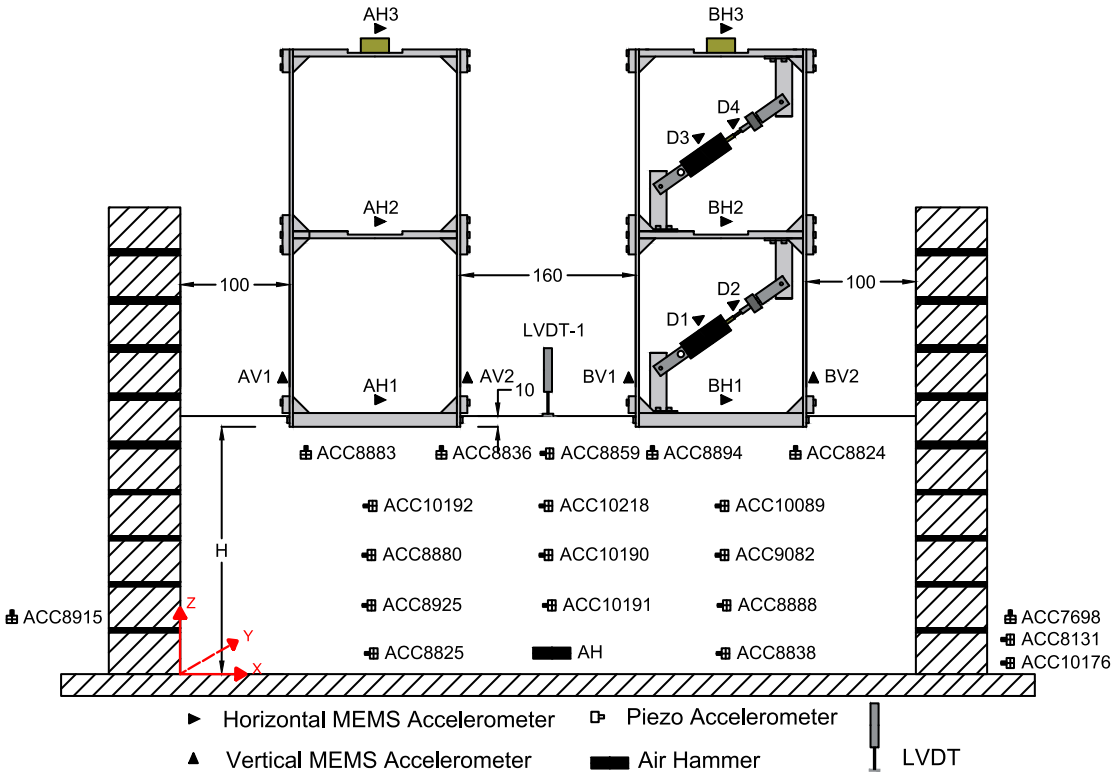

Tall-Light-Loose-D2			
H	226 mm	**I_d**	39 %
Instrument	Z (mm)	X (mm)	Y (mm)
AH	14	340	128
ACC8838	14	499	126
ACC8825	14	177	126
ACC8888	58	500	126
ACC10191	58	340	127
ACC8925	58	175	127
ACC9082	104	498	127
ACC10190	104	337	127
ACC8880	104	175	124
ACC10089	149	498	126
ACC10218	149	337	127
ACC10192	149	176	126
ACC8824	197	563	126
ACC8894	197	432	127
ACC8859	197	338	126
ACC8836	197	239	125
ACC8883	197	115	127

Base Excitation Sequence

E1: 39 Hz , 15 cycles , 1.0 V (peak input acc 0.07 g)
E2: 0 Hz to 60 Hz Sweep , 1.0 V (peak input acc 0.08 g)
E3: 58 Hz, 15 cycles , 0.8 V (peak input acc 0.08 g)
E4: 39 Hz, 15 cycles, 2.0 V (peak input acc 0.14 g)
E5: 58 Hz, 15 cycles, 1.0 V (peak input acc 0.13 g)
E6: Kobe boost, 0.25 V (peak input acc 0.19 g)
E7: Imperial Valley, 4.0 V (peak input acc 0.14 g)

Fig. 3.42 Typical experimental package layout for dry sand tests with the ESB container for the Tall frames.

Chapter 4

Prediction of Fixed-Base Dynamic Structural Response

4.1 Introduction

Before presenting and interpreting dynamic soil-structure interaction (SSI) data from the centrifuge, it is useful to develop mathematical models of the 2-DOF structures that, to within reasonable accuracies, can predict the experimental results for the simpler case of fixed-base structures subjected to base excitations. This chapter compares results from fixed-base centrifuge tests to numerical predictions obtained using simplified tools that can be implemented by engineers in practice during preliminary design. These tools include direct numerical integration of the equations of motion in the time domain to produce response history traces, and classical modal analysis of structures in the frequency-domain to determine peak response parameters. The mathematical models developed in this chapter are calibrated against dynamic fixed base structural responses recorded in the centrifuge. These models will be further expanded in Chapter 7 to include SSI effects at the foundation interface.

4.2 Time History Predictions for Bare Frames

Solving linear second order differential equations of motion in structural dynamics using approximate time-stepping techniques is a well-established method in literature (Chopra, 2012). For a 2-DOF shear structure (i.e. considering floor plates as rigid diaphragms and columns to be axially inextensible), the equations of motion for a fixed base structure are given by Equation 4.1:

$$\begin{bmatrix} m_1 & 0 \\ 0 & m_2 \end{bmatrix} \begin{Bmatrix} \ddot{u}_1 \\ \ddot{u}_2 \end{Bmatrix}_{i+1} + \begin{bmatrix} c_1+c_2 & -c_2 \\ -c_2 & c_2 \end{bmatrix} \begin{Bmatrix} \dot{u}_1 \\ \dot{u}_2 \end{Bmatrix}_{i+1} + \begin{bmatrix} k_1+k_2 & -k_2 \\ -k_2 & k_2 \end{bmatrix} \begin{Bmatrix} u_1 \\ u_2 \end{Bmatrix}_{i+1} = -\ddot{u}_{g,i+1} \begin{Bmatrix} m_1 \\ m_2 \end{Bmatrix}$$

$$[M]\{\ddot{u}\}_{i+1} + [C]\{\dot{u}\}_{i+1} + [K]\{u\}_{i+1} \;=\; \{p\}_{i+1} \tag{4.1}$$

where $\ddot{u}_i$, $\dot{u}_i$ and u_i are horizontal floor accelerations, velocities and displacements measured relative to the foundation, $\ddot{u}_g$ is input acceleration at the base, and $\{p\}$ is a vector of external forces acting on the degrees of freedom.

Using classical Newmark (linear acceleration, $\gamma = \frac{1}{2}, \beta = \frac{1}{6}$) integration (Chopra, 2012), acceleration and velocity at the time step $(i+1)$ can be expressed in terms of displacements by:

$$\ddot{u}_{i+1} = \frac{1}{\beta(\Delta t)^2}(u_{i+1} - u_i) - \frac{1}{\beta \Delta t}\dot{u}_i - (\frac{1}{2\beta} - 1)\ddot{u}_i \tag{4.2}$$

$$\dot{u}_{i+1} = \frac{\gamma}{\beta \Delta t}(u_{i+1} - u_i) + (1 - \frac{\gamma}{\beta})\dot{u}_i + \Delta t(1 - \frac{\gamma}{2\beta})\ddot{u}_i \tag{4.3}$$

Substituting Equations 4.2 and 4.3 into Equation 4.1, with re-arrangement gives:

$$[\hat{k}]\ \{u\}_{i+1} = \{\hat{p}\}_{i+1} \tag{4.4}$$

where

$$[\hat{k}] = [K] + a_1$$

and

$$\{\hat{p}\}_{i+1} = \{p\}_{i+1} + a_1\ u_i + a_2\ \dot{u}_i + a_3\ \ddot{u}_i$$

with Newmark integration constants

$$a_1 = \frac{\gamma}{\beta \Delta t}[C] + \frac{1}{\beta(\Delta t)^2}[M]$$

$$a_2 = \frac{1}{\beta \Delta t}[M] + (\frac{\gamma}{\beta} - 1)[C]$$

$$a_3 = (\frac{1}{2\beta} - 1)[M] + \Delta t(\frac{\gamma}{2\beta} - 1)[C]$$

Displacements $\{u\}_{i+1}$ are calculated from Equation 4.4 by taking the inverse of the modified stiffness matrix $[\hat{k}]$ (which includes damping and inertial effects):

$$\{u\}_{i+1} = [\hat{k}]^{-1} \{\hat{p}\}_{i+1} \tag{4.5}$$

From this, acceleration and velocity at time step $(i+1)$ can be calculated using Equations 4.2 and 4.3 respectively. By solving the equation of motion at $(i+1)$, the integration scheme used here is implicit. Figure 4.1 summarises the algorithm behind the integration procedure.

1. Problem Definition

1.1 Setup system mass [M] and stiffness [K] matrices

1.2 Compute undamped natural frequencies

1.3 Assume classical Rayleigh Damping with predefined modal damping ratios to construct damping matrix [C]

1.4 Define forcing vector {p} for base excitation

2. Initialising conditions for integration, i = 0

2.1 Time-stepping integration parameters for linear acceleration
$\gamma = 1/2$, $\beta = 1/6$

2.2 Compute Newmark integration constants: a_1, a_2, and a_3

2.3 Displacement, velocity, and acceleration vectors

$\{u\}=\{\dot{u}\}=\{\ddot{u}\}=\{0\}$

2.4 Assemble dynamic stiffness matrix

$[\hat{k}] = [K] + a_1$

3. At each time increment , i = 1, 2, 3, ...

3.1 Compute $\hat{p}_{i+1}$

3.2 Compute displacement u_{i+1}

3.3 Compute velocity $\dot{u}_{i+1}$

3.4 Compute acceleration $\ddot{u}_{i+1}$

4. Repeat Step 3 for the next time step i + 1

Fig. 4.1 Numerical integration scheme for fixed base bare structures.

In a time-domain assessment of structural response, it becomes crucial to define a damping force vector to properly replicate real structural dynamic behaviour. Unlike the stiffness matrix, the damping matrix cannot be physically quantified from structural properties; it is an accumulation of inherent processes in the frame, including material hysteresis in structural elements, energy losses at beam-column-connections, radiation of energy back into the ground etc. For structures with uniform stiffness distribution and frame construction along their height, implementation of a classical damping matrix to decouple the equations of motion is not uncommon. In this investigation, Rayleigh damping has been assumed for the model frames. The damped frames, on the other hand, present a nonlinear problem in which the damping forces require updating at every time step of the solution. This will be discussed in section 4.4.

Figures 4.2 and 4.3 depict successful application of Newmark's method to predict experimental floor accelerations for the squat frame and tall frame respectively. For these moderate excitations, the response can be replicated by a single constant stiffness matrix fairly accurately. Unfortunately, the same was not observed for the case of a strong near resonant frequency excitation as shown in Figure 4.4.

Upon using the same stiffness matrix for the bare tall frame as the one used to predict the results in Figure 4.3, a very clear mismatch in response amplitude and frequency is obtained during the strong near resonant frequency excitation. The experimental transfer function plots in Figure 4.4 show multiple peaks occurring close to the fundamental frequency; this is indicative of a shift in the fundamental frequency of the structure as it enters intense resonant shaking. To match this numerically, reductions in stiffness (within the order of 10 %) had to be implemented at different time instances of the excitation as shown in Figure 4.4. The same procedures also had to be implemented numerically for the bare squat frame to predict experimental fixed base results for a strong near resonant frequency excitation.

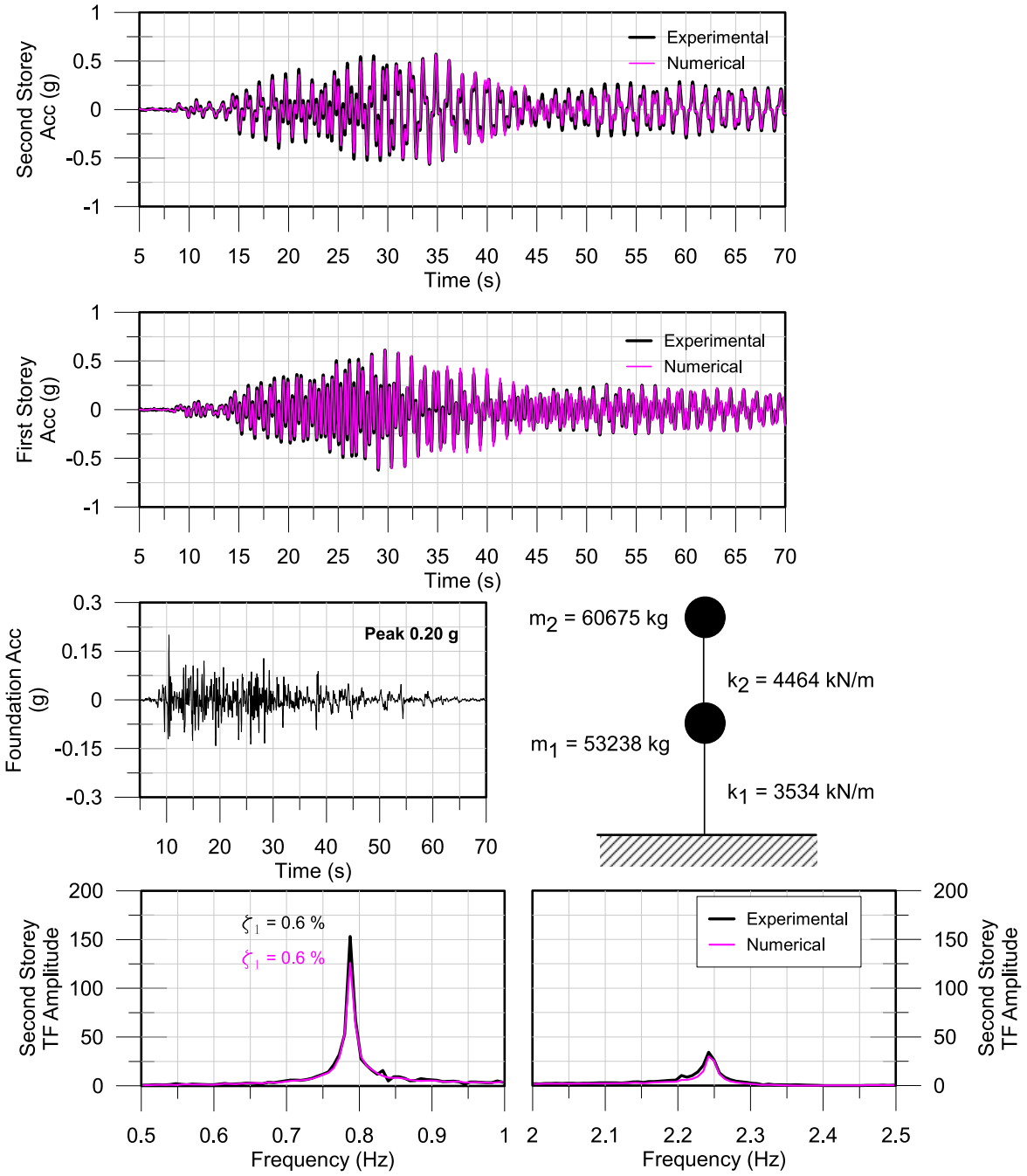

Fig. 4.2 Numerical predictions of time histories and second storey transfer function for the bare Squat frame without dampers during a scaled Imperial Valley excitation.

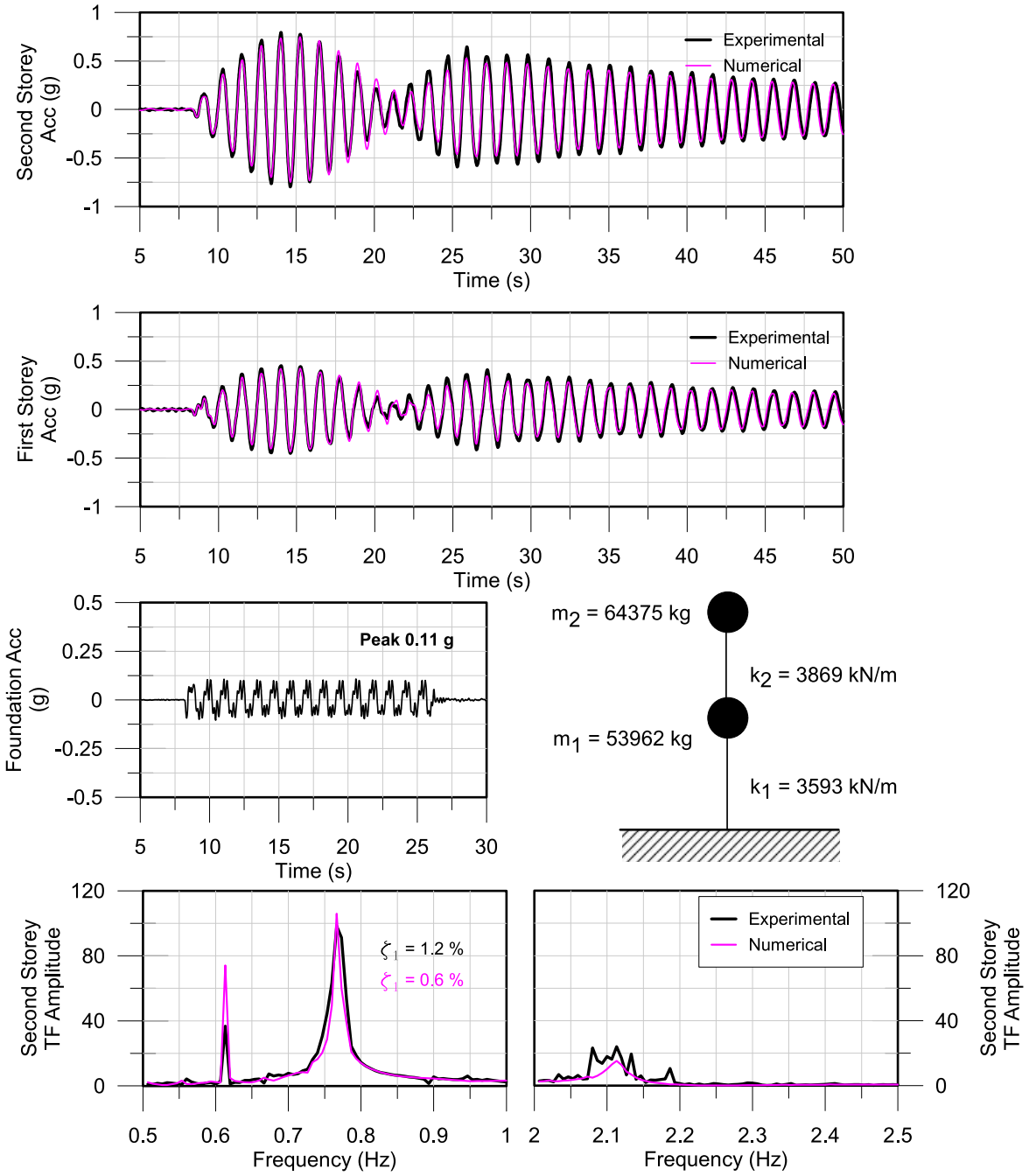

Fig. 4.3 Numerical predictions of time histories and second storey transfer function for the bare Tall frame without dampers during a weak near resonant frequency excitation.

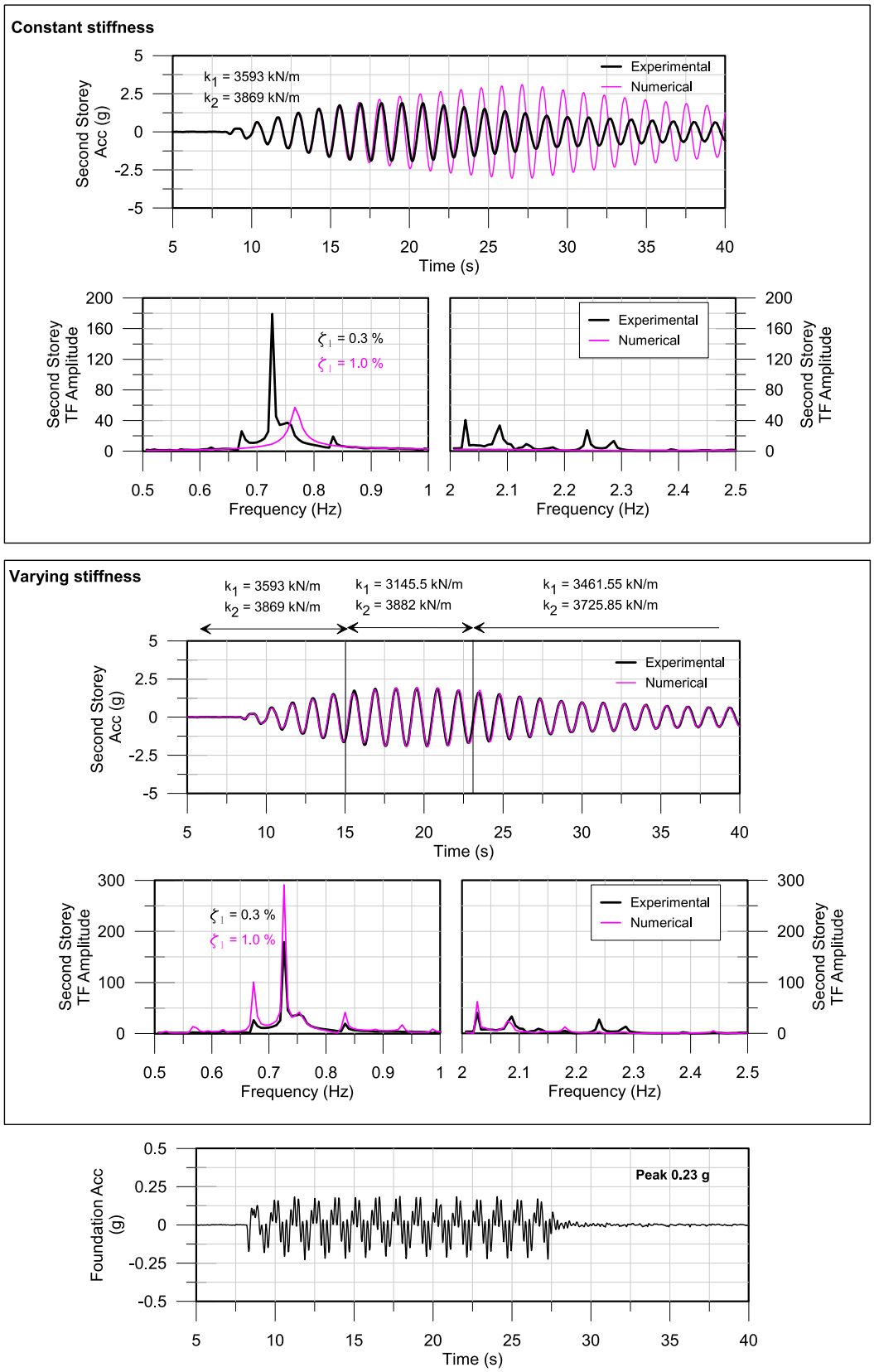

Fig. 4.4 Numerical predictions for the bare Tall frame during strong near resonant frequency excitation with (top) constant lateral storey stiffness (bottom) varying lateral storey stiffness.

To better understand the apparent shift in experimental fundamental frequency of the tall structure in Figure 4.4, a linear elastic finite element model of the bare tall structure was created in ABAQUS. The frame was simulated using 8-noded two-dimensional plane strain elements, with Rayleigh damping coefficients set to define a 1 % modal damping ratio. A fixed-base boundary condition was applied at the base of the structure, and the frame was subjected to the same base excitation as used in Figure 4.4. Some key results from ABAQUS are presented in Figure 4.5.

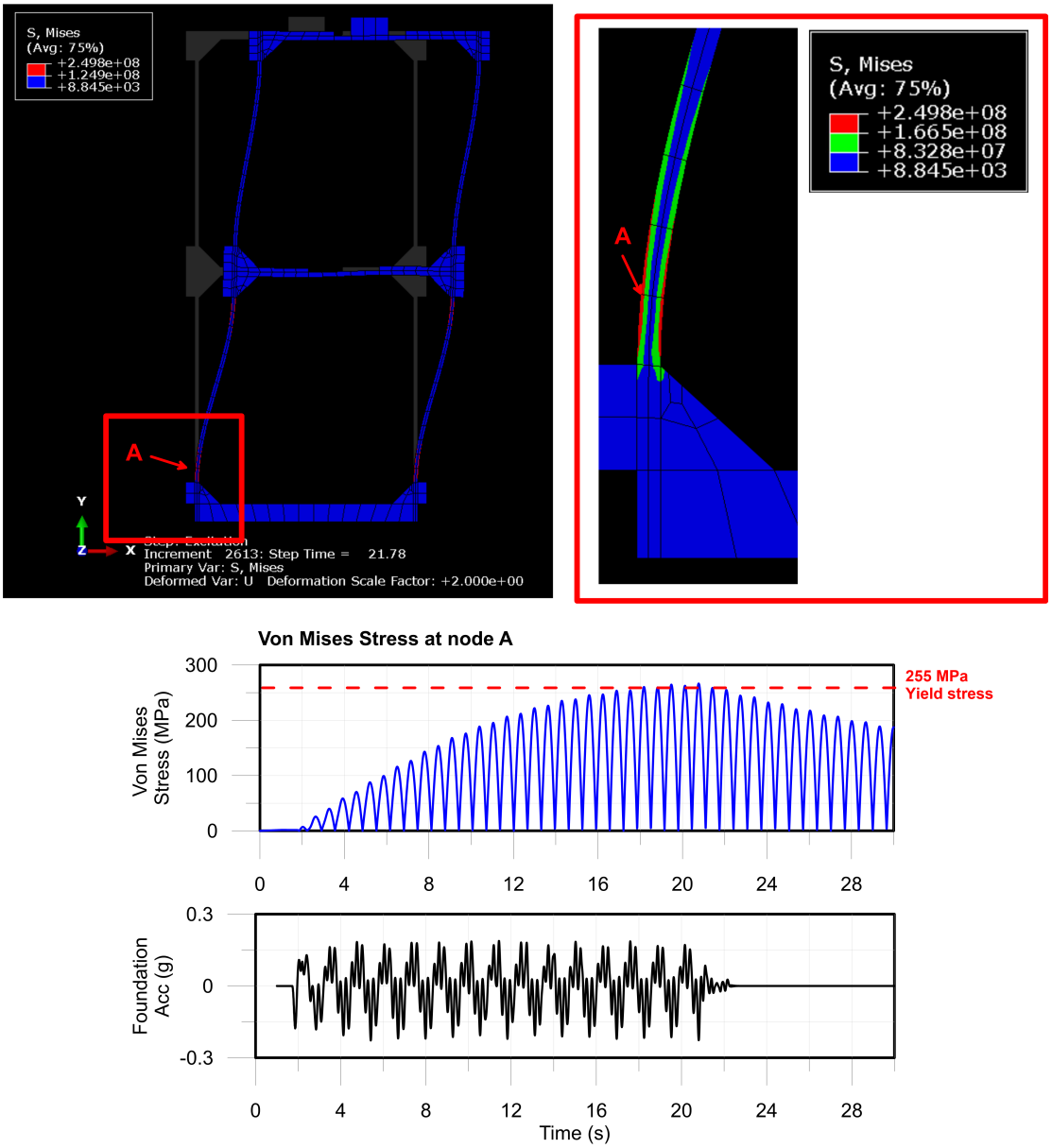

Fig. 4.5 Fixed-base finite element simulation of the bare Tall frame during strong near resonant frequency excitation.

Finite element analysis indicated that regions of stress concentrations may have formed along the external fibres of the side column plates, reaching peaks close to the foundation and the first floor plates. The same was observed for the bare Squat structure in Figure 4.6. During the strong near resonant frequency shaking, Von Mises stresses at these locations seem to approach the yield stress limit of the aluminium alloy material used in fabricating the model frames. This is illustrated by the red dashed lines in Figures 4.5 and 4.6, for the bare tall and squat structures respectively.

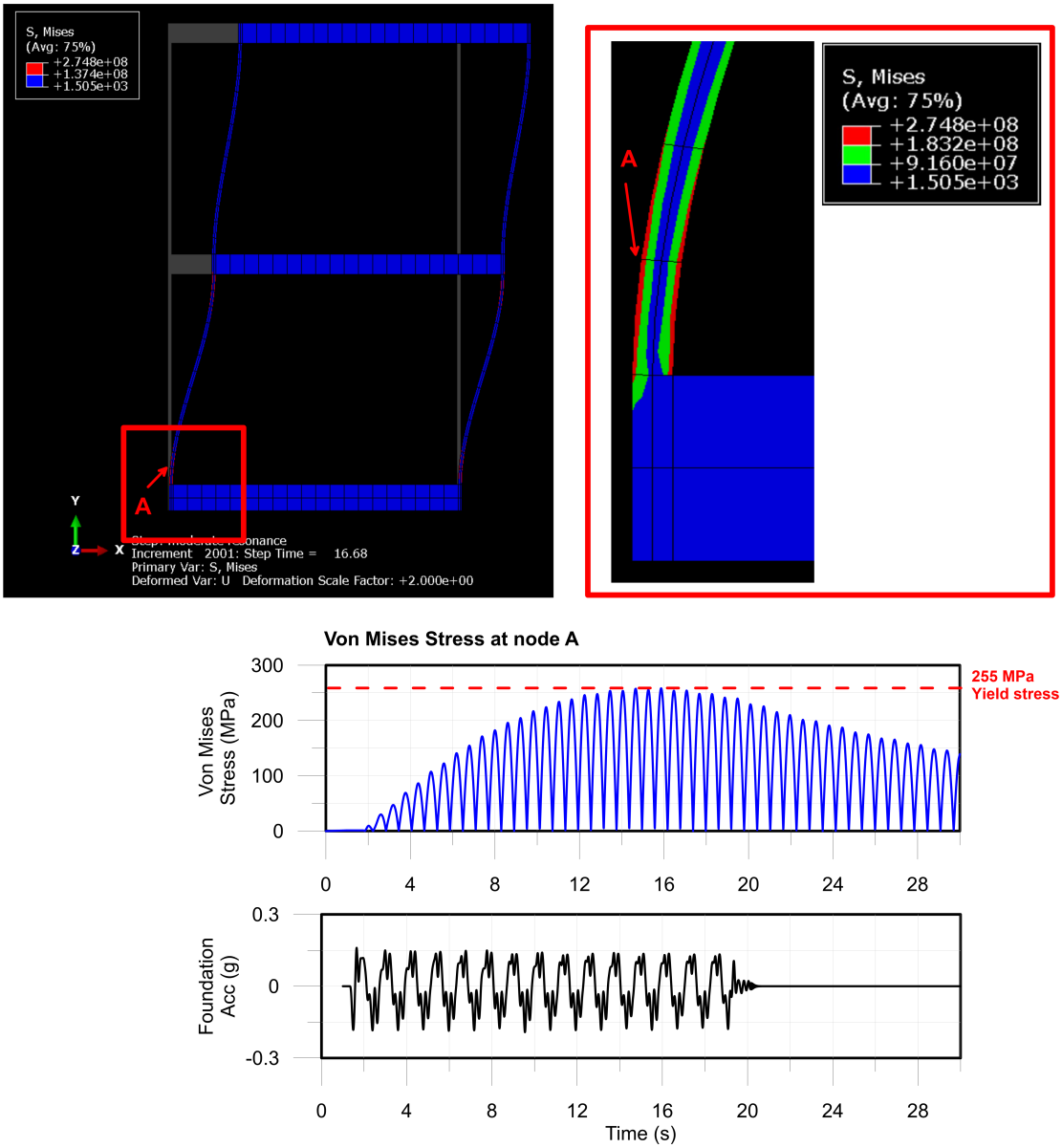

Fig. 4.6 Fixed-base finite element simulation of the bare Squat frame during strong near resonant frequency excitation.

As such, it is believed that the model frames may have experienced minor yielding close to their bases during these fixed-base strong near resonant frequency excitations. This explains the need for the stiffness matrix modifications presented in Figure 4.4, in order to attain better predictions of experimental floor acceleration data.

4.3 Mathematical Modelling of Miniature Oil Dampers

Section 3.4.2 of this study presented experimentally recorded damper force-velocity-displacement traces for the different oil damper configurations tested in the centrifuge. All miniature oil dampers exhibited nonlinearity, asymmetry and even compliance (i.e. flexibility) during shaking of the damped frames. From this point forward, a distinction will be made between the terms "miniature oil dampers" and "damping systems"; a damping system refers to a complete setup consisting of the oil damper, the load cell, and the two support plates located in between floors of the damped structure.

Mathematically, the damping system fitted into the damped frame can be represented by a complex arrangement of springs, dashpots and friction sliders as depicted in Figure 4.7. For the purpose of this investigation, the response of the complete damper system will be simplified by a combination of a nonlinear spring, a nonlinear dashpot and a friction slider all connected in parallel as shown in Figure 4.7. The dashpot simulates the velocity-dependant dissipative characteristics of the miniature oil damper; the friction slider is intended to account for friction at the damper o-ring seals. A nonlinear spring will be used to take into consideration elements of elasticity within the damper itself; this includes the volume-compensating air bladder, damping fluid compressibility, as well as the flexibility of the support plates connecting the dampers to the floors.

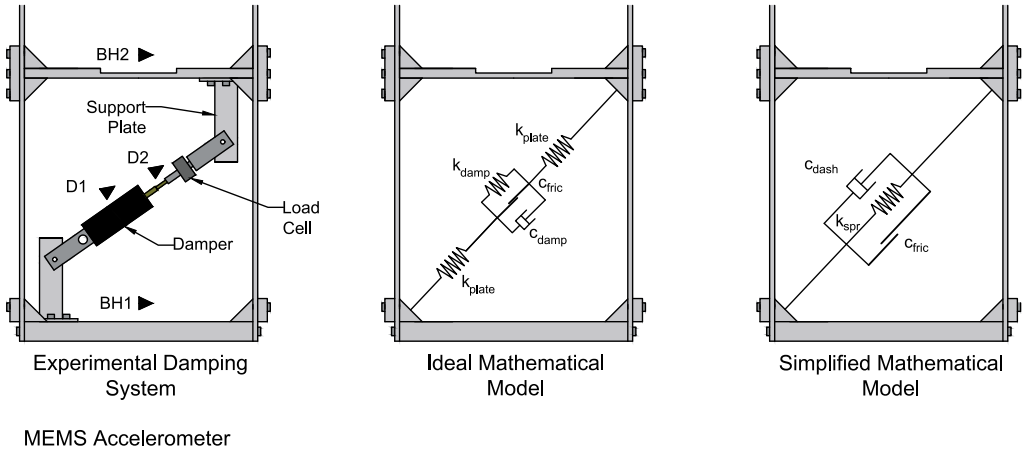

Fig. 4.7 Experimental, theoretical, and simplified mathematical model of a damping system.

The appeal of this spring-dashpot-slider arrangement lies in the ease with which the simplified model can be calibrated against experimental data. Given that the load cells are connected mechanically in-series to the damping systems, the force measurements recorded experimentally from the dampers also equate to the total force outputs from the damping systems. Following the simplified model in Figure 4.7, the measured force in a load cell can be treated as a summation of a displacement-proportional force component from the spring, and a velocity-proportional force component from the dashpot. For this simplified arrangement, the spring, dashpot and slider experience the same input displacements and stroke velocities.

Using experimentally derived velocity and displacement inputs into the damping system (i.e. data integrated from accelerations recorded by horizontal MEMS accelerometers on the floors BH1 and BH2), these two components of the total damping system force can be isolated from each other as discussed in Boksmati and Madabhushi (2020); load cell readings recorded close to peak inter-storey velocities are attributed to the dashpot component of the model, while load cell readings recorded close to peak inter-storey drifts are attributed to the spring component of the damping system. The friction-slider is accounted for by allowing non-zero spring forces to exist close to zero displacements.

Figure 4.8 is a visual illustration of how experimental damper force-velocity and force-displacement traces are used to derive the dashpot, spring and slider constitutive models for the D2 dampers as tested in the tall fixed base structure. For all base excitations fired during the test, maximum and minimum inter-storey velocities and inter-storey drifts are tracked in every cycle of structural response. The corresponding damper forces at these peaks are recorded as shown by the blue markers in Figure 4.8. By implementing this across all cycles for all input motions fired, scatter plots of dashpot force versus peak inter-storey velocity, and spring force versus peak inter-storey drift can be produced.

In line with the mathematical functions commonly used to describe prototype nonlinear damper behaviour, power functions are used to fit data points across the positive (extension) and the negative (compression) phases of the dashpot response. For the spring constitutive models, third-order polynomial functions were used to fit experimental data points of spring force versus peak inter-storey drift. Asymmetry in damper response, such as the one portrayed by both dampers in Figure 4.8, is not often encountered in prototype nonlinear dampers. This asymmetry is typical of dampers in vehicle shock-absorber assemblies, where less damping is need during suspension compression, and more damping is preferred on suspension re-coil.

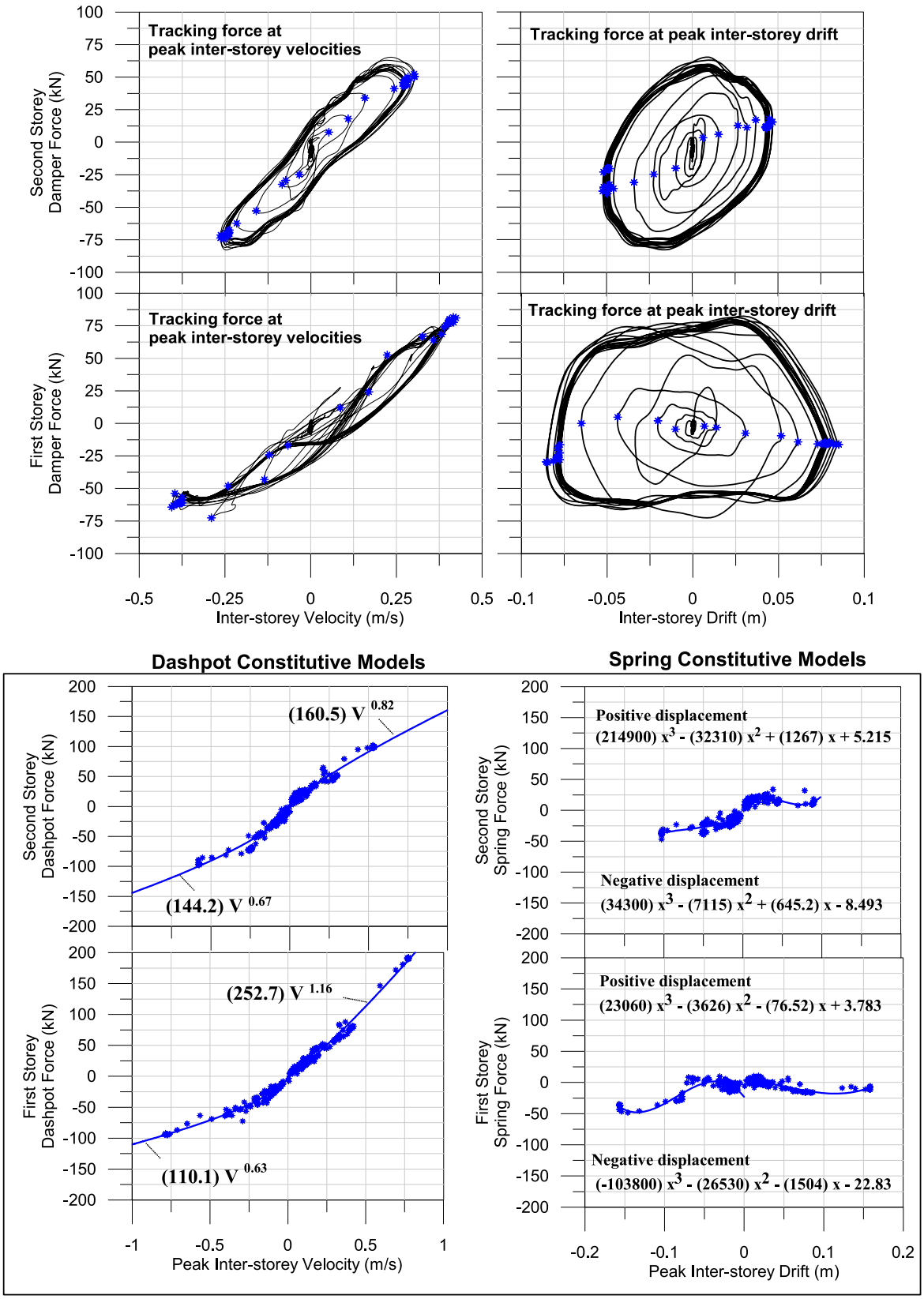

Fig. 4.8 Deriving dashpot and spring constitutive models for first storey and second storey miniature oil dampers D2 as used in the Tall damped structure.

Derivation of any constitutive model would need to account for this asymmetry. Therefore, two different power functions, with two different damping coefficients and damping exponents were used for the tension/compression phases of the dashpot response. The same approach was applied to the third-order polynomial functions describing the spring force. Figure 4.8 includes the nonlinear spring and dashpot constitutive equations derived for D2 dampers fitted into the tall damped structure.

The same process is repeated for the damped squat frame, tracking force at peak inter-storey drifts and velocities for every cycle of every earthquake. Experimentally derived dashpot and spring constitutive models are presented in Figures 4.9 and 4.10 for the three different damper configurations tested: D3, D2 and D1. The differences in damping characteristics and compression-extension asymmetry in the dashpot response are very clear. The miniature devices are clearly designed to produce higher damping force in the positive velocity range (extension) than in the negative velocity range (compression). Three dashpot power functions that best-fit the experimental data points are included for both the positive (extension) and negative (compression) phases of the dashpot response.

The smaller orifice diameters in the piston head of the D1 configuration results in the highest extension damping coefficient out of the three as expected. On the other hand, the difference in damping performance between the three configurations is less evident during the compression phases of the response. Experimental data points of spring-force versus peak inter-storey drifts for both first and second storey dampers do not seem to adhere to a specific mathematical trend. A third order polynomial function was deemed sufficient to capture the scatter to within reasonable accuracies.

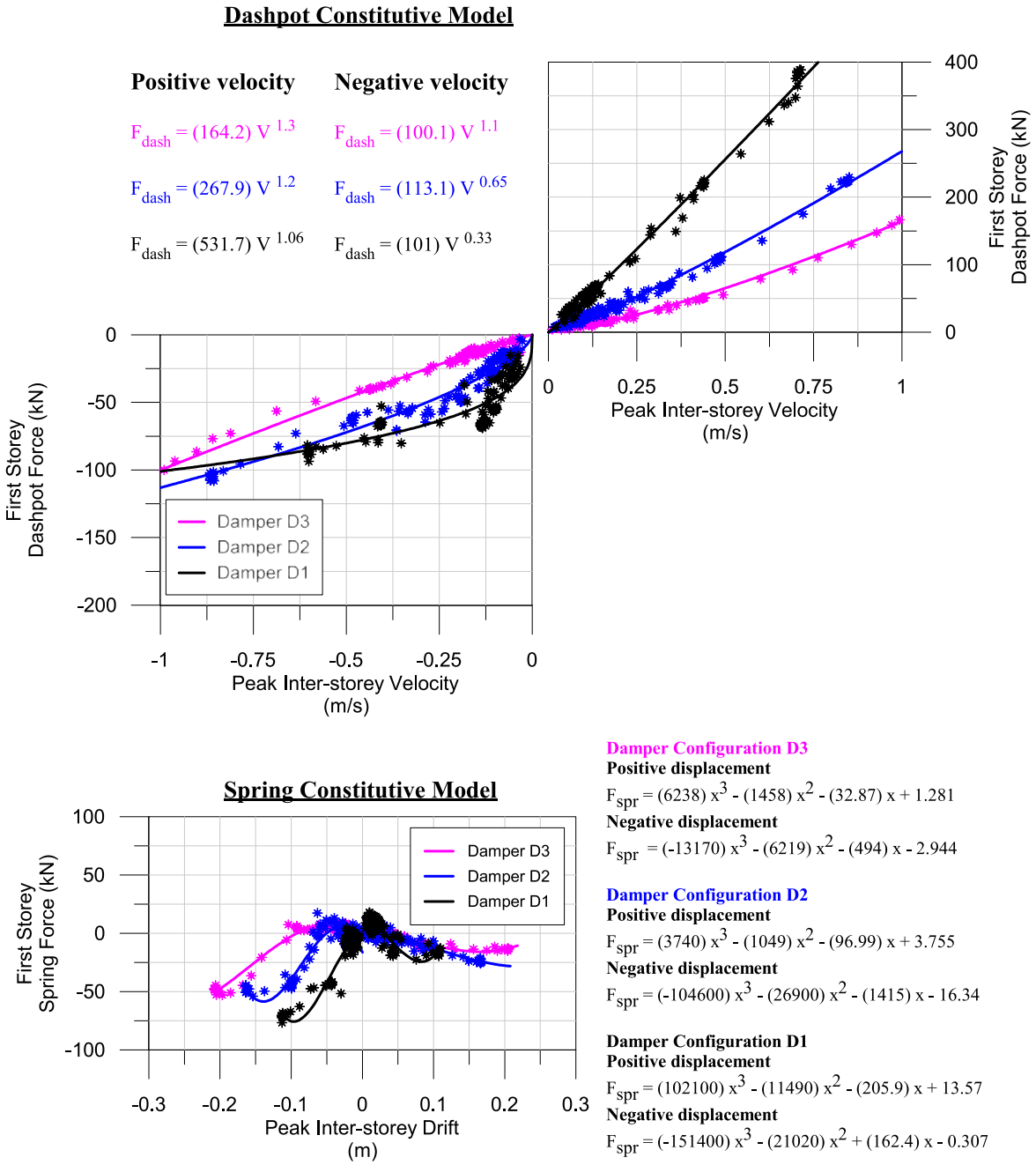

Fig. 4.9 First storey dashpot and spring constitutive models for oil dampers D3, D2 and D1 as used in the damped Squat frame.

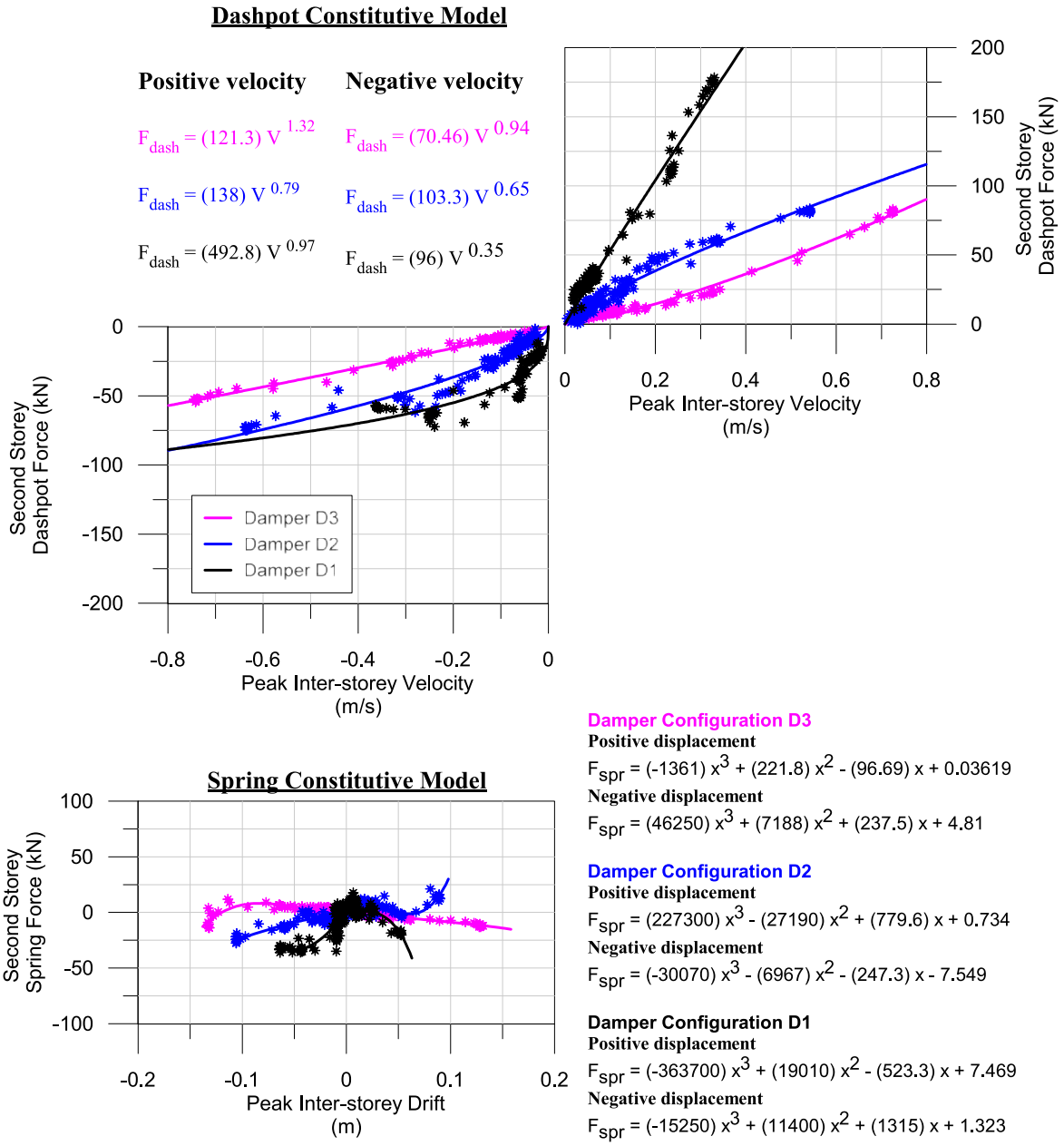

Fig. 4.10 Second storey dashpot and spring constitutive models for oil dampers D3, D2 and D1 as used in the damped Squat frame.

Curve-fitting equations defining the dashpot component of the first storey D2 damper in the tall structure (Figure 4.8) are very similar to those reported for the first storey D2 dampers in the squat frame (Figure 4.9). This gives confidence on the consistency of the damping devices between tests with different frames. However, the same cannot be said about the second storey D2 dampers. The difference in dashpot constitutive equations for the

damper higher up in the frame is believed to be the result of inherent dissimilarity in stiffness between the two structures.

4.4 Time History Predictions for Damped Frames

Nonlinearity in the damped frames used in this study is not a result of structural yielding, but rather a consequence of the nonlinear miniature oil dampers fitted into the model structures. The system of equations in 4.1 can be extended to include a vector of supplemental damper forces $\{F_d\}$:

$$[M]\{\ddot{u}\}_{i+1} + [C]\{\dot{u}\}_{i+1} + [K]\{u\}_{i+1} + \{F_d\}_{i+1} = \{p\}_{i+1} \tag{4.6}$$

An incremental variation of the integration method presented earlier in section 4.2 is implemented such that at every time step $(i+1)$, internal system forces are updated based on a residual force. The algorithm is summarised in Figure 4.11.

At the beginning of every time step $(i+1)$, internal restoring forces, damping forces, and degrees of freedom are initialised in Step 3.2. A residual force vector $\hat{R}_{i+1}$ is then calculated in Step 3.3; this is effectively the difference between applied external loads at the current time step $(i+1)$, and internal resisting forces in the system:

$$\{\hat{R}\}_{i+1} = \{\hat{p}\}_{i+1} - [\hat{k}]\ \{u\}_{i+1} - \{F_d\}_{i+1} \tag{4.7}$$

Instead of Equation 4.4, displacements are now obtained incrementally:

$$\{du\}_{i+1} = [\hat{k}]^{-1}\ \{\hat{R}\}_{i+1} \tag{4.8}$$

$$\{u\}_{i+1} = \{du\}_{i+1} + \{u\}_{i+1} \tag{4.9}$$

Once displacements are computed, internal restoring forces in the frame can be updated :

$$\{F_s\}_{i+1} = [K]\{u\}_{i+1} \tag{4.10}$$

Using Equation 4.3, velocities $\{\dot{u}\}_{i+1}$ can also be computed. These are fed into the dashpot constitutive equations derived in section 4.3 to update the damper force vector $\{F_d\}_{i+1}$ for use in the next time step.

1. Problem Definition

1.1 Setup system mass [M] and stiffness [K] matrices

1.2 Compute undamped natural frequencies

1.3 Assume Rayleigh damping to construct damping matrix [C]

1.4 Define forcing vector {p} for base excitation

2. Initialising conditions for integration, i = 0

2.1 Time-stepping integration parameters for linear acceleration
$\gamma = 1/2$, $\beta = 1/6$

2.2 Compute Newmark integration constants: a_1, a_2, and a_3

2.3 Initial displacement, velocity, and acceleration vectors

$\{u\}=\{\dot{u}\}=\{\ddot{u}\}=\{0\}$

2.4 Initial damper force vector $\{F_D\} = \{0\}$

2.5 Assemble dynamic stiffness matrix $[\hat{k}] = [K] + a_1$

3. At each time increment , i = 1, 2, 3, ...

3.1 Compute $\hat{p}_{i+1}$

3.2 Initialise

3.2.1 $\{u_{i+1}\} = \{u_i\}$, $\{\dot{u}_{i+1}\} = \{\dot{u}_i\}$

3.2.2 Damper force $\{F_{D,i+1}\} = \{F_{D,i}\}$

3.2.3 Structure restoring force $\{F_{S,i+1}\} = \{F_{S,i}\}$

3.3 Compute Residual force vector, $\{\hat{R}_{i+1}\}$

3.4 Compute incremental displacement {du}

3.4. 1 Update displacement $\{u_{i+1}\}$ and velocity $\{\dot{u}_{i+1}\}$

3.4.2 Update structure restoring force $\{F_{S,i+1}\}$

3.4.3 Update damper force vector $\{F_{D,i+1}\}$

3.5 Compute acceleration $\{\ddot{u}_{i+1}\}$

4. Repeat Step 3 for the next time step i + 1

Fig. 4.11 Numerical integration scheme for fixed base damped structures.

Figures 4.12 to 4.14 present numerical predictions of total floor accelerations and damper performance for the case of the squat frame subjected to strong near resonant frequency excitations. Results for three different damping configurations are shown: D3, D2 and D1. For each case, dashpot constitutive equations derived in section 4.3 are used in the numerical integration process to simulate forces from the supplemental dampers.

Predictions of total floor accelerations appear to be satisfactory for the three damper configurations, despite only including the dashpot (velocity-proportional) component of the damper force. In terms of damper performance, the numerical dashpots are able to capture the overall backbone curves of the experimental force-velocity traces during both compression and extension to within acceptable accuracy. Nevertheless, lag in force-velocity (i.e. damper compliance), as well as other higher order effects in the damper response are not captured by the numerical model, causing an underestimation of peak damper forces. For damping configurations D3 and D2, this is not significant. However, for dampers D1, distinctive flatness in experimental force-velocity was recorded during extension. This physically translates as a reduction in damping effectiveness in the structure, which cannot be captured numerically by the dashpots alone. As a result, the numerical model in Figure 4.14 slightly under predicts total floor accelerations.

Successful applications of numerical integration during multi-frequency component input motions are presented in Figures 4.15 and 4.16 for the cases of the damped squat frame and damped tall frame experiencing scaled Kobe and sine-sweep excitations respectively. Again, higher order effects and stiffness of the experimental dampers result in slightly higher peak damper forces, which cannot be fully captured by the numerical dashpots. However, inter-storey drifts and velocities are predicted reasonably well.

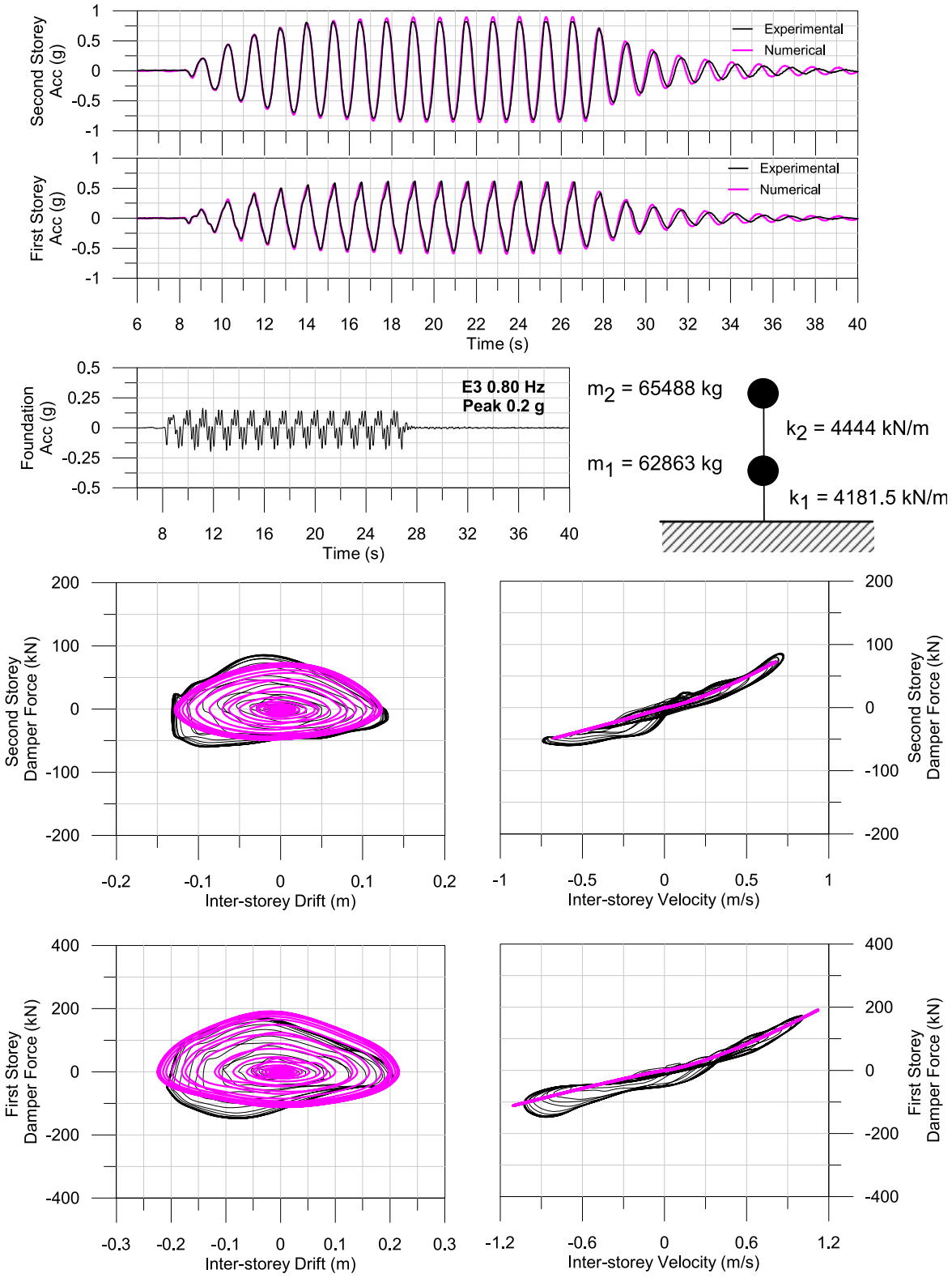

Fig. 4.12 Numerical predictions for the Squat frame during strong near-resonant frequency input motions equipped with D3 light damping configuration.

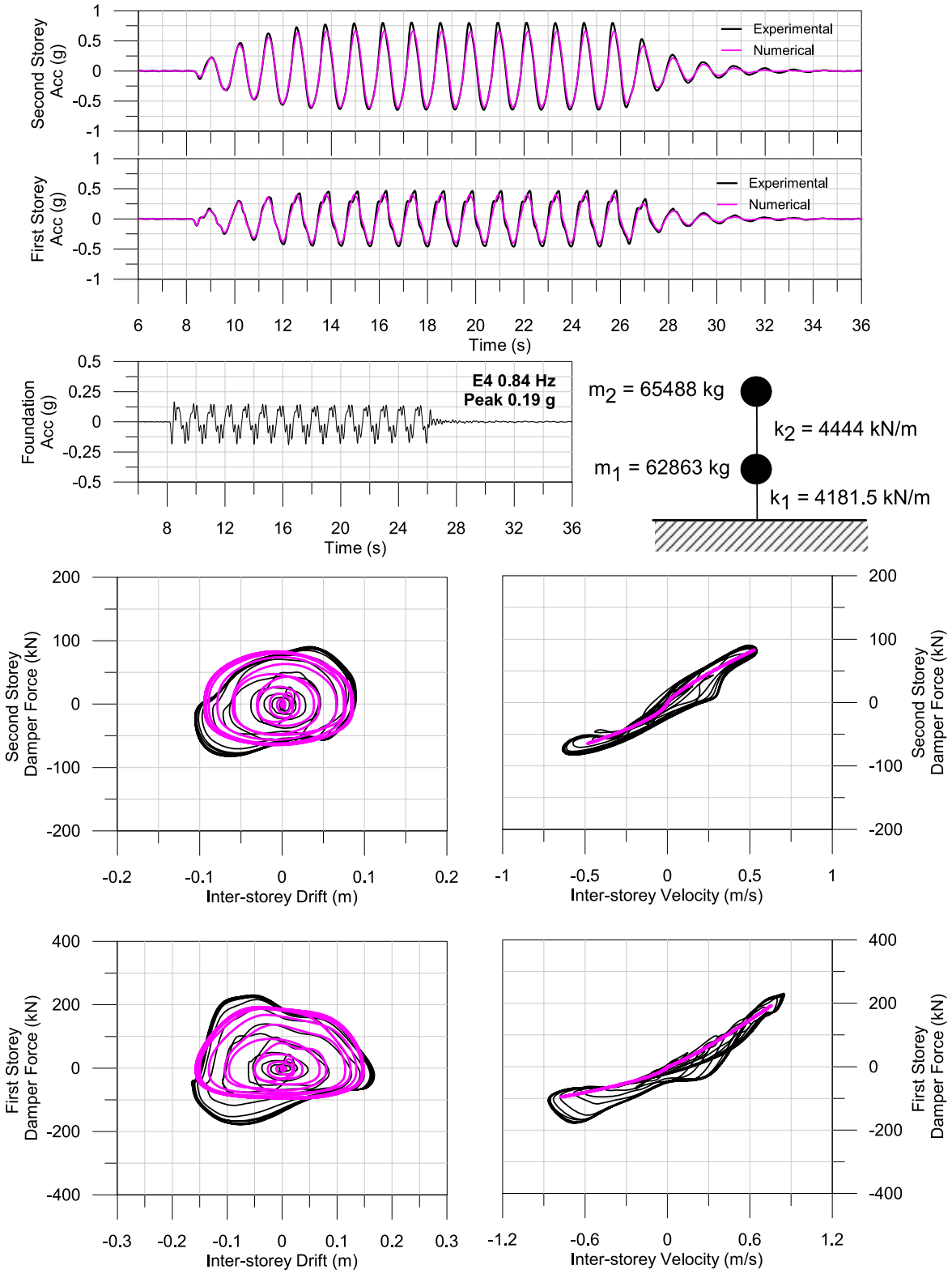

Fig. 4.13 Numerical predictions for the Squat frame during strong near-resonant frequency input motions equipped with D2 medium damping configuration.

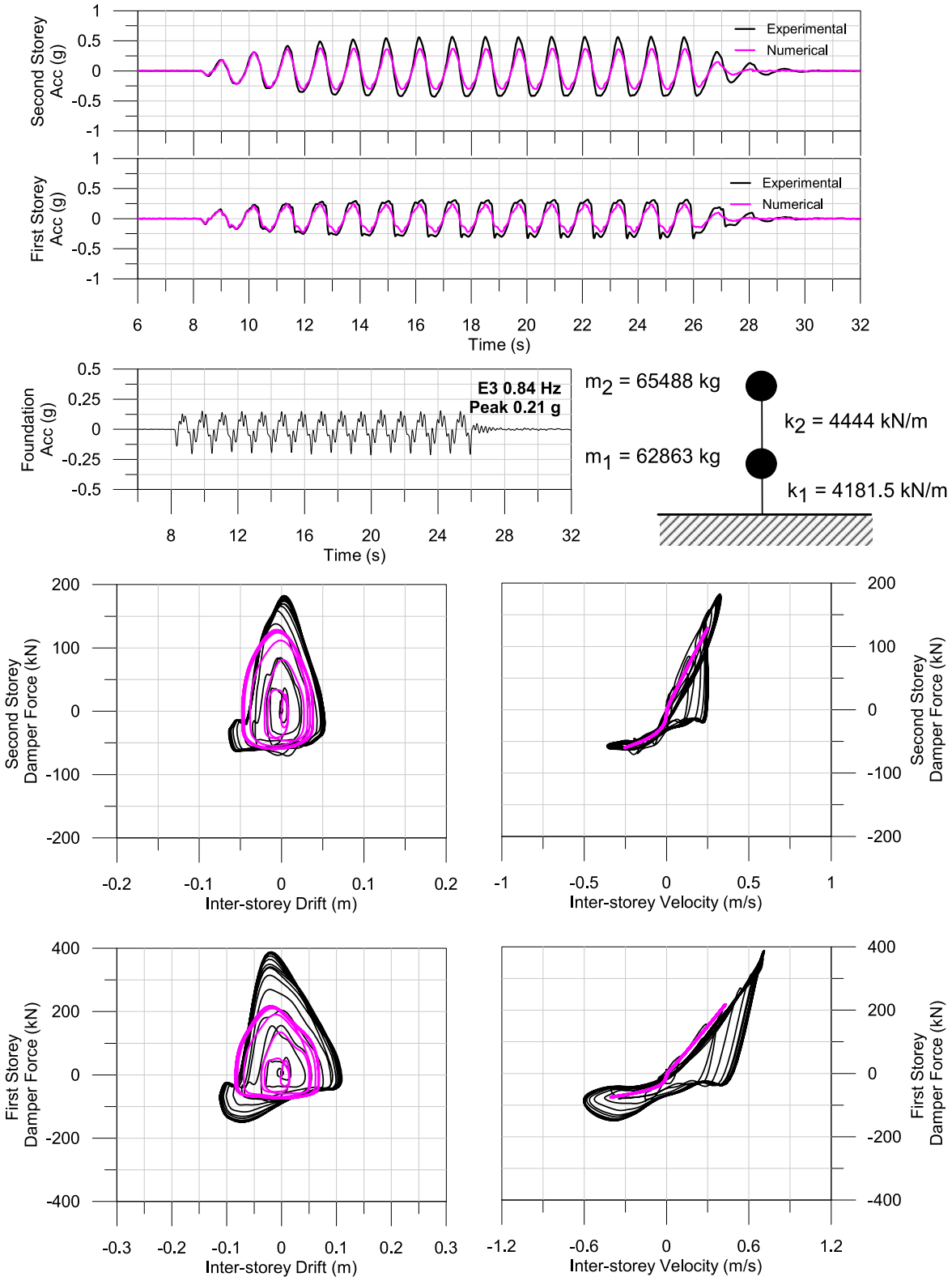

Fig. 4.14 Numerical predictions for the Squat frame during strong near-resonant frequency input motions equipped with D1 heavy damping configuration.

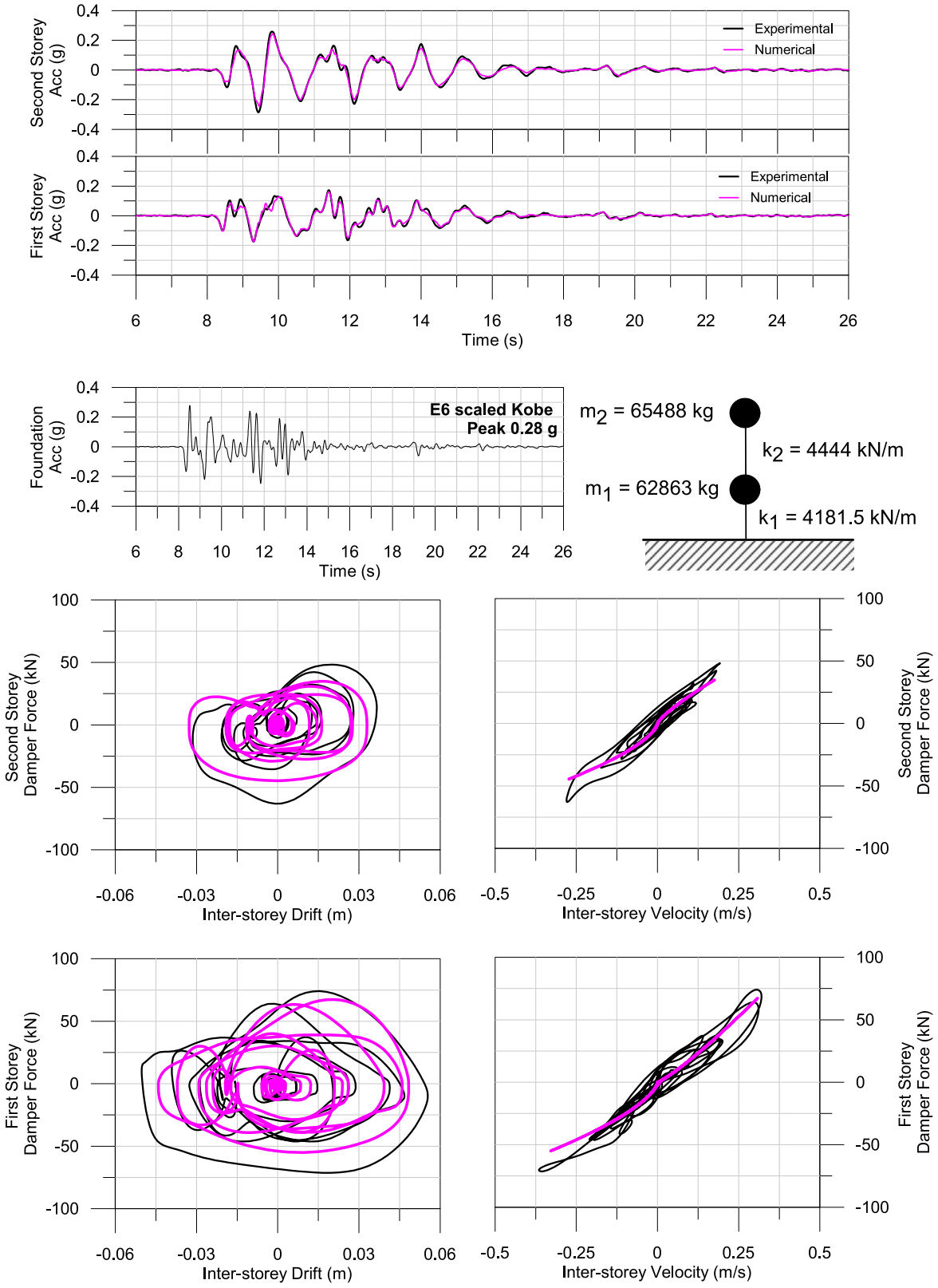

Fig. 4.15 Numerical predictions for the Squat frame equipped with D2 dampers during a scaled Kobe excitation.

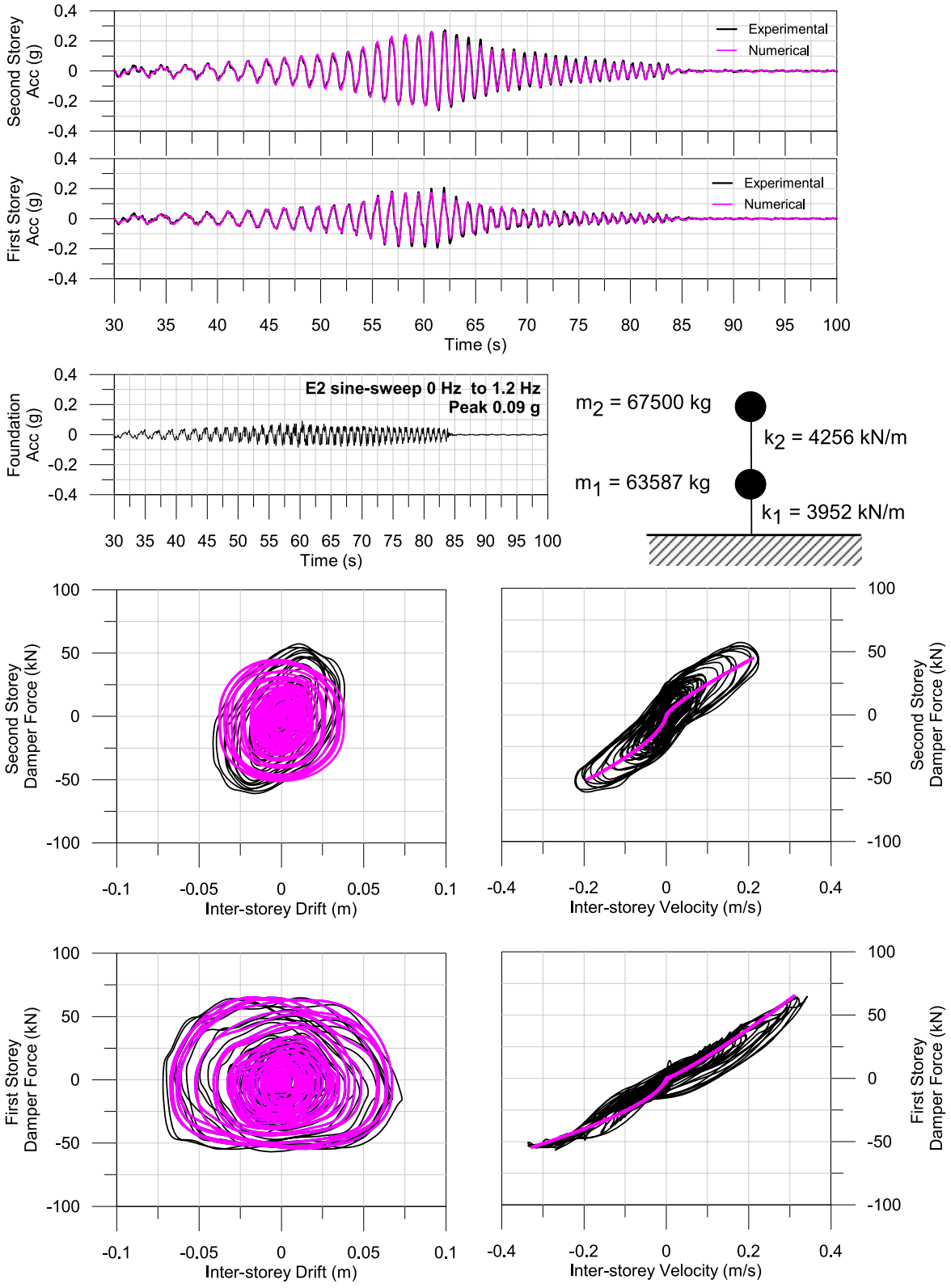

Fig. 4.16 Numerical predictions for the Tall frame equipped with D2 dampers during a sine-sweep excitation.

4.5 Response Spectrum Analysis (RSA)

Dynamic experimental testing of fixed-base, linear elastic, 2-DOF model structures in the centrifuge presents a unique opportunity to assess the adequacy of the simplified RSA procedure introduced in section 2.2.3. This method is used for preliminary assessments of effective damping ratios, inter-storey drifts, and storey shear forces for the design and analysis of structures equipped with supplemental velocity-dependant dampers.

Following the RSA procedure summarised in Figure 2.7, the first step is identification of the modal properties of the undamped bare structure. Mathematically, total floor displacements $\{u\}$ (relative to the foundation) can be estimated assuming a dominant contribution from the first mode of vibration by :

$$\begin{Bmatrix} u_1 \\ u_2 \end{Bmatrix}_1 = A \begin{Bmatrix} \phi_1 \\ \phi_2 \end{Bmatrix}_1 \tag{4.11}$$

where $\{\phi\}_1$ is the first mode shape vector, and A is the modal coordinate. For a roof normalised mode shape vector, A is effectively the contribution of the first mode to roof displacement. Contribution of the fundamental mode to inter-storey drift is:

$$\begin{Bmatrix} u_{drift,1} \\ u_{drift,2} \end{Bmatrix}_1 = A \begin{Bmatrix} \phi_{r1} \\ \phi_{r2} \end{Bmatrix}_1 = A \begin{Bmatrix} \phi_1 \\ \phi_2 - \phi_1 \end{Bmatrix}_1 \tag{4.12}$$

where $\{\phi_r\}_1$ is the modal drift vector. From this, inter-storey velocities can be estimated by:

$$\begin{Bmatrix} v_1 \\ v_2 \end{Bmatrix}_1 = A\omega_1 \begin{Bmatrix} \phi_{r1} \\ \phi_{r2} \end{Bmatrix}_1 \tag{4.13}$$

where ω_1 is the circular frequency of mode 1.

Using Equation 4.12, maximum strain energy per cycle of response at the fundamental mode of the structure can be computed using:

$$W_k = \frac{1}{2}{\omega_1}^2 A^2 \sum m_i \, {\phi_i}^2 \tag{4.14}$$

By equating energy dissipated by nonlinear dampers at the fundemental mode, to that dissipated by equivalent linear viscous dampers, Soong and Constantinou (1994) proposed the following equation for work done by dampers :

$$W_d = \sum n \, \lambda_i \, C_i \, {\omega_1}^{\alpha_i} (A\phi_{ri,1} \times cos\theta)^{1+\alpha_i} \tag{4.15}$$

where C is the damping coefficient of each device, n is the number of dampers on each floor, α is the damping exponent for the nonlinear dampers, θ is the angle of inclination of the dampers, and λ is

$$\lambda = 2^{2+\alpha_i} \frac{\Gamma^2(1+\alpha_i/2)}{\Gamma(2+\alpha_i)}$$

in which Γ is the gamma function. The predicted modal damping ratio at the first mode upon installation of the nonlinear dampers can be estimated by (Seleemah and Constantinou, 1997; Soong and Constantinou, 1994):

$$\zeta_{d,1} = \frac{W_d}{4\pi W_k} = \frac{\sum_i n\ \lambda_i\ C_i\ {\phi_{ri,1}}^{1+\alpha_i}\ \ (cos\theta_i)^{1+\alpha_i}}{2\ \pi\ {\omega_1}^{2-\alpha_i}\ A^{1-\alpha_i}\ \sum\ m_i\ {\phi_i}^2} \tag{4.16}$$

The RSA procedure as shown in Figure 2.7 is an iterative one; an initial assumption is first made for the modal coordinate A to obtain a first estimate of the first mode damping ratio. Reductions factors corresponding to this estimated damping ratio are then calculated from Ramirez et al. (2001) and ASCE 7-16 (2016) using:

$$B = \frac{1.65}{2.31 - 0.41\ \ln(100\ \zeta_{d,1})} \tag{4.17}$$

This reduction factor is applied to the 5% damped spectral acceleration to reduce it for higher damping. A first estimate of spectral displacement corresponding to the higher damping ratio can be easily obtained:

$$Sd_{\zeta,1} = \frac{Sa_{\zeta,1}}{\omega_1^2}$$

where $Sa_{\zeta,1}$ is the spectral acceleration reduced for higher damping. A refined value of modal coordinate A can be computed:

$$A = \Gamma_1\ Sd_{\zeta,1} \tag{4.18}$$

where Γ_1 is the modal participation factor of mode 1

$$\Gamma_1 = \frac{\sum_i\ m_i\ \phi_i}{\sum_i\ m_i\ \phi_i^2}$$

Using Equation 4.16, a new modal damping ratio can be calculated using the updated modal coordinate from Equation 4.18. This process is repeated until the modal damping ratio and modal coordinate converge to steady values.

Seleemah and Constantinou (1997) expanded the iterative procedure described above to include contributions of higher order modes of vibration. By treating higher order modes as small deformations occurring about the fundamental mode of vibration, they introduced the idea of linearising the nonlinear dampers at these higher order harmonics by assuming their constitutive relationships to be tangents to the nonlinear force-velocity curves at the points of first mode inter-storey velocities. Mathematically, this can be expressed as:

$$C_{linear,i} = \alpha_i \, C_i \, {v_{i,1}}^{\alpha_i - 1} \tag{4.19}$$

where $v_{i,1}$ is the damper velocity due to first mode deformations. Consequently, the equivalent viscous damping ratio for higher modes of vibration, assuming linear dampers, becomes:

$$\zeta_d = \frac{W_d}{4 \, \pi \, W_k} = \frac{\sum_i \, n \, C_{linear,i} \, \phi_{ri,2}^2 \, (cos\theta_i)^2}{2 \, \omega_2 \, \sum \, m_i \, \phi_i^2} \tag{4.20}$$

which is independent of the variable A, and does not require iteration.

With modal damping ratios computed for the first and higher modes of vibration of the damped structure, code-based reduction factors can be directly applied to the 5% damped SDOF response spectral values to compute traditional modal parameters such as inter-storey drifts, inter-storey velocities, etc. These can then be combined using the Square-Root-of-Sum-of-Squares (SRSS) approach to predict total structural response for the damped frame.

Determination of structural member forces for design using the RSA procedure is not straight forward process. Step 7 in Figure 2.7 highlights three cases at which frame forces should be evaluated. Step 7.3 is often critical for design as it occurs at an instance of super-positioning of stiffness and damping forces in the structure. FEMA-273 (1997) guidelines proposed the following equation, with modification factors $CF1$ and $CF2$, to relate pseudo-acceleration at maximum displacement to maximum acceleration for the damped structures:

$$Sa_{max} = Sa \, (CF1 + \frac{2\pi\zeta}{\lambda_i} \, CF2) \tag{4.21}$$

For linear dampers, Seleemah and Constantinou (1997) used:

$$CF1 = cos(tan^{-1}(2\zeta))$$

$$CF2 = sin(tan^{-1}(2\zeta))$$

For nonlinear dampers, Ramirez et al. (2001) proposed:

$$CF1 = cos(\frac{2\pi\alpha_i\zeta}{\lambda_i}^{\frac{1}{2-\alpha_i}})$$

$$CF2 = sin(\frac{2\pi\alpha_i\zeta}{\lambda_i}^{\frac{1}{2-\alpha_i}})$$

Once estimates of maximum accelerations in a damped structure are calculated, peak storey shear forces can be evaluated and used for preliminary sizing of structural members.

With the important equations for RSA established above, it is clear that the simplified method is based on two main underlying assumptions:

1. Response of a structure with uniform distribution of dampers can be approximated by modal superposition of its orthogonal undamped modes of vibration.

2. Damping ratio is estimated by equating work done in one cycle of vibration at the undamped natural frequency, to the energy dissipated by an equivalent linear viscous damped system.

Tables 4.1 and 4.2 compare peak structural response parameters obtained from RSA, to those predicted numerically by time integration, to those recorded experimentally in the centrifuge. The comparison is for the case of the tall damped frame experiencing realistic excitations: scaled Kobe and scaled Imperial Valley motions. Because of asymmetry in experimental damper response, only the positive dashpot constitutive parameters (C and α, as derived in section 4.3) have been used in the RSA procedure for the first and second storey dampers.

Table 4.1 Tall damped structure peak response as computed by simplified procedure, numerical integration, and as measured experimentally during scaled Kobe excitation.

Scaled Kobe excitation with D2 dampers						
Parameter	Floor	Mode 1	Mode 2	**SRSS**	**Numerical**	**Experimental**
Estimated damping ratio		9.3 %	17.8 %			13.2 %
Floor displacement	1	58.0	7.8	58.5	46.5	55.7
(mm)	2	91.7	-4.6	91.9	77.3	93.3
Inter-storey drift	1	58.0	7.8	58.5	46.5	55.7
(mm)	2	33.7	12.4	35.9	32.6	38.1
Inter-storey velocity	1	0.279	0.101	0.297	0.327	0.354
(m/s)	2	0.163	0.161	0.229	0.183	0.216
Damper Force	1	57.6	19.9	61.0	62.0	86.1
Output (kN)	2	36.5	25.7	44.6	31.8	64.8
Storey Shear at	1	234.1	32.5	236.3	432.2	468.4
Maximum Acceleration (kN)	2	147.7	55.9	157.9	260.4	300.2

Table 4.2 Tall damped structure peak response as computed by simplified procedure, numerical integration, and as measured experimentally during scaled Imperial Valley.

Scaled Imperial Valley with D2 dampers						
Parameter	Floor	Mode 1	Mode 2	**SRSS**	**Numerical**	**Experimental**
Estimated damping ratio		9.5 %	18.1 %			
Floor displacement	1	42.3	4.3	42.5	28.9	24.3
(mm)	2	66.9	-2.6	67.0	46.0	37.0
Inter-storey drift	1	42.3	4.3	42.5	28.9	24.3
(mm)	2	24.6	6.9	25.6	17.2	13.4
Inter-storey velocity	1	0.204	0.056	0.211	0.156	0.173
(m/s)	2	0.119	0.090	0.149	0.097	0.111
Damper Force	1	40.0	11.0	41.5	28.5	35.5
Output (kN)	2	28.2	14.8	31.8	17.9	32.8
Storey Shear at	1	170.9	18.2	171.9	292.2	321.3
Maximum Acceleration (kN)	2	107.8	31.3	112.3	161.8	179.7

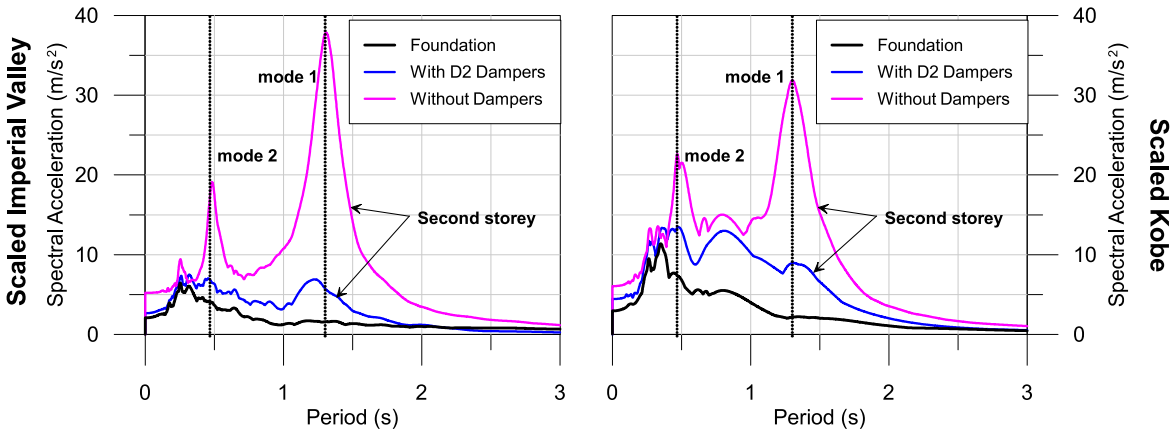

Fig. 4.17 5 % damped response spectral plots from experimental foundation and roof structural accelerations for the tall structures.

For input excitations such as Kobe, characterised by short velocity pulses, the RSA method produced satisfactory displacement and velocity predictions as shown in Table 4.1. The method, however, grossly underestimated maximum storey shear forces. For the case of a long-duration scaled Imperial Valley excitation in Table 4.2, RSA predictions of drifts and velocities are conservative, but once again, the method grossly underestimates maximum storey shear forces in the frame.

The validity of modal superpositioning for a structure fitted with supplemental oil dampers is believed to be the reason behind this under-prediction of maximum accelerations, hence storey shear forces. To investigate this further, response spectral plots derived from experimental roof and foundation acceleration traces are presented in Figure 4.17, to better visualise the distribution of signal intensity over the signal frequency content.

For the regular frame without dampers, distinctive peaks in response spectra in Figure 4.17, at the natural periods of the structure, may justify the use of modal superpositioning for such a system. However, the same is not true for the damped structure. During the short pulse-like Kobe excitation, the shape of response spectrum derived from the damped frame roof accelerations appears to follow closely that derived from the foundation accelerations, with little energy in the signal focused at the first mode of the structure; i.e. the damped frame did not have sufficient time to respond at its fundamental mode.

For the long duration Imperial Valley excitation, the shape of the response spectrum computed from the damped frame roof accelerations also follows that derived from the foundation accelerations. However, a clearer peak at the fundamental period can be observed; i.e. the base shaking was long enough for the damped frame to respond at its fundamental frequency.

For both excitations, Kobe and Imperial Valley, the response spectra derived from the damped frame roof accelerations in Figure 4.17 shows spectral peaks at high frequencies that are comparable in magnitude to those recorded at the fundamental frequency of the structure. This would be typical of realistic input motions that do not trigger significant resonance in the damped structure. By limiting response prediction in RSA to modal contributions only, and ignoring these high frequency contributions, the simplified method may underestimate peak response accelerations, thus predict lower maximum storey shear forces for design.

Peak response predictions using RSA for base excitations that trigger resonant response in the damped structures are presented in Tables 4.3 and 4.4, for the tall frame and squat frame respectively. As shown by the roof acceleration response spectra in Figure 4.18, these excitations trigger a response primarily at the fundamental frequency of the structures. Unlike the spectral plots for Kobe and Imperial Valley in Figure 4.17, the damped frame roof accelerations appear to be dominated by the fundamental mode. This presents an ideal case to check the suitability of modal superpositioning in RSA to predict peak response parameters for damped structures.

Table 4.3 Tall damped structure peak response as computed by simplified procedure, numerical integration, and as measured experimentally during sine-sweep excitation.

Sine-sweep excitation with D2 dampers						
Parameter	Floor	Mode 1	Mode 2	**SRSS**	**Numerical**	**Experimental**
Estimated damping ratio		8.9 %	17.4 %			10.7 %
Floor displacement	1	108.3	2.4	108.3	68.8	73.3
(mm)	2	171.4	-1.4	171.4	108.4	110.9
Inter-storey drift	1	108.3	2.4	108.3	68.8	73.3
(mm)	2	63.0	3.8	63.1	39.7	38.3
Inter-storey velocity	1	0.522	0.03	0.523	0.309	0.342
(m/s)	2	0.304	0.05	0.307	0.216	0.224
Damper Force	1	118.9	6.4	119.1	58.5	64.8
Output (kN)	2	60.7	7.5	61.2	36.9	57.2
Storey Shear at	1	436.5	10.0	436.6	335.7	339.4
Maximum Acceleration (kN)	2	275.3	17.2	275.8	202.2	199.8

Table 4.4 Squat damped structure peak response as computed by simplified procedure, numerical integration, and as measured experimentally during strong near resonant frequency excitation.

Near resonance sinusoidal excitation with D2 dampers						
Parameter	Floor	Mode 1	Mode 2	**SRSS**	**Numerical**	**Experimental**
Estimated damping ratio		8.2 %	18.1 %		10.9 %	9.2 %
Floor displacement	1	210.7	3.5	210.8	148.8	168.0
(mm)	2	334.2	-2.1	334.2	235.0	257.6
Inter-storey drift	1	210.7	3.5	210.8	148.8	168.0
(mm)	2	123.5	5.7	123.6	86.3	89.9
Inter-storey velocity	1	1.055	0.048	1.056	0.757	0.851
(m/s)	2	0.618	0.076	0.623	0.528	0.543
Damper Force	1	285.3	15.1	285.7	193.1	230.8
Output (kN)	2	94.3	9.2	94.7	83.2	90.5
Storey Shear at	1	896.7	15.7	896.8	749.9	797.0
Maximum Acceleration (kN)	2	562.0	26.9	562.7	442.5	451.4

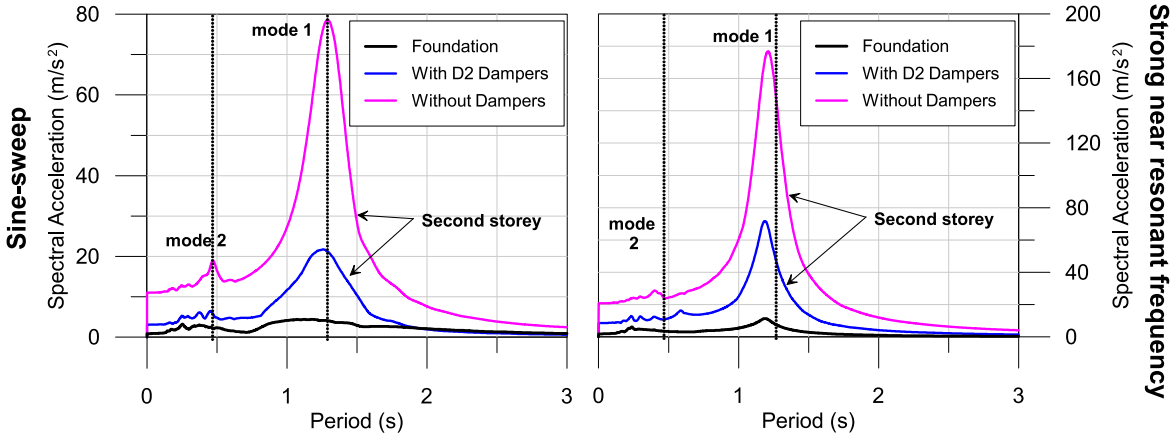

Fig. 4.18 5 % damped response spectral plots from experimental foundation and roof structural accelerations for (left) Tall frames (right) Squat frames during near resonant frequency shaking.

RSA predictions in Tables 4.3 and 4.4 show a consistent over-prediction, albeit, satisfactory estimates of drifts, inter-storey velocities and maximum storey shear forces when a damped frame is subjected to near resonant frequency shaking. The limitation of RSA here is not a question of how dominant is the fundemental mode in the overall damped frame response, but rather a question of how nonlinear dampers are considered in the simplified method.

Whilst accounting for the energy dissipation effects of nonlinear dampers (refer to Equation 4.15), RSA is incapable of capturing the time-varying stiffenning effects that arise in the damped structure as damper forces and frame restoring forces get superimposed over each other during shaking; this is especially important for nonlinear oil dampers that depict an almost rectangular force-displacement hysteresis loop, such as the devices used in this study.

These time-varing effects are inherently included in the numerical time-stepping integration scheme, but cannot be incorporated into RSA. Therefore, even though the numerical model only accounted for the nonlinear dashpot component of the miniature oil dampers, the numerical predictions of drifts, velocities, and maximum storey shear forces are much closer to the experimental values in Tables 4.3 and 4.4, compared to the ones obtained by RSA. Nevertheless, damper force predictions from the numerical model are consistently lower than their experimental counterparts due to higher order damper device characteristics (i.e. friction and stiffness) being neglected in the integration scheme.

4.6 Summary

This chapter investigated the suitability of using conventional analysis tools to predict the fixed-base dynamic response of the 2-DOF model frames as tested in the centrifuge. Mathematical representation of the model frames, and application of direct numerical time integration to solve equations of motion, were demonstrated in this chapter for a fully rigid base condition. Numerical predictions of fixed-base experimental results revealed the following:

1. Time-stepping techniques with a classical damping matrix approximation for bare frames can produce excellent dynamic response predictions. For reduced-scale centrifuge structures, inherently low damping levels in the frames make the dynamic response highly sensitive to variations in frame stiffness. This is less of an issue for broad-frequency spectrum base excitations, but can become important for intense near-resonant frequency shaking. At the onset of yield, fine-tuning of frame stiffness is required.

2. The mechanical response of the inter-storey miniature oil dampers in the damped frames can be mathematically recreated by a suitable arrangement of springs, dashpots, and sliders. A parallel arrangement was adopted for this study due to the ease with which such an analytical configuration can be calibrated from experimental damper measurements.

3. The Response Spectrum Analysis (RSA) method can result in unconservative storey shear force estimates for multi-frequency component excitations that do not trigger considerable resonance in the damped frame. This arises mainly due to high frequency components in the actual damped frame response that do not get accounted for when conducting modal analysis in RSA.

4. If base excitation at a site is expected to trigger resonance in a structure equipped with nonlinear oil dampers, it was shown that RSA provides satisfactory, albeit, conservative response predictions. This is mainly due to the simplified method's inability to capture time-varying stiffening effects caused by superpositioning of damper forces and frame restoring forces during shaking.

Based on peak structural response comparisons between RSA, numerical time integration, and fixed-base centrifuge data, it was shown that implementing RSA during early-stage design of structures with oil dampers can result in acceptable, albeit, conservative estimates of peak inter-storey drifts and velocities. Designers should be cautioned that the extent of this conservatism seems to worsen the more the predicted ground excitations at a site trigger resonance in the damped structure.

With regards to peak floor acceleration predictions, i.e. storey shear forces used in structural member sizing, designers are advised to resort to lumped-parameter models solved numerically in the time domain, rather than RSA. This is mainly due to the ability of the numerical models to account for damping-stiffness force superpositioning in the structure during shaking. This was shown to be a much better approach to predict experimental storey shear forces, rather than relying on empirically-derived combination factors (CF), to estimate maximum accelerations from pseudo-accelerations for structures with high damping.

Even with highly idealised structural models, and low-fidelity dashpot constitutive equations, direct time-integration presents a more elegant approach for the preliminary analysis of structures with oil dampers, compared to the simplified RSA procedure currently implemented in industry guidelines.

Chapter 5

Soil-Structure System Response

5.1 Introduction

In the event of an earthquake, lateral force resisting frames in structures resist seismic inertial loads, and provide safe continuous load paths down to the foundation systems. Foundations, in turn, are required to safely mobilise reaction forces from the surrounding soil to ensure global system equilibrium. The extent to which this inertial interaction at the foundation-soil interface affects the dynamic response of a superstructure depends on several key factors:

1. **Stiffness contrast** between the superstructure and the subsoil beneath its foundations
2. **Aspect ratio** of the superstructure and its inherent tendency to rock during shaking
3. **Foundation bearing pressures** and the associated stress-states induced in the soil

This chapter uses experimental observations from centrifuge testing to investigate how these aforementioned factors impact the seismic response of bare and damped frames during ground excitation. The experimental programme consists of sixteen centrifuge tests classified into two subsets; one set for the tall model frames, and another set for the squat structures. In each series of tests, the model frames are tested with three different base fixity conditions: fixed-base, embedded into dry dense and dry loose sand beds.

For each of the sand cases, the frames are tested with two different foundation bearing pressures: ≈ 40 *kPa* and ≈ 75 *kPa*. Supplemental data was also collected for the seismic response of the damped squat frame with different damping levels (using dampers D1, D2, D3, and D4). Even though these tests are not exhaustive in nature, they provide a unique insight into how different damping levels in the superstructure impact inertial interaction at the foundation-soil interface.

The discussions presented herein focus primarily on the total soil-structure system response, utilising data either measured directly or derived from MEMS accelerometers attached to the model frames in the centrifuge. Figure 5.1 defines the positive sign convention that will be adopted for displacements, velocities, accelerations and floor inertial loading. Foundation accelerations recorded experimentally ($\ddot{u}_f$) are absolute quantities that take into account both ground accelerations ($\ddot{u}_g$), as well as any relative sliding that may occur between the raft and the subsoil ($\ddot{u}_r$). In this investigation, it is assumed that the passive resistance of sand onto the side-walls of the embedded raft, and the foundation interface friction with the subsoil, are sufficient to minimise any global sliding. As such, ground acceleration at the foundation level ($\ddot{u}_g$), and foundation acceleration ($\ddot{u}_f$), are assumed to be equal. Foundation rotational accelerations ($\ddot{\theta}$) are computed using a pair of vertical MEMS accelerometers, ($\ddot{v}_1$) and ($\ddot{v}_2$), located on either sides of the foundation. Rotations and rotational accelerations are taken as the difference in vertical measurements on either side of the foundation divided by the foundation width (L).

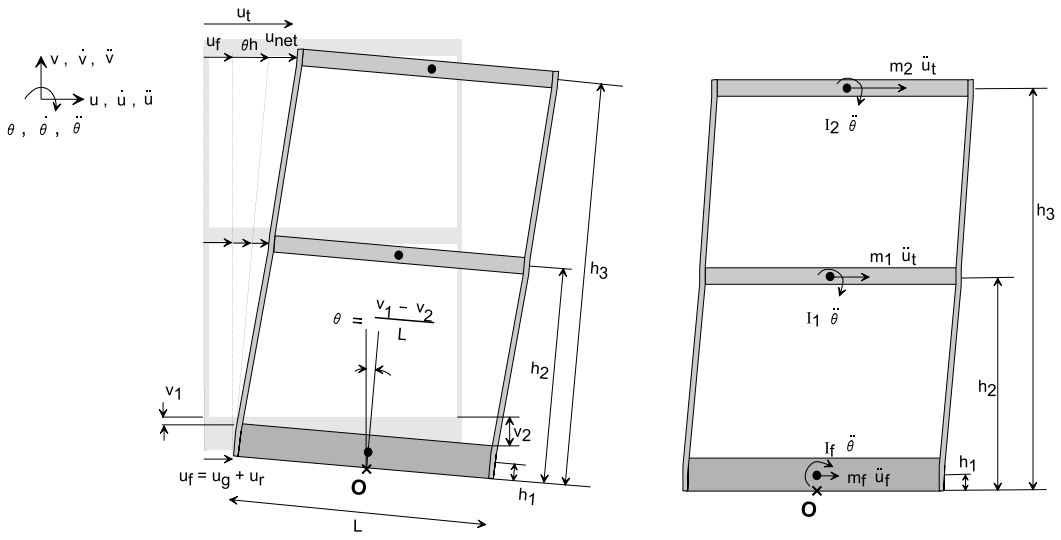

Fig. 5.1 Definition of positive sign convention for displacements, velocities, accelerations and inertial loading on a model frame.

It is important to highlight that the experimental nature of this study imposed physical limits on the possible range of parameters which can be investigated for each of the three soil-structure-interaction (SSI) factors identified earlier. For instance, only flexible structures (with fundamental periods close to 1.2 s prototype) were tested in the centrifuge; this ensured that storey drifts would be large enough at model scale to trigger relative motion between the damper ends during shaking. As a result, the stiffness contrast in this investigation is limited to what could be attained between flexible model frames, and dry sand beds of different relative densities. Notwithstanding this, concurrent dynamic testing of bare and damped

frames in the centrifuge provides a unique opportunity to compare natural energy dissipation levels at the foundation-soil interface, to those engineered into the superstructure by means of supplemental damping devices.

5.2 Sand-bed Characterisation

A total of eleven dry sand beds have been prepared for centrifuge testing following the procedures described in section 3.5.2 of Chapter 3; six of these tests consisted of packages with uniform dry dense sand, and five with uniform dry loose sand. Figure 5.2 reports the relative densities achieved for the dense and loose dry sand beds being investigated. Automated air-pluviation is shown to produce fairly consistent sand densities, given the measurement accuracies associated with computing volume of sand pour. For the purpose of this investigation, the term "Dense" and "Loose" will be used to refer to each category of sand beds.

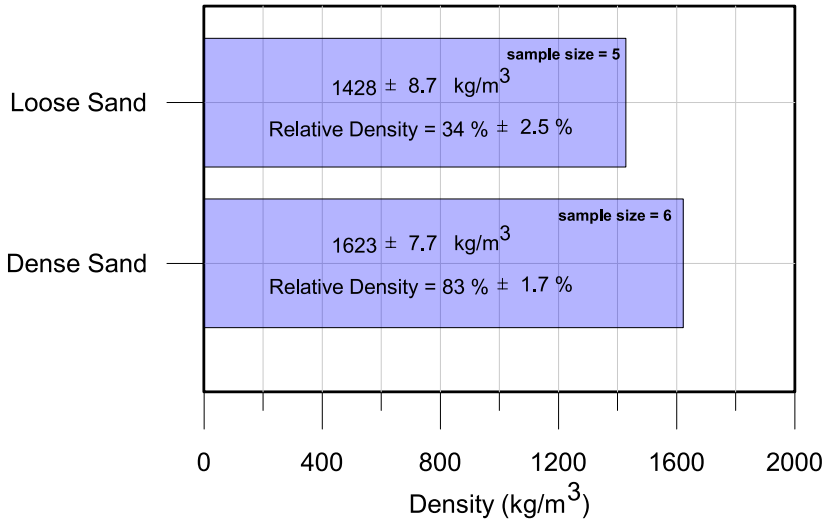

Fig. 5.2 Average densities of dense and loose sand prepared for dynamic centrifuge testing.

Piezo-electric accelerometers and air hammer instrumentation in the sand can be used to measure shear wave velocities and small-strain stiffness at specific points along the vertical sand bed profile. During flight, an air hammer is activated to trigger pulse-like horizontally polarised vertically propagating shear waves from the bottom of the sand profile up to the surface. An array of accelerometers above the air hammer device pick this signal up as shown in Figure 5.3.

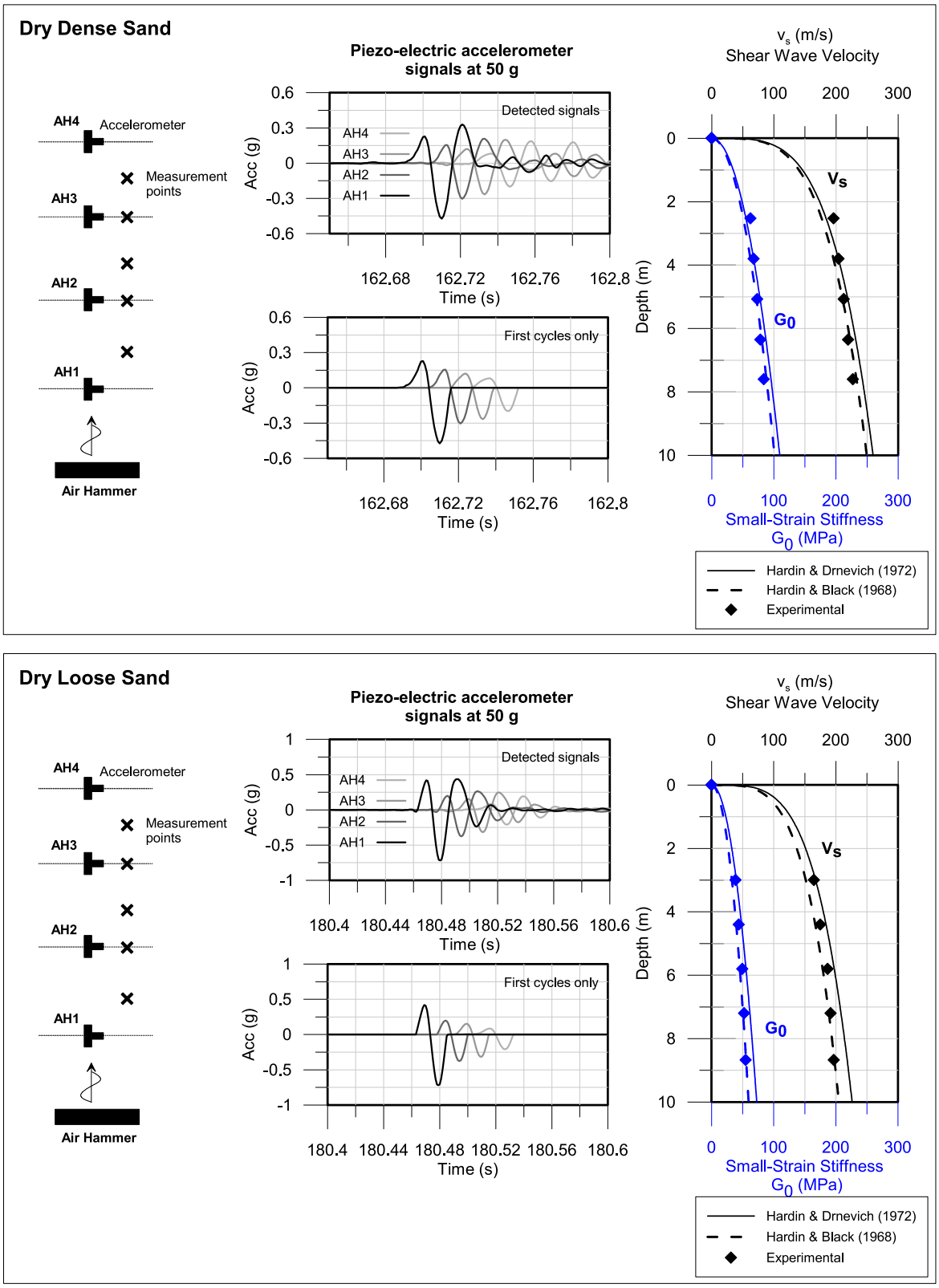

Fig. 5.3 Experimental shear wave velocity and small-strain stiffness measurements from air hammer testing.

For the purpose of computing experimental shear wave velocity profiles, the first cycles of signal arrival are isolated for each accelerometer, then the cross-correlation of each signal with respect to the traces from its neighbouring accelerometers is computed to identify signal time lag. This lag is the time required for the shear wave to travel the distance between two piezo-electric accelerometers.

With records of instrument depths measured during pouring, the distance between accelerometers can be divided by this time lag to evaluate shear wave velocity of sand in between the two accelerometers. With multiple instruments in the array, experimental data points of shear wave velocity and small-strain stiffness can be extracted and plotted as shown in Figure 5.3. The experimental data points lie within theoretical predictions set forth by Hardin & Drnevich (1972) and Hardin & Black (1968).

Figure 5.4 demonstrates the level of input acceleration amplification that was recorded within the dry sand-bed profiles, as the SH waves vertically propagate from bedrock up to the surface. Experimental transfer functions derived for the dense and loose sand profiles in Figure 5.4, point to a soil column fundamental frequency of approximately 5 Hz; this is close to the theoretical estimate of 4.3 Hz for an 11 m deep soil column, with an average shear wave velocity of 190 m/s. The testing condition recreated in this study is therefore one where the ground (fundamental frequency $\approx$ 5 Hz) being shaken is stiffer than the supported structures (fundamental frequency $\approx$ 0.8 Hz).

As depicted by the transfer functions in Figure 5.4, frequencies less than 4 Hz in the bedrock acceleration signals see limited amplification. However, if a considerable portion of the input motion intensity is focused within that frequency bandwidth, the limited amplification can become noticeable in the near surface acceleration traces. Frequencies close to 5 Hz will be amplified considerably by the dry sand-beds during shaking. This was not a problem here as these frequency components appear to be weak for the input motions tested in this study. The absence of pore-pressures, and their associated impact on effective stresses in the soil, prevents the base excitations used in this study from provoking considerable soil nonlinearity that would otherwise cause attenuation, rather than the amplification, observed in Figure 5.4.

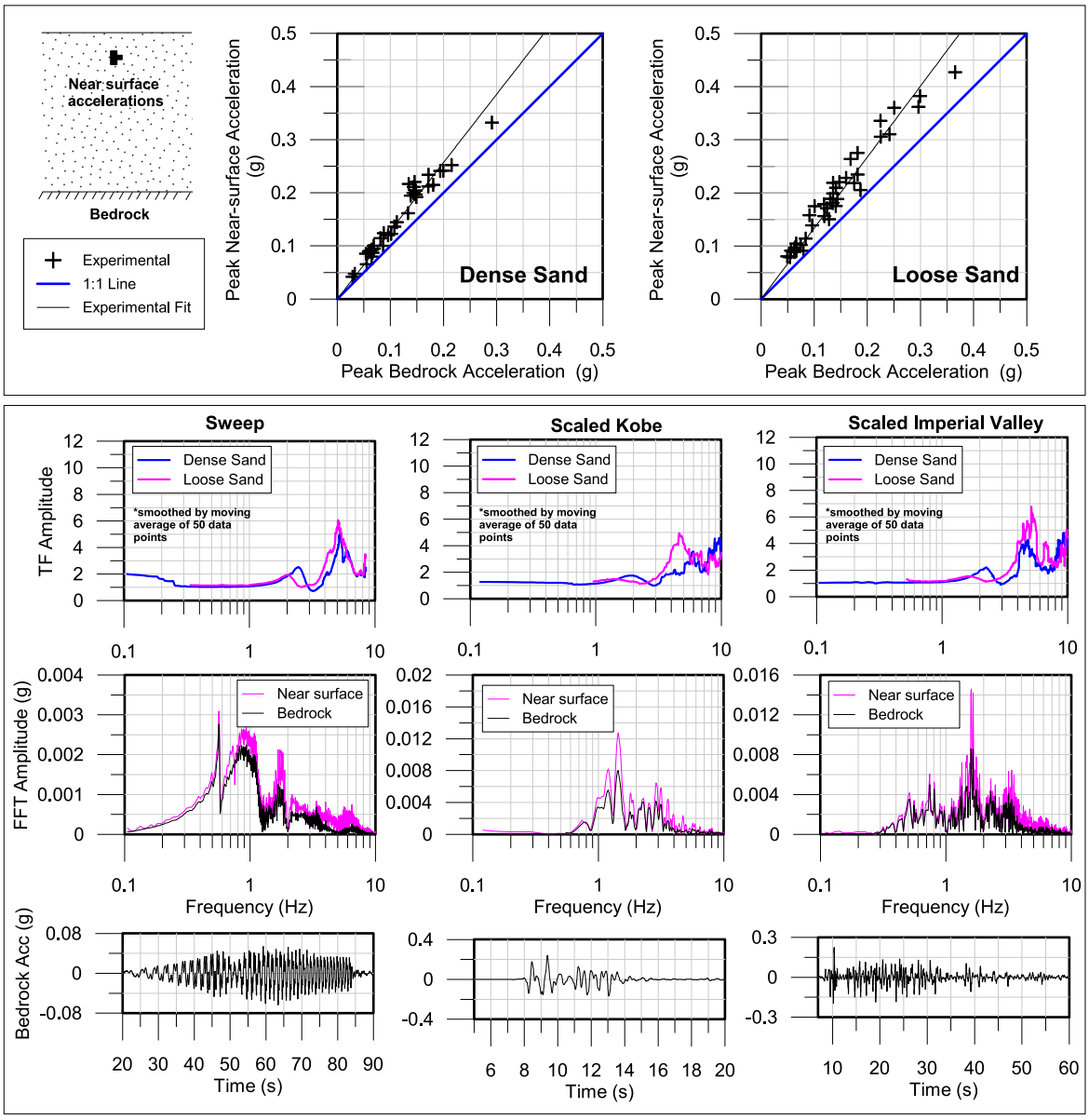

Fig. 5.4 Bedrock acceleration transmission and amplification in dry dense and loose sand.

5.3 System Transfer Functions

The release of foundation kinematic restraints during soil-structure interaction introduces additional global degrees-of-freedom into the problem, thus reducing the fundamental frequency of the system relative to fixed-base. In addition to period elongation, inertial interaction increases damping in the overall system via geometrical and material nonlinearities at the foundation-soil interface.

To investigate this experimentally, transfer functions were produced for the squat and tall model frames, for different base fixity conditions and foundation bearing pressures, during a weak 0 Hz to 1.2 Hz sine-sweep base excitation (peak foundation acceleration of $\approx 0.09\ g$). Results are presented in Figure 5.5.

To estimate experimental transfer functions for each test, foundation input accelerations and second storey output accelerations were first transformed from the time domain to the frequency domain using the Fast-Fourier-Transfrom (FFT) algoritm in MATLAB. The ratio of the complex-valued output FFT to the input FFT is then evaluated for each centrifuge test. For the bare regular frames, the transfer functions are taken as the magnitude of the resulting complex-valued ratios, and are plotted directly in Figure 5.5.

Transmissibility functions for the damped squat and tall model structures, on the other hand, had to be numerically smoothed by a moving average window of 4 data points, prior to plotting in Figure 5.5. This was deemed necessary as the transfer functions of damped structures exhibited spurious spikes at random frequencies; these peaks are not characteristic of the soil-structure systems, but rather a consequence of dividing by a small denominator when evaluating the output-to-input FFT ratios.

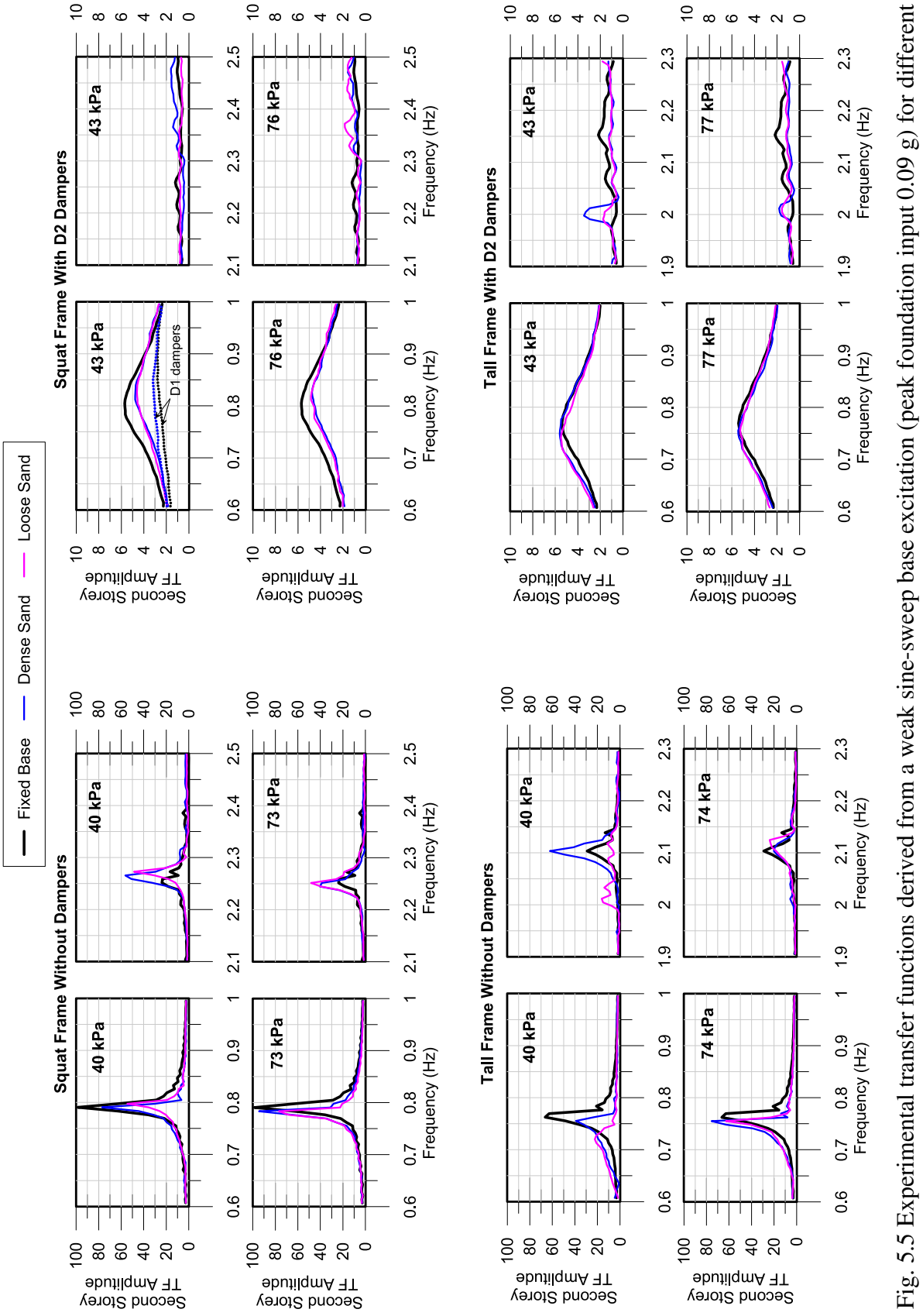

Fig. 5.5 Experimental transfer functions derived from a weak sine-sweep base excitation (peak foundation input 0.09 g) for different sand densities and foundation bearing pressure cases.

Transfer function plots for the regular squat and tall frames in Figure 5.5 demonstrate clearly how frame aspect ratio can influence the degree of soil-structure-interaction during dynamic shaking. For low foundation bearing pressures, the tall frame exhibited considerable period elongation and increase in damping levels as ground flexibility increased. This, however, was less prominent for the heavy foundation case. Despite continuing to exhibit reductions in fundamental frequency, amplitudes of the transfer functions for the tall frame with the heavy foundation did not drop as sharply as they did for the light foundation case with increasing base flexibility. This implies that a different mechanism of inertial interaction occurs at the heavy foundation-soil interface, compared to the light bearing pressure case.

Section 5.4 will explore this point further by looking at acceleration time traces of foundation rotations for each bearing pressure case. The tendency of the squat frame to deform more in internal shear rather than global rocking is demonstrated by the consistently higher transfer function amplitudes attained by the soil-structure system when compared to its tall frame counterpart. Even though fundamental period elongation is not as noticeable in the squat frame as it is in the tall frame, inertial interaction at the foundation-soil interface of the squat frame continues to increase system damping as the soil becomes softer.

Transfer function amplitudes for the damped squat and tall structures in Figure 5.5 are almost an order of magnitude lower than their undamped counterparts. Supplemental damping in the frames seems to flatten the shape of the transfer functions, with no distinct peaks to identify precise fundamental frequencies for the dynamic systems being considered. As damping in the superstructure increases, flattening of the transfer function is exacerbated, as demonstrated by the dashed lines in Figure 5.5 for the squat frame with D1 dampers.

Distribution of similar inter-storey oil dampers across both floors of the model frames seems to have suppressed the second mode of the 2-DOF structures. Even more interesting is the nearly identical transfer function plots for the damped frames on dense sand and loose sand in Figure 5.5. For the weak broad frequency spectrum excitation being investigated, it is believed that the dampers in the superstructures have considerably reduced seismic actions onto the foundations, to the extent that base flexibility differences between dry dense and loose sand became less consequential.

5.4 Absolute Floor Accelerations

Near resonant frequency excitations

Seismic over-turning demands on the foundation of a flexible structure correlate directly to the magnitude of floor inertial loads during base excitation. Close to resonance of the soil-structure system, floors in the superstructure experience peak inertial loading which provokes considerable interaction at the foundation-soil interface. Experimental floor acceleration traces normalised by peak foundation input are presented in Figures 5.6 and 5.7 for the case of squat and tall frames, with light foundations, responding to sinusoidal excitations of different intensities.

The effectiveness of floor acceleration control by means of installing supplemental dampers in the superstructure appears to be optimal for the case of frames rigidly fixed at their base. For this level of fixity, during a moderate intensity near resonant frequency motion, the normalised second floor acceleration traces in Figures 5.6 and 5.7 exhibit a 60 % and a 65 % drop in peak accelerations, for the damped squat and tall frames respectively.

During soil-structure interaction with sand beds of different densities, the level of damper control over floor accelerations appears to drop as the sand gets softer. For instance, fitting dampers into the squat frame with a light foundation reduced peak second floor accelerations by 31 % and 17 %, for the dense and loose sand cases respectively. This is to be compared against the 60 % reduction recorded during fixed-base. While these numbers may hint towards a degradation in the level of damper control over floor accelerations for softer ground, the observation is merely the result of significant improvements in the seismic performance of the bare frames during SSI, as shown by the floor amplification traces in Figures 5.6 to 5.8. For moderate and strong intensity excitations, the bare squat and tall frames embedded in dry sands begin to exhibit floor amplification traces that are very close in magnitude to those observed in the damped structures. These findings suggest that the natural energy dissipation due to SSI in these regular frames can be comparable to the supplemental damping invoked in the superstructure by the inter-storey oil dampers.

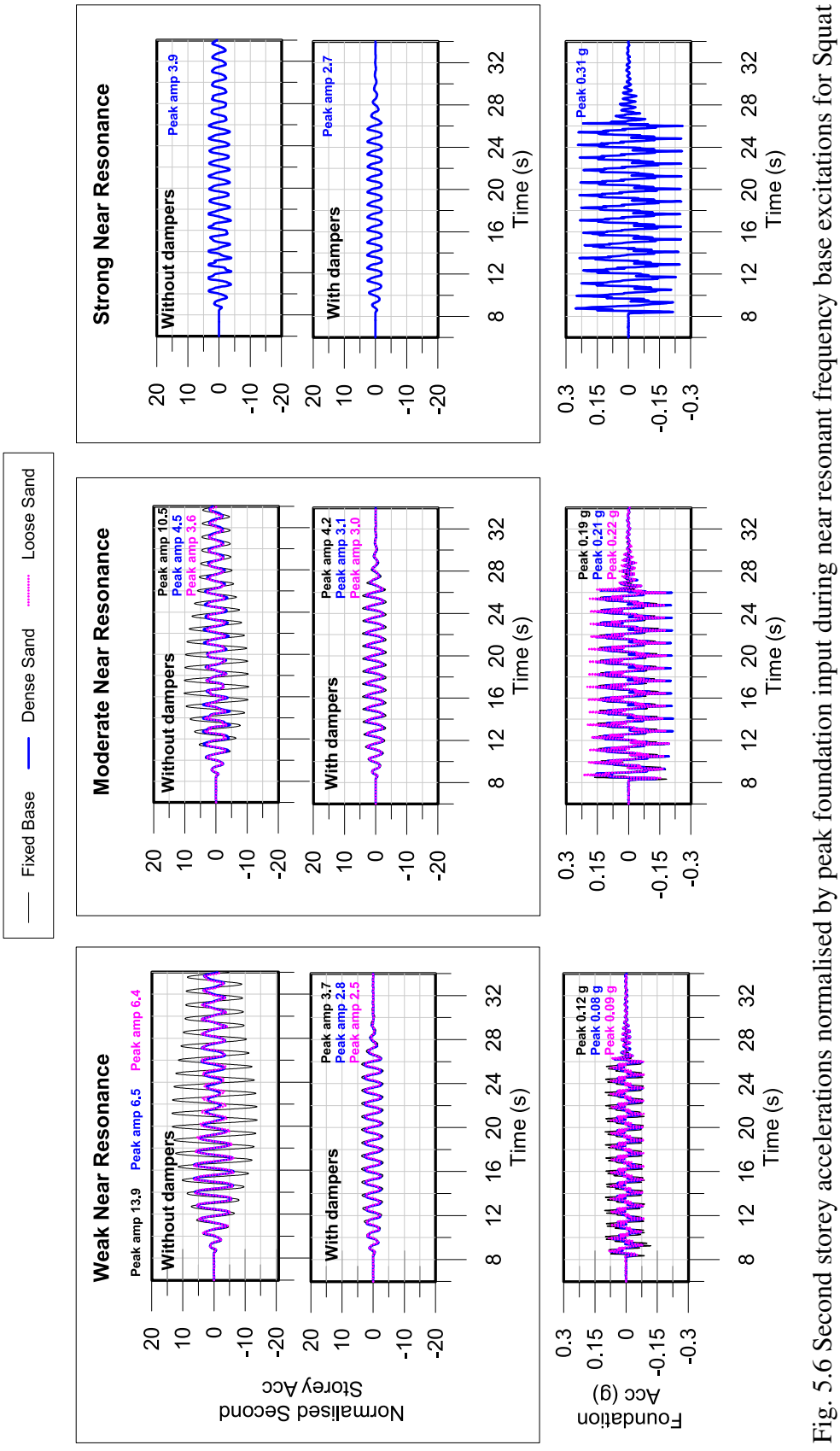

Fig. 5.6 Second storey accelerations normalised by peak foundation input during near resonant frequency base excitations for Squat frames with Light foundations and D2 dampers.

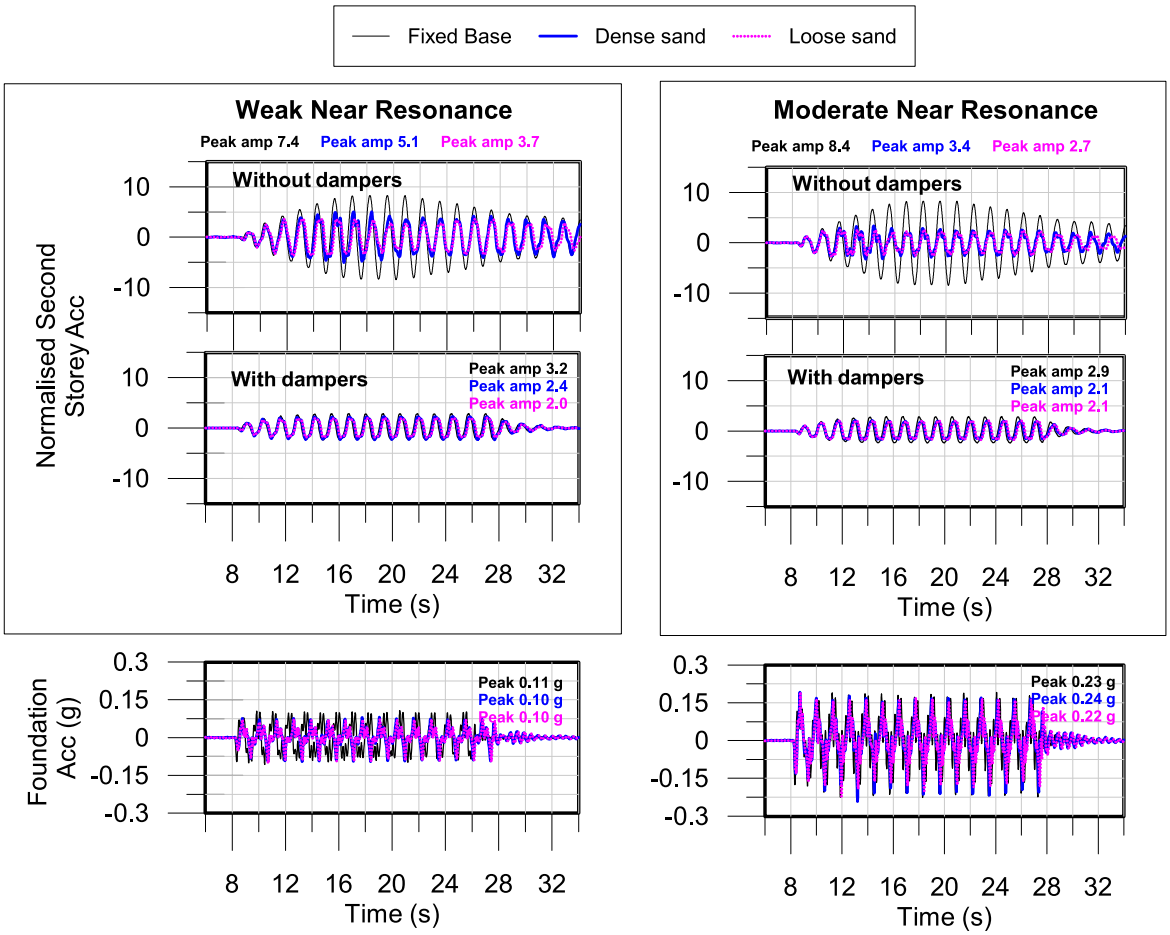

Fig. 5.7 Second storey accelerations normalised by peak foundation input during near resonant frequency base excitations for Tall frames with Light foundations and D2 dampers.

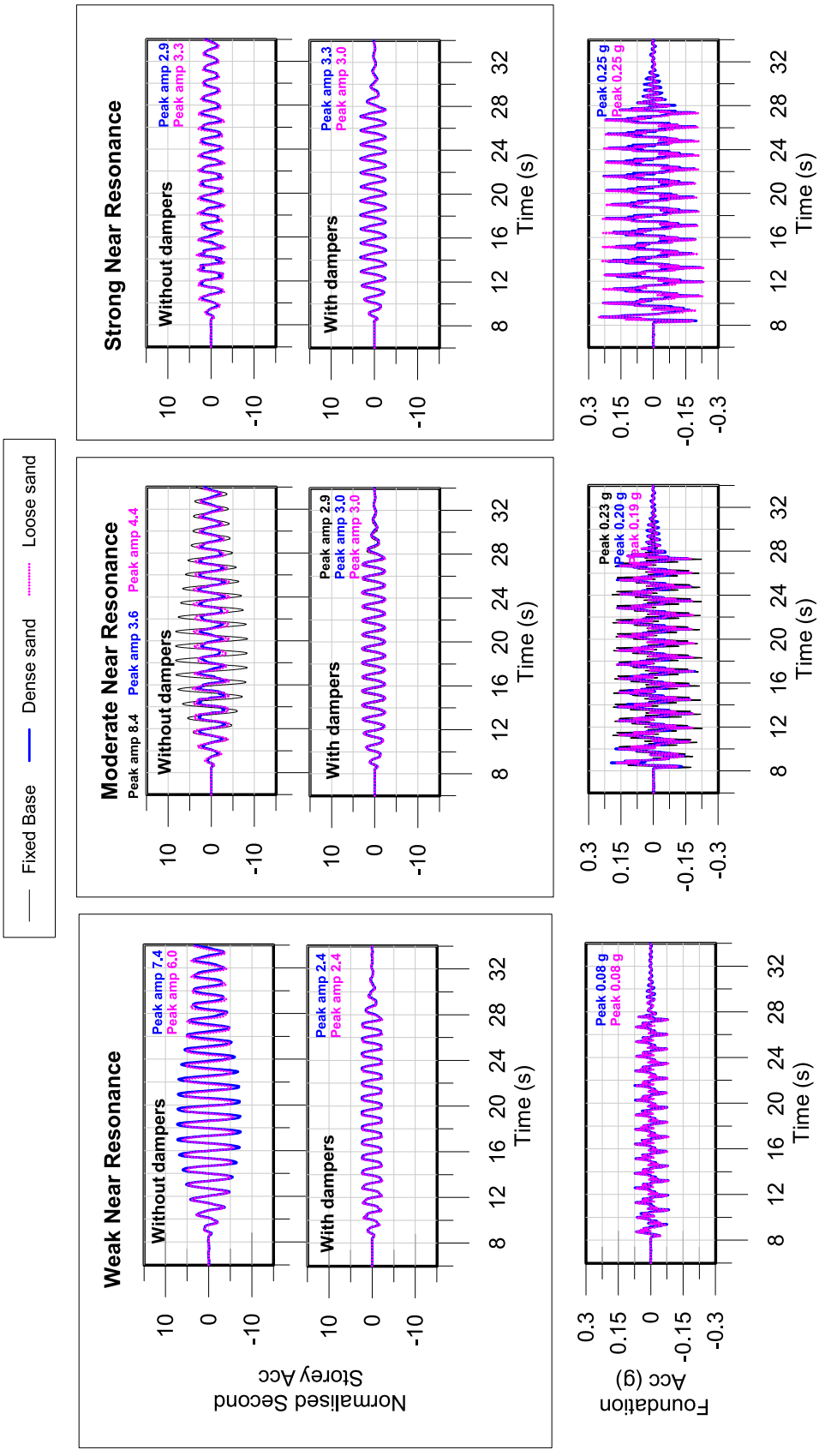

Fig. 5.8 Second storey accelerations normalised by peak foundation input during near resonant frequency base excitations for Tall frames with Heavy foundations and D2 dampers.

Interestingly, floor amplification traces for the damped frames only show marginal reductions in accelerations as base flexibility and input motion intensity are increased. As shown in Figures 5.6 to 5.8, the drops in floor amplifications for the damped structures embedded in sand are small compared to fixed-base, even after doubling the intensity of the input motions. For a regular frame on sand, a big portion of the input energy into the soil-structure system is manifested as rotations and work done by the foundation in shearing the soil beneath. For a damped soil-structure system however, most of the input energy is dissipated by the inter-storey dampers in the superstructure, with little inertial interaction occurring at the foundation. Therefore, even if the input motion intensity is doubled, the additional energy demand on the damped soil-structure system will be mostly dissipated by the inter-storey dampers in the frame, with limited seismic overturning actions transferred to the foundation. As described in Boksmati et al. (2021), and demonstrated in Figures 5.6 to 5.8, floor acceleration amplifications for the damped structures do not appear to be as sensitive to input motion intensity and foundation inertial interaction as they are for regular frames experiencing considerable SSI.

As foundation bearing pressure increases, traces in Figure 5.8 demonstrate an increase in floor acceleration amplification for both, the regular and the damped tall structures. The same trend was also observed for the regular and damped squat frames. To better understand this, foundation rotational acceleration traces are plotted in Figures 5.9 and 5.10, for the tall frames with light and heavy foundations respectively.

For near resonant frequency base excitations on dense sand, the regular tall frame almost always exhibits spikes in rotational acceleration. These distinctive pulses in rotation appear to be asymmetric in nature, and occur once every one cycle of shaking. This behaviour is consistent with foundation uplift and re-impact, which in this case is biased towards one direction of rotation. Similar observations were made on foundation impact by Pelekis et al. (2018). As the foundation begins to partially uplift, contact area with the soil reduces, which in turn increases effective bearing pressure on the soil. The softer the ground beneath the foundation, the more likely the soil would yield and deform in a plastic manner; for soft soils, settlement of the foundation during rotations increases footing contact area with the ground, which in turn limits foundation uplift. This is neatly illustrated in Figures 5.9 and 5.10, in which lower rotational acceleration peaks were measured for the loose sand cases compared to those recorded during the dense sand tests.

For weak near resonant frequency base excitations, increasing foundation bearing pressures have significantly limited foundation uplift on dense sand, and almost completely suppressed it for the loose sand case. This explains the considerable increase in floor amplifications observed in Figure 5.8, compared to the amplifications reported in Figure 5.7.

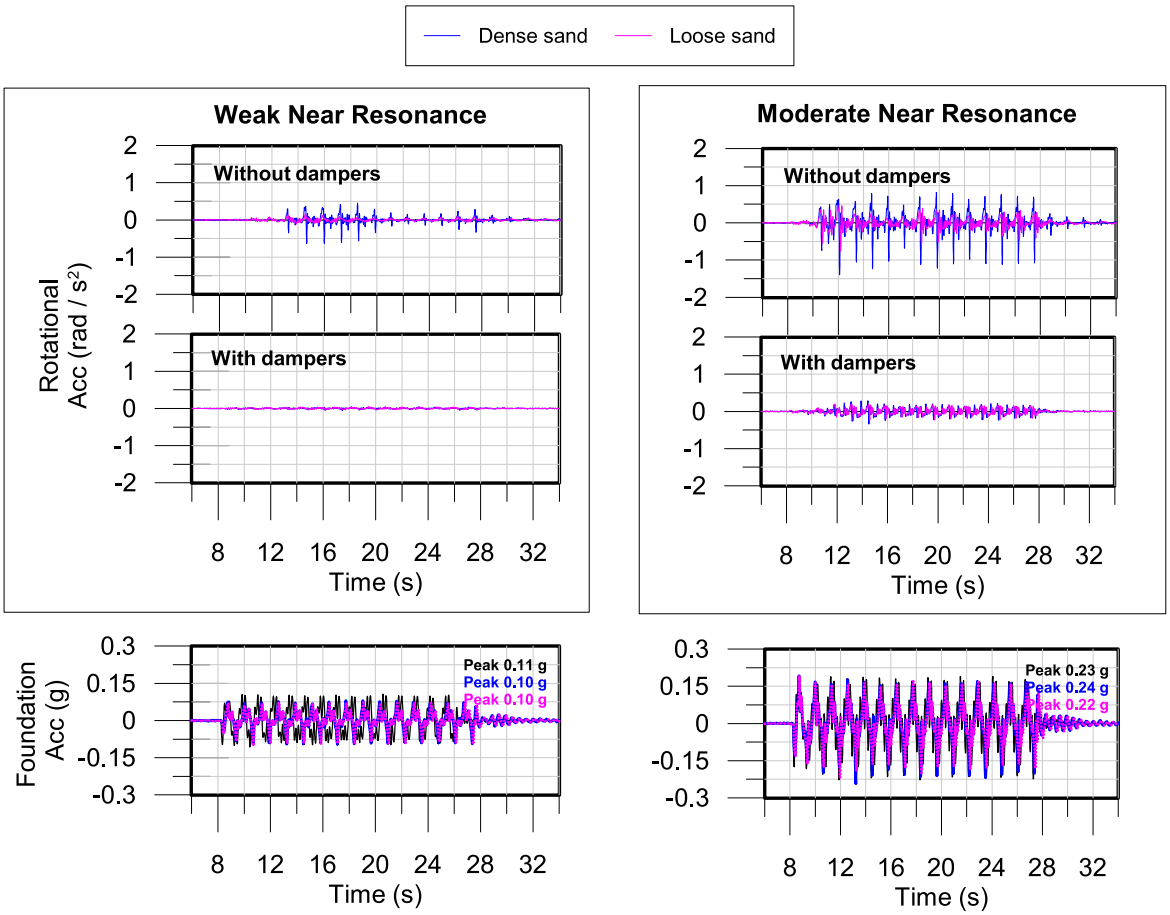

Fig. 5.9 Foundation rotational acceleration traces during near resonant frequency excitations for Tall frames with Light foundations and D2 dampers.

The rotational acceleration response of the tall damped structure in Figures 5.9 and 5.10 is very small compared to its bare frame counterpart. Even for moderate to strong near resonant frequency input motions, inertial interaction at the foundation is shown to be very limited, and less sensitive to variations in soil stiffness and input motion intensity. The same was observed for the damped squat structure.

While regular frames utilise inertial interaction with the soil to naturally dissipate energy during shaking, it appears that the installation of inter-storey oil dampers into the superstructure comes at a cost to this free dissipative interaction at the foundation. This, however, is not necessarily an impediment. In some instances, regular frames cannot invoke sufficient SSI to attain the desired energy dissipation levels from the soil-structure system. In these occasions, oil dampers in the superstructure would be capable of delivering a consistently controlled response over a wide range of input motion intensities and ground conditions.

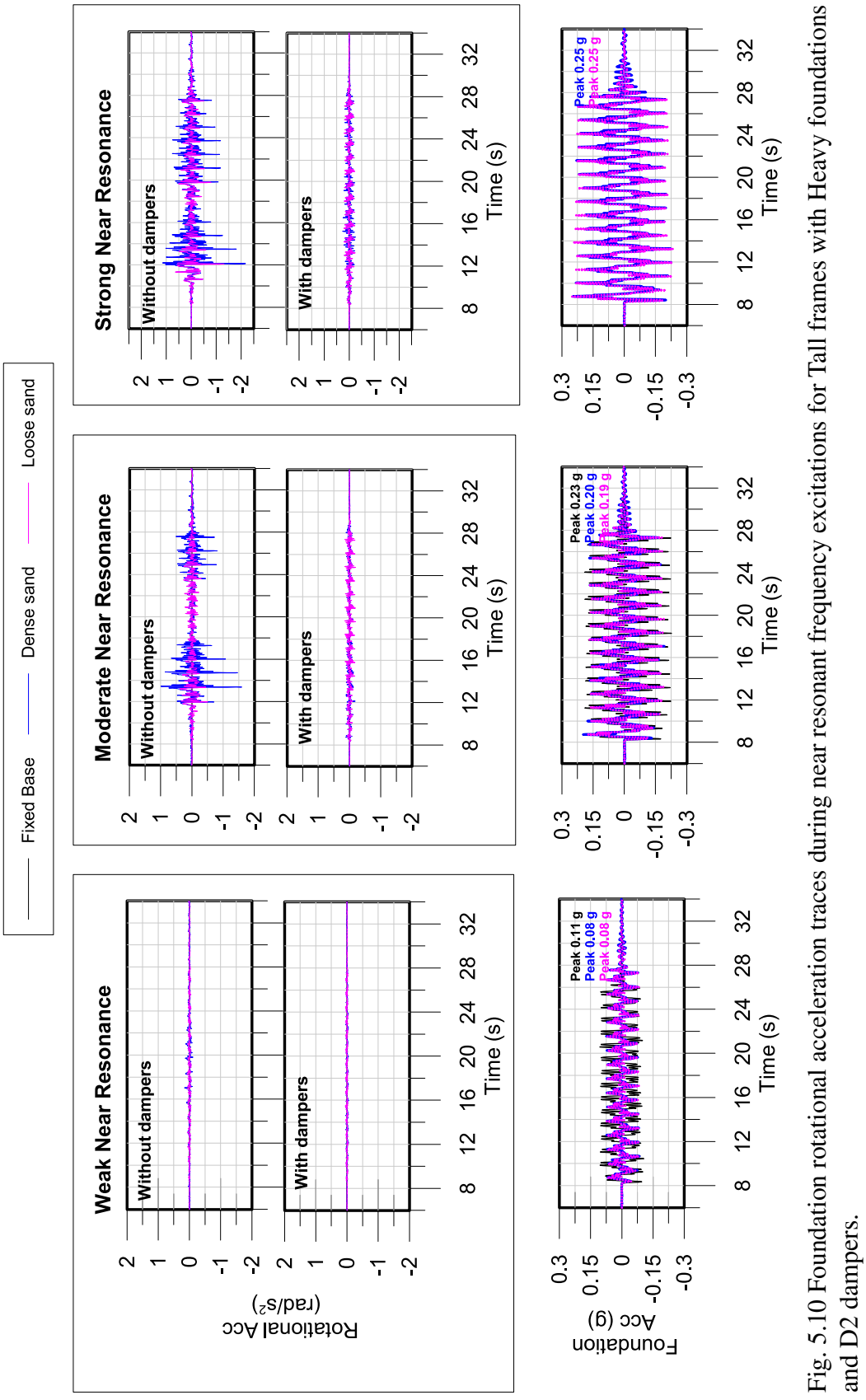

Fig. 5.10 Foundation rotational acceleration traces during near resonant frequency excitations for Tall frames with Heavy foundations and D2 dampers.

Figure 5.11 presents floor accelerations and foundation rotational accelerations recorded while driving the soil-structure systems at frequencies close to the second natural frequency of the bare frames; the experimental traces are for the case of squat and tall structures with heavy foundations embedded in sands of different relative densities.

As previously illustrated by the experimental transfer function plots in Figure 5.5, the addition of similar dampers across both floors of the structures suppressed the second mode of the frames. As shown in Figure 5.11, while the bare squat and tall structures enter a resonant response during shaking, the damped frames recorded approximately 15 % of the bare frame floor accelerations; the damped structures responded as equivalent SDOF systems.

While inertial interaction of the damped frames was limited for the case of excitations near the fundamental frequency of the structures, foundation rotational accelerations for the damped frames now become comparable in magnitude to those exhibited by the regular structures. Plots of foundation rotational accelerations for the squat and tall structures are superimposed over traces of foundation input accelerations in Figure 5.11. The time traces reveal that the rotational accelerations are in-phase with foundation input, implying an almost rigid-body type rocking response that is more prominent in the damped frames during this high frequency shaking.

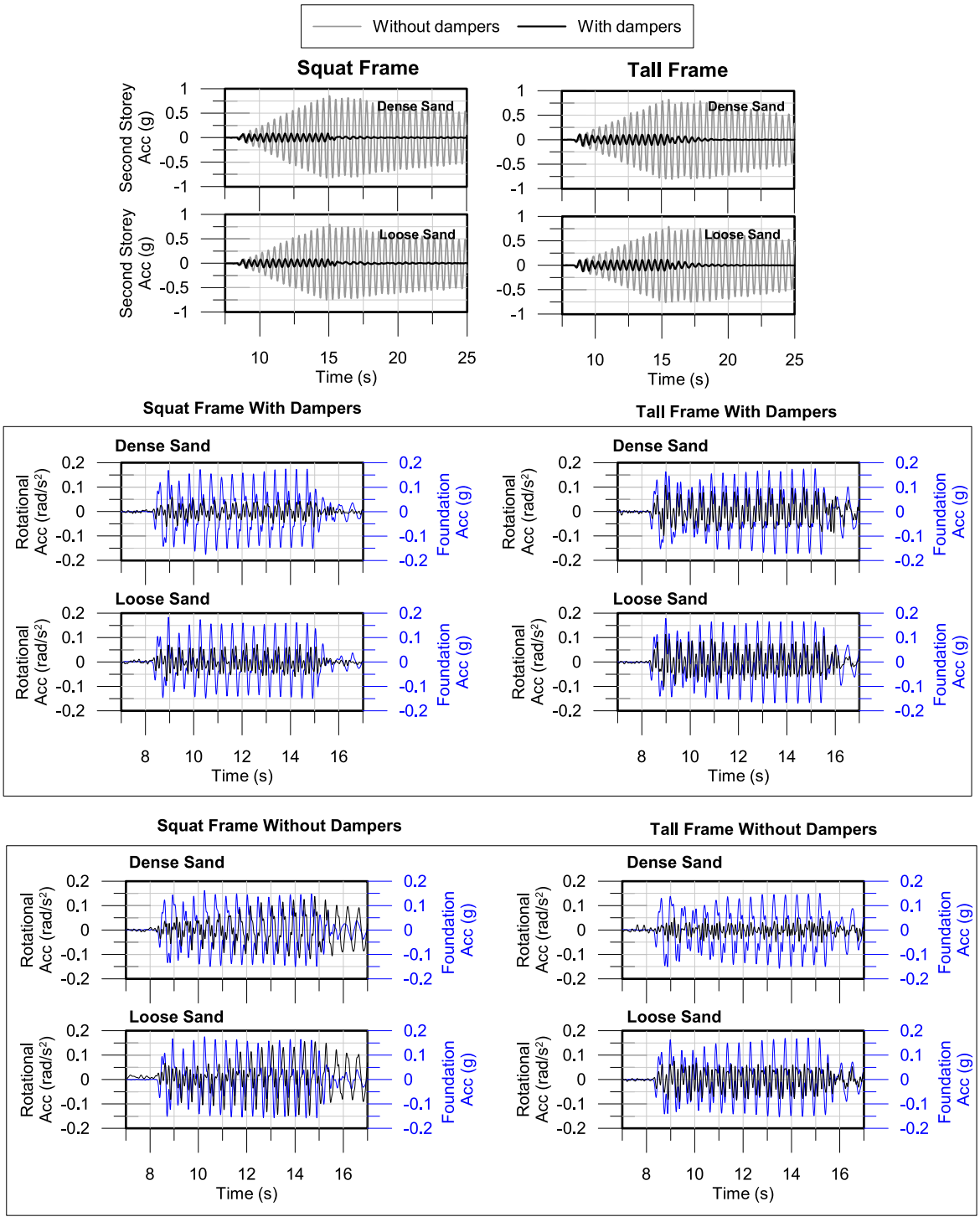

Fig. 5.11 Second storey accelerations and foundation rotational accelerations for Squat and Tall structures during a sinusoidal base excitation close to Mode 2 of the frames.

Multi-frequency component excitations

Whilst sinusoidal base motions at selected frequencies help investigate specific aspects of a dynamic problem, it is important to study the performance of the model frames during realistic multi-frequency component excitations. Second floor acceleration traces normalised to peak foundation inputs are presented in Figure 5.12 for the case of the tall frames with heavy foundations embedded in loose sand. Floor amplification traces exhibited by the frames during full base fixity are included for comparison.

The dynamic response of the frames is compared for three distinct types of input motions: (1) a weak sine-sweep excitation with energy in the signal focused around the fundamental frequency of the structures (2) a scaled Kobe motion with short consecutive velocity pulses, and (3) a scaled Imperial Valley motion characterised by high frequencies and long duration. For all of the broad-frequency spectrum input motions fired in this study, the addition of inter-storey oil dampers to the superstructures improved the seismic performance of the frames, even with inertial interaction at the foundation-soil interface. Nevertheless, the extent of this improvement does depend on the characteristics of the input motion .

For cases where the predicted ground accelerations at a site can trigger resonance in the superstructure, inertial interaction at the foundation-soil interface of a regular frame can be considerable enough to limit floor accelerations. This is neatly demonstrated in Figure 5.12 for the weak sine-sweep excitation; results from the sinusoidal motions in Figure 5.8 point to the likelihood of a much greater convergence in floor accelerations between the regular frame and the damped frame had the intensity of the sine-sweep been higher.

The beneficial inertial-interaction that the regular frame provokes during shaking appears to diminish once the base excitation stops. As the oil dampers bring the damped frame vibrations to a quick halt, the regular frame enters a long phase of free vibration as shown by the experimental traces in Figure 5.12. Weissman and Prevost (1991) attributed this extended vibration decay to reduced radiation damping at the foundation level, given that the superstructure is more flexible than its supporting soil column.

For excitations such as the scaled Kobe and Imperial Valley records in Figure 5.12, with limited energy contents at the fundamental frequency of the structure, inertial interaction at the foundation-soil interface may not be sufficient enough to be used as a reliable energy dissipation source during shaking. In these instances, resorting to supplemental oil dampers in the superstructure will ensure a consistent improved seismic response, particularly for long multi-cycle excitations such as Imperial Valley.

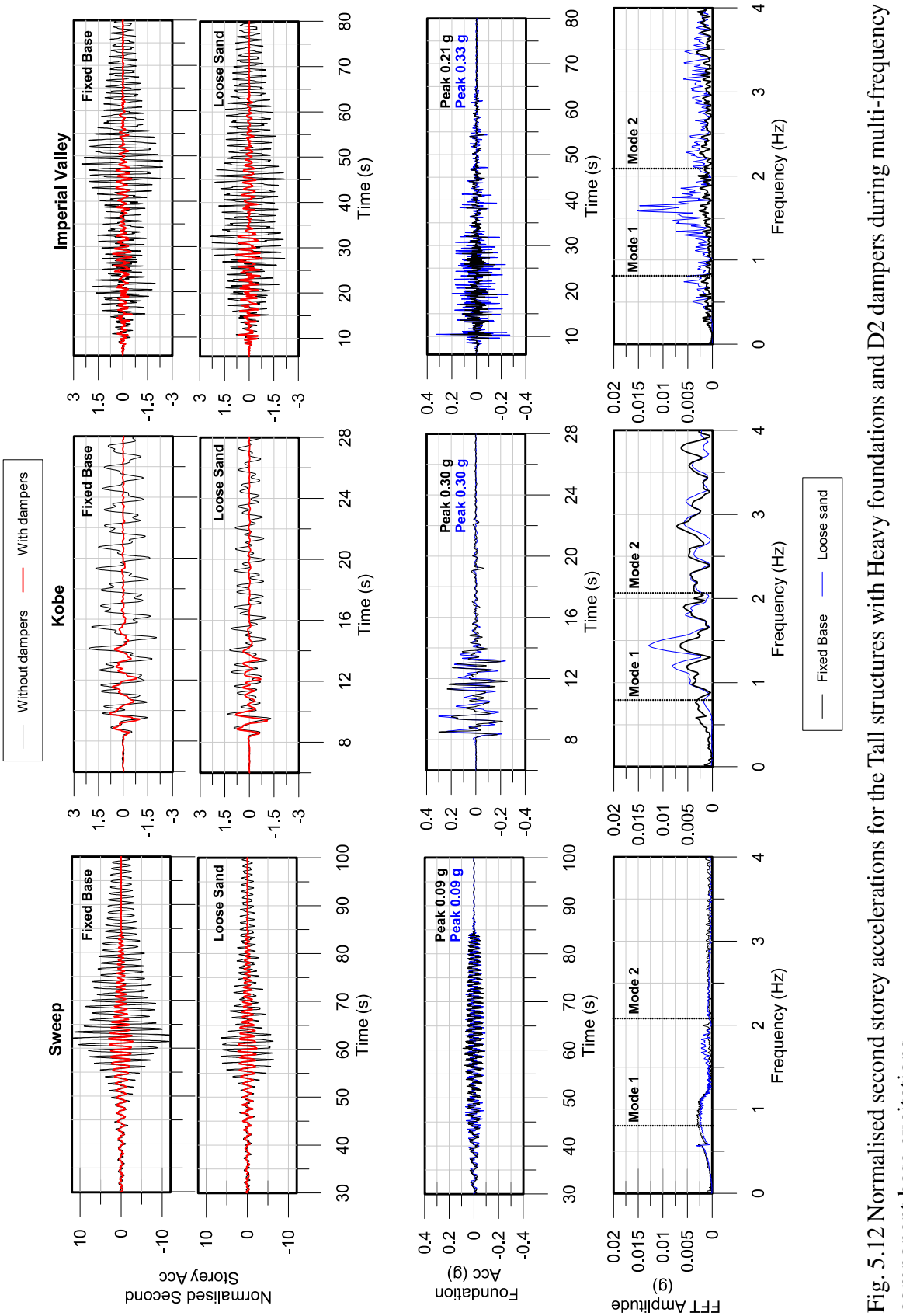

Fig. 5.12 Normalised second storey accelerations for the Tall structures with Heavy foundations and D2 dampers during multi-frequency component base excitations.

Effect of damping levels in the superstructure

As a consequence of early testing of different miniature oil damper configurations in the centrifuge, enough data was collected for a concise investigation into the effects of different supplemental damping levels on the inertial interaction at the foundation-soil interface of a damped frame. Second floor acceleration amplification traces (accelerations normalised to peak foundation inputs) for the damped squat structure fitted with four different damper configurations are presented in Figure 5.13, for the case of a light foundation embedded in dry dense sand.

D3, D2 and D1 are miniature oil dampers type B (with reference to section 3.4.2 of Chapter 3) arranged in order of lowest damping to the highest damping configuration; D4 refers to miniature oil dampers type A, in reference to devices described in section 3.4.1 of Chapter 3. Where available, experimental results recorded during the dense sand tests in black are compared to those recorded during fixed base tests in blue. Any drop in acceleration amplification between these two different base fixity conditions is indicative of the level of inertial interaction that the damped squat structure provokes during shaking.

For the weak near resonant frequency excitation case in Figure 5.13, increasing supplemental damping in the superstructure reduced inertial interaction at the foundation-soil interface, until no discernible differences in amplification between the fixed base case and the dry dense sand case could be identified for the squat frame fitted with D1 dampers. The same trend is observed for the sine-sweep motion. Opting for higher supplemental damping in a structure, although beneficial, does come at a cost to the natural energy dissipation at the foundation-soil interface.

As shaking intensity of the near resonant frequency motion increases from weak to strong in Figure 5.13, floor acceleration amplification traces for the three damper configurations D3, D2 and D1, start to become comparable for the dense sand case (black traces). Out of the three, the damped frame equipped with D3 dampers demonstrated the greatest reduction in floor amplification as input motion intensity increased from weak to strong. This reinforces the conclusion that structures with lower supplemental damping are more likely to utilise foundation-soil nonlinearities during shaking.

For short impulse-type base motions such as the scaled Kobe record, floor acceleration control in Figure 5.13 seems to be less sensitive to damping levels compared to excitations which trigger resonance in the frame. Despite the fact that D1 dampers result in an equivalent damping ratio in the squat frame that is almost 1.5 times that attained with the D2 devices (as demonstrated in section 3.4.2 of Chapter 3), normalised second storey acceleration traces recorded during the scaled Kobe motion only show minor reductions in peak amplification for these strong devices.

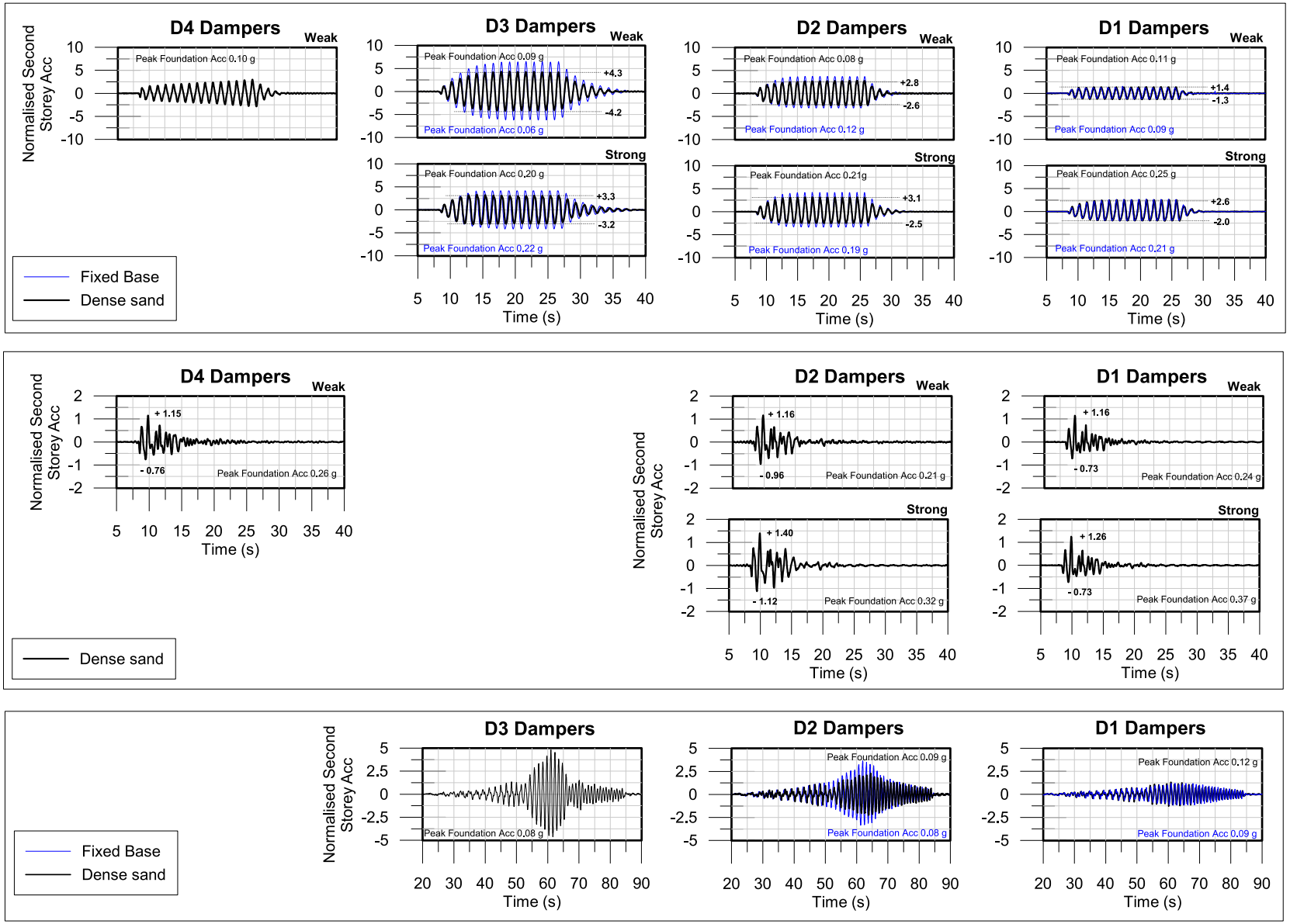

Fig. 5.13 Normalised second storey accelerations for the damped Squat structure with a Light foundation embedded in dry Dense sand with different damper configurations.

5.5 Foundation Moment-Rotation Behaviour

During base excitation of a flexible frame, inertial loads concentrated at the floors of the superstructure exert seismic over-turning moments onto the building's foundation. For the 2-DOF frames in this investigation, total acceleration measurements recorded at each floor are multiplied by the floor lumped mass values prescribed in Chapter 4, to compute floor inertial loads. These forces are then multiplied by the distance from the centre of gravity of each floor to the base of the foundation to evaluate applied moments. Contributions of floor rotational inertia about their respective centres of gravity, although small, are added to the total moments. Mathematically, seismic overturning moments for the 2-DOF structures are given by:

$$M_R = m_f \ddot{u}_f h_f + m_1 \ddot{u}_1 h_1 + m_2 \ddot{u}_2 h_2 + (I_f + I_1 + I_2)\ddot{\theta} \tag{5.1}$$

where $\ddot{u}_f$, $\ddot{u}_1$, and $\ddot{u}_2$ are foundation, first and second floor total accelerations; h_f, h_1, and h_2 are distances from floor centres of gravity to base of foundation; I_f, I_1 and I_2 are foundation and floor mass moments of inertia about their respective centres of gravity; $\ddot{\theta}$ is global frame rotational accelerations.

Figure 5.14 presents experimental moment-rotation plots for the squat and tall structures, both bare and fitted with D2 dampers, embedded in dense and loose sands during moderate near resonant frequency excitations.

Foundation-soil systems for the regular frames with low bearing pressures exhibit considerable nonlinearities with increasing rotations. The "s" shaped hysteresis loops are typical of subsoil yielding with partial uplifting of the foundations during shaking. These mechanisms impose a cap on the maximum over-turning moments that the foundation-soil systems can mobilise. Such a limit on foundation moments is effectively a limit on the maximum floor accelerations that are allowed to develop in the superstructure.

As bearing pressure of the regular squat frame is increased, foundation rotations become dominated by shearing of sand rather than uplift, as evident by the limited flatness in peak moments in Figure 5.14. The tall frame, on the other hand, continues to show plateaus in moment-rotation, albeit at a higher moment threshold. The increase in peak moments reflects the higher mass moment of inertia of the foundation, and the increased stiffness of the foundation-soil systems due to higher confining stresses in the soil. Most importantly, all moment-rotation plots for the bare frames progress in a clockwise manner, implying a phase lag between applied seismic moments and frame rotations. Such behaviour is typical of an energy dissipative response.

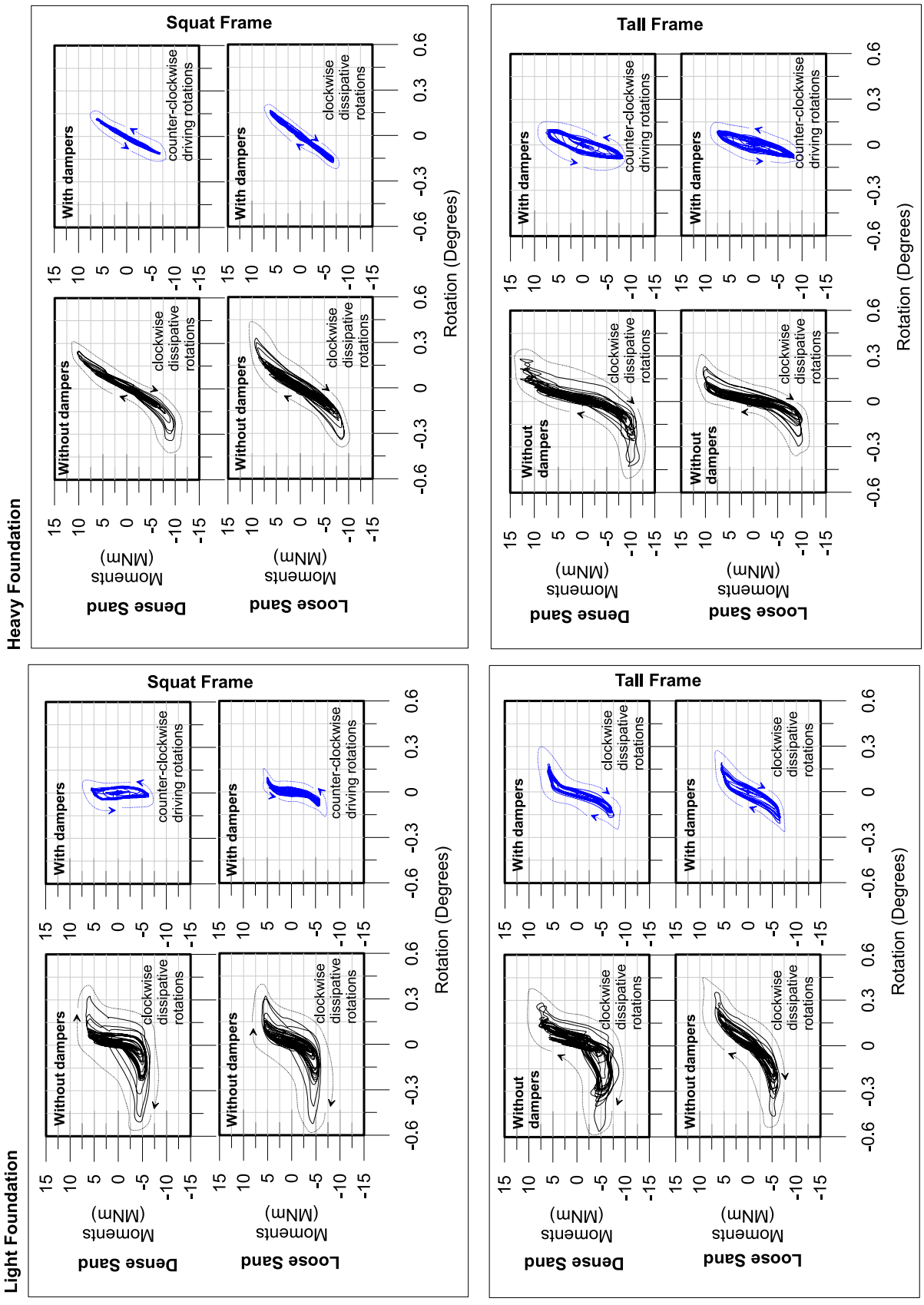

Fig. 5.14 Moment-rotation loops for the model structures during moderate near resonant frequency excitations.

Contrary to expectations, there is experimental evidence of instances of counter-clockwise moment-rotation loops for the damped structures excited close to resonance as shown in Figure 5.14; i.e. foundation rotations in the damped frames sometimes lead moments in time rather than lag behind. In addition to horizontal foundation excitations during ground shaking, such observation points to the existence of an additional component that drives foundation rotations during near resonant frequency shaking of a damped structure. There are three possible sources that can contribute to this anomaly:

1. Built-in filters in the MEMS accelerometers, coupled with band-pass filtering of vertical acceleration data during processing from accelerations to rotations, can have an affect on the instances of zero-crossings in the foundation rotations signal.

2. Three-dimensional effects of raft settlement during shaking can affect vertical acceleration measurements in the experiment, particularly if the rotations of the damped structure are small.

3. Increasing system damping, by installing inter-storey oil dampers in a structure, tends to modify the dynamic response away from that of a typical bare frame structure, when responding close to resonance.

The first two sources are unavoidable due to the nature of the experimental setup and instrumentation used in the centrifuge. Successful application of the data acquisition and filtering processes to the regular bare frames in Figure 5.14 offer a counterargument to the first two points raised above. Nevertheless, it is recognised that there is a measurable reduction in intensity of foundation rotational accelerations between the bare frames and the damped structures, as previously illustrated in Figures 5.9 and 5.10. This does raise some concerns over the quality (i.e. the signal-to-noise ratio) of the vertical acceleration traces recorded for the damped frames, in comparison with those recorded for the regular structures.

Figure 5.15 investigates the third source of this anomaly by overlapping experimental time traces of moments (as defined by Equation 5.1), first storey damper forces, and foundation rotations for the damped structures, during moderate near resonant frequency excitations. For the squat frame embedded in dense sand in Figure 5.15, the higher order effects in rotations are very clear; there are two rotational peaks, a main one in phase with the seismic overturning moments as expected from a flexible structure, and a secondary peak that drives an earlier zero-crossing in the rotational signal compared to the moment trace. This early peak in foundation rotations appears to coincide with the build-up of first storey damper forces as shown by the dashed vertical lines in the zoomed-in plots of Figure 5.15.

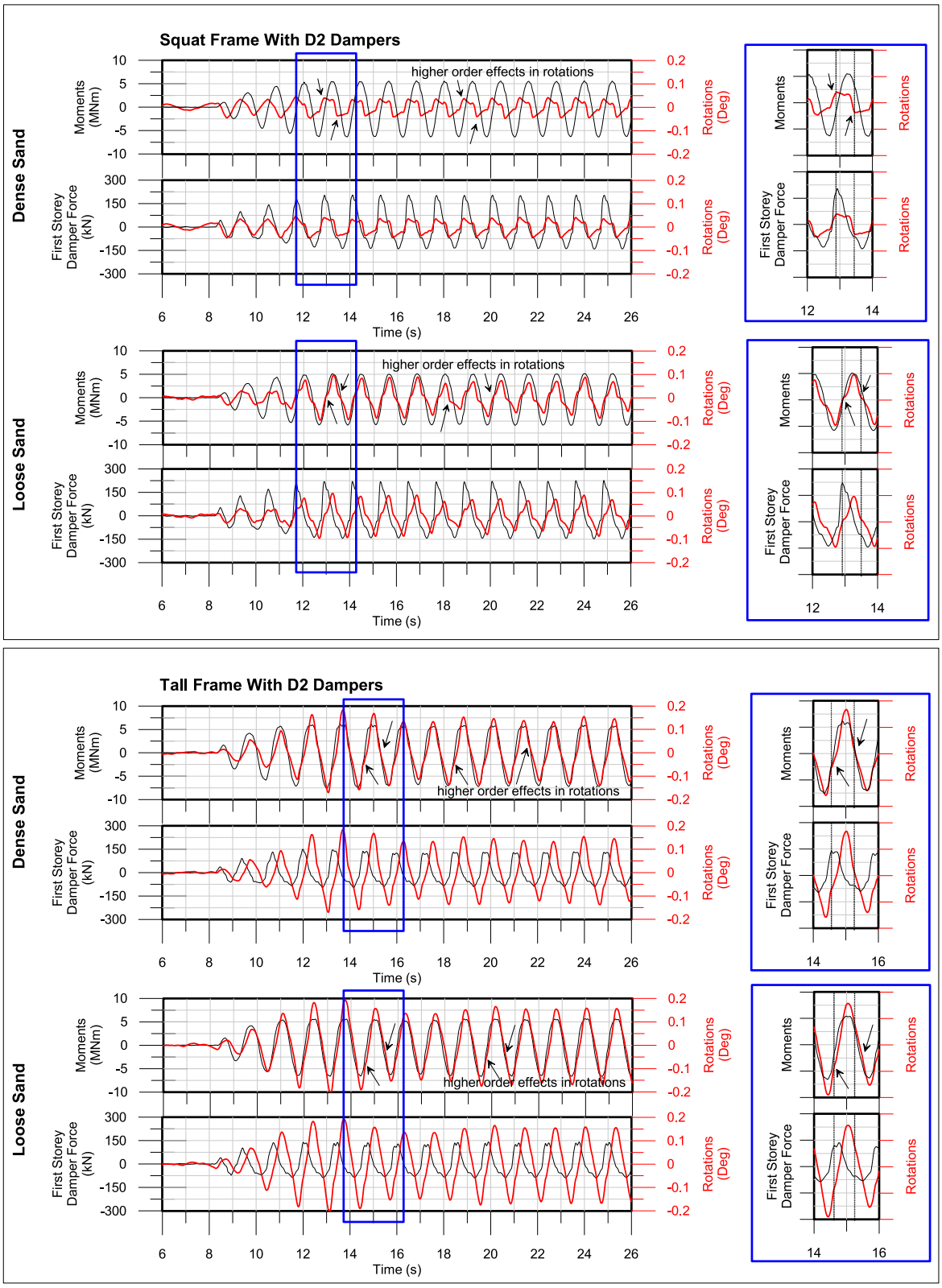

Fig. 5.15 Moments, first storey damper forces, and frame rotations for the damped structures with Light foundations during moderate near resonant frequency excitations.

Upon embedment of the damped squat frame in loose sand, traces in Figure 5.15 show the foundation recording higher peak rotations compared to the dense sand case, implying greater subsoil deformation during shaking. The dominant peaks in foundation rotations are now in-phase with peak moments. However, evidence of higher order effects in foundation rotations continue to exist, and coincide with the build-up of first storey damper forces. Although not as dominant as recorded for the dense sand case, these higher order effects are large enough to drive early zero-crossings of foundation rotations compared to the moments trace, resulting in the counter-clockwise moment-rotation loops observed in Figure 5.14.

As the centre of gravity of the damped structure is increased for the case of the tall frame in Figure 5.15, the foundation experiences even higher peak rotations in-phase with overturning moments. Evidence of higher order effects coinciding with the build-up of first storey damper forces remain visible in the rotational signal, but are not large enough to drive early zero-crossing of foundation rotations. The damped tall structure with a light foundation embedded in dense and loose sand exhibited dissipative clockwise moment-rotation loops in Figure 5.14, similar to its bare-frame counterpart.

Higher order effects observed in the foundation rotational traces plotted in Figure 5.15 hint to the existence of a relationship between the build-up of first storey oil damper forces, and a rotational "driving" component at the foundation of the damped structure for near resonant frequency excitations. Section 6.3 of Chapter 6 will explore this point further, and attribute this foundation rotational driving component to the phase difference recorded between the damped frames' foundations and upper floors during near resonant frequency shaking; increasing supplemental damping of a flexible structure tends to modify the phase difference between its foundation and floors compared to a lightly damped frame, thereby influencing the rotational behaviour of the soil-structure system. The traces in Figure 5.15 demonstrate that the impact of this becomes less prevalent in the moment-rotation behaviour of the damped structure as the foundation deforms more of the soil at peak seismic overturning moments.

A more definitive experimental investigation into the rotational response of oil-damped frames on compliant ground is warranted. Utilisation of modern experimental imaging techniques, such as high-speed camera tracking of dynamic foundation rotations in the centrifuge, can provide useful insights into this problem.

5.6 Summary

Dynamic high gravity centrifuge testing was used to investigate the effects of soil-structure interaction on the seismic performance of damped structures fitted with inter-storey oil dampers. Three parameters were varied in this investigation: (1) frame aspect ratio (2) foundation bearing pressure (3) dry sand relative density. Concurrent dynamic testing of regular 2-DOF structures, and their damped counterparts, revealed the following:

1. From a frequency response perspective, supplemental oil damping in the superstructure has considerably reduced any period elongation effects caused by soil-structure interaction. The overall soil-structure system of a damped frame, whether squat or tall, is less responsive to variations in ground flexibility compared to a regular undamped structure.

2. Oil damper floor acceleration control, measured relative to floor accelerations in regular bare structures, is optimal for fixed-base conditions. Upon shallow embedment into dry sands, the level of damper control over floor accelerations drops considerably, particularly for near resonant frequency excitations. This drop is not due to subpar performance of the oil dampers themselves, but rather due to the beneficial role of SSI (soil-structure-interaction) at limiting floor accelerations in regular frames.

3. Damped frames, both squat and tall, do not exhibit the same reductions in floor accelerations caused by SSI as regular undamped structures would. It appears that supplemental damping in the superstructure comes at a cost to the natural energy dissipation that would normally occur at the foundation-soil interface. Reduction in floor accelerations after damper installation limits overturning actions onto the foundations, and thus limits inertial interaction with the soil during shaking.

4. In the event of strong near-resonant frequency excitations, regular frames can mobilise natural energy dissipation levels at the foundation-soil interface, comparable to the dissipation levels engineered into a frame with inter-storey dampers. Investing in supplemental damping in the superstructure however, ensures consistent floor acceleration control over a wide range of input motion intensities and frequency contents. This is especially important for when regular frames are expected to provoke limited SSI for the ground excitations predicted at a particular site.

5. Experimental results have shown the presence of higher-order effects in foundation rotations of damped structures. These effects appear to be in-phase with the build-up of damper forces in the frame, as the structure responds close to resonance. This led to the assertion that foundation rotations of shallow founded frames equipped with inter-storey oil dampers, responding close to resonance, are in fact a superposition of two components: (1) a driving rotational component attributed to the modified phase difference between the foundation and floors of a flexible structure equipped with high supplemental viscous damping (2) rotations in-phase with floor inertial loading (i.e. seismic overturning moments), similar to what is expected from regular flexible structures.

It is important to highlight that these experimental findings pertain primarily to the combination of model frame stiffness, ground conditions, foundation type, and miniature oil dampers tested in this investigation. Nonetheless, the observations reported in this section are believed to underpin the basis of dynamic soil-structure-interaction of damped structures on flexible ground.

Chapter 6

Seismic Demand on the Superstructures

6.1 Introduction

The overall performance of regular and damped structures, considering dynamic soil-structure interaction, was explored in the previous chapter through examination of total system parameters including absolute floor accelerations, global frame rotations, and foundation moment-rotations. This section will focus more on the superstructure response of the damped and undamped systems, by using key design indicators such as storey shear forces and inter-storey drifts. The performance of inter-storey oil dampers in the damped frames is also examined in greater detail for different frame base fixity conditions. This helps to identify any deviation in damper operations once a frame is founded on flexible ground, compared to a fixed-base condition. Lastly, seismic input energy into soil-structure systems is estimated and tracked, to better understand how energy dissipation and recovery in regular frames compare with those recorded for damped structures on compliant ground.

6.2 Storey Shear and Inter-storey Drifts

Storey shear and inter-storey drift experimental traces are derived using horizontal and vertical acceleration data recorded by MEMS accelerometers fixed to the model structures. Figure 6.1 illustrates the definition of storey shear that will be adopted in this section, along with the equations used to compute inter-storey accelerations and drifts.

Shear forces at every floor, represented by V_2 and V_1 for the second storey shear and base shear respectively, are the product of absolute accelerations ($\ddot{u}_t$) multiplied by the respective floor lumped masses. Inter-storey accelerations are mathematically derived from total floor accelerations, and rotational accelerations, as per the equations stated in Figure 6.1. These

accelerations, following the data processing steps described in section 3.7 of Chapter 3, are then subjected to double-integration and high-pass filtering to evaluate inter-storey velocities and drifts for the linear elastic frames considered in this study.

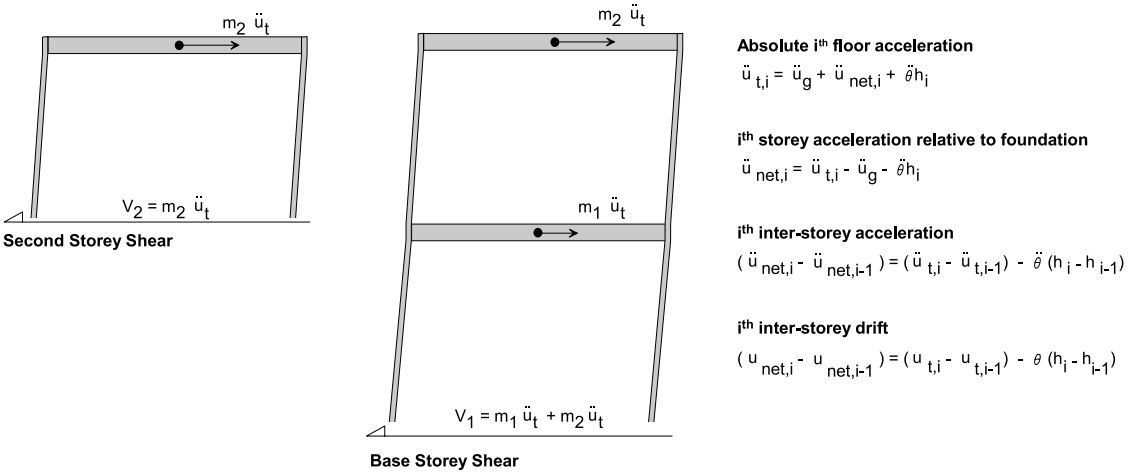

Fig. 6.1 Definition of storey shear and inter-storey drifts from experimental acceleration data.

Multi-frequency component base excitations

Maxima and minima storey shear and storey displacement values are plotted in Figures 6.2 and 6.3 for the cases of the squat frames with light foundations, and tall frames with heavy foundations, experiencing multi-frequency component excitations.

Given the primary operation of oil dampers on inter-storey velocities, the devices are able to limit floor accelerations (i.e. storey shear) and inter-storey drifts simultaneously, thus reducing overall inertial interaction at the foundation-soil interface for the damped structures. This is evident in Figures 6.2 and 6.3 by the limited changes in peak storey shear forces and displacements as base fixity for the damped frames is reduced from fixed base, to shallow embedment into dry loose sands.

The most effective level of damper control over storey shear forces and structural deformations was reported during the scaled Imperial Valley excitations, as shown in Figures 6.2 and 6.3. Such long duration excitations, characterised by a wide frequency bandwidth, are bound to trigger resonant responses in the structures at their natural frequencies, yet have limited energy contents at the fundamental frequency for the regular frames to capitalise on dynamic SSI. For the regular bare frames in Figures 6.2 and 6.3, this implies contributions to the total dynamic response from both, the first and the second mode, resulting in comparatively high peak storey shear forces and drifts. On the other hand, a cyclic response at the fundamental mode for the damped structures, over the long duration Imperial Valley excitations, presents

an ideal condition for the operation of the viscous oil dampers, resulting in the tangible reductions reported in Figures 6.2 and 6.3.

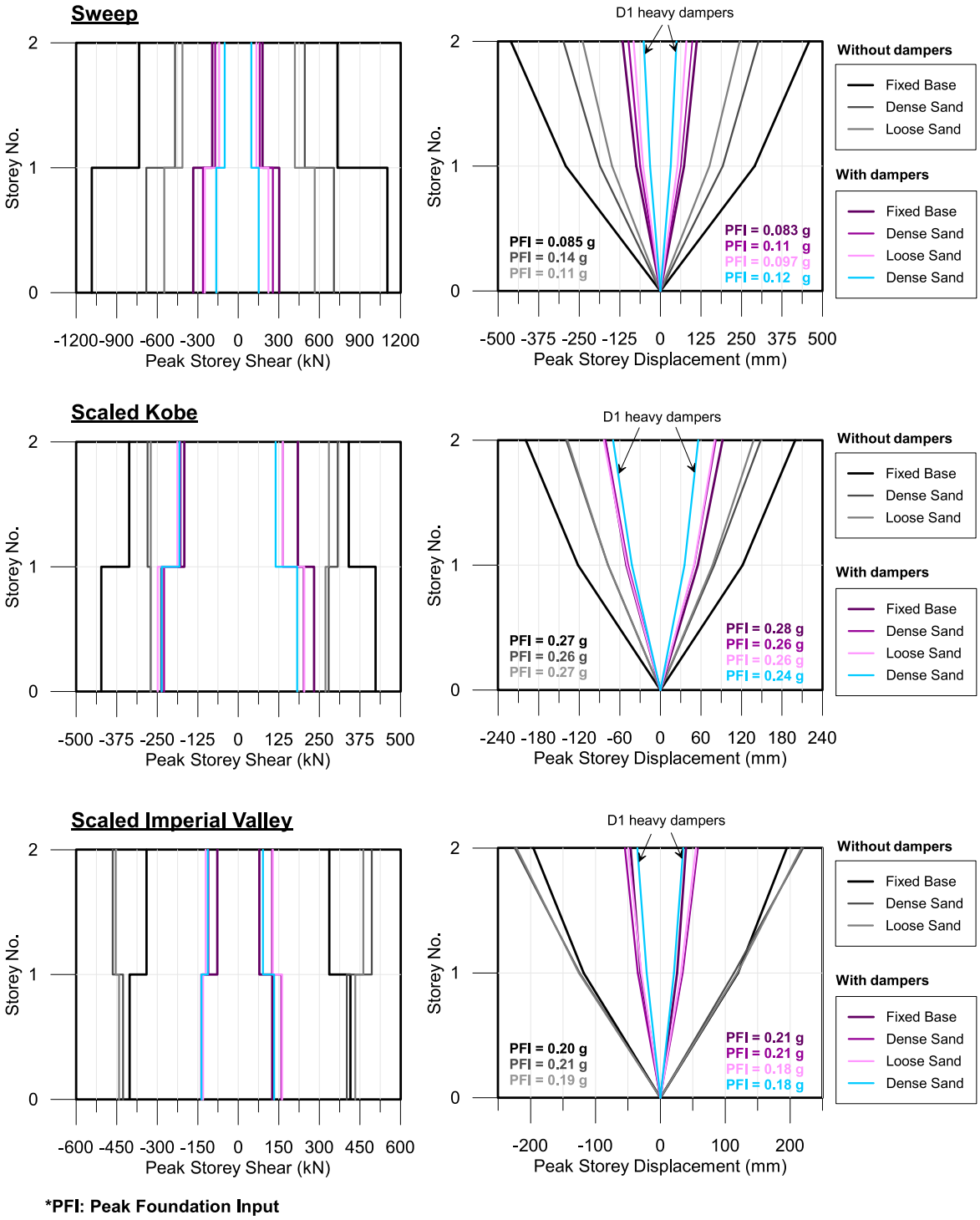

***PFI: Peak Foundation Input**

Fig. 6.2 Peak storey shear forces and storey displacements during sine-sweep and scaled realistic excitations for Squat frames with Light foundations and D2 dampers.

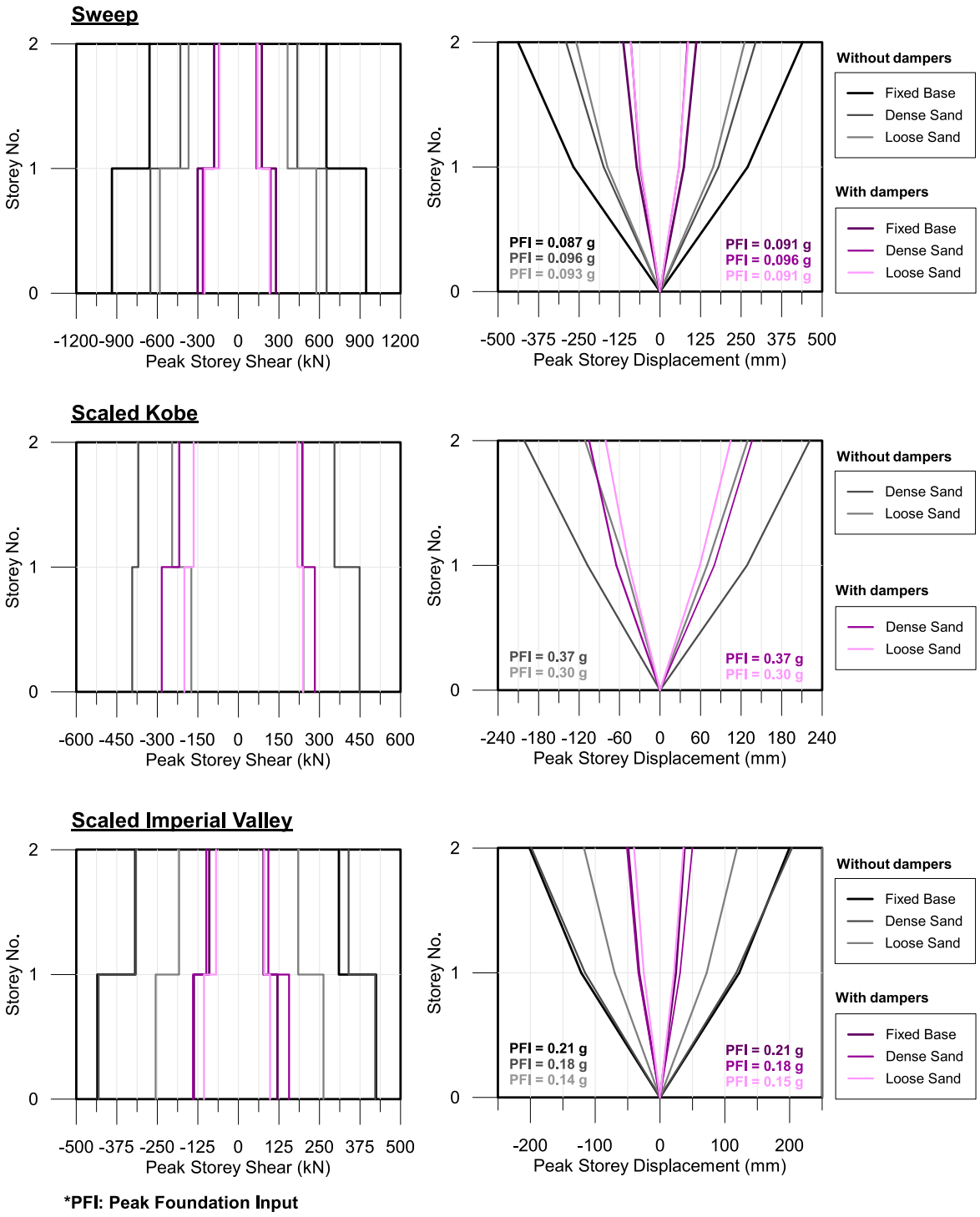

Fig. 6.3 Peak storey shear forces and storey displacements during sine-sweep and scaled realistic excitations for Tall frames with Heavy foundations and D2 dampers.

For long duration motions such as the sine-sweep excitation, with considerable energy in the signal focused close to the fundamental frequency of the frames, damped structures embedded in dry sands continue to exhibit a refined performance over their regular counterparts, albeit, not to the extent recorded during the scaled Imperial Valley motions. Experimental data for the sine-sweep excitations in Figures 6.2 and 6.3 shows both frames benefiting from dynamic SSI, by means of reduced peak storey shear forces and structural deformations, as the sand beneath the foundation gets softer.

During near-fault excitations such as the scaled Kobe motion, peak base shear forces and storey displacements for the regular squat frame in Figure 6.2 were higher, albeit close, to those measured in the equivalent damped frame with D2 dampers. As the centre of gravity gets higher for the tall frames in Figure 6.3, storey shear forces and drifts in the regular structure start to become comparable to those measured in the tall damped structure for the loose sand case. For such types of impulse excitations on soft ground, inter-storey oil dampers may prove to be redundant if the regular structure can provoke sufficient SSI during shaking.

Near resonant frequency excitations

Sinusoidal base excitations at, or close to, the fundamental frequency of the model frames allow for an examination of how equivalent viscous damping ratios in the damped structures change as shaking intensity and base fixity conditions are varied during peak SSI.

Before discussing experimental data, Figure 6.4 illustrates the definition of damping ratio that will be adopted in this section. For an ideal symmetric hysteretic loop, damping ratio is computed by the following equation:

$$\zeta = \frac{1}{4\pi} \times \frac{E_{dissipated}}{E_{stored}} \tag{6.1}$$

where $E_{dissipated}$ is the enclosed area of the hysteretic loop, and E_{stored} is the energy stored in the system, taken as the area of the shaded blue triangle (A3) in Figure 6.4. With nonlinear inter-storey oil dampers, and highly nonlinear inertial interaction at the foundation-soil interface of the structures tested in this study, experimental hysteretic loops tend to be both, irregular and asymmetric. Examples of these are presented in Figure 6.4.

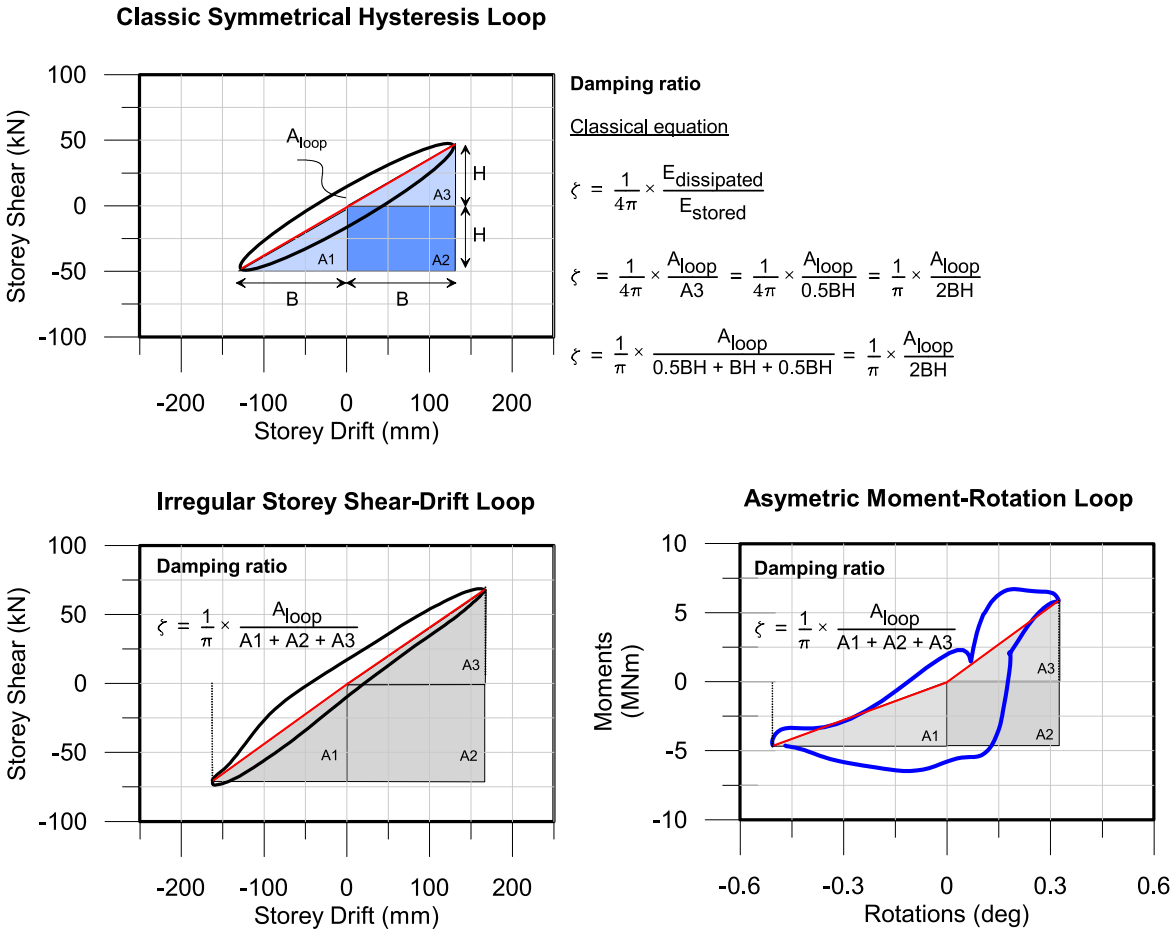

Fig. 6.4 Definition of equivalent viscous damping ratio for classical, irregular and asymmetrical hysteresis loops.

A more generalised definition of E_{stored} is thus necessary when computing damping ratios for the irregular loops. For such cases, energy stored is taken to be the total area of the shaded grey regions (A_1,A_2 and A_3), as shown in Figure 6.4. For a symmetrical loop, this would be equivalent to four times the area of the blue triangle (A3). Damping ratio is thus calculated by:

$$\zeta = \frac{1}{\pi} \times \frac{A_{loop}}{A_1 + A_2 + A_3} \tag{6.2}$$

Experimental storey shear forces and inter-storey drifts are presented in Figures 6.5 to 6.7 for the squat and tall model structures experiencing near resonant frequency excitations. Relaxing foundation rotational restraints by shallow embedment into dry sand beds allowed bare frames to exhibit structural deformations and storey shear forces that are close to, albeit never lower, than those measured for their damped counterparts.

Close to resonance, results for the tall bare frame in Figure 6.6 show it performing better than the regular squat structure in Figure 6.5, with lower storey shear forces and drifts, for both the light and heavy foundation cases. This is directly attributed to the higher centre of gravity of the tall bare frame which enables it to provoke greater inertial interaction at foundation-soil interface during shaking. Relying solely on natural rocking , the regular tall structure on loose sand with a light foundation in Figure 6.6 recorded a 30 % decrease in base shear and first storey drift compared to its response during the fixed base test. However, the beneficial outcomes of SSI are not always that prominent.

As shown by the bare frame results with the heavy foundation cases in Figures 6.5 and 6.6, stiffer foundation systems tend to increase seismic force and drift demands on the bare frames during shaking. The degree to which soil-structure interaction improves the seismic response of a structure is clearly conditional, depending on factors such as frame aspect ratio, input motion intensity, input motion frequency content, foundation type and subsoil stiffness. This variability in outcome is what makes engineering supplemental damping into the superstructure an attractive alternative. Inter-storey oil dampers in both, squat and tall frames, resulted in consistent improvements to the seismic response of the structures in Figures 6.5 and 6.6, regardless of base flexibility or foundation system stiffness.

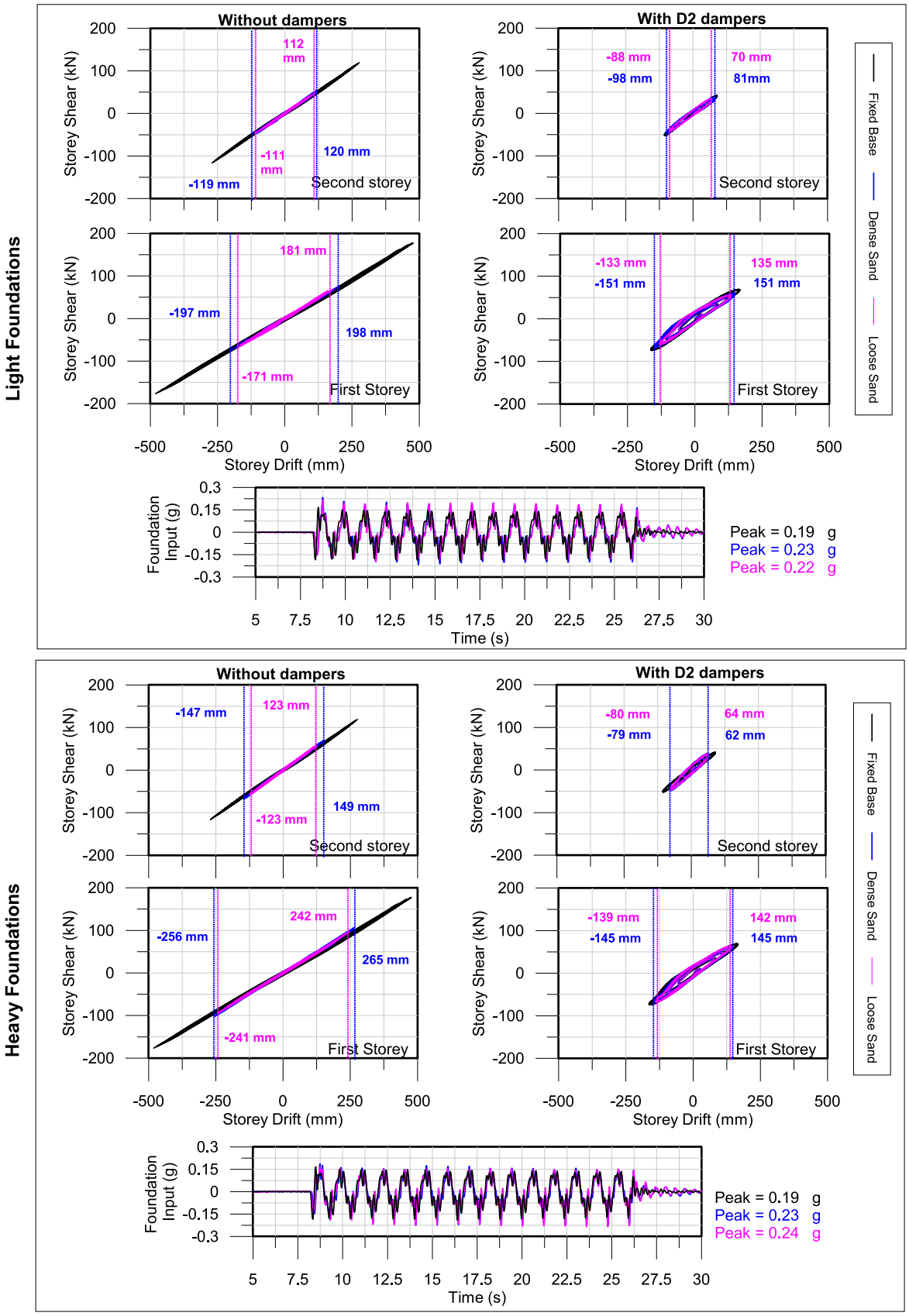

Fig. 6.5 Storey shear forces and inter-storey drifts during moderate near resonant frequency excitations for the Squat frames.

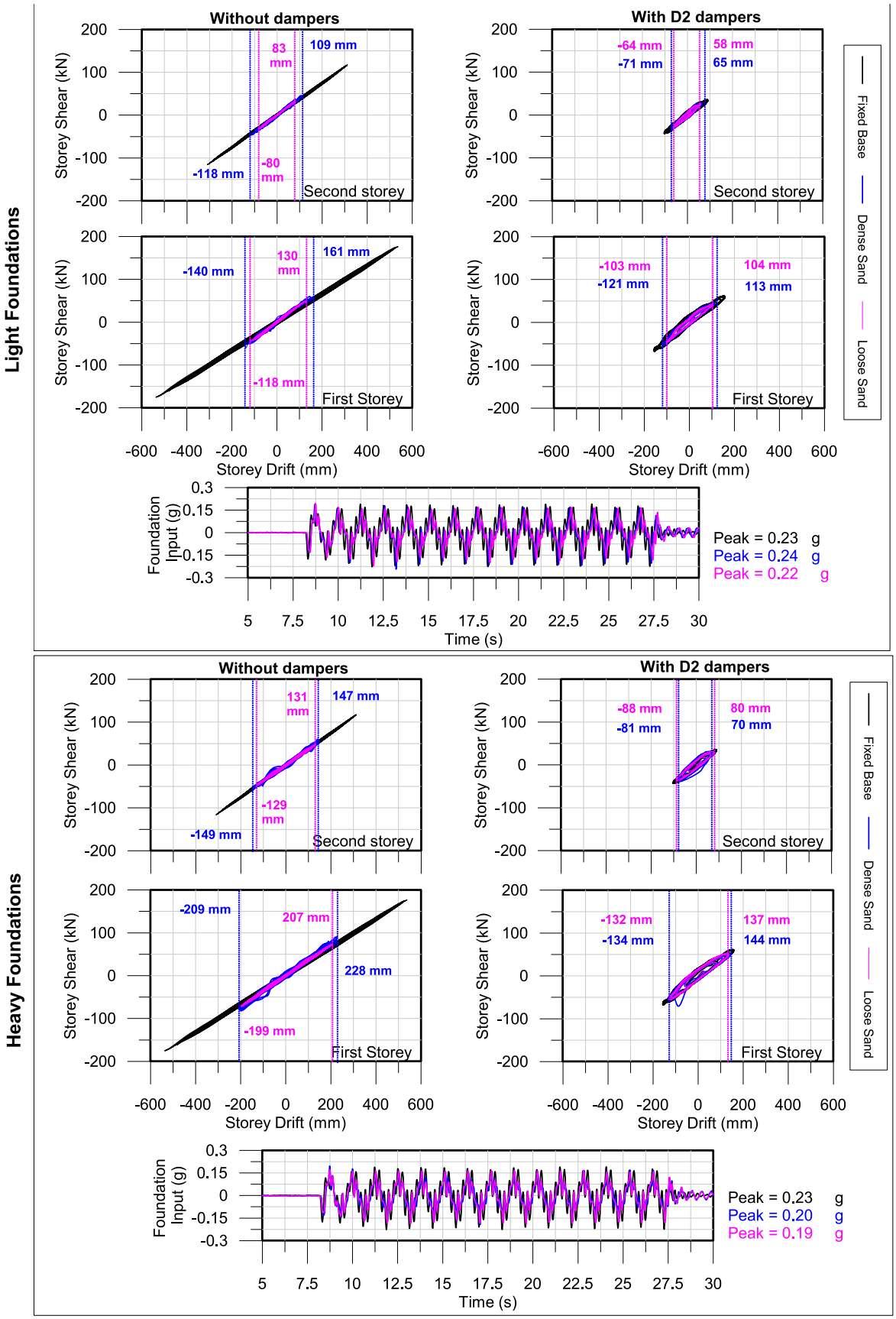

Fig. 6.6 Storey shear forces and inter-storey drifts during moderate near resonant frequency excitations for the Tall frames.

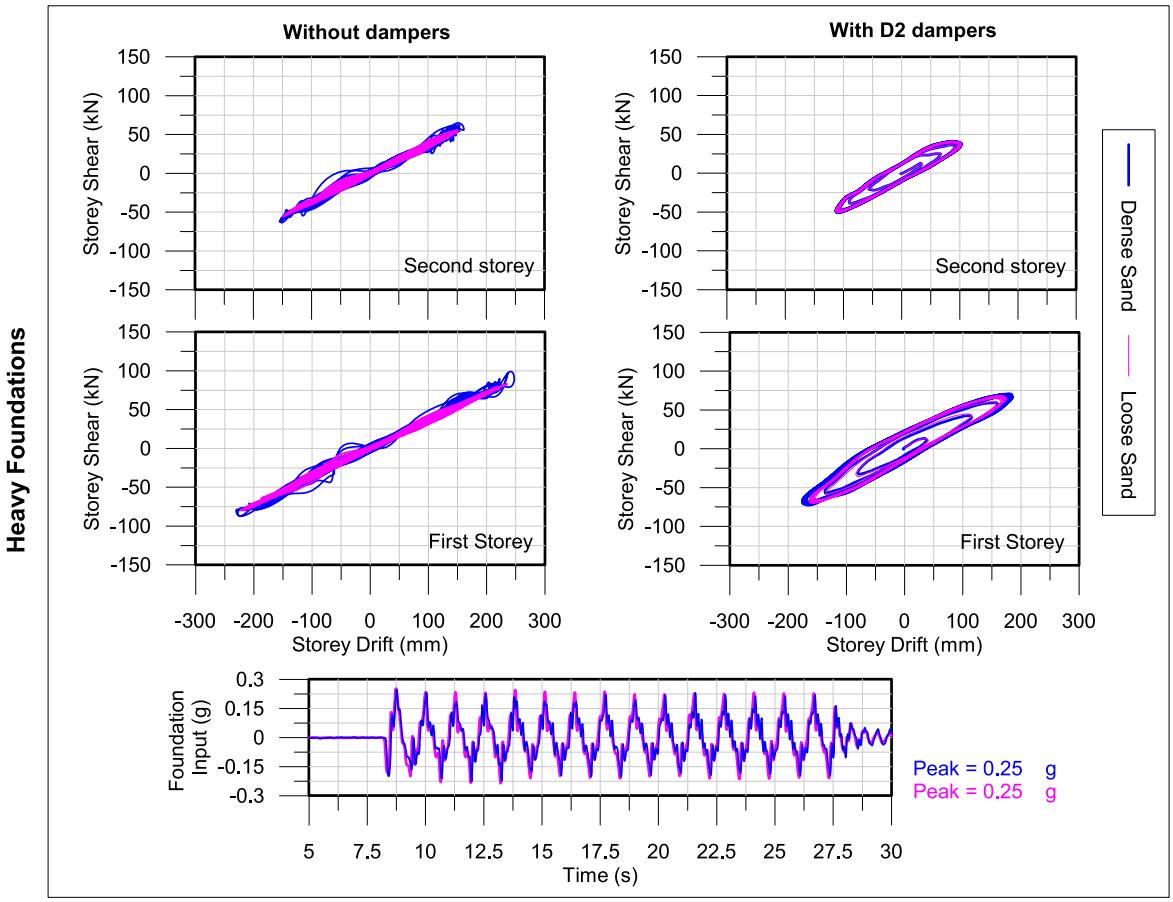

Fig. 6.7 Storey shear forces and inter-storey drifts during strong near resonant frequency excitations for the Tall frames.

Figure 6.7 neatly illustrates how for the same input motion, two different energy dissipation strategies: soil-structure interaction in the regular frame, and inter-storey oil dampers in the damped structure, can yield similar storey shear forces and drifts, provided of course that the problem parameters permit it. For the damped structure in Figure 6.7, energy dissipation is localised primarily in the inter-storey dampers, as evident by the elliptical storey shear versus drift hysteresis loops. On the other hand, the regular bare frame maintains a seemingly linear elastic response with limited hysteresis, all while achieving similar storey shear forces and drifts as its damped counterpart; for the regular structure, seismic energy dissipation is not focused in the superstructure, but rather at foundation-soil interface.

Using Equation 6.2, along with the storey shear force versus drift loops recorded experimentally during near resonant frequency sinusoidal motions, equivalent viscous damping ratios for the damped structures can be evaluated and tracked over different cycles of the base excitation. Results from this analysis are presented in Figure 6.8.

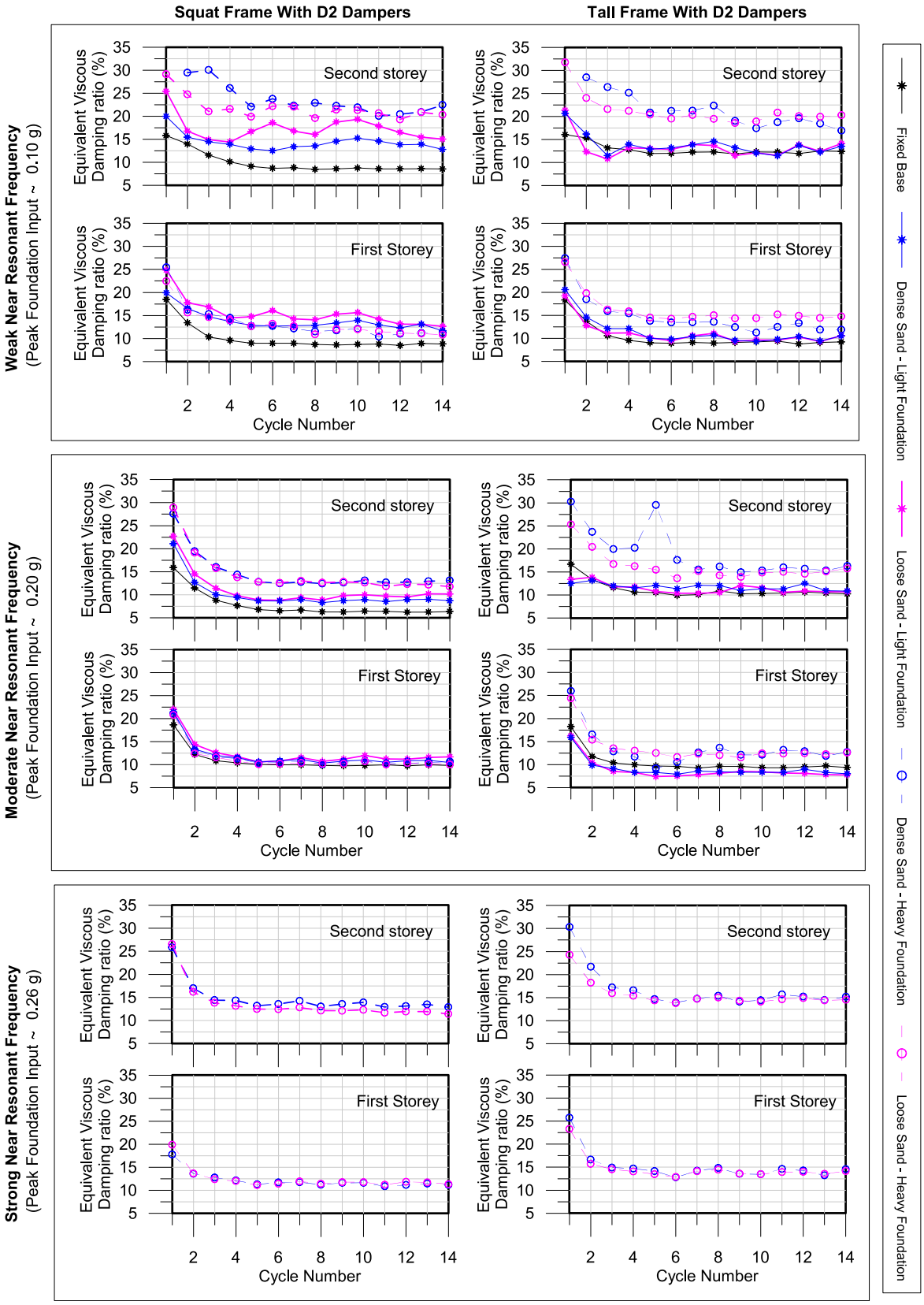

Fig. 6.8 Equivalent viscous damping ratios computed from damped frame storey shear versus inter-storey drift loops.

The estimated damping ratios are compared for different base fixity conditions and input motion intensities at frequencies near resonance. As evident by the black fixed-base data points in Figure 6.8, the miniature oil dampers are indeed successful at delivering constant energy dissipation during shaking. This is demonstrated by the consistent damping ratio estimates once steady-state of the structures is attained, usually within the first four cycles of excitation.

Results in Figure 6.8 suggest that shallow embedment of damped frames into compliant soil has the overall effect of increasing damping ratio estimates for the damped structures, relative to what would be recorded for an idealised fixed-base case. The second floor in the frame appears to exhibit a greater increase in damping ratio compared to the first storey. This increase appears to be a function of input motion intensity, foundation system stiffness, and appears to be more prominent in the short squat frame relative to its taller counterpart. These findings are quite unique and will be explored in the next section.

Analogous to the rounded hysteretic storey shear versus inter-storey drift loops of the damped structures, Figure 6.9 presents moment-rotation loops for the bare frames at peak rotation cycles. Following Equation 6.2, and the logic presented in Figure 6.4, an equivalent viscous damping ratio was also computed for each moment-rotation cycle at different input motion intensities, sand densities, and foundation bearing pressures.

The nonlinearity of the foundation-soil systems in Figure 6.9 is clear, with damping ratios at peak rotations that are well within the range of ratios computed for the damped structures with inter-storey oil dampers. Despite that, storey shear forces and drifts reported in Figures 6.5 and 6.6 demonstrated that the bare frames continue to fall short of matching the performance of the their damped counterparts. The reason lies in the nature of the damping forces in each of these systems.

Oil dampers in structures are velocity devices, generating resistive forces that are ahead of structural deformations and stiffness forces in terms of phase. This gives oil dampers direct control over drifts and accelerations in the structure. Damping at the foundation-soil interface however, is primarily hysteretic in nature (assuming small contributions from radiation damping (Madabhushi, 1991; Prevost and Scanlan, 1983)), generating resistive damping forces that are proportional to soil deformations. The beneficial outcomes of such type of damping are best realised during low-probability seismic events (moderate to strong shakes), in which the superstructure applies considerable over-turning moments onto the foundation to sufficiently deform the subsoil and invoke measurable hysteretic damping.

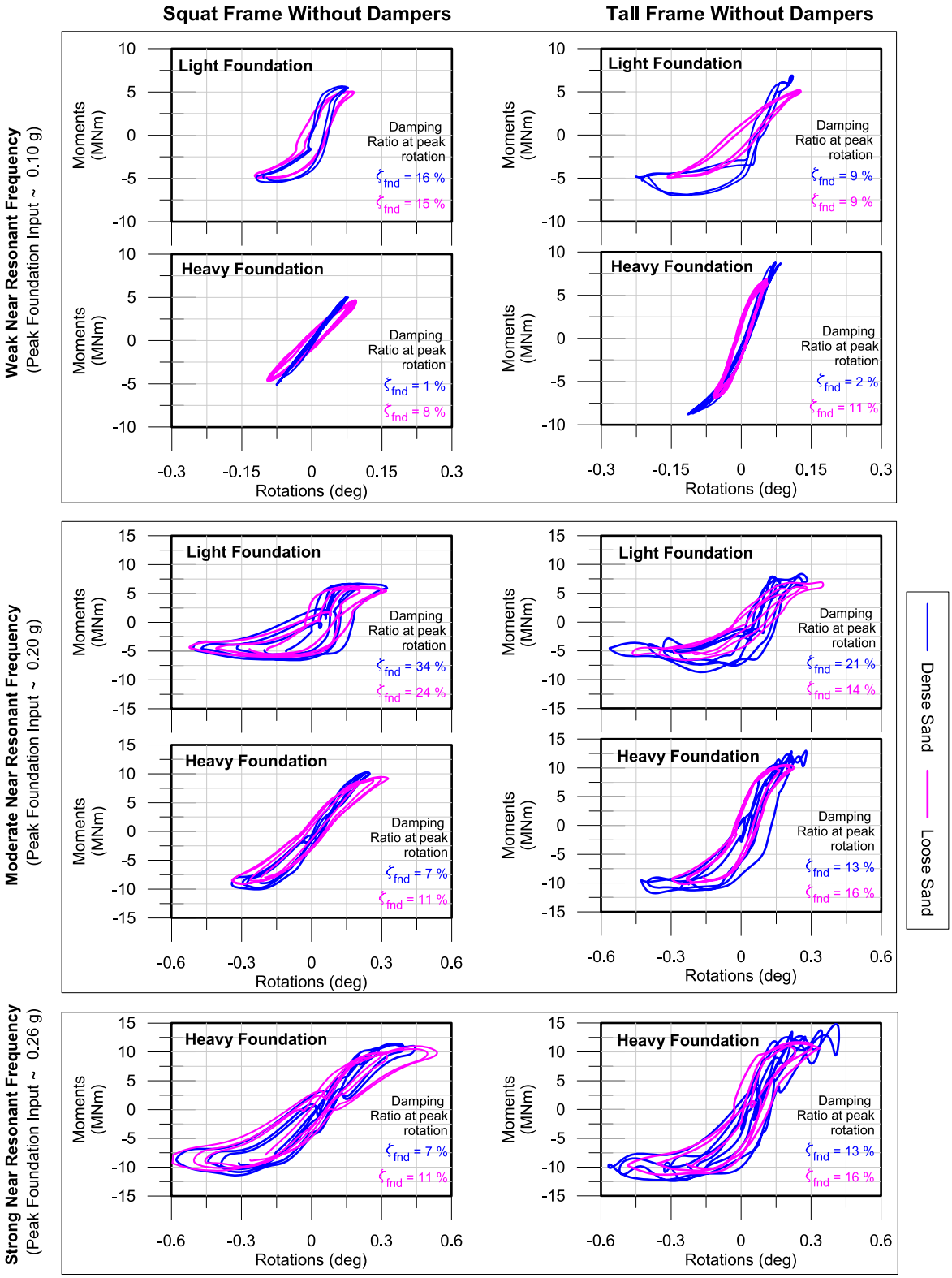

Fig. 6.9 Equivalent viscous damping ratios computed from bare frame moment-rotation loops at cycles of peak rotations.

Figure 6.9 offers a nice comparison of the foundation response for different vertical factors of safety (i.e. bearing pressures). Light foundations are able to deform sand and partially uplift at weaker intensity motions, thus achieving higher damping ratios than the heavy foundation cases which primarily yield the subsoil. Partial sand yielding and foundation uplifting are marked by a characteristic flatness in the moment-rotation loop. This flatness sets a natural limit on the floor accelerations allowed to develop in the superstructure (i.e. natural rocking isolation). This observation of foundation uplift being more effective at dissipating energy compared to subsoil yielding alone, is in line with observations of Heron (2013) for foundations with different bearing pressures.

6.3 Inter-storey Oil Damper Performance

Recalling Equation 6.2, damping ratio is simply a mathematical representation of the energy dissipation characteristics of a dynamic system. With limited foundation moment reaction during dynamic soil-structure interaction, floor inertial loads in a flexible structure reduce relative to the fixed-base case. This drives reductions in structural deformations and elastic energy stored in the frame. Intuitively, any inter-storey dampers fitted into the superstructure would simultaneously experience reduced stroke displacements and reductions in energy dissipation. With reductions in both the numerator and denominator, damping ratio would be expected to either remain the same or vary slightly when considering dynamic SSI in the damped structures. However, results in Figure 6.8 showed this variation to be significant. This implies that the drop in elastic strain energy in the damped frames during SSI is much greater than the corresponding drop in energy dissipated by the dampers, causing damping ratios to rise.

To investigate this further, a simple case of a generic fixed-base SDOF structure equipped with a linear viscous damper is first considered. Recalling the dynamic equilibrium equation of a SDOF system subjected to horizontal base excitation:

$$m\ddot{u}_{net} + c\dot{u}_{net} + ku_{net} = -m\ddot{u}_g \tag{6.3}$$

where $\ddot{u}_g$ is ground acceleration, $\ddot{u}_{net}$ is storey acceleration relative to base, $\dot{u}_{net}$ is storey velocity relative to base, and u_{net} is storey drift relative to the base. Re-arranging this equation, damping force is equal to:

$$c\dot{u}_{net} = -m(\ddot{u}_g + \ddot{u}_{net}) - ku_{net} \tag{6.4}$$

For an ideal linear viscous damper, peak damper force will occur at peak inter-storey velocity, when u_{net} and $\ddot{u}_{net}$ are equal to zero. Therefore, for a fixed-base condition, peak damping force on the lumped mass is:

$$(c\dot{u}_{net})_{peak} = -m\ddot{u}_g \tag{6.5}$$

Although simple in nature, Equation 6.5 shows that the peak force demand on a viscous damper in a SDOF structure is the product of the lumped mass and the ground acceleration at the instant of zero storey drift. Changing damper properties (specifically damping coefficient "c") will not alter the peak force demand on the damper, but rather control the inter-storey velocity and inter-storey drift of the system.

Expanding this to a 2-DOF system on a flexible base, internal damper forces in the structure can be mathematically derived from dynamic equilibrium equations of the floor lumped masses and shown to be:

Second storey

$$F_{damp,2} = -m_2\ (\ddot{u}_g + \ddot{u}_{net,1} + [\ddot{u}_{net,2} - \ddot{u}_{net,1}] + \ddot{\theta}h_2) - k_2(u_{net,2} - u_{net,1}) \tag{6.6}$$

where $[\ddot{u}_{net,2} - \ddot{u}_{net,1}]$ and $[u_{net,2} - u_{net,1}]$ are inter-storey accelerations and drifts respectively,

First storey

$$F_{damp,1} = F_{damp,2} + k_2(u_{net,2} - u_{net,1}) - m_1\ (\ddot{u}_g + \ddot{u}_{net,1} + \ddot{\theta}h_1) - k_1\ u_{net,1} \tag{6.7}$$

where $\ddot{\theta}h_i$ is the horizontal component of foundation rotational accelerations resolved at h_i, taking h_i as the heights from the centres of gravity of the lumped masses to the base of the foundation.

For the highly idealistic case of a classical mode in the damped frame, where all floors pass through their respective neutral positions (i.e. $u_{net} = 0$) at the exact same time, the linear viscous dampers will experience simultaneous peak forces. At that instant, $u_{net,1} = u_{net,2} = \ddot{u}_{net,1} = \ddot{u}_{net,2} = 0$, and peak damper forces become:

$$(F_{damp,2})_{peak} = -m_2\ (\ddot{u}_g + \ddot{\theta}h_2) \tag{6.8}$$

$$(F_{damp,1})_{peak} = (F_{damp,2})_{peak} + -m_1\ (\ddot{u}_g + \ddot{\theta}h_1) \tag{6.9}$$

In realistic cases where nonlinear oil dampers are fitted into a frame, Equations 6.8 and 6.9 do not apply; dampers do not exhibit peak forces at the exact same time instant. Equations 6.6 and 6.7 depict the mathematical complexity that would exist once the response of the two inter-storey dampers is linked. Notwithstanding this, the classical mode assumption underpinning Equations 6.8 and 6.9 helps emphasise how the phase relationship between foundation rotational accelerations, and foundation horizontal accelerations, might affect peak damper force demands and energy dissipation during SSI.

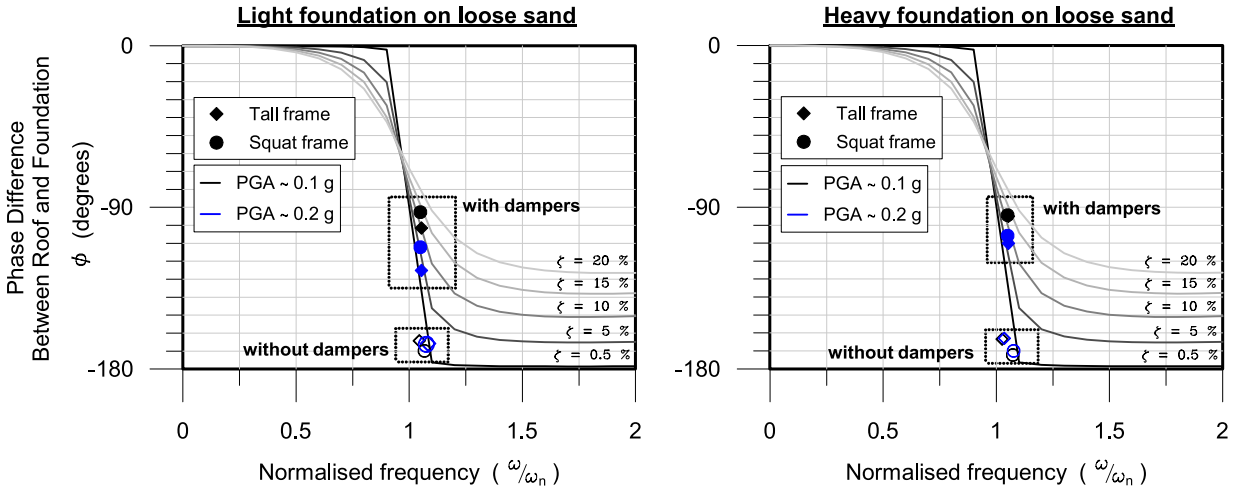

Fig. 6.10 Total acceleration phase delay between roofs and foundations of tested structures embedded in loose dry sands with different bearing pressures and D2 dampers.

For the regular structures excited near resonance, phase data in Figure 6.10 shows the bare squat and tall frames exhibiting a 170° phase lag between total roof and foundation accelerations. It is typically the case that rotational accelerations of a flexible bare structure are in close phase with total floor accelerations. This puts rotational accelerations in near anti-phase with horizontal foundation accelerations for a 170° floor-to-foundation phase difference. Referring to Equations 6.8 and 6.9, peak viscous damper forces in a damped structure would be expected to drop as a result of this anti-phase relationship. However, experimental phase relationships computed in Figure 6.10 shows the roofs and foundations of the damped frames responding approximately 100° out-of-phase when responding close to resonance; this is quite a deviation from what was recorded for the regular bare structures. Whilst not being critical for fixed-base or very stiff foundation systems, such a phase lag between a building's roof and its foundations can alter the rotational dynamics of the system, especially if the damped structure is founded on shallow foundations that are allowed to rotate during shaking.

Figure 6.11 illustrates the foundation-floor velocity relationships for a generic one-storey structure, responding to a theoretical sinusoidal horizontal foundation excitation. Two cases have been sketched, one for a 180° foundation-floor phase difference, similar to what was recorded for the regular structures in Figure 6.10, and one for a 90° foundation-floor phase difference, similar to what was recorded for the damped frames.

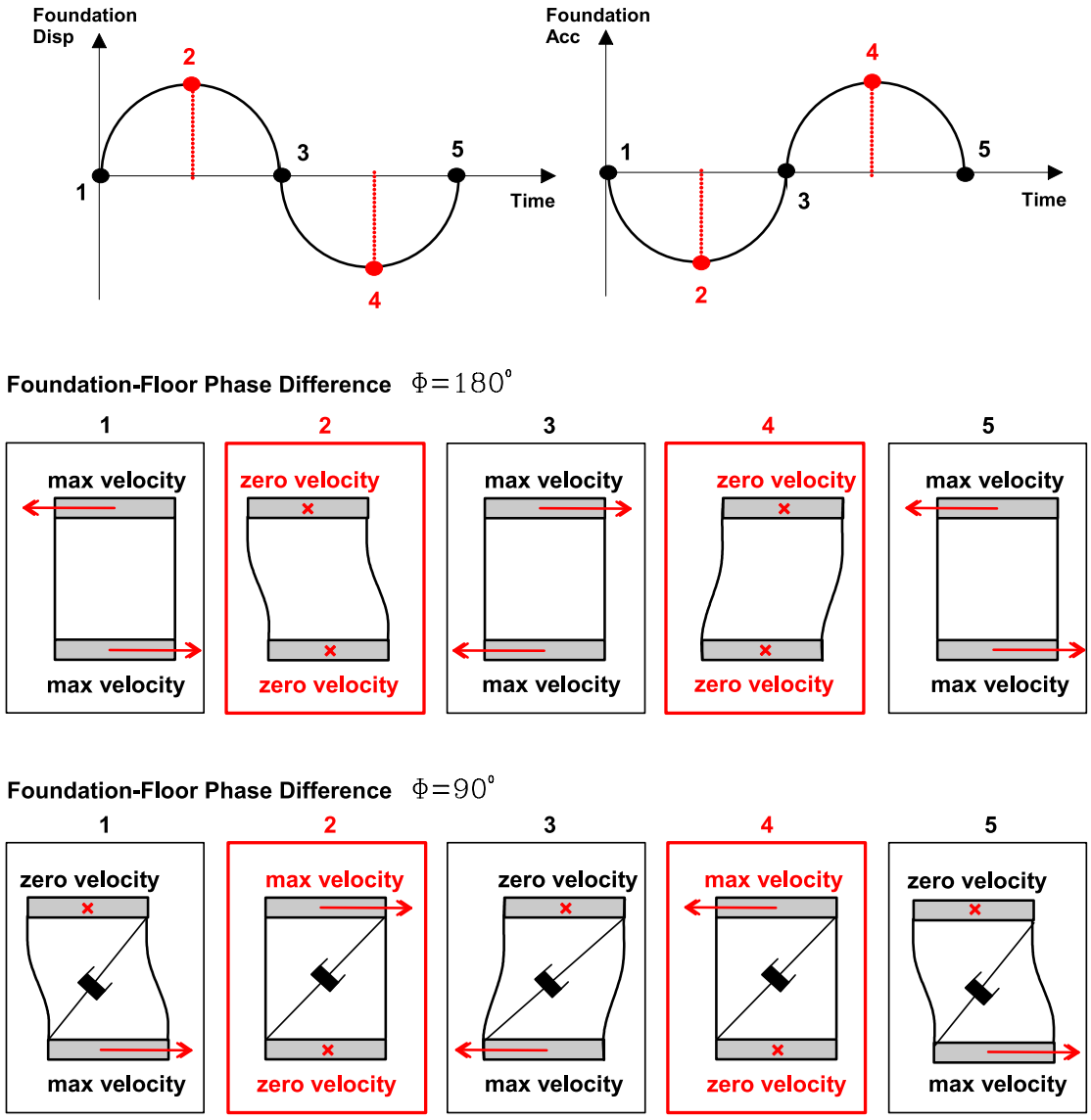

Fig. 6.11 Illustration of different foundation-floor phase differences for a generic one-storey structure experiencing sinusoidal horizontal foundation accelerations.

As shown in Figure 6.11, for a 180° phase difference, the floor and the foundation of the one-storey structure reach instances of immediate rest, and instances of peak velocity, almost at the same time, albeit, in opposing directions during shaking. The dynamic response for a 90° phase difference relationship is quite different. There are instances during the sinusoidal excitation at which the foundation of the structure decelerates to instantaneous rest, while the floor would be accelerating to peak velocity, and vice versa. Of particular interest is the velocity relationship close to points (2) and (4) in Figure 6.11, where the accelerating floor of the damped structure builds angular momentum relative to the decelerating foundation during horizontal base excitation.

Figure 6.12 examines this more closely by tracing floor inertial load (i.e. seismic overturning moments applied onto the foundation), internal frame forces, and floor-foundation velocities for the same one-storey structure equipped with a viscous damper responding at a 90° foundation-floor phase difference. Referring to the time instance between points (2) and (3) in Figure 6.12, as the foundation approaches peak horizontal accelerations, and the viscous damper is building up force, angular momentum of the accelerating floor relative to the decelerating foundation is expected to drive counter-clockwise rotations at the foundation. This foundation rotational component, driven by the foundation-floor phase difference, opposes the direction of the floor inertial load (i.e. overturning moments) as shown between points (2) and (3) in Figure 6.12. If the damped frame provokes very limited subsoil deformations at peak seismic overturning moments, these "driving" rotations can result in counter-clockwise moment-rotation loops as previously discussed in section 5.5 of Chapter 5. In terms of seismic demand on the superstructure, these "driving" rotational accelerations at the foundation are expected to occur close to peaks in horizontal foundation accelerations, thereby imposing additional force demands on the floor, as sketched in Figure 6.12.

The actual behaviour of the tested damped frames in this research is much more complex at resonance than as depicted by the simplified one-storey structure in Figure 6.12. The complexity lies in the nonlinearity and compliance of the oil damper setup in the 2-DOF structures, which complicates the superpositioning of damper forces and stiffness forces within the frames, resulting in a nonclassical mode of vibration. Figure 6.13 presents experimental velocity, rotational and horizontal foundation acceleration time traces for the damped squat and tall frames embedded in loose sands. The red vertical lines in the plot highlight the experimental phase difference between the foundations and the upper floors of the damped structures; instances of instantaneous foundation rest during near resonant frequency shaking, appear to coincide with peak floor velocities, and vice versa.

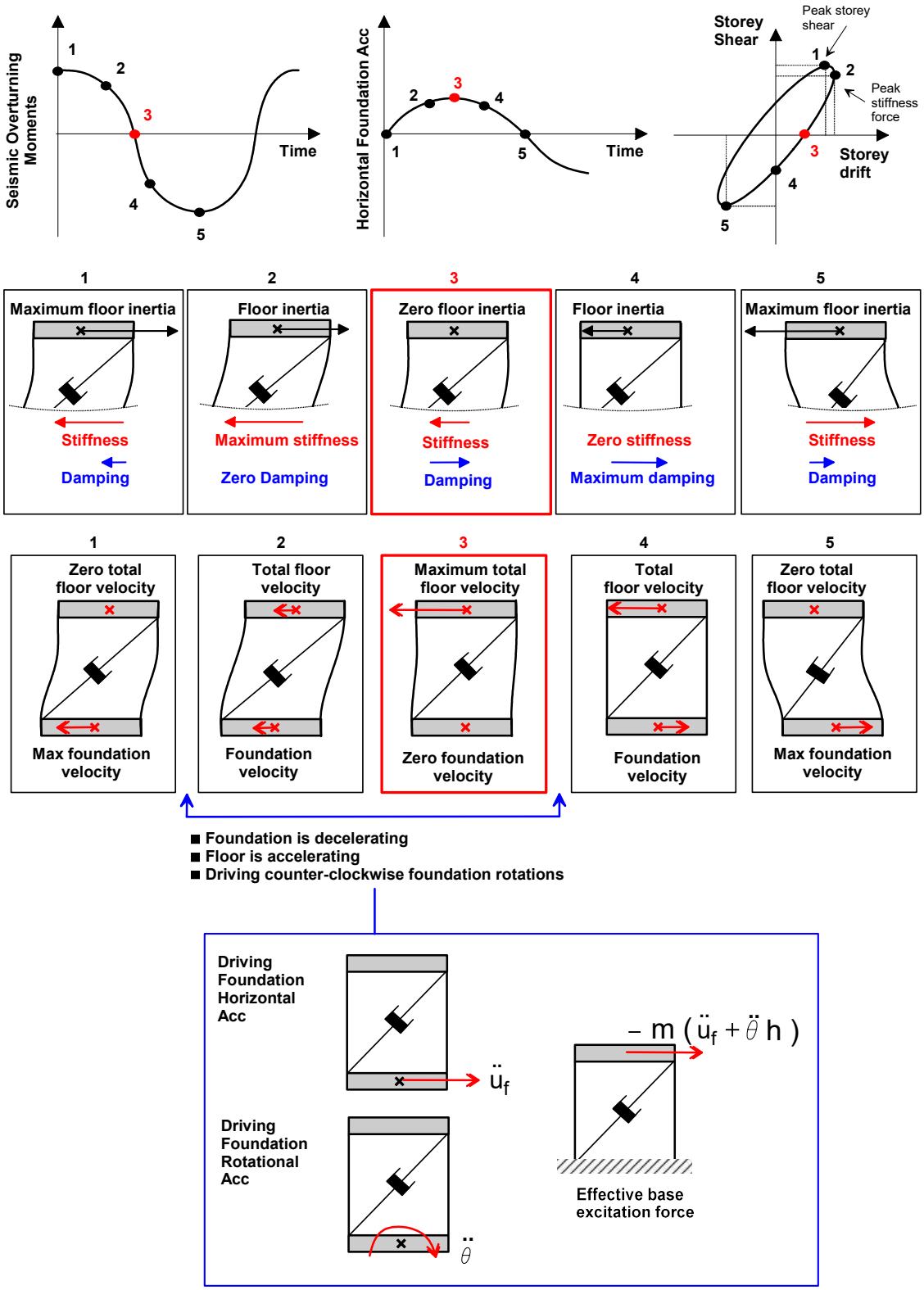

Fig. 6.12 Floor inertial load, internal frame forces, and velocities for an idealistic one-storey structure, equipped with a linear viscous damper, responding at a 90° foundation-floor phase difference during a sinusoidal horizontal base excitation.

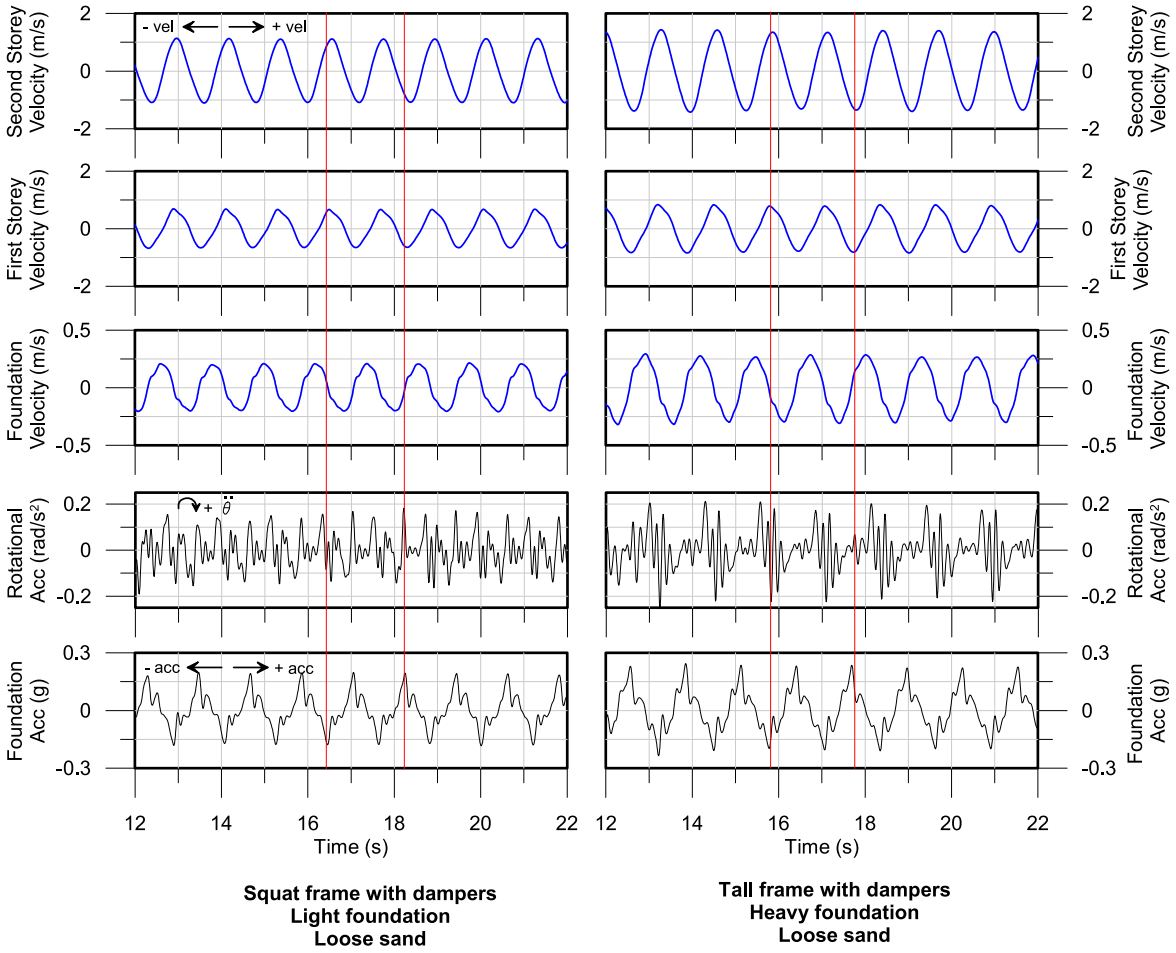

Fig. 6.13 Total floor velocities and rotational acceleration traces for the frames with D2 dampers embedded in Loose sand during near resonant frequency excitations.

As conceived in Figure 6.12, foundation rotational acceleration traces in Figure 6.13 exhibit peaks that are in-phase with the maxima and minima of the horizontal foundation accelerations. According to Equations 6.6 and 6.7, these "driving" foundation rotational accelerations, provoked by the foundation-floor phase difference of the damped structures, can impose additional demands on peak damper forces in the frame; the damping devices have to resist inertial loads at each floor due to both, foundation horizontal accelerations, and foundation rotational accelerations resolved horizontally at each storey. This would explain the relationship observed previously in Figure 5.15 of Chapter 5, between the higher order effects in foundation rotations, and the build-up of first storey damper forces in the structures.

Experimental measurements of inter-storey oil damper forces allow for the tracking of damper hysteresis in the damped frames during different base fixity conditions. Figure 6.14 shows experimental damping hysteresis loops of oil dampers as they do work against inter-storey drifts in the squat frame, during moderate near resonant frequency excitations.

The cumulative damper energy time traces were produced using the following equation:

$$E_{damp,i} = \oint F_{d,i}\, cos\theta \;\; du_{net,i}$$

$$E_{damp,i} = \int_0^t F_{d,i}\, cos\theta \;\; \dot{u}_{net,i} \;\; dt \tag{6.10}$$

where $E_{damp,i}$ is the energy dissipated by the damper at the ith floor, F_d is the damper force at the ith floor inclined at an angle θ, and $\dot{u}_{net,i}$ is the ith floor inter-storey velocity. Equation 6.10 is integrated numerically over the duration of the excitation to obtain the cumulative dissipated energy. For each damper, energy time traces in Figure 6.14 are normalised to the total energy dissipated by the same dampers during fixed base. This facilities comparison of work done by the dampers for different base fixity conditions.

Also in Figure 6.14 are plots for the recoverable strain energies stored at each floor normalised to the strain energy recorded during the fixed base case. Recoverable strain energies are derived from storey stiffness and drifts using the following equation:

$$E_{elastic,i} = \frac{1}{2}\, k_i\, (u_{net,i} - u_{net,i-1})^2 \tag{6.11}$$

where k_i is the lateral storey stiffness of the ith floor, and $u_{net,i}$ is the ith floor displacement measured relative to the foundation.

Figure 6.14 demonstrates the adverse effects that dynamic SSI can have on the work done by the inter-storey oil dampers in the damped squat frame. An even clearer reduction in energy dissipated by the oil dampers is observed for the damped tall structure in Figure 6.15 for both, the light and heavy foundation cases, demonstrating the effects of a higher frame aspect ratio.

For the damped squat structure in Figure 6.14, the reductions in damper hysteresis are primarily driven by a drop in damper input strokes (i.e. inter-storey drifts), with insignificant changes to peak damper forces. This of course is accompanied by a corresponding drop in the recoverable elastic energy in the frame due to SSI. Experimental results show strain energies dropping faster than work done by the dampers for the dry sand cases, provoking the increase in damping ratios reported earlier in Figure 6.8.

In comparison, the tall damped structure in Figure 6.15 exhibited drops in both, damper input strokes and peak damper forces, for the light foundation case where the tall frame is more likely to rock on dry sand during shaking. As the foundation bearing pressure increased, peak damper forces in the tall structure embedded in sand returned to fixed base levels, thus negating the effects of increasing the frame aspect ratio.

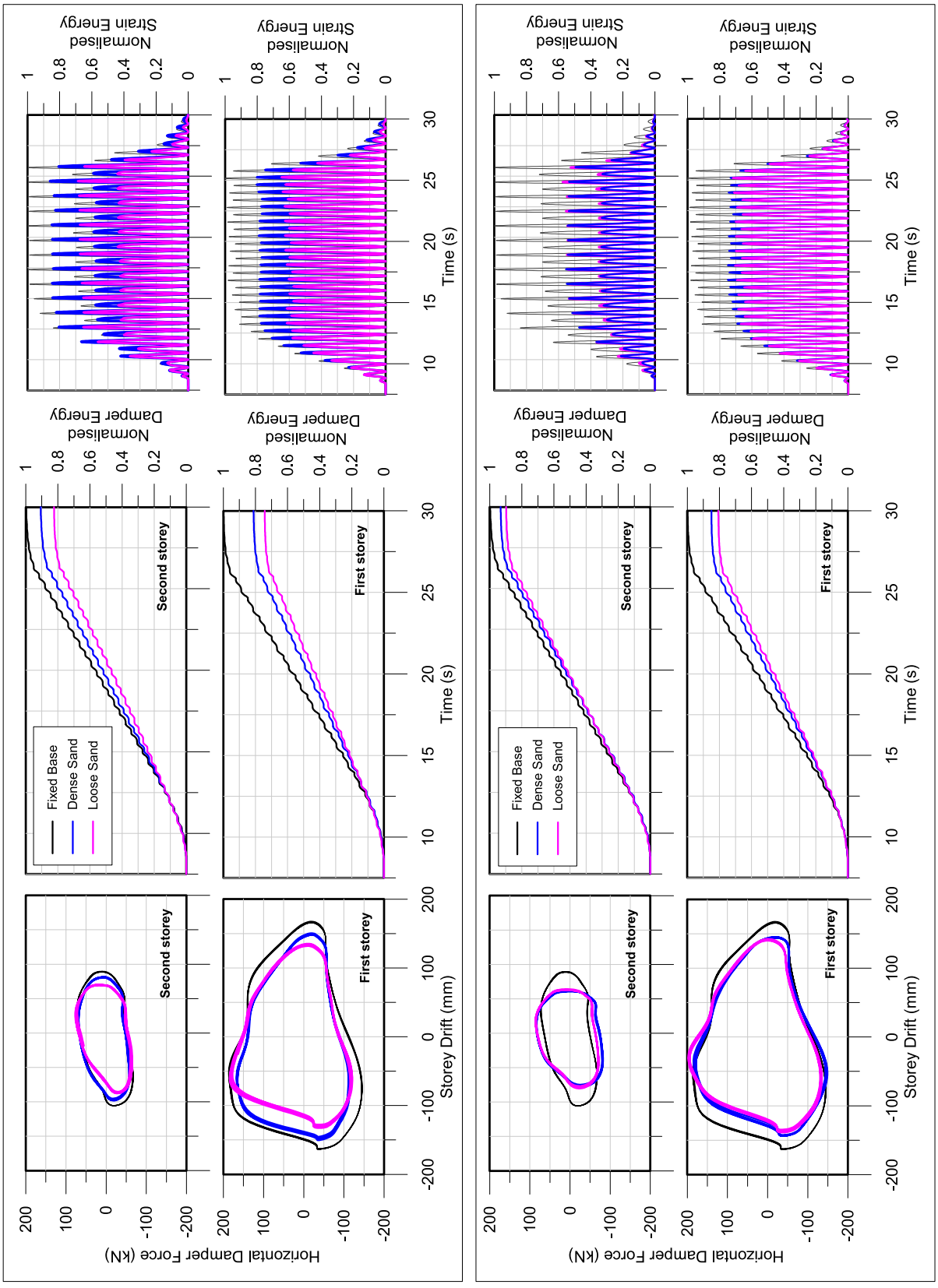

Fig. 6.14 Comparison of inter-storey oil damper energy dissipation and frame recoverable strain energy for the damped Squat frame with D2 dampers at different base fixity conditions during moderate near resonant frequency excitations.

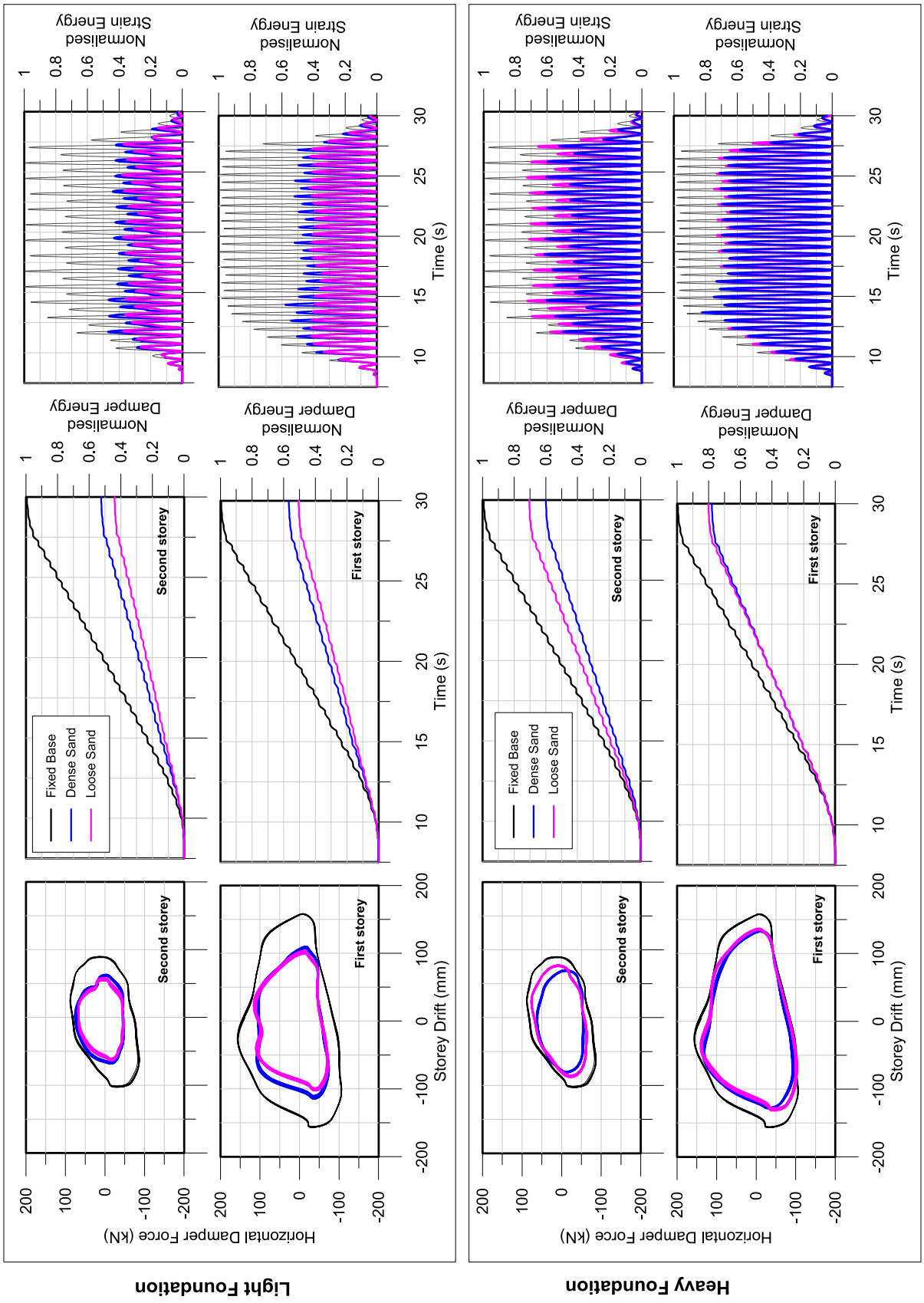

Fig. 6.15 Comparison of inter-storey oil damper energy dissipation and frame recoverable strain energy for the damped Tall frame with D2 dampers at different base fixity conditions during moderate near resonant frequency excitations.

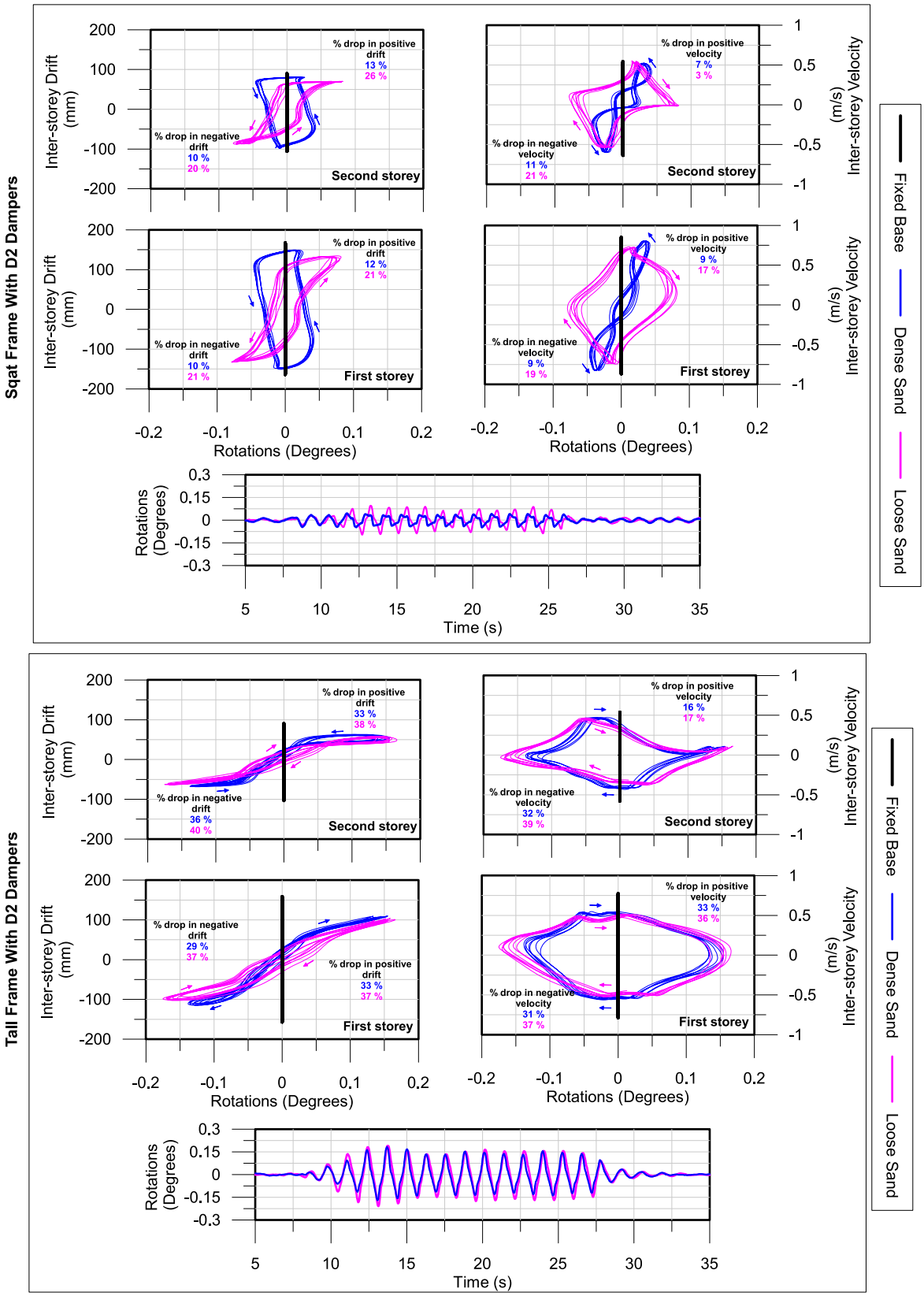

Fig. 6.16 Comparison of damper inputs at different base fixity conditions for the damped structures with light foundations during moderate near resonant frequency excitations.

Figure 6.16 examines in further detail the variation of inter-storey drifts (i.e. damper input strokes) and inter-storey velocities (i.e. damper input velocities) with foundation rotations for the case of the damped frames with light foundations. Here the effect of frame aspect ratio on the damper performance becomes clear. The taller frame exhibited larger dynamic rotations during shaking, which in turn capped inter-storey drifts and velocities going into the oil dampers, causing a more adverse drop in damper hysteresis. Inter-storey drifts and velocities going into the oil dampers in the squat frame showed limited deviations from what was recorded during fixed base.

Section 6.2 demonstrated how moment reactions at the foundation during SSI can limit inertial forces, accelerations, and structural deformations in a regular bare frame. Figure 6.17 overlays instances of peak first storey damper forces, over experimental moment-rotation loops for the tall damped structure, to check whether moment reactions can influence the magnitude of peak oil damper forces in the superstructure.

As discussed in Boksmati et al. (2021), and observed in Figure 6.15, peaks in first storey oil damper forces for the light foundation case in loose sand appear to be limited in comparison to the fixed base case. Indeed, Figure 6.17 shows these peaks in damper force occurring close to instances of explicit rotational stiffness degradation as the frame yields sand and partially uplifts. For the heavy foundation case where the moment-rotation loop progresses in a counter-clockwise direction, no distinctive reduction in rotational stiffness is observed. In fact, for all cases involving the damped squat frame, or the damped tall frame with a heavy foundation, moment reaction did not appear to be an influential limiting factor on the internal oil damper forces in the frames, at least for the intensity of excitations fired in this investigation.

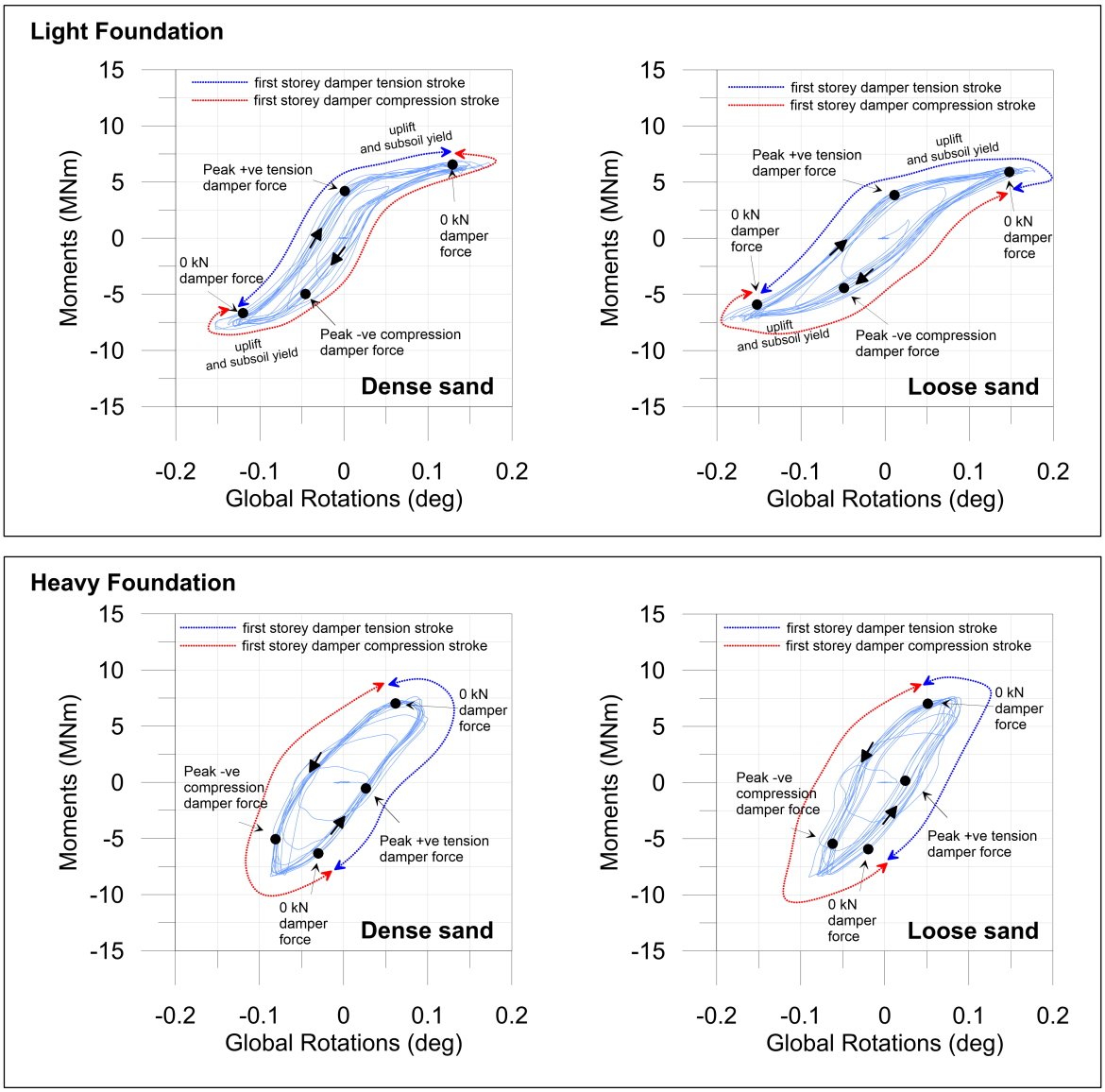

Fig. 6.17 Experimental moment-rotation loops for the damped Tall frame with D2 dampers during moderate near resonant frequency excitations.

6.4 Seismic Input Energy Distribution

Total input energy during horizontal base excitation of a soil-structure system can be computed as the work done by the base interaction shear force (N), on the horizontal ground displacement (u_g), as depicted in Figure 6.18. Mathematically, this can be written as:

$$E_{input} = \oint N \, du_g$$

$$E_{input} = \int_0^t \left(m_2 \, \ddot{u}_{t,2} + m_1 \, \ddot{u}_{t,1} + m_f \, \ddot{u}_f\right) \dot{u}_g \, dt \tag{6.12}$$

where m_i and m_f are floor and foundation lumped masses respectively, $\ddot{u}_t$ and $\ddot{u}_g$ are total floor and foundation accelerations respectively, and $\dot{u}_g$ is ground velocity. Equation 6.12 is integrated over the duration of the excitation to obtain total input energy into the soil-structure system due to horizontal ground excitation.

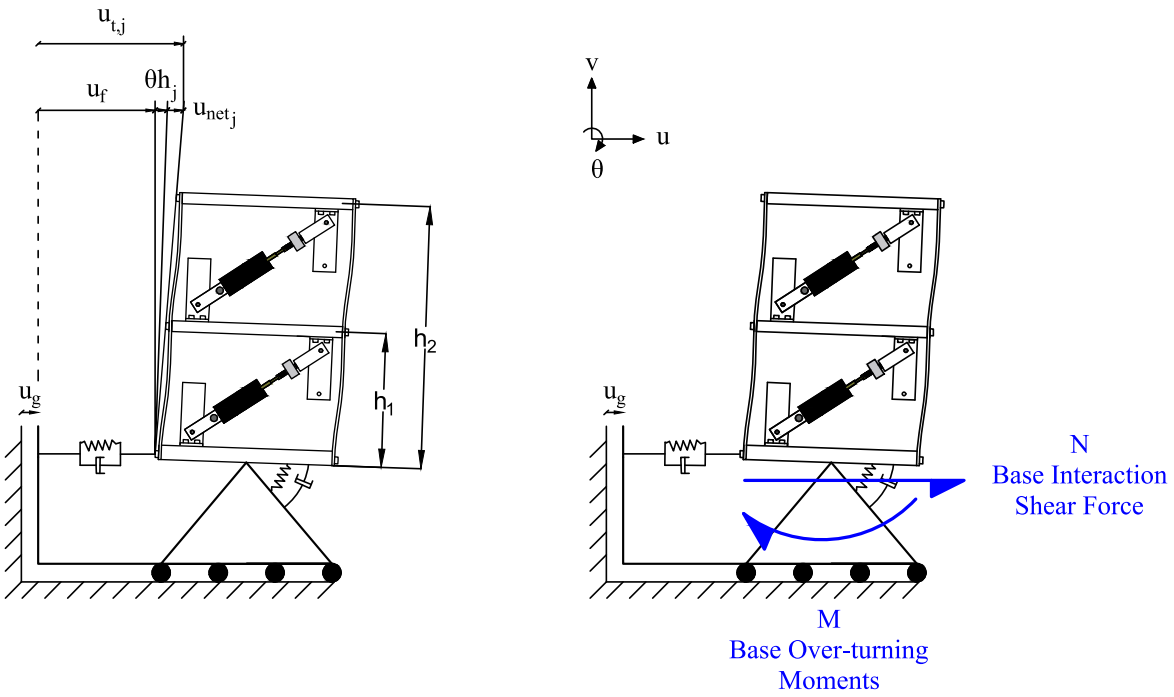

Fig. 6.18 Illustration of horizontal ground acceleration input into a soil-structure system with the corresponding frame reaction forces during shaking.

Work done by the foundation on deforming the subsoil in rotations can be computed using the following equation:

$$E_{rot} = \oint M \, d\theta$$

$$E_{rot} = \int_0^t \left(m_2 \, \ddot{u}_{t,2} \, h_2 + m_1 \, \ddot{u}_{t,1} \, h_1 + m_f \, \ddot{u}_f \, h_f + (I_2 + I_1 + I_f) \, \ddot{\theta}\right) \dot{\theta} \, dt \tag{6.13}$$

where M is the over-turning moments at the base of the foundation, h_i represents distances from centres of gravity of masses to the base of the foundation, I_i are the mass moments of inertia of the floors and the foundation respectively about their centres of mass, and $\dot{\theta}$ is frame rotational velocity. Once integrated over the entire duration of the excitation and floor free-vibration, Equation 6.13 will compute cumulative work done by the frame's inertial loads on rotation.

Internal work done by the seismic inertial loads on inter-storey shear deformations in the structure can be computed by the following equation:

$$E_{str} = \oint \left(m_2 \, \ddot{u}_{t,2}\right) du_{drift,2} + \oint \left(m_2 \, \ddot{u}_{t,2} + m_1 \, \ddot{u}_{t,1}\right) du_{drift,1}$$

$$E_{str} = \int_0^t \left(m_2 \, \ddot{u}_{t,2}\right) \dot{u}_{drift,2} \, dt + \int_0^t \left(m_2 \, \ddot{u}_{t,2} + m_1 \, \ddot{u}_{t,1}\right) \dot{u}_{drift,1} \, dt \tag{6.14}$$

where $m_i \, \ddot{u}_{t,i}$ represents floor inertial loading, and $\dot{u}_{drift,i}$ is inter-storey velocity. For frames without dampers, E_{str} represents energy dissipated by inherent damping in the superstructure. For the frames fitted with inter-storey dampers, this term represents total energy dissipated by both, inherent and supplemental damping.

Figure 6.19 presents energy time traces for the tall structures with light foundations, under different base fixity conditions, subjected to sine-sweep and near resonant frequency excitations. It is worth mentioning that foundation input accelerations during each of the three different base fixity cases are very similar in magnitude. The effect of natural rocking isolation for both, the regular and the damped structure, is neatly illustrated in Figure 6.19, by virtue of lower total input energies into the soil-structure systems as the ground beneath the frames gets softer.

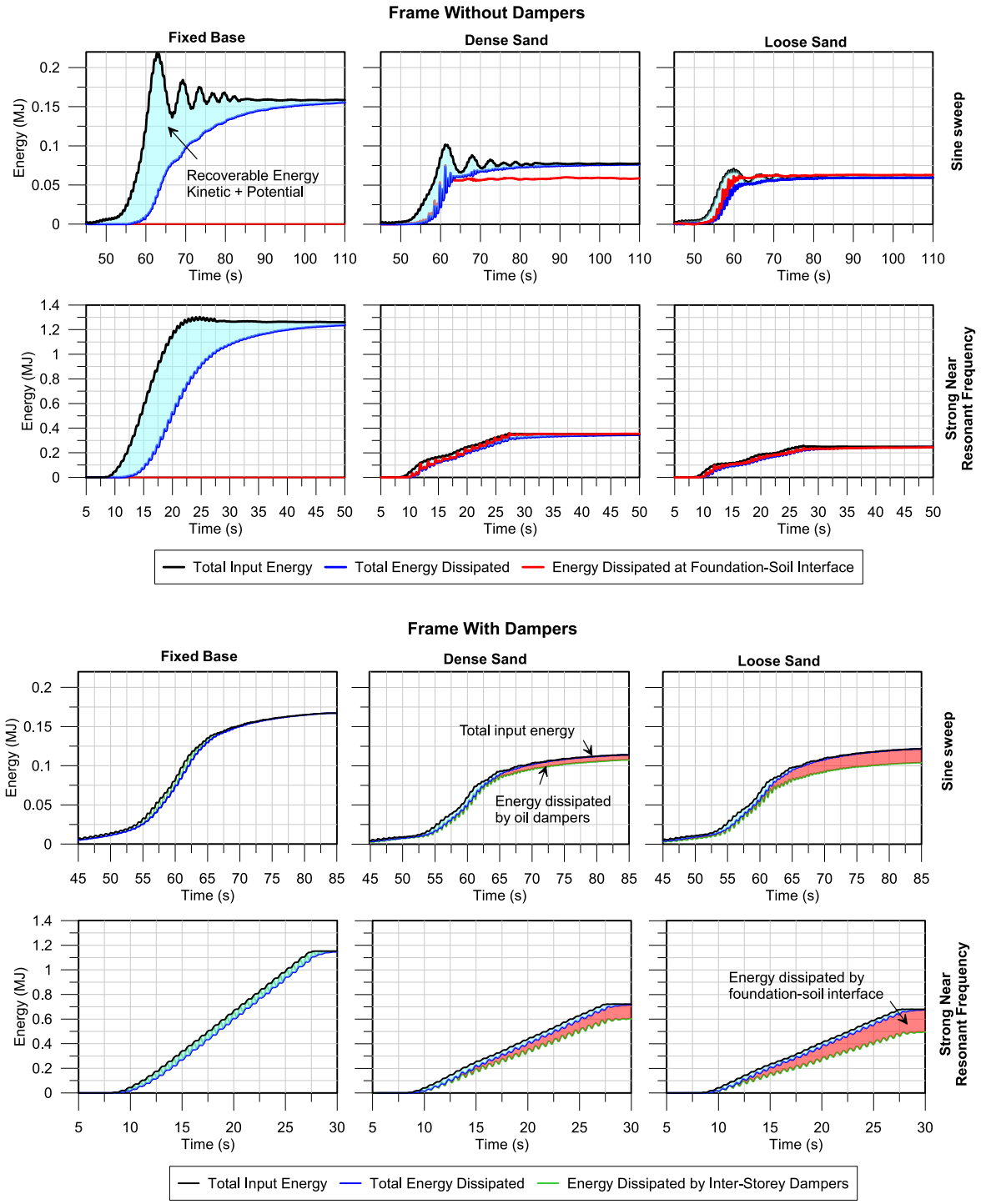

Fig. 6.19 Energy traces for the Tall structures with D2 dampers for different base fixity conditions during sine sweep and near resonant frequency excitations.

For a fixed base condition, a considerable portion of the input energy into a regular frame manifests in the superstructure as recoverable kinetic and potential energies, as highlighted by the blue regions in Figure 6.19. This form of energy is closely associated with deformations and potential for damage in the superstructure. With the installation of inter-storey oil dampers in Figure 6.19, a considerable portion of the input energy gets dissipated as work done by the oil dampers, leaving minimal recoverable energy to manifest in the superstructure.

Upon embedment of the regular frame into dry sands, Figure 6.19 shows recoverable energy levels in the superstructure dropping significantly, in conjunction with an increase in the work done by the seismic over-turning moments on frame rotations. In fact, during the strong near resonant frequency excitations in Figure 6.19, input energy into the tall regular structure embedded in dry sands is shown to be almost completely dissipated at the foundation-soil interface, leaving very limited recoverable energy to enter the superstructure.

For the tall frame equipped with inter-storey oil dampers in Figure 6.19, energy dissipated at the foundation-soil interface constitutes a small portion of the total input energy. The work done by the dampers continues to be the main source of dissipation for such a system, even during strong near resonant frequency shaking. However, as discussed in Boksmati et al. (2021), the highlighted red regions in Figure 6.19 show that for softer ground, with increasing input motion intensity, the portion of energy dissipated at the foundation-soil interface of a damped frame does increase at the expense of the work done by the oil dampers.

In order to better visualise how input energy gets distributed for different soil-structure systems, energy time traces, normalised to the cumulative input energy in each case, are presented in Figure 6.20 for the tall frames embedded in loose sand, subjected to near resonant frequency motions of increasing intensities. The trends for the light foundation cases in Figure 6.20 confirm the points raised above for the regular and damped structures. A heavier foundation-soil system for the regular frame is shown to limit energy dissipated at the foundation-soil interface, transferring more energy into the superstructure, compared to the same frame allowed to rock with a light foundation.

A heavy foundation for the tall damped structure in Figure 6.20 shows negative work done by seismic over-turning moments on frame rotations; i.e. rotations feed energy into the system, rather than dissipate it. This is directly associated with the counter-clockwise nature of the experimental moment-rotation loops presented in section 5.5 of Chapter 5. Not withstanding this, it appears that this component of energy is getting less negative with stronger excitations, as the primary component of rotation in phase with seismic overturning moments become more dominant in the overall rotational response of the damped structure.

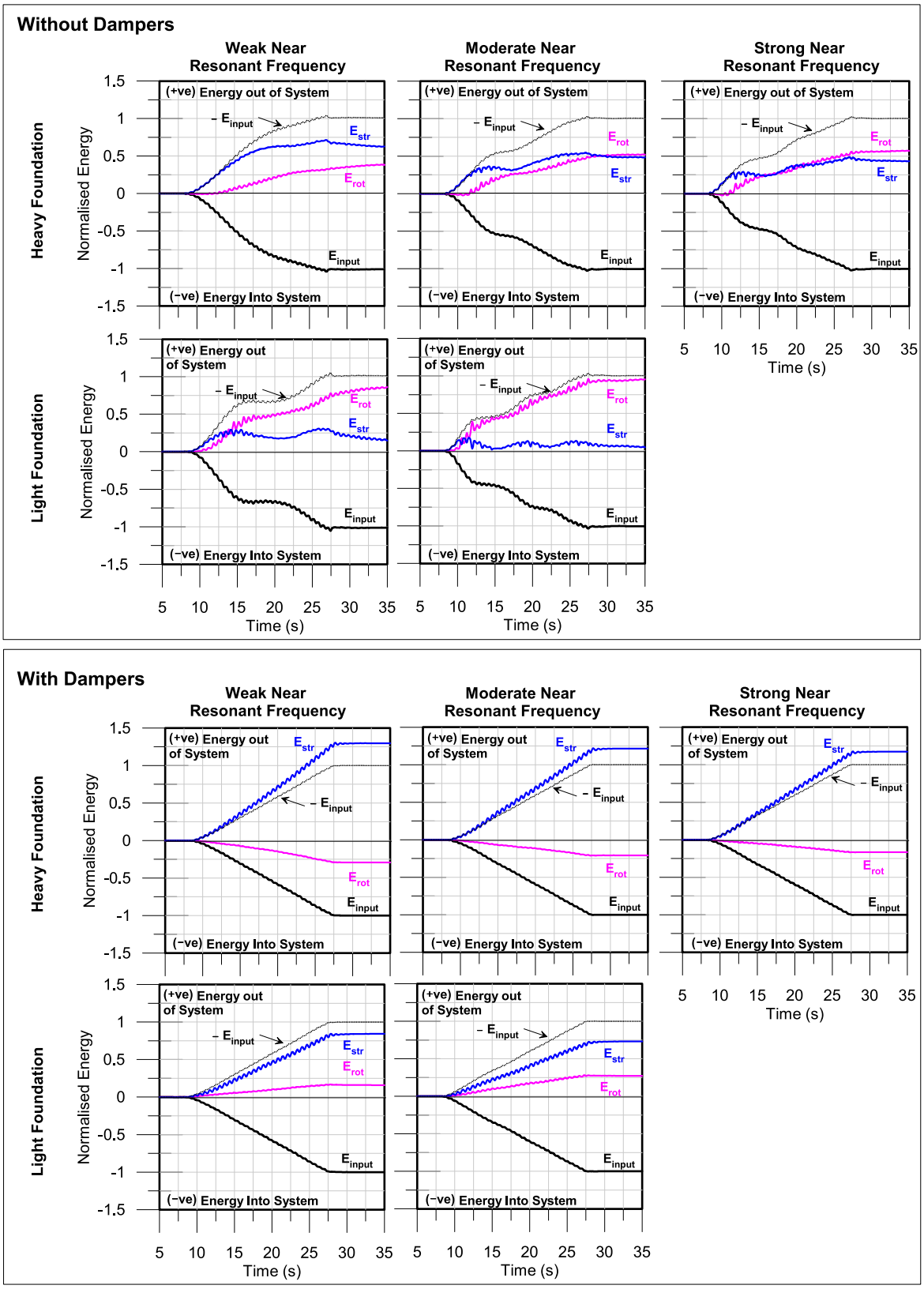

Fig. 6.20 Normalised energy traces for the Tall structures with D2 dampers embedded in Loose sands during near resonant frequency excitations of different intensities.

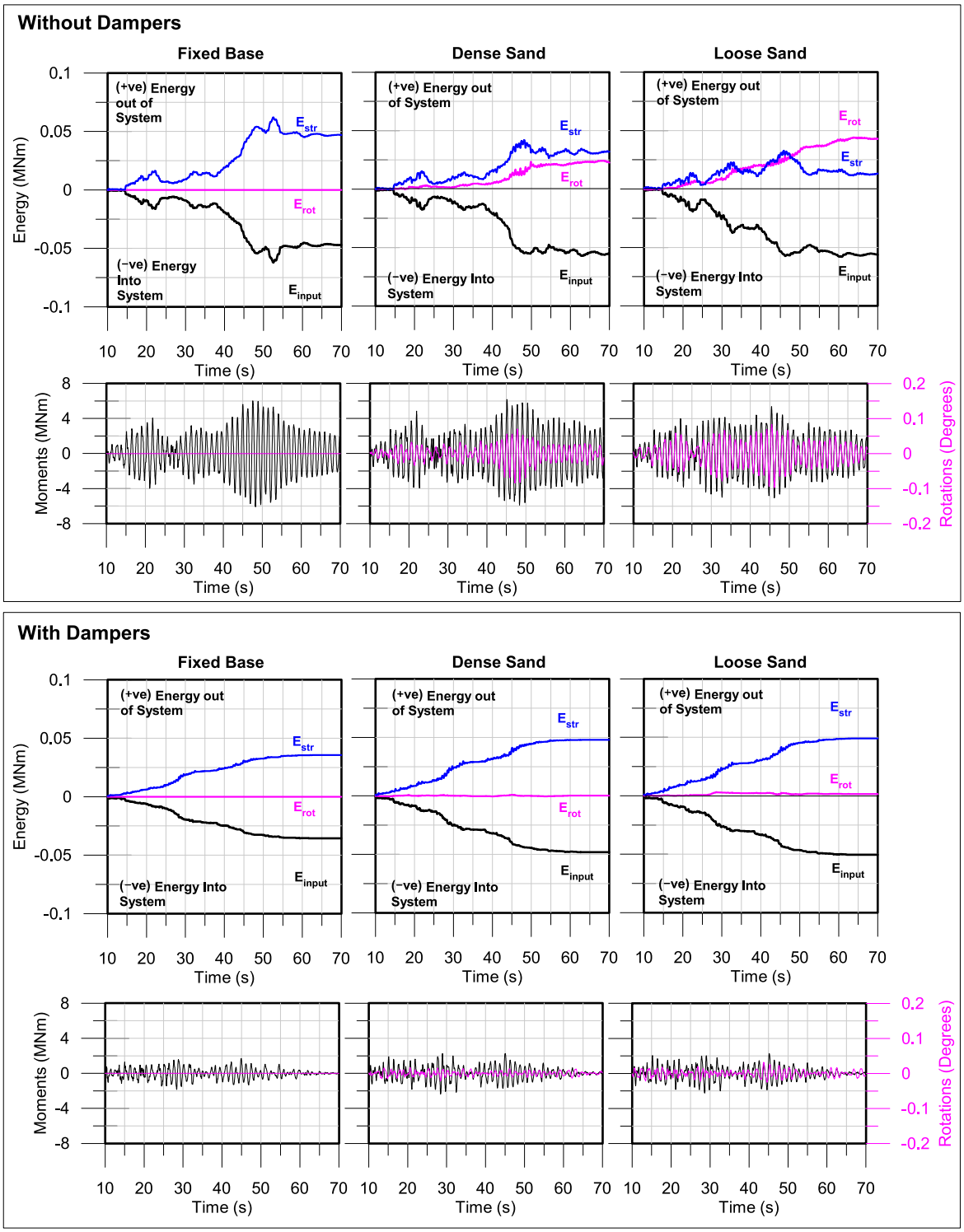

Fig. 6.21 Energy traces for the Tall structures with D2 dampers for different base fixity conditions during scaled Imperial Valley input motions.

Figure 6.21 extends this energy tracing concept to a realistic scaled Imperial Valley excitation. While dynamic SSI for the regular frame embedded in loose sand is shown to be capable of provoking energy dissipation levels at the foundation-soil interface (E_{rot}) comparable to those reported for the inter-storey oil dampers (E_{str}), the dynamic response is nowhere near that of the damped structure; energy dissipation in the oil dampers is instantaneous, and remains consistent throughout the excitation, albeit, at a cost to the natural damping at the foundation-soil interface (E_{rot}) of the damped structure.

6.5 Summary

This chapter examines the superstructure performance of shallow founded regular and damped frames in the high gravitational field of the centrifuge, during dynamic soil-structure interaction. Experimental measurements of the frames' inertial forces, and instrumentation of inter-storey oil dampers in the model structures, provided a unique opportunity to examine the effects of realistic foundation impedance on the seismic demands of oil-damped structures. Results from the centrifuge revealed the following:

1. For weak to moderate, realistic multi-frequency component excitations, the level of storey drift control, and storey shear reductions brought about by the inter-storey oil dampers remain unmatched by the hysteretic damping that accompanies dynamic soil-structure interaction in regular frames.

2. For the intensity of excitations fired in this study, and for the foundation-soil systems tested in the centrifuge, it appears that base flexibility and inertial interaction at the foundation-soil interface are less consequential for damped frames, than they are for the regular structures.

3. When subjected to moderately strong excitations close to resonance, regular frames can invoke sufficient energy dissipation through partial subsoil yielding and foundation uplift to approximate the drifts and storey shear of equivalent structures fitted with inter-storey oil dampers. However, this is proven to be tentative and variable, depending on the problem parameters at hand, primarily frame aspect ratio, bearing pressure and foundation-soil system stiffness.

4. Inter-storey oil dampers in the superstructure proved to be a reliable energy dissipation source, capable of delivering consistent improvements to the structural performance, even with inertial interaction at the foundation-soil interface.

5. Shallow embedment of structures fitted with inter-storey oil dampers in dry sands has the overall effect of increasing equivalent viscous damping ratios relative to those reported for a fixed base condition. Inertial interaction at the foundation-soil interface has greater limiting effects on the recoverable strain energies in the damped structures (i.e. inter-storey drifts) than it does on oil damper hysteresis.

6. During a near resonant frequency sinusoidal excitation, the phase difference that exists between the accelerating floors and the decelerating foundation of a damped structure is shown to drive foundation rotations. These "driving" foundation rotational accelerations are in-phase with peaks in foundation horizontal accelerations, which can impose additional force demands on the inter-storey oil dampers during soil-structure interaction.

7. Moment reactions mobilised by the foundation-soil systems of damped frames are in dynamic equilibrium with inertial loads from the superstructure, which in turn are in dynamic equilibrium with frame internal stiffness and damper forces. Therefore, foundation tilt and ground reaction at the instance of occurrence of peak damper forces in the frame can affect the magnitude of damper forces that develop. This proved to be a limiting factor for the tall damped structure with a light foundation, as it rocked considerably during shaking.

The intensities of the input motions fired in this investigation were intended to maintain linear elastic responses in the superstructures. These would be typical of high-probability seismic events, during which design engineers would rely on inter-storey oil dampers in frames to ensure immediate occupancy and safe operation post-earthquake.

For such weak to moderate excitations, soil-structure interaction in the damped squat frames tested in this investigation have only generated beneficial outcomes in terms of reducing input strokes into the dampers. The raft foundations of the squat frames did not deform the sand enough for moment reaction to be a limiting factor on internal damper force generation.

The tall damped frame with higher centre of gravity, on the other hand, has shown evidence of subsoil yielding and foundation uplift for the low bearing pressure cases, which limited damper performance. Energy time traces show that the drop in damper energy was compensated for by an equivalent increase in energy dissipated at the foundation-soil interface. This behaviour is expected to amplify with softer soils and stronger excitations, warranting consideration by engineers when assessing the efficiencies of their selected dampers.

Chapter 7

Prediction of Dynamic Soil-Structure System Response

7.1 Introduction

Conventional time-stepping integration techniques were implemented in Chapter 4 to solve equations of motion for discrete mathematical models. These models have been successful at recreating dynamic fixed-base responses for both, the regular frames and the damped frames, as recorded in the centrifuge. This chapter aims to develop this further by incorporating foundation-soil systems with these mathematical models to include the effects of dynamic soil-structure interaction (SSI).

The envisaged discrete model to represent the soil-structure system is not one of high fidelity, but rather a simplistic design tool that is grounded on established engineering principles. Such a tool would capture important facets of the overall response of regular and damped frames, whilst taking into account nonlinear foundation-soil interaction, and nonlinear oil damper response. This would be a more elegant approach to address nonlinearities in the problem, rather than relying on full base fixity assumptions, or linear analysis in the frequency domain, as often advocated by literature and design guidelines on the subject.

7.2 Modelling of Foundation-Soil Systems

7.2.1 Wolf Discrete-Element Model

Referring to section 2.3.1, it is not uncommon in literature to model foundation-soil systems using discrete-element models. These models are often characterised by a pre-defined number of parameters, which have been calibrated by curve-fitting techniques, to match theoretical half-space solutions.

Madabhushi (1991) demonstrated the potential application of using a rotational spring to capture the experimental rocking behaviour of tower structures founded on saturated sands. Similar attempts were made by Mitrani (2006) and Jabary (2016) using horizontal springs to replicate experimental dynamic responses of model structures as measured in the centrifuge. This section attempts to use a lumped-parameter model developed by Wolf (1988) to capture foundation rocking response on dry sand during shaking. The discrete foundation model is visualised in Figure 7.1, taking into account the rotational degree of freedom only. Wolf (1988) proposed the following equation for the rotational spring K_{ry}:

$$K_{ry} = \frac{Gb^3}{1-\nu}\ [3.73(\frac{l}{b})^{2.4} + 0.27]\ [1 + \frac{e}{b} + \frac{1.6}{0.35 + (\frac{l}{b})^4}\ (\frac{e}{b})^2] \tag{7.1}$$

where G represents the shear modulus of soil, ν is Poisson's ratio, b and l relate to the foundation geometry as defined in Figure 7.1, and e is foundation embedment.

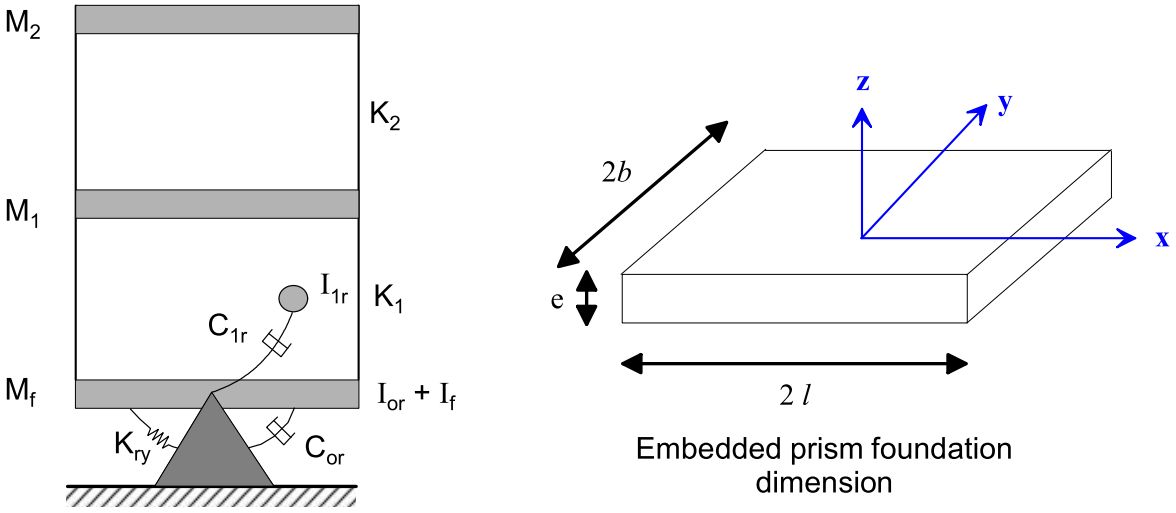

Fig. 7.1 Lumped parameter model for an embedded prism foundation after Wolf (1988) inserted beneath the 2-DOF frame.

An expression for G in MPa was put forward by Oztoprak and Bolton (2013):

$$G = \frac{A(\gamma)\ p_a}{(1+e)^3} \left(\frac{p'}{p_a}\right)^{m(\gamma)} \tag{7.2}$$

where $A(\gamma)$ and $m(\gamma)$ are shear strain dependant parameters that converge to 5760 and 0.5 at small-strain values respectively, e is voids ratio, p' is the mean effective stress in kPa at a specific reference point in the soil, and p_a is a normalising pressure of 100 kPa. The reference point for computing p' in the soil is taken at a depth equal to half of the foundation dimension along the shaking direction.

With the small-strain values of A and m set, the small-strain shear modulus G_{max} can be calculated using Equation 7.2. Substituting G_{max} into Equation 7.1 produces an initial estimate of K_{ry}, which would be applicable primarily at the early stages of base shaking. The lumped parameter model in Figure 7.1 also includes dashpots C_r, as well as fictitious masses (in this case mass moments of inertia) I_r. By curve-fitting to elastic halfspace solutions, Wolf (1988) derived these parameters to be:

$$C_{0r} = \frac{b}{v_s} K_{ry}\ (\gamma_0 + 2\zeta) \tag{7.3}$$

$$C_{1r} = \frac{b}{v_s} K_{ry}\ \gamma_1 \tag{7.4}$$

$$I_{0r} = \frac{b^2}{{v_s}^2} K_{ry}\ (\mu_0 + (\gamma_1 + \gamma_0)\zeta) \tag{7.5}$$

$$I_{1r} = \frac{b^2}{{v_s}^2} K_{ry}\ \mu_1 \tag{7.6}$$

where

$$v_s = \sqrt{\frac{G}{\rho}}$$

$$\gamma_0 = \mu_0 = 0$$

$$\gamma_1 = 0.45 + 0.23\left(\frac{l}{b} - 1\right)$$

$$\mu_1 = 0.34 + 0.55\left(\frac{l}{b} - 1\right)$$

in which v_s is the shear wave velocity of soil in m/s, ρ is the density in kg/m^3, and ζ is the damping ratio.

While Gazetas (1983) argues that the added masses in lumped parameter models are purely fictitious and only included to match frequency variation of stiffness and damping in halfspace solutions, the subject is still debatable; there is not yet a definitive approach of quantifying this participating mass. In this section, the added masses defined in Equations 7.5 and 7.6 will be used as suggested by Wolf (1988). A damping ratio of $\zeta = 10$ % is selected for use in Equations 7.3 and 7.5, following the damping ratios evaluated experimentally from the foundation moment-rotation traces in Figure 6.9. The system in Figure 7.1 can be mathematically described by:

$$\begin{bmatrix} m_1 & 0 & m_1h_1 & 0 \\ 0 & m_2 & m_2h_2 & 0 \\ m_1h_1 & m_2h_2 & I_{total}+I_{0r} & 0 \\ 0 & 0 & 0 & I_{1r} \end{bmatrix} \begin{Bmatrix} \ddot{u_1} \\ \ddot{u_2} \\ \ddot{\theta_0} \\ \ddot{\theta_1} \end{Bmatrix}_{i+1} + \begin{bmatrix} c_1+c_2 & -c_2 & 0 & 0 \\ -c_2 & c_2 & 0 & 0 \\ 0 & 0 & C_{0r}+C_{1r} & -C_{1r} \\ 0 & 0 & -C_{1r} & C_{1r} \end{bmatrix} \begin{Bmatrix} \dot{u}_1 \\ \dot{u}_2 \\ \dot{\theta}_0 \\ \dot{\theta}_1 \end{Bmatrix}_{i+1}$$

$$+ \begin{bmatrix} k_1+k_2 & -k_2 & 0 & 0 \\ -k_2 & k_2 & 0 & 0 \\ 0 & 0 & K_{ry} & 0 \\ 0 & 0 & 0 & 0 \end{bmatrix} \begin{Bmatrix} u_1 \\ u_2 \\ \theta_0 \\ \theta_1 \end{Bmatrix}_{i+1} = -\ddot{u}_{g,i+1} \begin{Bmatrix} m_1 \\ m_2 \\ m_1h_1+m_2h_2 \\ 0 \end{Bmatrix} \tag{7.7}$$

where θ_0 is the rotation of the foundation, and θ_1 is the rotation of the fictitious inertial mass I_{r1}. The integration scheme described in section 4.2 for a linear elastic system can be implemented here to solve the system of Equations in 7.7. Results from this numerical integration are presented in Figure 7.2, for the case of the regular squat and tall frames embedded in dry dense sand during sine-sweep excitations.

For such weak input motions that trigger limited resonance in the superstructure, a foundation-soil model that uses a linear spring derived from small-strain shear modulus of soil can result in satisfactory response history predictions as shown in Figure 7.2. The rudimentary assumption of foundation-soil linearity however, does lead to gross underestimation of foundation dynamic rotations, and overestimation of peak overturning moments. The Wolf (1988) lumped parameter model becomes unusable in the case of moderate to strong excitations that trigger considerable nonlinearity at the foundation-soil interface. An example of this is presented in Figure 7.3 for a strong near resonant frequency excitation.

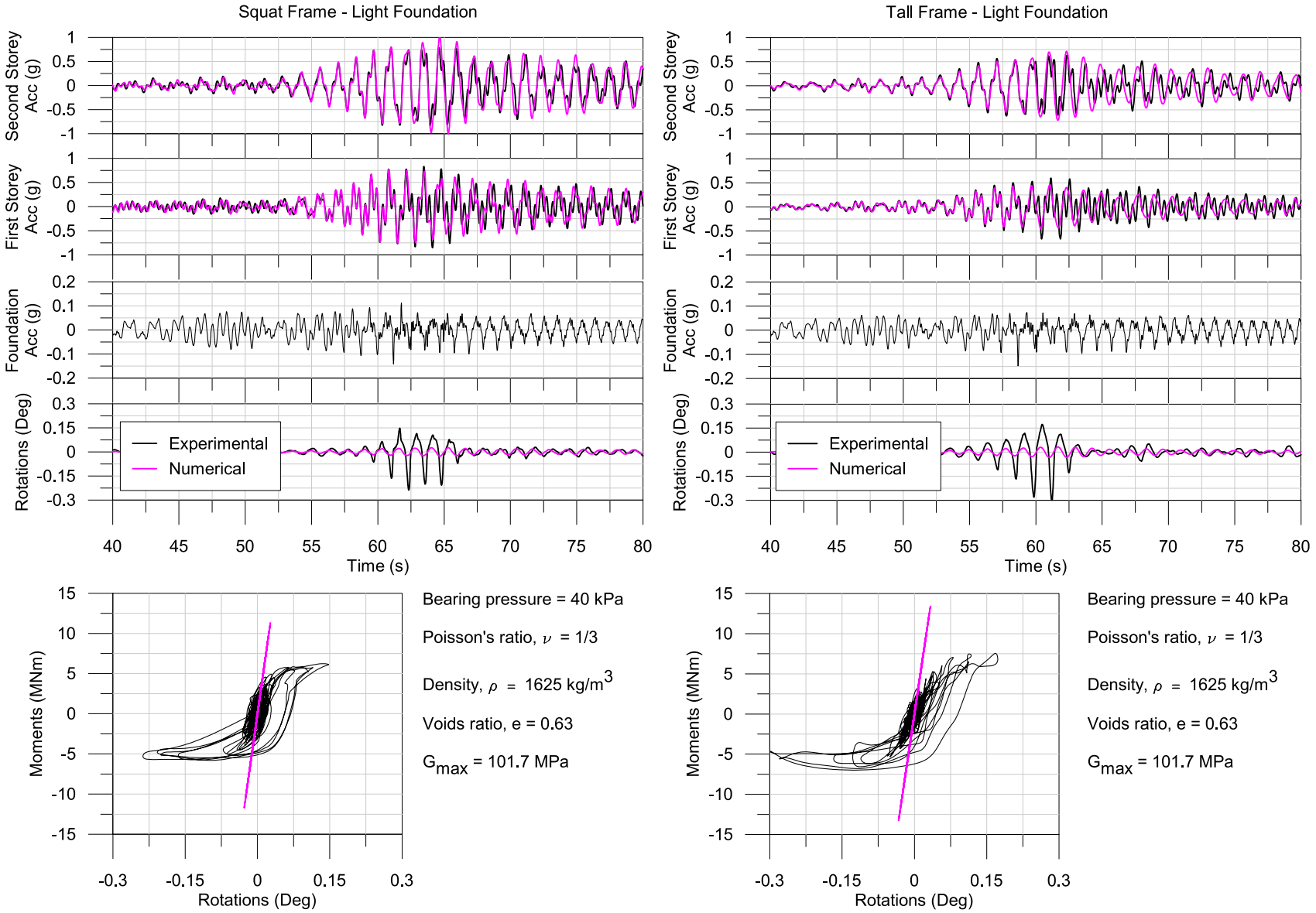

Fig. 7.2 Numerical predictions using the Wolf (1988) lumped parameter model for the regular Squat and Tall structures embedded in Dense sand during a sine-sweep excitation.

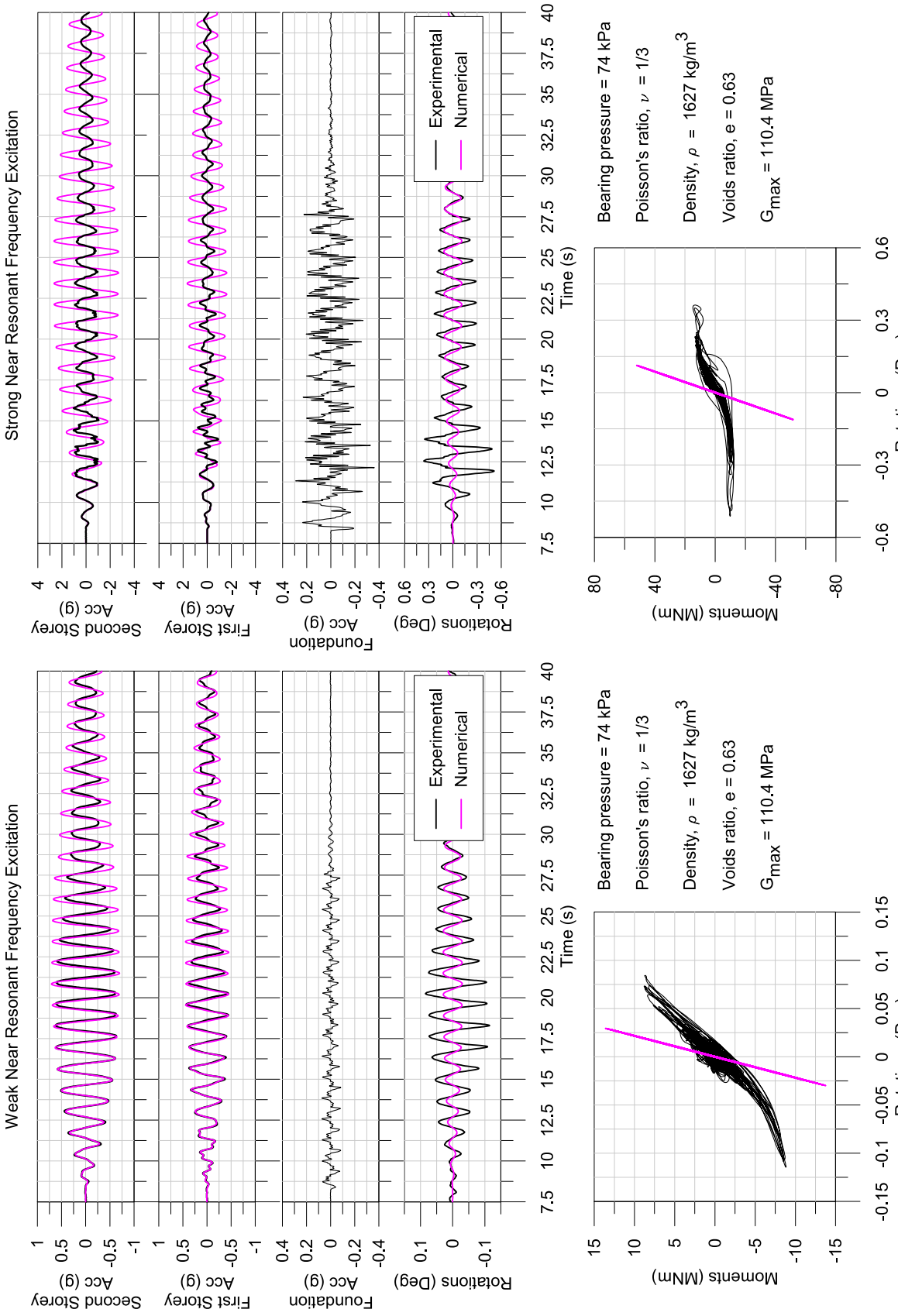

Fig. 7.3 Numerical predictions using the Wolf (1988) lumped parameter model for the regular Tall structure with a Heavy foundation embedded in Dense sand during near resonant frequency excitations of different magnitudes.

Previous studies (Jabary, 2016; Madabhushi, 1991; Mitrani, 2006) addressed this limitation by forcing manual reductions in soil shear modulus (G). The resulting drop in rotational stiffness would be evaluated based on peak shear strain values recorded experimentally in the soil, as the horizontally polarised vertically propagating shear (SH) waves travel up to the surface during shaking; often a hyperbolic shear modulus degradation relationship (either Hardin and Drnevich (1972) or Oztoprak and Bolton (2013)) would be used to compute a reduced soil shear modulus G from G_{max} for use in Equation 7.1.

The effect of reducing soil shear modulus on the numerical predictions is demonstrated in Figure 7.4 for the case of a regular squat frame, embedded in loose sand, experiencing a strong near resonant frequency excitation. With a 70 % reduction applied to G_{max}, total floor acceleration results from the numerical integration start to approximate those recorded experimentally.

By implementing a Wolf (1988) lumped parameter model to a highly nonlinear dynamic SSI problem, the process of making accurate predictions of peak soil shear strains for a specific base excitation, and then reducing soil shear modulus accordingly, becomes critical. The introduction of these "estimated" variables into the problem can restrict the model's ability to produce satisfactory blind predictions. As such, this mathematical representation of the foundation-soil system is dropped in favour of the Heron et al. (2015) hyperbolic model described in the next section.

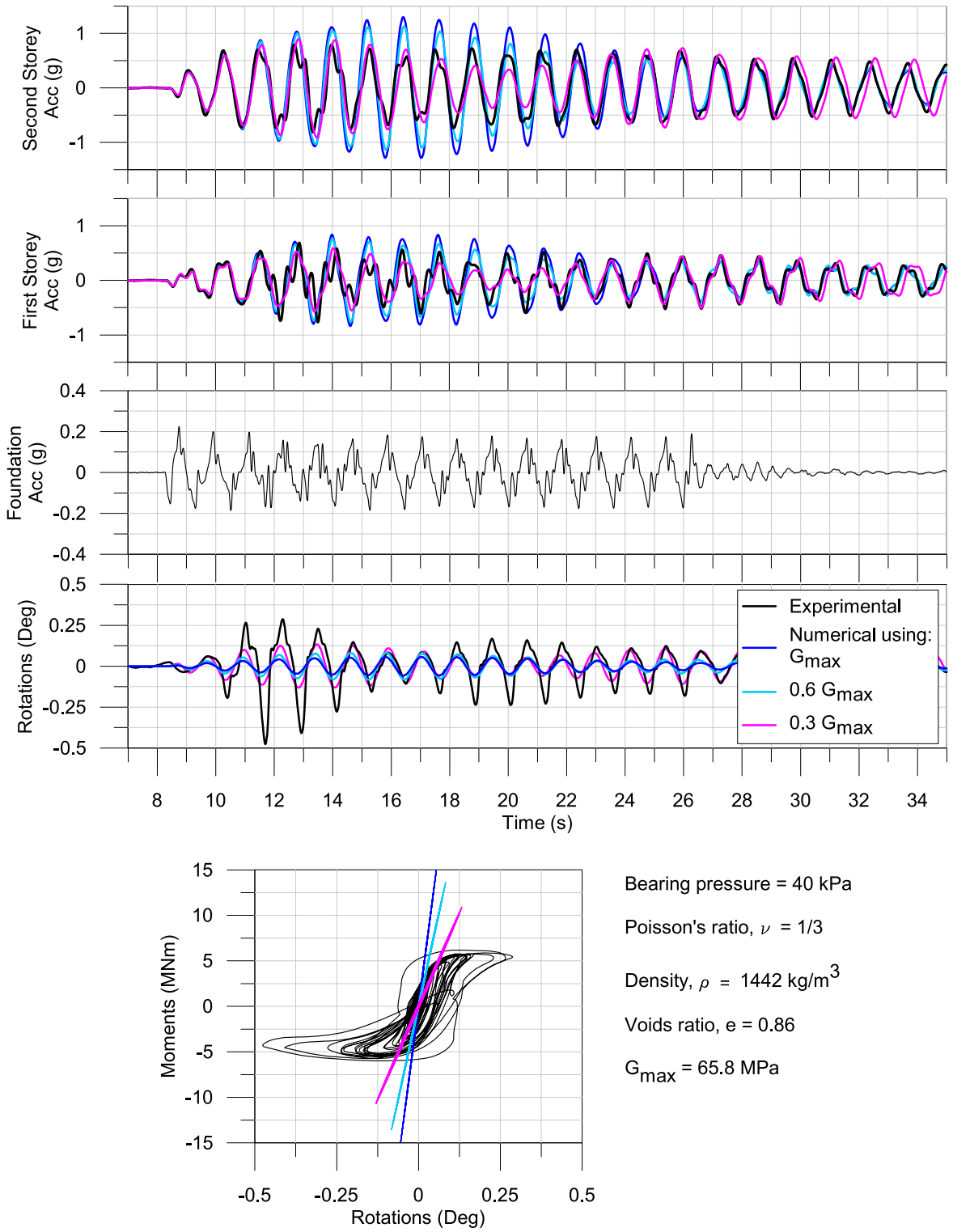

Fig. 7.4 Effect of soil shear modulus variation on numerical predictions for the regular Squat structure with a Light foundation embedded in Loose sand during a strong near resonant frequency excitation.

7.2.2 Hyperbolic Model

Grounded within the framework of mobilised strength design, Heron (2013) proposed an experimentally derived macro-element model that can approximate the dynamic rotational response of a foundation-soil system. Central to this procedure is an experimentally calibrated moment-rotation backbone curve that uses scalar coefficients, R and S, to correlate foundation moments (M) and rotations (θ), to representative values of shear stress (τ_{rep}) and strain (γ_{rep}) in the soil beneath (Heron, 2013):

$$\tau_{rep} = R \times M \tag{7.8}$$

$$\gamma_{rep} = S \times \theta \tag{7.9}$$

Establishing this correlation allows the numerical moment-rotation backbone curve to follow well-established strain-dependant soil stiffness degradation relationships. One such relationship is the one proposed by Oztoprak and Bolton (2013):

$$\frac{G}{G_{max}} = \frac{1}{1 + (\frac{\gamma - \gamma_e}{\gamma_r})^a} \tag{7.10}$$

where γ is shear strain, a, γ_e and γ_r are parameters defined by:

$$a = {U_c}^{-0.075}$$

$$\gamma_e(\%) = (8 \times 10^{-5})\,(\frac{p'}{p_a}) + (6 \times 10^{-4})$$

$$\gamma_r(\%) = 0.008\,(\frac{p'}{p_a}) + (0.032)$$

in which U_c is the coefficient of uniformity of the sand, p' is the mean effective stress, and p_a is a normalising pressure of 100 kPa. For Hostun sand with a U_c of 1.67, the parameter a is equal to 0.96 (Heron, 2013). Table 7.1 summarises the stiffness degradation parameters as computed for each bearing pressure case and sand relative density.

The mathematical Equation for soil shear modulus in 7.10 can be used to link Equations 7.8 and 7.9 to give the following expression for foundation moments (Heron, 2013):

$$M = \frac{G_{max}\,\frac{S}{R}\,\theta}{1 + \left(\frac{S\,|\theta| - \gamma_e}{\gamma_r}\right)^a} \tag{7.11}$$

Table 7.1 Soil shear modulus degradation parameters.

Bearing Pressure	40 kPa		73 kPa	
Relative Density	39 %	84 %	39 %	84 %
***Confining pressure, p' (kPa)**	39.3	41.5	59.4	61.5
****G_{max} (MPa)**	58.9	85.6	72.4	104.3
γ_e **(%)**	0.00063	0.00063	0.00064	0.00065
γ_r **(%)**	0.035	0.035	0.036	0.037

*computed at a depth of $1/4$ times the foundation dimension (Heron, 2013)
**using Equation 7.2

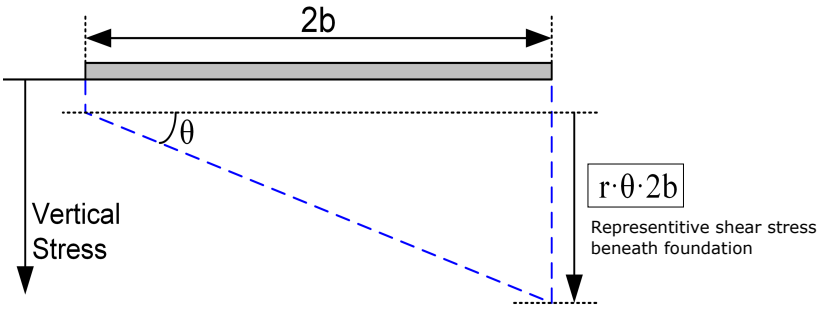

Fig. 7.5 Linear variation of vertical stress assumed beneath the foundation subjected to overturning moments (Heron, 2013).

During seismic shaking, a foundation resists overturning moments from the superstructure by adjusting the vertical stress distribution beneath its surface. Heron (2013) assumes a triangular distribution of stress acting on the soil as shown in Figure 7.5. Representative shear stress is defined by:

$$\tau_{rep} = (f)\ (r)\ (2b\ \theta) \tag{7.12}$$

where r is a scalar that correlates vertical displacements to vertical stresses in the soil, and f is another scalar that correlates vertical stresses into a representative shear stress. Taking moments about the centre of the foundation in Figure 7.5, Heron (2013) derives the following expression for moments:

$$M = \frac{2r\theta\ b^3}{3} \tag{7.13}$$

therefore

$$R(\theta) = \frac{\tau_{rep}}{M} = \frac{3f}{b^2} \tag{7.14}$$

Based on calibrations from experimental moment-rotation loops of centrifuge model structures founded on raft foundations in dry sand, Heron (2013) proposed a value of $f = 1$ for use in Equation 7.14. For blind prediction applications of this model, Heron (2013) proposes the parameters stated in Table 7.2. These values have been selected following a statistical analysis conducted in that study using their entire experimental subset of moment-rotation traces. With these parameters defined, a numerical foundation moment-rotation backbone curve can be generated using Equation 7.11.

Table 7.2 Selected model parameters from Heron (2013)

Strain scalar (S)	0.515
Stress scalar (R)	$3 / b^2$
Hyperbolic degradation parameter (a)	0.96

The suitability of implementing such a hyperbolic model for blind-prediction purposes is demonstrated in Figures 7.6 and 7.7, for weak and strong near resonant frequency excitations respectively. Each red backbone curve is the result of inputting experimental rotations recorded in this study, into Equation 7.11, using the parameters defined in Tables 7.1 and 7.2, to output a predicted moment value. Considering the statistical nature of this hyperbolic model, and its underlying simple assumptions and correlations, the red numerical backbone curves show promising applications.

As anticipated, there are instances in Figures 7.6 and 7.7 where the hyperbolic backbone curve traces perfectly over the experimental moment-rotation loops, and other cases where the model over predicts both, peak moments and the small-rotation stiffness. These two variables are closely associated with the chosen value of the strain scalar (S). It is also important to highlight that there are other sources of experimental uncertainties that can contribute to the observed dissimilarities in Figures 7.6 and 7.7. These typically include the time-varying changes in foundation width (b) as the foundation rocks during experimental shaking, and local densification of sand beneath the foundation; both of these can change the stiffness of the overall foundation-soil system, and are not accounted for in the hyperbolic model used here.

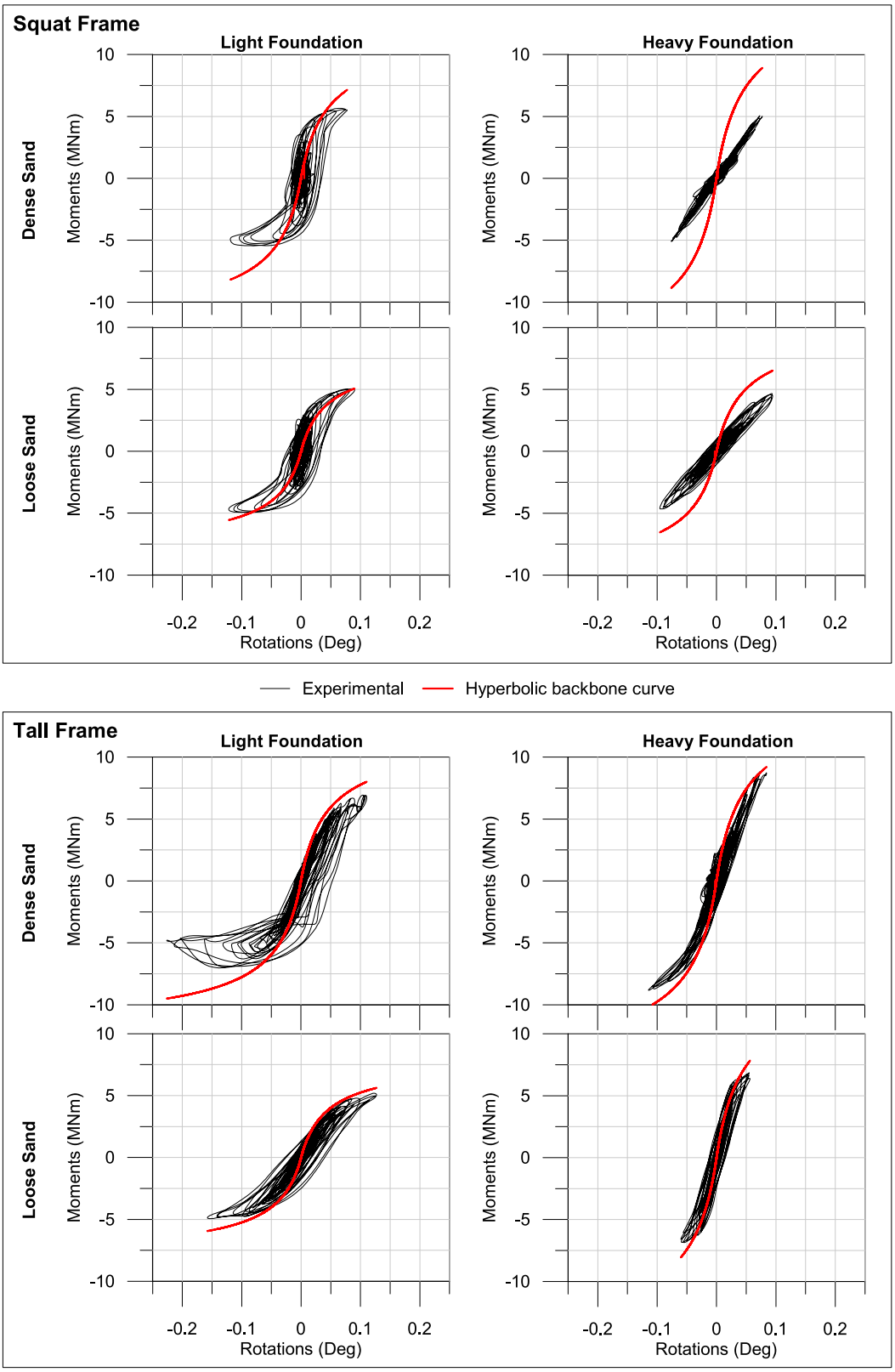

Fig. 7.6 Comparing the hyperbolic backbone curve to experimental moment-rotation loops for the regular squat and tall frames during weak near resonant frequency excitations.

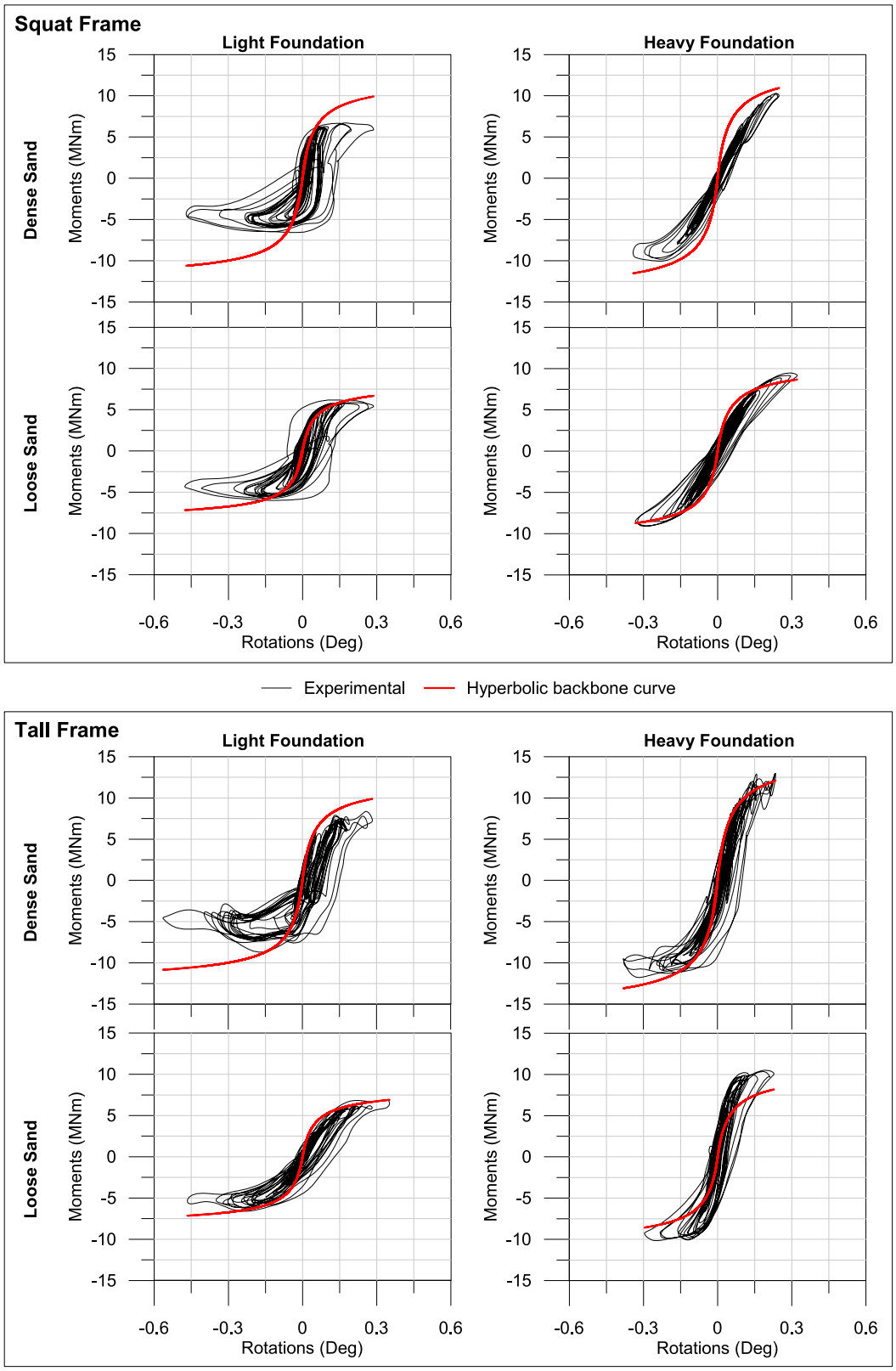

Fig. 7.7 Comparing the hyperbolic backbone curve to experimental moment-rotation loops for the regular squat and tall frames during strong near resonant frequency excitations.

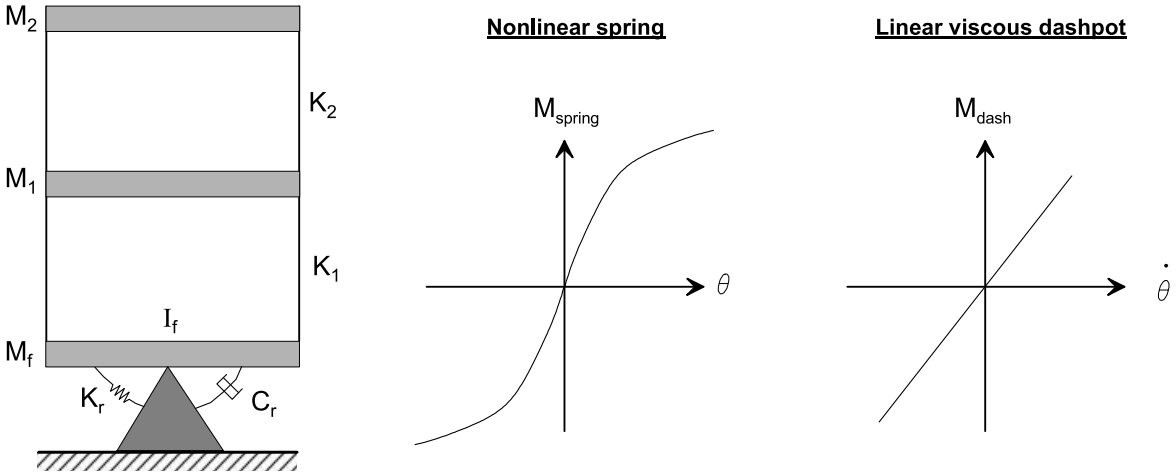

Fig. 7.8 Visualising the hyperbolic moment-rotation model as a parallel assembly of a nonlinear soil spring and a linear dashpot at the foundation.

The envisaged soil-structure system, encompassing this hyperbolic model, is visualised in Figure 7.8. Mathematically, the system can be described by:

$$[M]\{\ddot{u}\} + [C]\{\dot{u}\} + [K]\{u\} = -\ddot{u}_{g,i+1}\begin{Bmatrix} m_1 \\ m_2 \\ m_1h_1 + m_2h_2 \end{Bmatrix}$$

substituting for the mass, damping and stiffness matrices,

$$\begin{bmatrix} m_1 & 0 & m_1h_1 \\ 0 & m_2 & m_2h_2 \\ m_1h_1 & m_2h_2 & I_{total} \end{bmatrix}\begin{Bmatrix} \ddot{u}_1 \\ \ddot{u}_2 \\ \ddot{\theta} \end{Bmatrix}_{i+1} + \begin{bmatrix} c_1+c_2 & -c_2 & 0 \\ -c_2 & c_2 & 0 \\ 0 & 0 & C_r \end{bmatrix}\begin{Bmatrix} \dot{u}_1 \\ \dot{u}_2 \\ \dot{\theta} \end{Bmatrix}_{i+1} + \begin{bmatrix} k_1+k_2 & -k_2 & 0 \\ -k_2 & k_2 & 0 \\ 0 & 0 & K_r \end{bmatrix}\begin{Bmatrix} u_1 \\ u_2 \\ \theta \end{Bmatrix}_{i+1}$$

$$= -\ddot{u}_{g,i+1}\begin{Bmatrix} m_1 \\ m_2 \\ m_1h_1 + m_2h_2 \end{Bmatrix} \tag{7.15}$$

where h are the distances from the centres of gravity of the floors to the base of the foundation, and K_r is the tangential stiffness of the nonlinear soil spring at a rotation θ.

As shown in Figure 7.8, a linear dashpot element is inserted in-parallel combination with the nonlinear spring. The dashpot is mainly for numerical stability, and is not intended to accurately represent moment-rotation hysteresis at the foundation-soil interface. The damping coefficient (C_r) of the dashpot is set to ensure the global frame rotational degree of

freedom has an equivalent viscous damping ratio of $\zeta = 5\ \%$:

$$C_r = 2\zeta \sqrt{K_{r,max}\, I_{total}} \tag{7.16}$$

where

$$K_{r,max} = G_{max}\, \frac{S}{R}$$

$$I_{total} = I_f + m_1 {h_1}^2 + m_2 {h_2}^2$$

where G_{max} is the small-strain shear modulus of soil, $K_{r,max}$ is the nonlinear soil spring stiffness at small rotations, and I_f is the mass moment of inertia of the foundation.

Application of this model in numerical integration requires an iterative algorithm that takes into account the nonlinear moment-rotation relationship of the soil spring. Newmark's nonlinear integration scheme (Chopra, 2012), briefly introduced in section 4.4 of Chapter 4, is used here to solve the system of equations in 7.15. The procedure is summarised in Figure 7.9. Central to this procedure is the iteration in step 3.4, which incrementally updates the system degrees of freedom $\{u\}$, and internal resisting forces $\{F_s\}$, at each time step until equilibrium with external forces is achieved; here, iteration is stopped when the residual moment drops below 0.001 Nm. The tangential rotational stiffness of the soil spring is updated in step 3.4.3 for every iteration of rotations, following the numerical backbone curve defined in Equation 7.11.

Results from this numerical integration are presented in Figures 7.10 to 7.12, for the regular squat and tall structures during different base excitations. For weak sinusoidal input motions, application of the hyperbolic model results in lower, albeit satisfactory, predictions of total floor accelerations as shown in Figure 7.10. The same is observed for the multi-frequency component excitations in Figure 7.11. The consistent under prediction of absolute floor accelerations is believed to be a consequence of the rudimentary treatment of foundation damping forces by the numerical model. By not scaling the moment-rotation backbone curve for loading / unloading during dynamic rotations (i.e. not implementing Masing rules for hysteresis), numerical estimates of instantaneous moment reactions at the foundation will be different than what is recorded experimentally during shaking. For instance, during the loading branch of a moment-rotation cycle, underestimating foundation damping forces in the numerical model can lead to lower instantaneous foundation moment reactions compared to what is measured in the experiments. A consequence of this would be lower floor acceleration predictions in the superstructure. Although not significant, evidence of this is seen across the time history traces presented in Figures 7.10 to 7.12.

1. Problem Definition

1.1 Setup system mass [M] and stiffness [K] matrices

1.2 Compute undamped natural frequencies

1.3 Assume Rayleigh damping to construct damping matrix [C]

1.4 Define forcing vector {p} for base excitation

2. Initialising conditions for integration, i = 0

2.1 Time-stepping integration parameters for linear acceleration
$\gamma = 1/2$, $\beta = 1/6$

2.2 Compute Newmark integration constants: a_1, a_2, and a_3

2.3 Initial displacement, velocity, and acceleration vectors

$\{u\}=\{\dot{u}\}=\{\ddot{u}\}=\{0\}$

2.4 Assemble dynamic stiffness matrix $[\hat{k}] = [K] + a_1$

3. At each time increment , i = 1, 2, 3, ...

3.1 Compute $\{\hat{p}_{i+1}\}$

3.2 Initialise for nonlinear iteration, j=1

3.2.1 $\{u_{i+1}\}^{(j)} = \{u_i\}$, $\{\dot{u}_{i+1}\}^{(j)} = \{\dot{u}_i\}$

3.2.2 System restoring force $\{F_{S,i+1}\}^{(j)} = \{F_{S,i}\}$

3.3 Compute Residual force vector, $\{\hat{R}_{i+1}\}^{(j)}$

3.4 If residual moments < 0.001 Nm, go to step 3.5, else apply iteration j=2,3,...

3.4.1 Compute {du} = $[\hat{k}]^{-1}\{\hat{R}_{i+1}\}^{(j)}$

3.4.2 Update displacement and velocity vectors

$\{u_{i+1}\}^{(j)}$, $\{\dot{u}_{i+1}\}^{(j)}$

3.4.3 Update stiffness matrix $[K]^{(j)}$ with the tangential stiffness of the nonlinear soil spring

3.4.4 Update system restoring force $\{F_{S,i+1}\}^{(j)}$

3.4.5 Update dynamic stiffness matrix $[\hat{k}]^{(j)} = [K]^{(j)} + a_1$

3.4.6 Update Residual force vector $\{\hat{R}_{i+1}\}^{(j)}$

3.4.7 Check convergence of residual moments

3.5 Compute acceleration $\{\ddot{u}_{i+1}\}$

4. Repeat Step 3 for the next time step i + 1

Fig. 7.9 Newmark solution algorithm for a regular frame with a hyperbolic foundation-soil model.

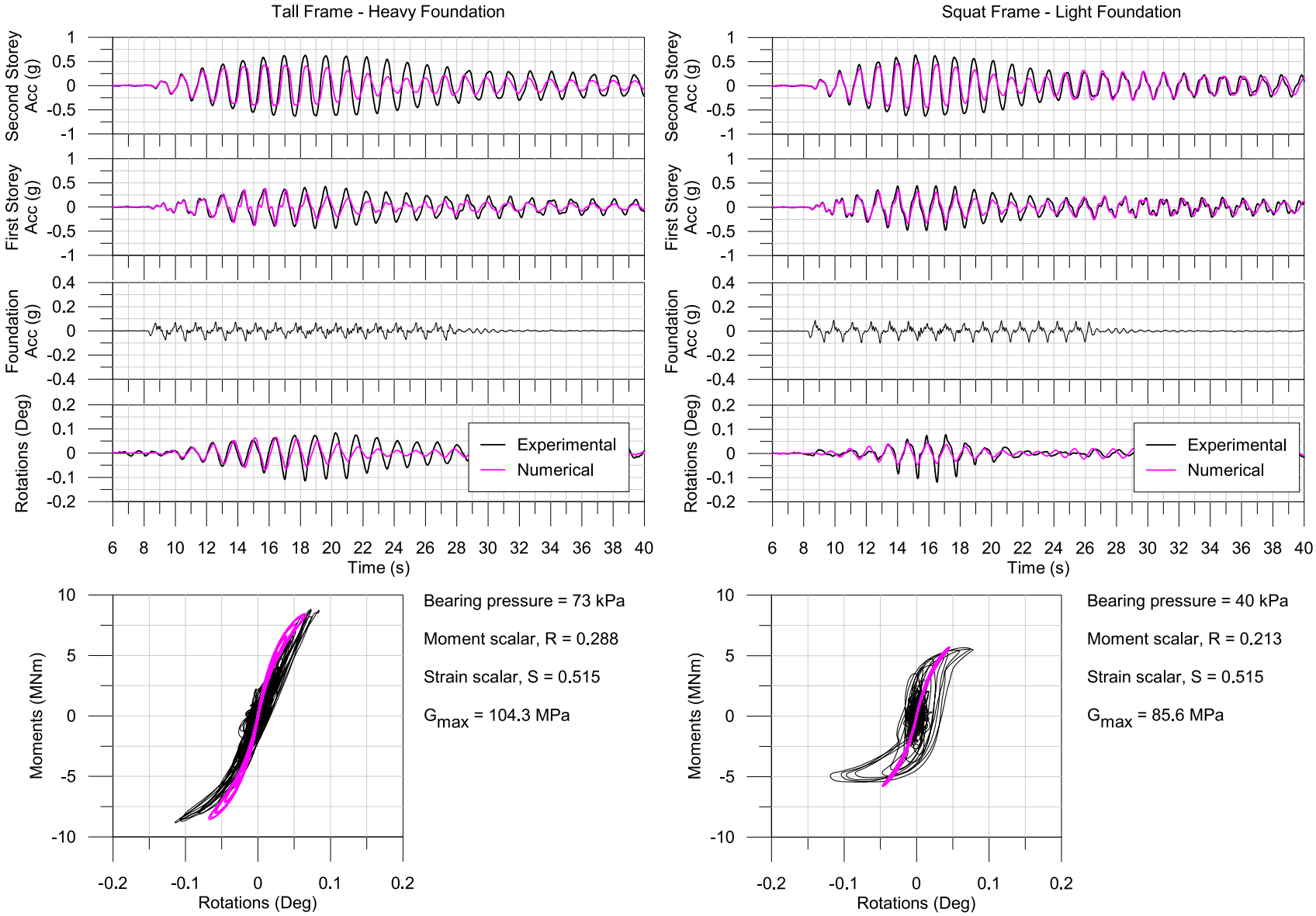

Fig. 7.10 Numerical predictions using the Heron (2013) hyperbolic model for the regular Tall and Squat structures embedded in Dense sand during weak near resonant frequency excitations.

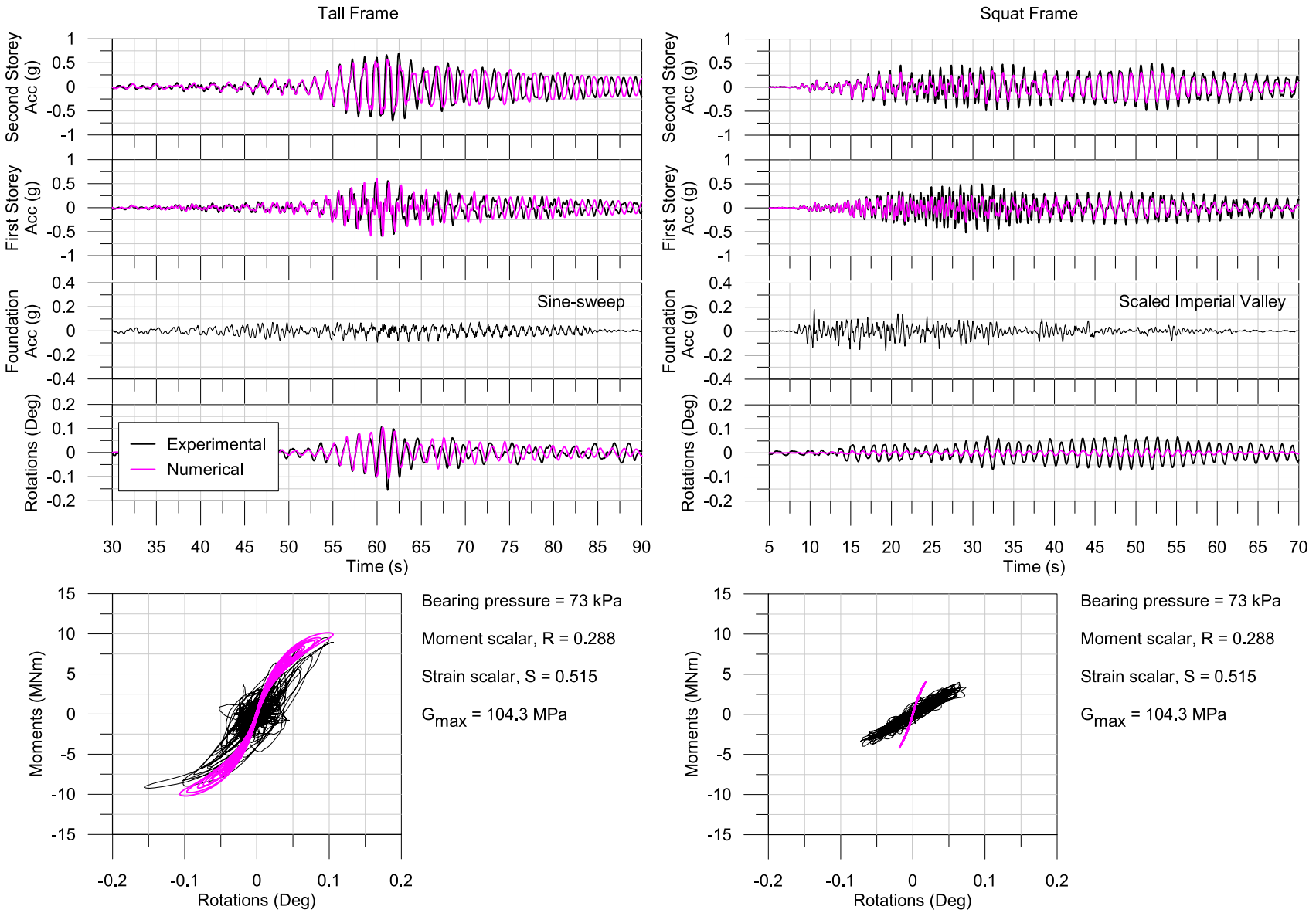

Fig. 7.11 Numerical predictions using the Heron (2013) hyperbolic model for the regular Tall and Squat structures with Heavy foundations embedded in Dense sand during sine-sweep and scaled Imperial Valley excitations respectively.

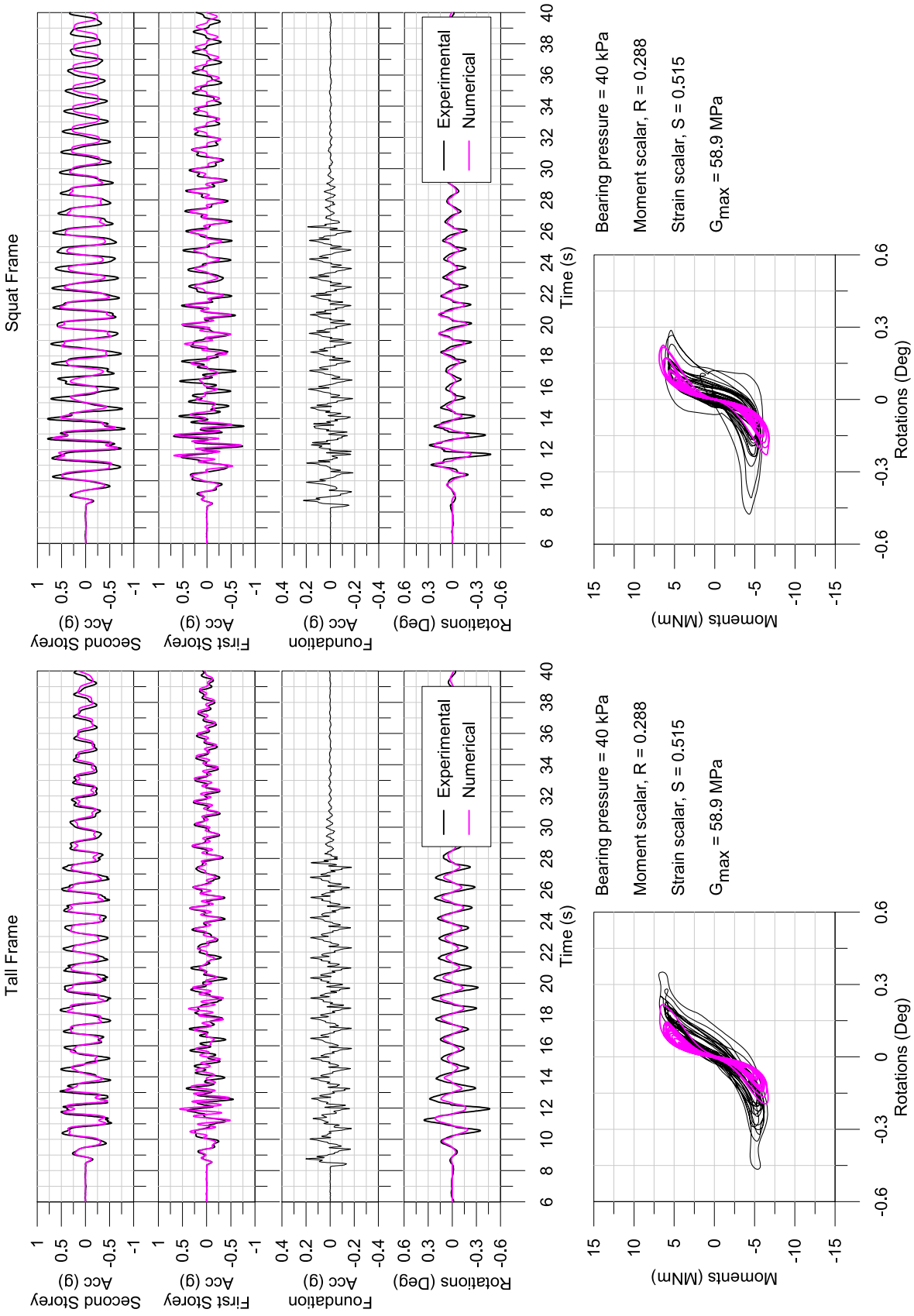

Fig. 7.12 Numerical predictions using the Heron (2013) hyperbolic model for the regular Tall and Squat structures with Light foundations embedded in Loose sand during strong near resonant frequency excitations.

For the strong excitations in Figure 7.12, the model successfully captures the degrading rotational stiffness behaviour seen in experimental moment-rotation loops, and results in reasonable estimates of peak floor accelerations, peak moments and dynamic rotations, without the need for manual user intervention to reduce soil shear modulus. It is important to highlight however, that peak rotations are almost always underestimated for the hyperbolic foundation-soil model implemented here. This is believed to be the result of not accounting for foundation lift-off in the numerical model.

Also, incorrect numerical representation of foundation-soil hysteresis appears to overestimate higher frequency contributions to the overall system response; evidence of a slightly amplified second mode response is clearly visible in the first storey numerical acceleration traces in Figure 7.12.

7.3 Frames with Inter-storey Oil Dampers

The suitability of making blind dynamic response predictions for the regular frames without dampers using the hyperbolic foundation-soil model was investigated in the previous section. Here, the numerical model is expanded to take into account the nonlinear dashpots in the superstructure. The problem is visualised in Figure 7.13.

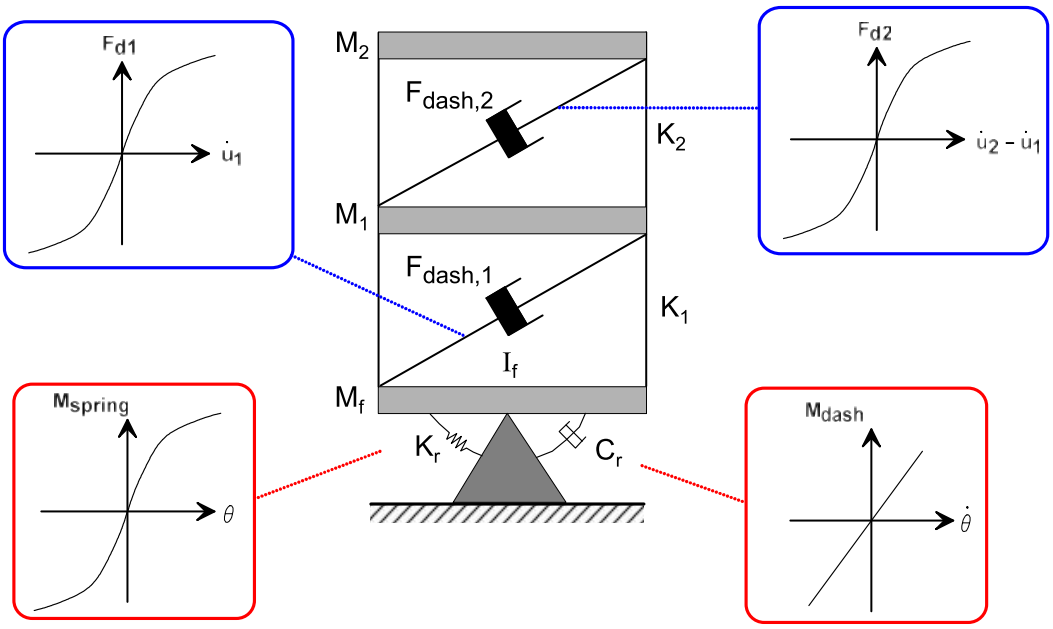

Fig. 7.13 Visualising the damped structures as 2-DOF systems with nonlinear dashpots, and a hyperbolic foundation-soil model inserted at the centre of the foundation.

Mathematically, Equation 7.15 is still applicable, with an additional vector for the nonlinear dashpot forces $\{F_d\}$, added to the internal resisting forces in the system. Newmark's nonlinear integration scheme, as described in Figure 7.9 is used, with an additional step in the iterations in step 3.4 to update the dashpot forces as new velocity estimates are computed; the experimentally derived piece-wise dashpot equations derived in section 4.3 of Chapter 4 are used for this purpose. Some results from the numerical integration are presented in Figures 7.14 to 7.18 for both, the damped squat and tall structures.

The fixed base numerical predictions for the damped frames overall appear to be satisfactory. This is inline with the findings of Chapters 5 and 6, in which frames with supplemental oil dampers demonstrated less susceptibility to base flexibility effects compared to their regular bare frame counterparts, at least for the moderate input motion intensities tested in this investigation. However, there are benefits to incorporating a hyperbolic foundation-soil model for the case of a slender damped structure prone to considerable rocking, as illustrated by the tall frame in Figure 7.17, or for the case of a damped structure fitted with light supplemental oil damping, as illustrated by the squat frame with D3 dampers in Figure 7.18; for the latter case, inertial interaction at the foundation-soil interface of the lightly damped structure can still be significant.

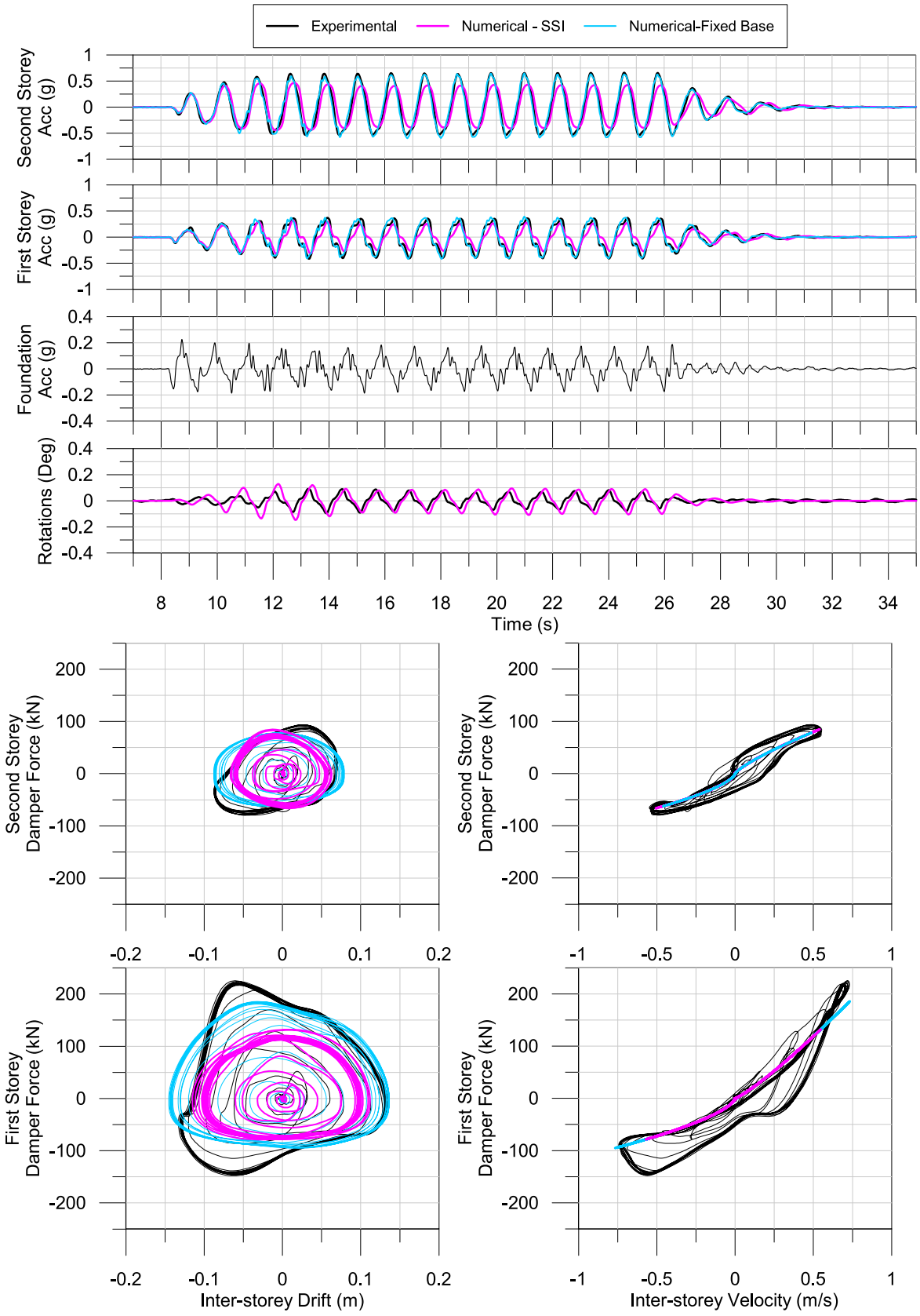

Fig. 7.14 Numerical predictions for the damped Squat structure with a Light foundation and D2 dampers (medium damping), embedded in Loose sand during a strong near resonant frequency excitation.

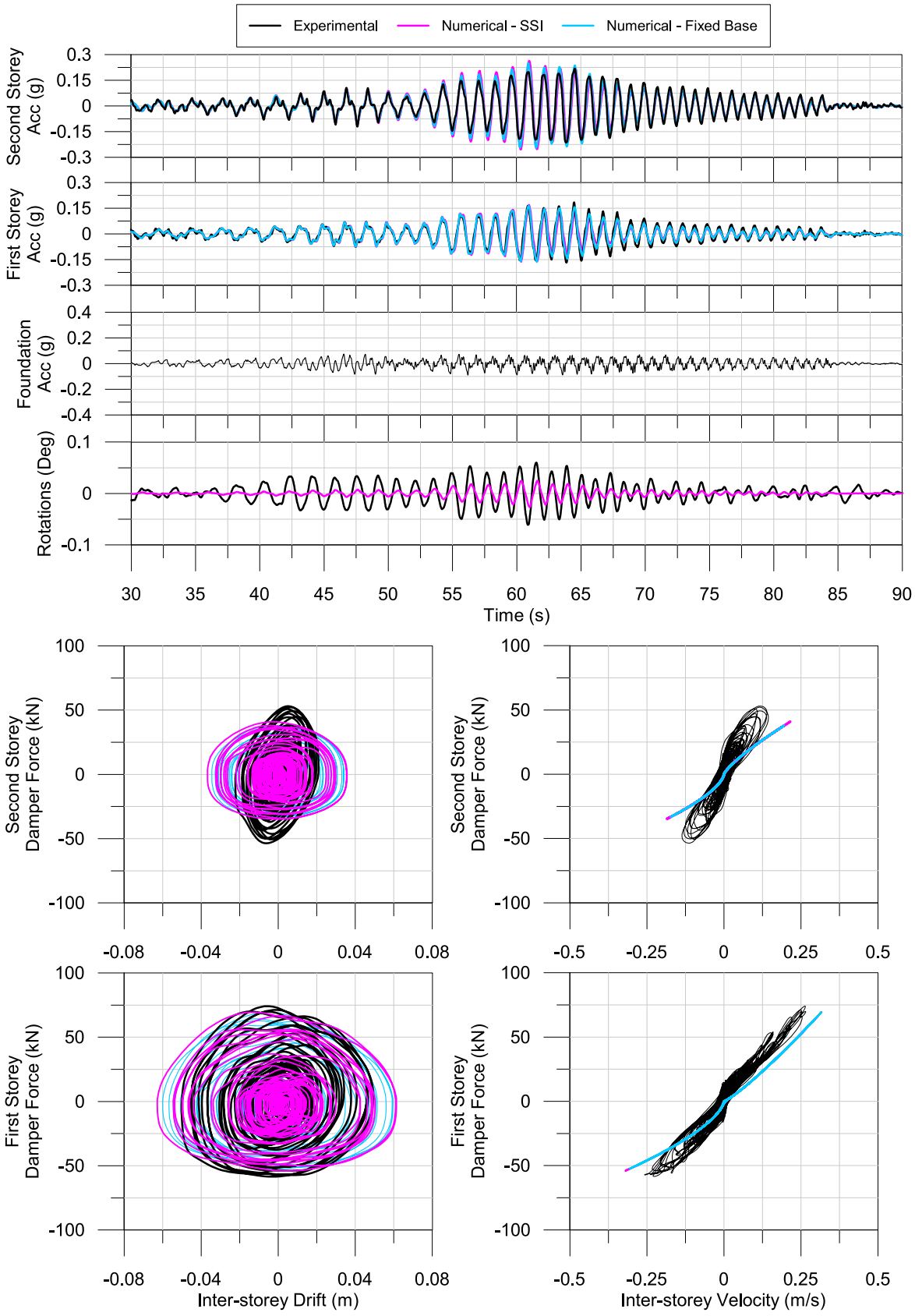

Fig. 7.15 Numerical predictions for the damped Squat structure with a Heavy foundation and D2 dampers (medium damping), embedded in Loose sand during a sine-sweep excitation.

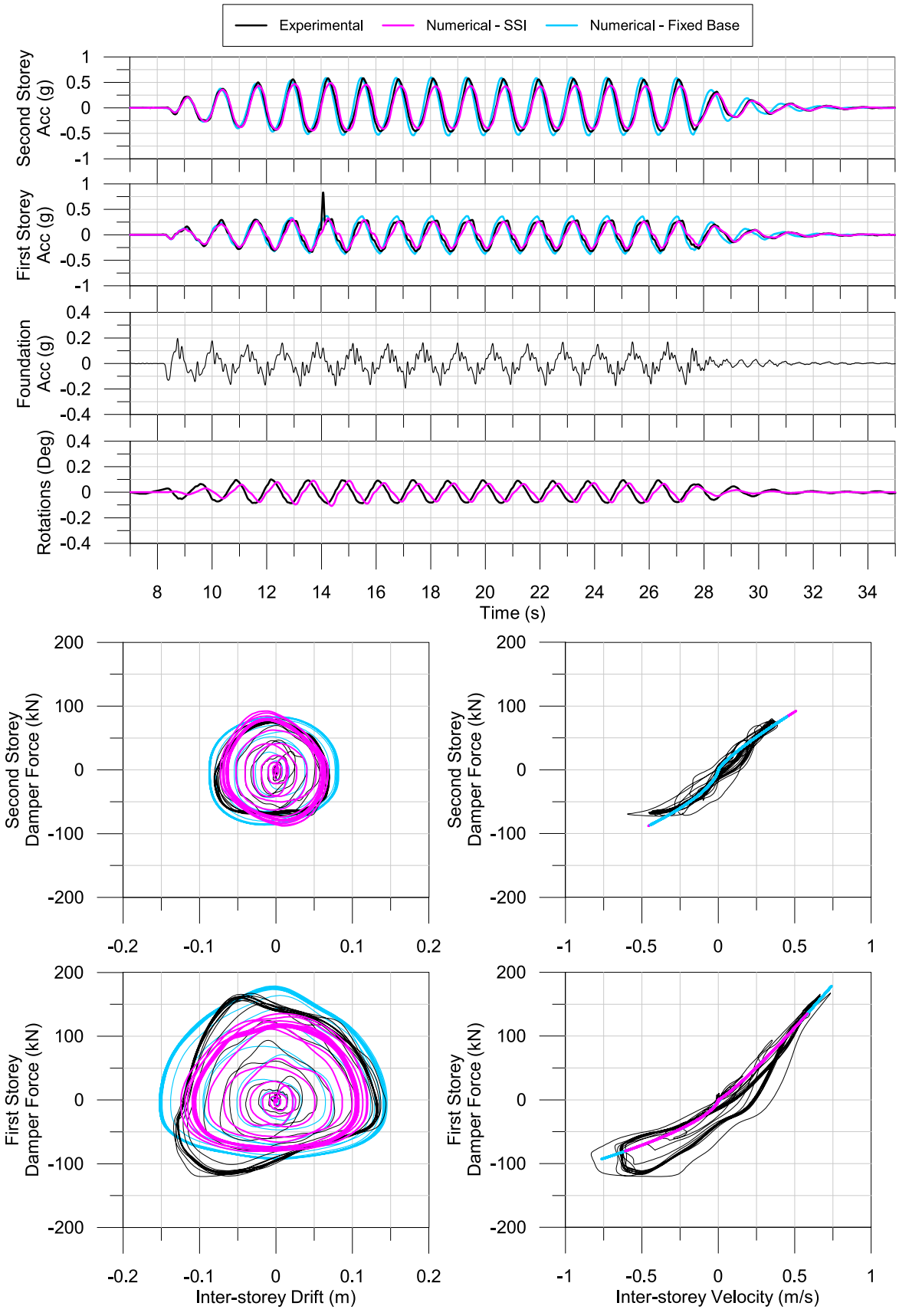

Fig. 7.16 Numerical predictions for the damped Tall structure with a Heavy foundation and D2 dampers (medium damping), embedded in Dense sand during a strong near resonant frequency excitation.

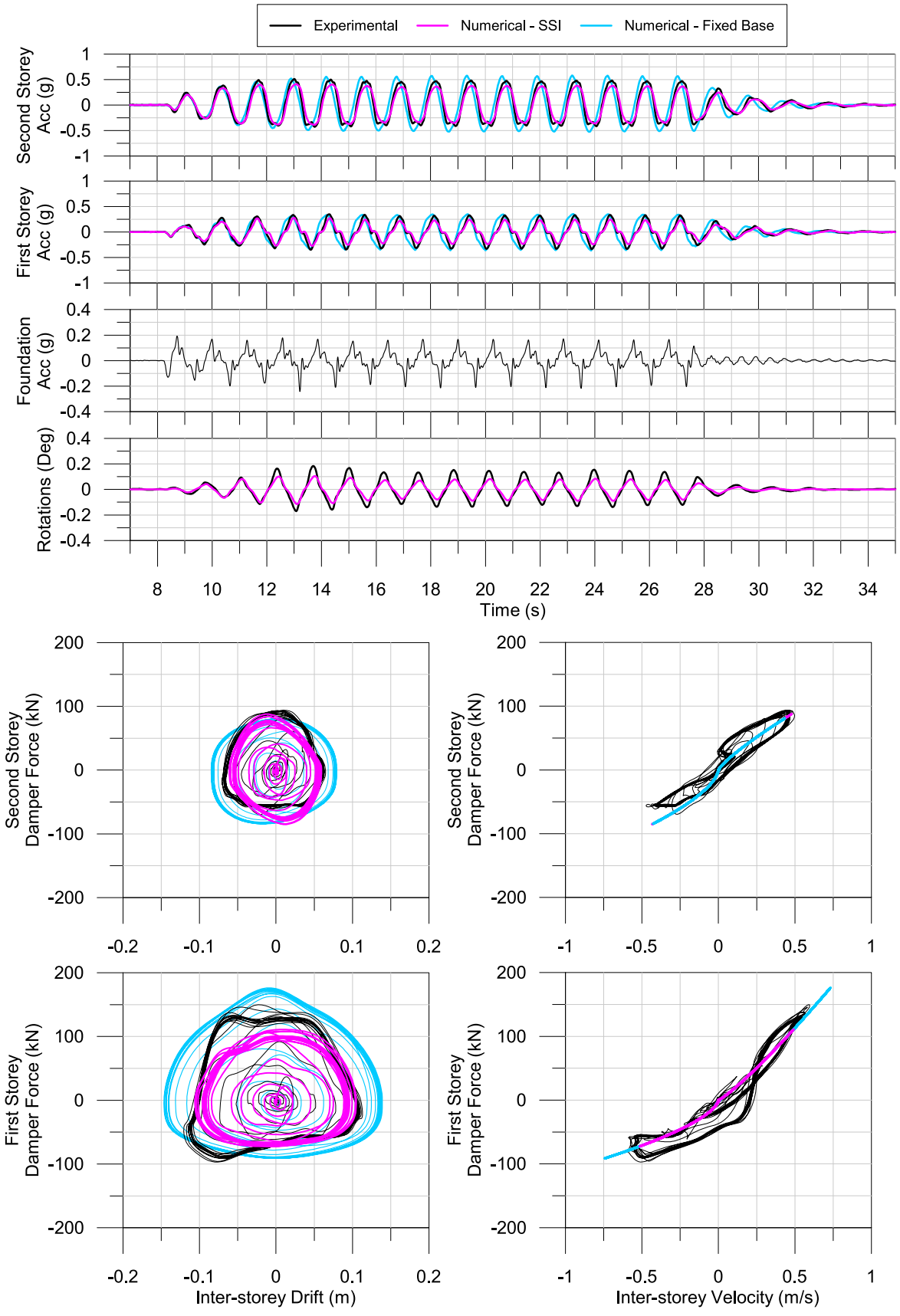

Fig. 7.17 Numerical predictions for the damped Tall structure with a Light foundation and D2 dampers (medium damping), embedded in Dense sand during a strong near resonant frequency excitation.

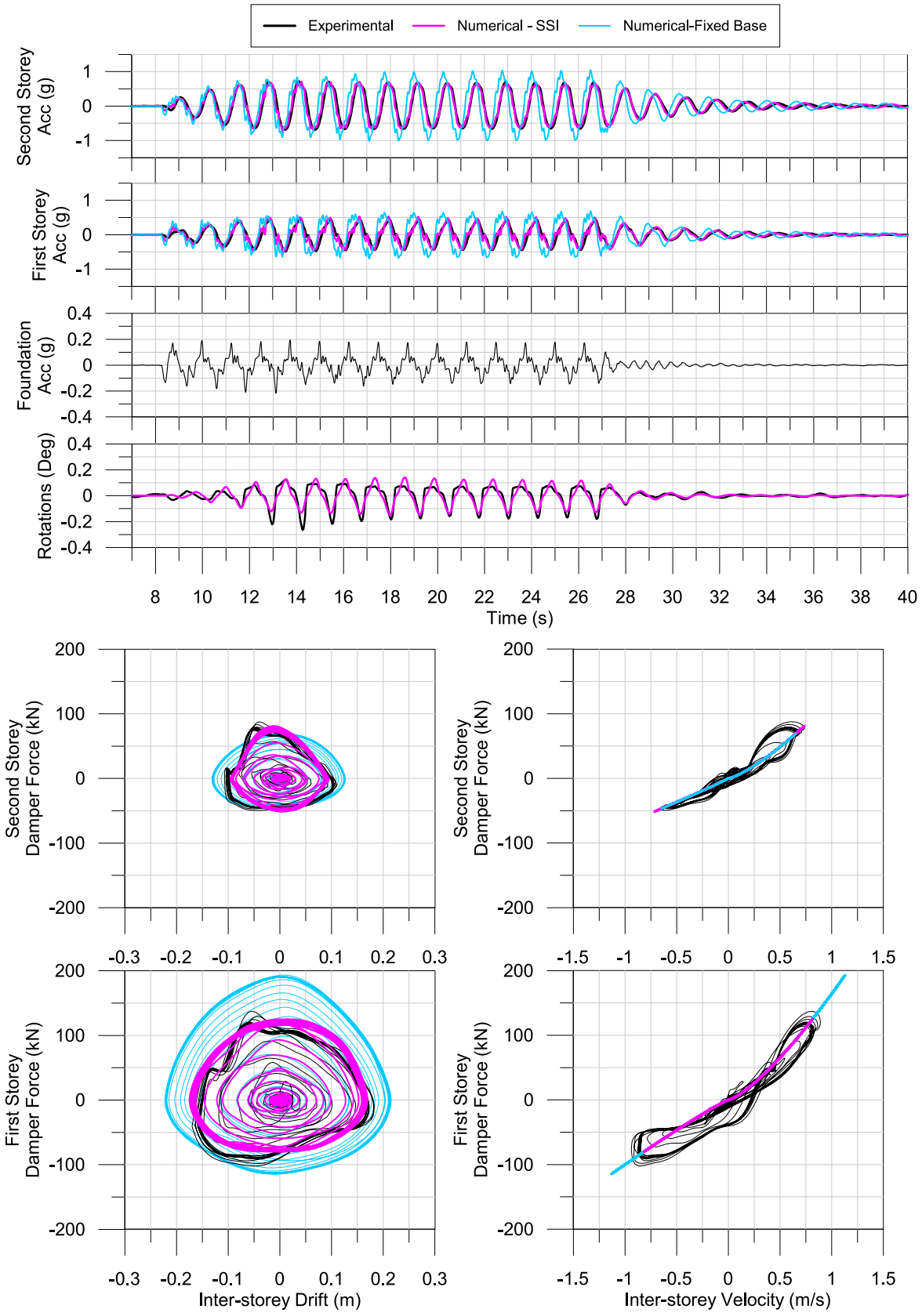

Fig. 7.18 Numerical predictions for the damped Squat structure with a Light foundation and D3 dampers (light damping), embedded in Dense sand during a strong near resonant frequency excitation.

Implementation of a discrete-element model, with a hyperbolic foundation-soil representation, would enable blind predictions to be made for stronger input motions that have not been fired in the centrifuge. Figures 7.19 and 7.20 present examples of such time history predictions for the bare and damped structures during scaled realistic excitations; the dampers assumed in these structures follow the D2 dashpot equations derived in Chapter 4.

The traces in Figure 7.19 show the beneficial aspects of accounting for base flexibility when it comes to predicting response for the regular structures. Figure 7.20 illustrates how input motion characteristics can influence the decision on whether or not to install oil dampers in a structure; for sites where long duration excitations such as the scaled Imperial Valley motion are expected, installation of oil dampers will result in tangible improvements to the dynamic response. For sites where near fault pulse-like excitations such as Kocaeli in Figure 7.20 are predicted, a detailed SSI analysis for the regular bare structure is warranted prior to considering dampers.

The lumped-parameter models can also be used to conduct early stage parametric studies. Structural deformations in a regular frame can be estimated for a specific input motion intensity and frequency content, prior to deciding on the need for supplemental oil dampers. Figure 7.21 presents results for the tall structures embedded in loose sand; foundation input accelerations recorded during weak near resonant frequency excitations are used as reference input motions into the models. The input motion is amplified by multipliers to investigate the effects of foundation-soil nonlinearity during stronger excitations.

Using normalised peak inter-storey drifts as performance indices, results in Figure 7.21 correctly capture the convergence of normalised drifts between the regular and the damped structures for stronger base excitations. The effects of reducing soil shear modulus (upon shallow embedment into cohesive soils for instance) can be approximated as shown by the bottom plots in Figure 7.21. Intuitively, the softer the ground, the closer the dynamic response of the regular frame is to its damped counterpart.

Installing oil dampers with different damping characteristics can also be investigated as shown in Figure 7.22; results from the numerical models predict that the effect of different damper properties (i.e. damper sizes) on normalised peak inter-storey drifts becomes less influential as shaking intensity increases. Trends from the parametric studies in Figures 7.21 and 7.22 are generic examples demonstrating the potential applications of such a simplified tool during preliminary design.

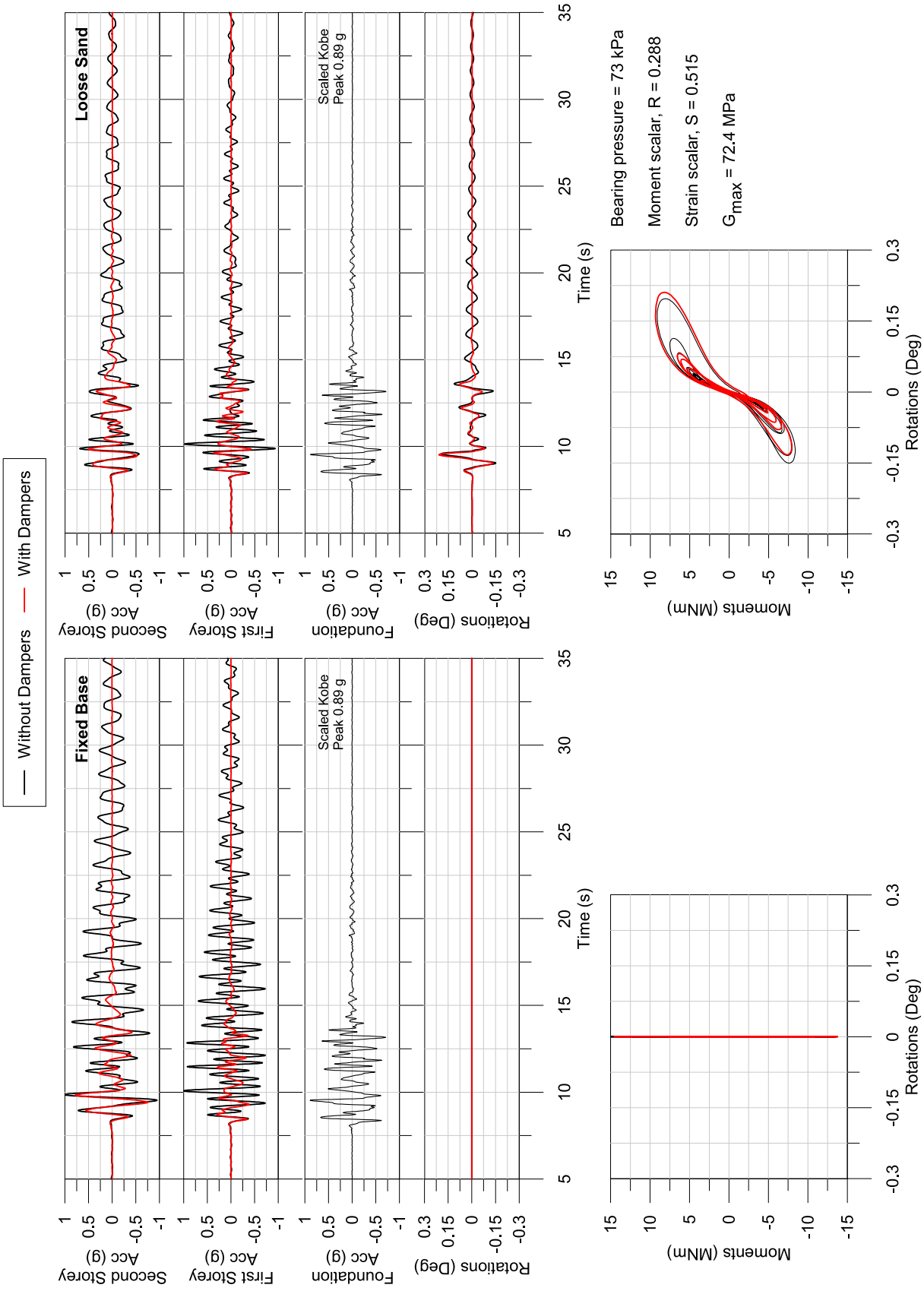

Fig. 7.19 Time history predictions from lumped-parameter models for the Tall structures during a theoretical scaled Kobe excitation with fixed-base conditions, and embedment of Heavy foundations into dry Loose sand.

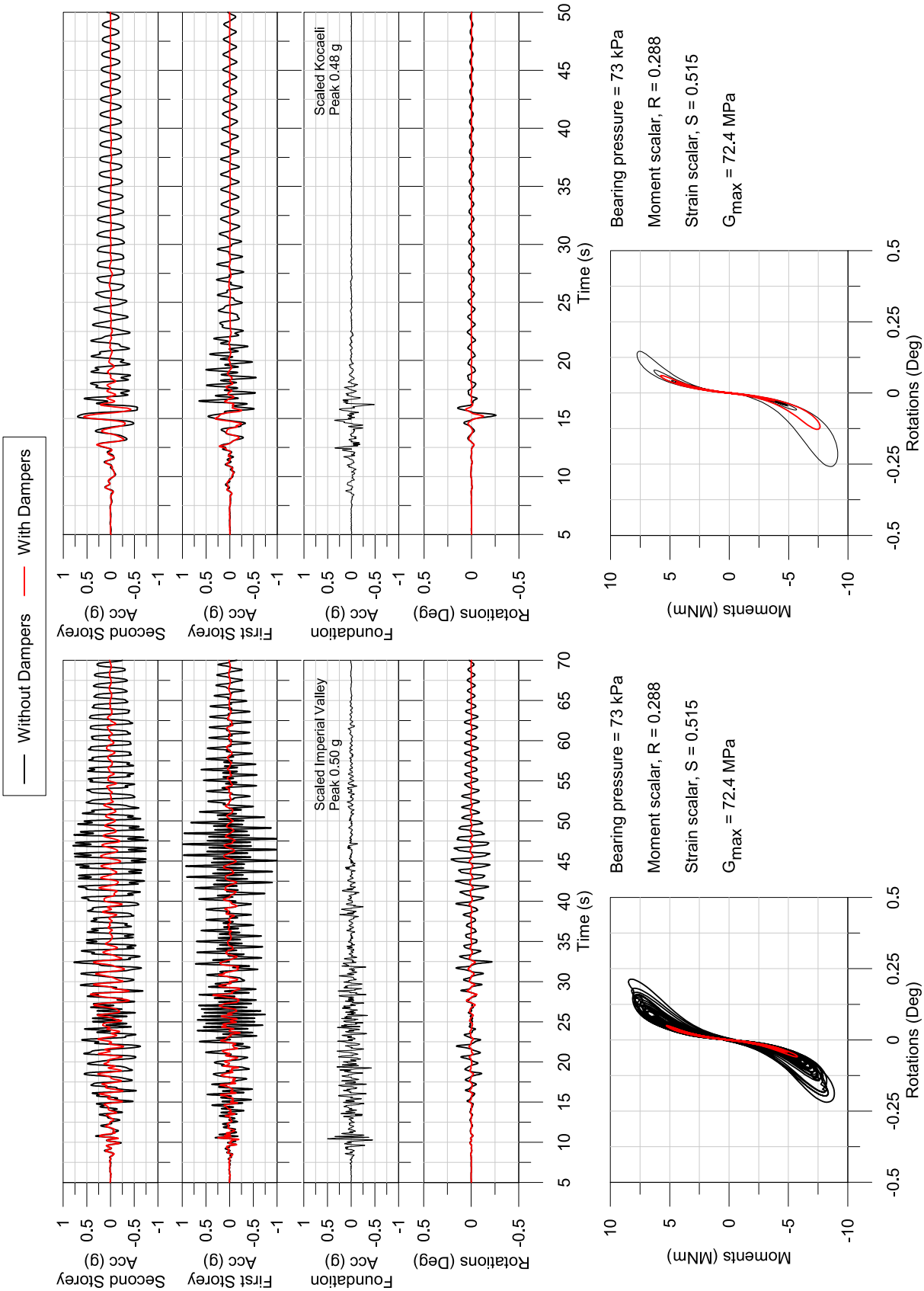

Fig. 7.20 Time history predictions from lumped-parameter models for the Squat structures during theoretical scaled Imperial Valley and Kocaeli excitations, for the case of Heavy foundations embedded in dry Loose sand.

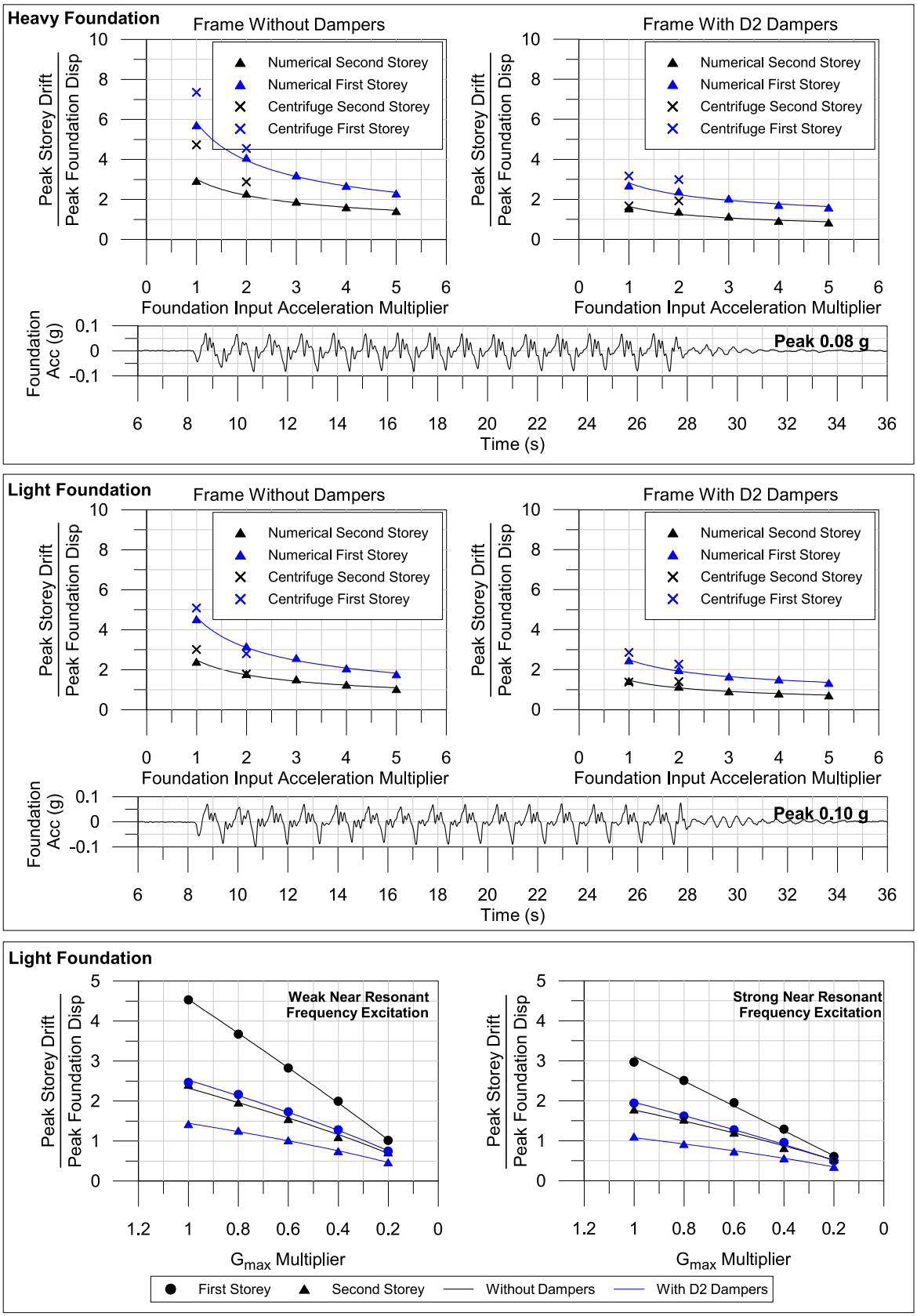

Fig. 7.21 Investigating the effects of foundation input motion intensity and soil small-strain shear modulus of soil on normalised peak inter-storey drifts during embedment in loose sand.

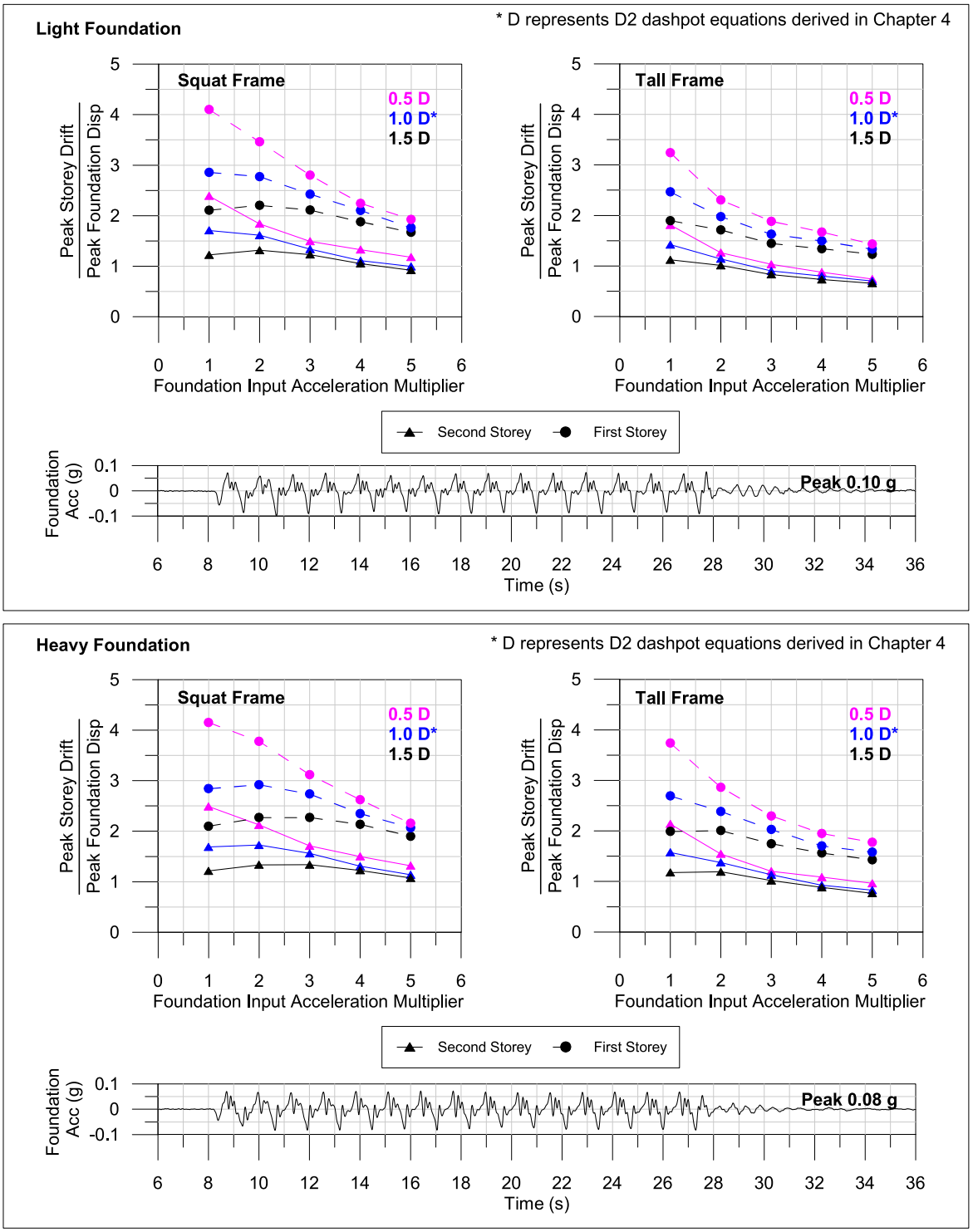

Fig. 7.22 Investigating the effects of foundation input motion intensity and different damper properties on normalised peak inter-storey drifts during embedment in loose sand.

7.4 Summary

This chapter demonstrates the applicability of using conventional time domain analysis methods to predict results from the dynamic soil-structure interaction of regular and damped structures as observed in the centrifuge. Addressing nonlinearities in a simplified mathematical model, founded on established engineering principles, can prove to be very useful during early stage design for cases where the need for oil dampers is still being assessed, or for when the size and distribution of oil dampers in a structure is still being evaluated.

During the development of such models, it was found that commonly used lumped-parameter foundation-soil assemblies, such as the ones proposed by Wolf (1988), may be satisfactory for weak intensity excitations. However, their empirical origin as analogues to elastic halfspace solutions limits their predictive properties, particularly for strong excitations that trigger considerable nonlinearity at the foundation-soil interface.

The hyperbolic model proposed by Heron et al. (2015) proved to possess better predictive abilities than that of the lumped-parameter model. Despite its statistical origins and reliance on simplified correlation factors, the experimentally derived moment-rotation backbone curve for foundations on dry sand resulted in satisfactory predictions of peak seismic overturning moments, foundation rotations, and absolute floor accelerations for the bare frames tested in the centrifuge. Even though Heron (2013) expanded the mathematics to include foundation lift-off and modified Masing rules for foundation-soil hysteresis, these advancements were not implemented here to keep the model as simple and as generalised as possible for blind prediction purposes. There is potential for further experimental testing with different soil types, frame aspect ratios, etc. to come-up with a larger experimental database for refined generalised parameters that would encompass such complex mechanisms.

It was demonstrated in previous chapters that the installation of oil dampers in the superstructure reduces inertial interaction at the foundation-soil interface. For the intensity of input motions fired in this investigation, numerical response predictions reported in this chapter assuming a fixed base condition, resulted in satisfactory predictions for the damped squat structures equipped with medium to heavy damping, regardless of the foundation bearing pressures. The same was observed for the case of the tall frame equipped with medium damping and a stiff (i.e. heavy) foundation system.

Implementation of the hyperbolic foundation-soil model to damped structures was found to give more accurate predictions for the case of damped structures equipped with light damping, and for the case of a tall structure with a light foundation. Damped frames with lower levels of supplemental damping, and / or higher centres of gravity, will provoke greater inertial interaction at the foundation-soil interface during shaking; the greater the inherent tendency of a damped frame to rock, the more suitable would be the application of the hyperbolic foundation-soil model when making predictions.

Overall, considering the simplicity of its underlying principles, and the ease with which it can be coded into mathematical softwares, the proposed mathematical model for the soil-structure system (with and without inter-storey oil dampers) can see promising applications during early stage design. Further work would be required to validate it for different soil conditions and number of floors in the superstructure.

Chapter 8

Conclusions

This research presented one of the first experimental attempts at studying the dynamic soil-structure interaction of damped structures fitted with inter-storey oil dampers in a geotechnical centrifuge. Concurrent dynamic testing of shallow founded damped structures with their undamped bare counterparts in dry sand beds allowed for a unique comparison to be made between fitting costly supplemental damping into a superstructure, as opposed to utilising natural energy dissipation at the foundation-soil interface.

The experimental programme examined different base fixities for the structures, varying support conditions from fully rigid fixed base, to shallow embedment of raft foundations into dry dense and loose sand beds. Structural aspect ratios and soil bearing pressures were also varied. Acceleration and force instrumentation of the regular and damped structures permitted valuable examination of experimental foundation moment-rotation loops, inter-storey drifts, and tracking of experimental oil damper hysteresis across the different aspect ratios and base fixity conditions tested.

This chapter presents a summary of the findings reported in this study, and potential implications for practising engineers who are considering the use of such seismic mitigation technology. Finally, recommendations are made for further work in this field.

8.1 Research Findings

The findings summarised in section 8.1.1 pertain to a comparison of the seismic performance of structures, with and without inter-storey oil dampers. Section 8.1.2 summarises more specifically how dynamic soil-structure interaction influenced the response of the damped structures.

8.1.1 Performance With & Without Oil Dampers

For almost all of the excitations fired in this investigation, the frames equipped with inter-storey oil dampers performed better in terms of total floor accelerations, structural deformations, and global frame rotations compared to the regular structures. However, this level of improvement appears to vary depending on the problem parameters at hand.

Base Fixity Conditions

Optimal oil damper control over total floor accelerations and deformations in the structures was recorded during fixed base conditions. As the shallow founded frames get embedded into dry sand beds of different densities, the level of control in most cases begins to drop, depending on the nature of the input excitation. Figure 8.1 summarises the reductions in peak floor accelerations measured relative to the regular bare frames, after the installation of oil dampers during different base fixity conditions. It is important to highlight that the reduction in damper control with increasing base flexibility is not driven by a deterioration in the performance of the oil dampers per se, but rather by an improvement in the seismic response of the regular frames being used as a comparative benchmark. The experimental trends in Figure 8.1 indicate that in order for a damped structure embedded in soft ground to achieve the levels of peak floor acceleration reductions measured during fixed base, higher damping levels would be required. This is often achieved by installing larger and more expensive oil dampers throughout the superstructure.

Earthquake Excitations

Results from this study confirm that the level of vibration control expected in a structure equipped with inter-storey oil dampers does have a dependency on the characteristics of the input motions predicted at a particular site. For short-return period, long duration motions, such as the weak sine-sweep excitations or the scaled Imperial Valley records fired in this study, the structures equipped with inter-storey oil dampers, both squat and tall, exhibited remarkable reductions in seismic response compared to the bare frames, regardless of the ground conditions being tested. Examples of this are shown in Figure 8.1. Such type of motions, characterised by a broad frequency bandwidth, are long enough to trigger cyclic responses in the structures at their respective natural frequencies; this is an optimal condition for the operation of the oil dampers.

For near-fault, pulse-type excitations such as the scaled Kobe motion, oil dampers did not provide the same level of control over peak response parameters. For such earthquakes, regular frames embedded in loose sand, particularly the taller frame with the higher centre of gravity, benefited considerably from subsoil deformation and inertial interaction at the foundation-soil interface, bringing peak structural drifts and total accelerations closer to their damped counterparts. This is also illustrated in Figure 8.1, in which lower percentage reductions in acceleration for the dry sand cases were recorded on average for Kobe, compared to the sine-sweep or scaled Imperial Valley excitations.

The effect of earthquake intensity on the level of control provided by the inter-storey oil dampers was found to be more prevalent in excitations with considerable energy content focused around the fundamental frequency of the superstructures. Evidence of this is can be seen in Figure 8.1 by comparing percentage reduction in accelerations achieved during the sine-sweep motion, to those recorded during the strong near resonant frequency excitation. As the amplitude of near resonant frequency motions increased, peak response parameters measured in the regular bare frames embedded in sand begin to approach, but never drop below, those recorded in their damped counterparts, especially as the ground becomes softer. This was experimentally demonstrated in this study by comparing floor acceleration amplification traces, and storey shear versus drift loops for the damped and the undamped bare structures. The reduction trend for the strong near resonant frequency motion in Figure 8.1 reiterates this, showing percentage drops in peak roof accelerations after the installation of oil dampers reaching as low as 15 % for the tall structures with light foundations embedded in loose sand, compared to a 65 % drop recorded during fixed base. Notwithstanding this, it is important to highlight that any beneficial reductions in dynamic response invoked by SSI in the regular frames during shaking tend to diminish once the base excitation stops. While the frames equipped with oil dampers come to a rapid halt, regular frames enter a long phase of free-vibration decay.

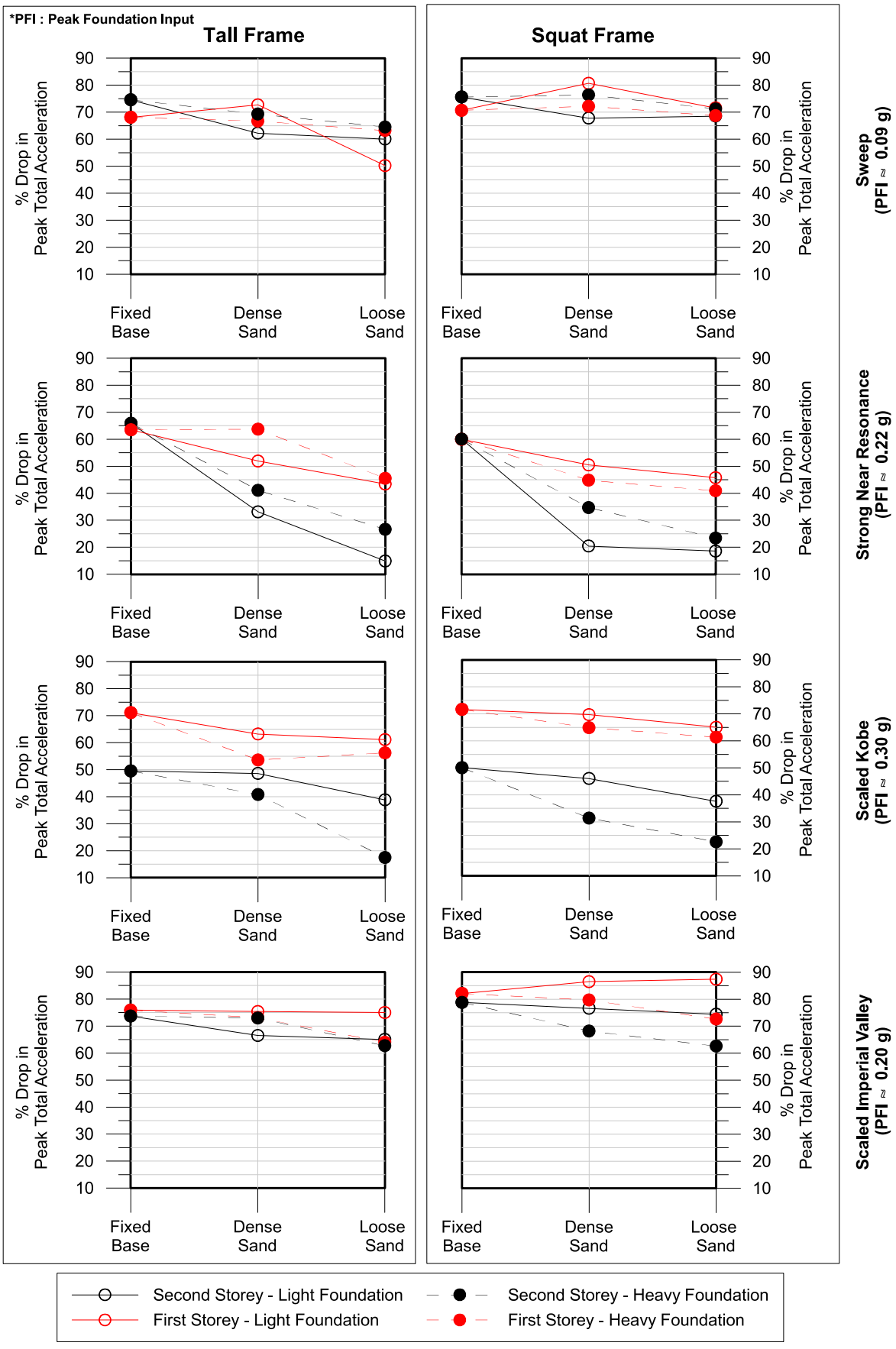

Fig. 8.1 Percentage drop in peak total floor accelerations after D2 oil damper installation for different ground conditions and base excitations.

Soil Bearing Pressures

Foundation bearing pressures on soil were varied in this study to trigger different levels of rotations during shaking. Experimental foundation moment-rotation traces for the regular bare frames with light foundations embedded in sand exhibited distinctive plateauing in moments for increasing frame rotations. A limit on the maximum moment reaction at the foundation is effectively a limit on the maximum floor accelerations (i.e. inertial forces) allowed to develop in the superstructure. As the soil bearing pressure was increased from ≈ 40 kPa to ≈ 70 kPa, a proportional increase in the mobilised peak foundation moments was measured. The stiffer foundation-soil system allowed for higher floor accelerations and drifts to develop in the bare frames, as summarised in Figure 8.2. The benefits of natural rocking isolation, represented here by the light foundation cases, become more prominent as shaking intensity increases. Additional acceleration and drift demands on the superstructure with increasing bearing pressure is not limited to the bare frames alone, but can also affect the damped structures as shown in Figure 8.2. However, the increase in storey drifts for the heavier foundation cases is very limited compared to the regular frames.

Structure Aspect Ratio

Despite the limitations on frame aspect ratios that could be tested experimentally (due to the physical size of the instrumented miniature oil dampers), two ratios 3.1 (Squat) and 4.6 (Tall) were tested. The effect of frame aspect ratio on structural response as measured in this study is summarised in Figure 8.2, for near resonant frequency excitations. Overall, higher storey drifts were measured for the squat frames, both with and without oil dampers, as the higher centre of gravity of the taller structures allows them to provoke greater dynamic SSI at their foundation-soil interfaces. However, the difference in response between the two aspect ratios almost diminishes for the heavy foundation cases, and for the damped structures fitted with oil dampers. Perhaps a greater contrast in frame aspect ratios and centre of gravity heights would have resulted in clearer differences in the response. The scatter trend of data points in Figure 8.2 re-affirms what was observed in section 5.3 of Chapter 5, when examining the effects of SSI on system transfer functions for the damped and bare frames; installation of oil dampers in a structure considerably reduced the system's sensitivity to base flexibility effects, frame aspect ratio, and foundation-soil system stiffness, at least for the intensity of excitations fired in this investigation. The clustering of data points in Figure 8.2 for the frames with dampers is to be compared against the significant scatter recorded for the bare frames, highlighting the considerable variation in response SSI inflicts on regular structures.

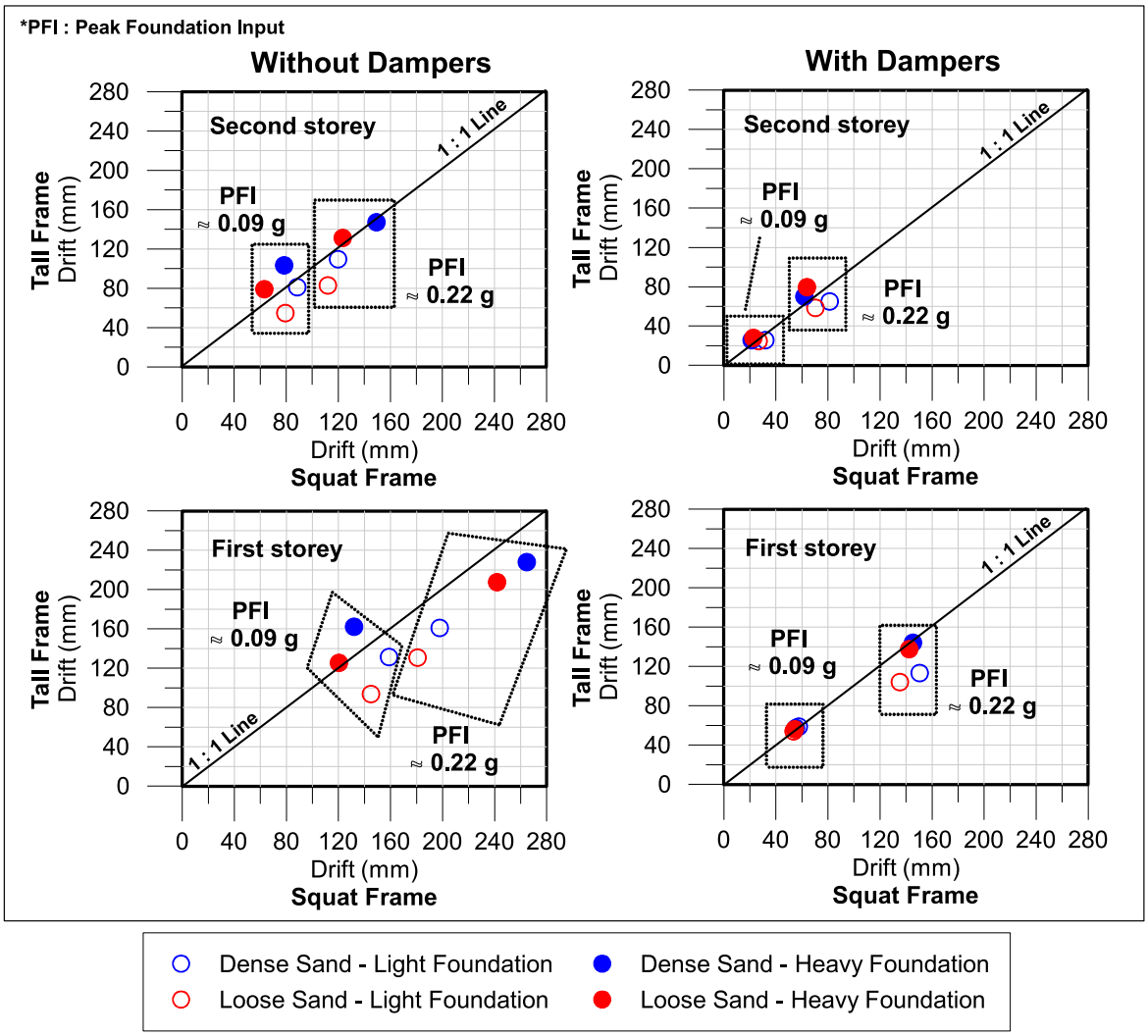

Fig. 8.2 Peak inter-storey drifts for the Tall and Squat structures with D2 dampers measured during weak and strong near resonant frequency excitations.

Dissipation of Seismic Input Energy

The dissipation of seismic input energy in a soil-structure system during horizontal ground shaking was tracked for the regular and damped structures with different base fixity conditions and input motions. The beneficial aspects of natural rocking isolation during SSI were demonstrated for both, the bare frames and the damped structures, by virtue of lower total input energies going into the systems compared to what was measured for the same excitations during fixed base.

A significant portion of energy going into a fixed base regular frame manifests as recoverable strain energy in the structure; a quantity closely associated with deformations and damage. In comparison, a considerable portion of input energy going into a structure with oil dampers gets dissipated by the damping devices, thus reducing the intensity of recoverable energy accommodated in the parent frame.

Releasing the rotational kinematic restraint at the foundation of a structure by shallow embedment into dry sand allows the system to do work against an additional degree of freedom, global frame rotations. This, in effect, channels a portion of the seismic input energy away from inducing shear deformations and damages in the structure, towards deforming the supporting subsoil as the frame rotates. Energy traces derived from experiments have shown that it is possible for a soil-structure system consisting of a frame founded on soft soil, experiencing moderately strong near resonant frequency excitations, to dissipate most of the seismic input energy as work done against foundation rotations. However, the effectiveness of such natural seismic mitigation measure is shown to be highly variable, depending on the soil-structure parameters at hand, and the predicted excitations at the site. For the damped structures with inter-storey oil dampers, the devices continue to be the primary source of energy dissipation in the soil-structure system, despite inertial interaction at the foundation-soil interface. This will be further discussed in the next section.

8.1.2 Effects of SSI on Structures With Oil Dampers

Dynamic soil-structure interaction as tested in this investigation did not have adverse consequences on the seismic performance of the frames fitted with inter-storey oil dampers; i.e. there were no cases where embedment of the damped frames in sand resulted in an increase in floor accelerations or structural deformations relative to what was recorded for a fixed base condition. This needs to be emphasised, as most literature on the subject conclude that increasing base flexibility for a damped structure will reduce damper effectiveness in the frame. While experimental findings from this study show evidence of reduced oil damper hysteresis as the ground becomes softer, the statement is not entirely accurate and can be misleading. The effects of SSI on different response parameters are discussed below.

Oil Damper Performance

Force instrumentation of the miniature oil dampers, coupled with stroke displacements derived from experimental accelerations, allowed oil damper hysteresis to be tracked for different frame base fixity conditions, during near resonant frequency excitations of the damped structures. Experimental evidence points to a reduction in the work done by the dampers as the ground beneath the structure gets softer. The reductions in damper hysteresis

were greater for the tall damped structure, and reached a maximum for the light foundation case; i.e. the greater the tendency of the structure to rock during shaking, the less work the oil dampers would perform. It is difficult to discern exactly which of the storey dampers exhibit greater reductions in hysteresis as it is different for the squat and tall frames. However, for the tall damped structure, which is more prone to rocking, the damper higher up in the frame showed a greater decline in energy dissipation compared to the first storey damper. For almost all of the configurations tested in the study, for the squat and tall damped structures with light and heavy foundations, reductions in input displacements into the oil dampers (i.e. storey drifts) appear to drive the decline in damper hysteresis.

For most cases, no noticeable drops in peak oil damper forces were observed with reducing base fixity, except for the case of the tall damped structure with light foundations. On closer inspection of the phase difference between the input (i.e. foundation) and output (i.e. floors) acceleration traces for the damped structures, it appears that supplemental damping confined the phase lag between the two to around 90 to 100 degrees for the near resonant frequency excitations tested in this study. If the frame is allowed to rotate at its base, this phase difference between the floors and the foundation can impose driving rotations onto the damped structure, in addition to the horizontal shaking of the foundation. This was confirmed by the detection of peaks in the rotational acceleration traces of the damped structures that are in-phase with peaks in foundation horizontal accelerations, and in-phase with peaks in the first storey damper forces; i.e. during SSI in the sand cases, the inter-storey oil dampers resisted floor accelerations due to both, the horizontal shaking of the foundation, and the horizontal component of foundation rotational accelerations resolved at each floor. This is believed to have limited any reductions in peak oil damper forces during SSI. An indirect consequence of this was a measured increase in damping ratios for the damped structures in sand relative to the fixed base tests. Effectively, the damped frames exhibited bigger drops in strain energy in the parent frames, compared to the reductions in oil damper hysteresis, driving an increase in damping ratio.

For the tall damped structure with a light foundation embedded in sand, a cap on the peak damper force for the first storey damper was observed during near resonant frequency excitations compared to fixed base. By superpositioning key stages in one damper compression-extension cycle over foundation moment-rotation loops for the tall damped frame, it appears that peak first storey damper forces occured close to instances of rapid changes in the rotational stiffness of the foundation (i.e. partial lift-off and subsoil yielding). Therefore, it is possible, albeit not common, for moment reaction to influence oil damper forces in the frame, especially if the foundation experiences considerable lift-off and reduction in contact area with the subsoil.

Foundation Rotations

Contrary to the usual clockwise (i.e. dissipative) moment-rotation loops observed for foundations experiencing dynamic over-turning moments on soil, experimental loops for the damped structures depicted a counter-clockwise orientation, implying rotations are leading seismic overturning moments in time. Further inspection of the rotational traces for the damped structures showed higher order effects in the signals, with one peak in-phase with overturning moments on the foundation, as typically expected from a flexible structure, and another peak earlier in time, in-phase with first storey oil damper forces and foundation horizontal accelerations. This second peak would often cause an earlier zero-crossing of the rotations signal compared to the overturning moments, causing the counter-clockwise moment-rotation orientation.

Further to the discussion raised previously on the phase difference between floors and foundations in the damped structures, it appears that the oil-damped frames should not be treated as regular flexible structures. As floors vibrate from minimum, to neutral, to maximum drift positions, velocity-dependant oil damper forces in the frame transition from near zero at minimum floor drifts, to maximum forces close to zero storey drifts (i.e. the dampers are similar to solid braces in the frame at this time instant), and then back to zero as the floors slow down towards their maximum drift position. In effect, the damped frame has instances were it responds as a flexible structure (when forces in the inter-storey oil dampers are near zero), and other instances were it responds as a semi-rigid body (when forces in the inter-storey oil dampers are near maximum). This would explain the higher order effects observed in the rotational traces for the damped structures.

The only case in which the damped frames exhibited typical clockwise moment-rotation loops was for the tall damped structure with a light foundation; the foundation rotational signal for the tall damped frame in this instance was dominated by peaks in-phase with seismic overturning moments, as expected from a flexible structure. The higher-order effects in foundation rotations, driven by the foundation-floor phase difference, were not large enough to drive early zero-crossings of the rotational signal.

Floor Accelerations and Drifts

For a specific excitation, it was experimentally shown that a shallow founded damped structure embedded into dry sand beds of different densities would often result in lower, at most similar, floor accelerations and structural deformations as measured during fixed base. Even during strong near resonant frequency excitation of the damped frames, floor accelerations in the damped structure continue to drop, albeit marginally, as base fixity was reduced from fully rigid to embedment into loose sands. This behaviour may seem peculiar at

first, especially that oil damper instrumentation reported a reduction in the energy dissipated in the oil dampers during SSI; i.e. the dampers should be less effective. However, energy time traces for the damped soil-structure systems show the damped frames benefitting from natural rocking isolation discussed in the previous section; the total seismic input energy into the damped soil-structure system is lower during SSI compared to the fixed base cases for a specific excitation. Therefore, the dampers have to do less work.

For the case of the tall damped structure with a light foundation, work done by the frame on rotations was positive (i.e. dissipative). As shaking intensity for this structure increased, a rise in the energy dissipated by frame rotations was observed. This rise appears to come at the cost of a corresponding drop in the work done by the dampers; i.e. energy dissipation at the foundation-soil interface starts to take a bigger portion of the overall energy dissipation in the damped soil-structure system. Therefore, any concern of a reduction in damper effectiveness during SSI, is compensated for by natural energy dissipation at the foundation-soil interface of the damped structure. This, with natural rocking isolation, explains why floor accelerations in the damped frames continued to drop with reduced base fixity.

Damping Levels

The squat frame with a light foundation case embedded in dense sand was fitted with different oil damper configurations to produced different damping ratios: low damping (≈ 6 % of critical), medium damping (≈ 10 % of critical), and high damping (≈ 16 % of critical). For short-return period excitations, or long duration motions that do not trigger considerable resonance in the superstructure, the increased control over floor accelerations and structural deformations with stronger dampers was clear, with roof acceleration amplifications for the high damping configuration measured at almost $1/3$ of that recorded for the low damping configuration.

For moderate to strong excitations that trigger resonance, the added benefits of selecting higher damping in the superstructure begin to diminish. This is, in part, driven by the nonlinear oil damper characteristics which reduce tangential damping coefficients as device input velocities increase (i.e. softening of the oil damper force-velocity relationship), but more importantly by the different levels of inertial interaction occurring at the foundation-soil interface of the damped structure. For the low damping configuration case, roof acceleration amplification traces showed noticeable reductions from that recorded during fixed base. On the other hand, the squat frame with high damping showed little variation in roof amplification trace when base fixity conditions changed from fixed base to embedment into dense sand. For such moderate to strong excitations, changing the damping configuration from low to high only reduced peak roof acceleration amplifications by 37 %. This is compared against

the 70 % drop measured for weaker motions. It follows that during strong excitations that trigger resonance, structures engineered with lower damping levels can capitalise more on the natural energy dissipation that occurs at the foundation-soil interface during SSI, compared to structures fitted with stronger dampers. For near-fault pulse-like excitations such as Kobe, the added benefits of higher damping in the frame are not that prominent. However, the stronger dampers are still able to provide marginally better control of peak structural response.

8.2 Implications of Research to Practice

Inter-storey oil dampers have undoubtedly proven to be reliable sources of energy dissipation in a structure. The devices demonstrated effective structural control over a wide range of base excitations, input motion intensities, frame aspect ratios, and even base fixity conditions. At the same time, this study demonstrated the variability and uncertainty associated with using dynamic soil-structure interaction as a natural form of seismic mitigation for regular structures. During early stage design, when the need for inter-storey oil dampers in a structure is still being assessed, it would be very useful for practising engineers to have a simple tool that would allow them to do the following:

1. Estimate the seismic performance of the structure in its bare form, taking into consideration dynamic soil-structure interaction effects, before deciding on the need for supplemental dampers.

2. Evaluate the complete soil-structure system response for the frame with different oil damper configurations, until the desired seismic performance is achieved.

To this date, structural engineers looking to incorporate inter-storey oil dampers into their designs to mitigate earthquake loads are likely to refer to the guidelines in Chapter 9 of FEMA-273 (1997), or Chapter 18 of ASCE 7-16 (2016). The procedures for preliminary analysis of structures with supplemental damping presented in these documents are underpinned by modal analysis, given its simplicity and popularity in practice. Peak response predictions using the Response Spectrum Analysis (RSA) procedure were compared in Chapter 4 against actual measurements recorded from fixed base centrifuge tests. The comparisons revealed the following issues related to RSA:

1. In the frequency domain, a structure with supplemental oil dampers has a lower and flatter transfer function, characterised by a wide frequency bandwidth at the fundamental frequency peak. As a result, the damped structure is likely to transmit most of the frequency content of the foundation accelerations, with slightly greater

amplification close to the fundamental frequency. It was shown that for realistic multi-frequency component excitations, contributions to the frame response from frequencies other than the fundamental frequency can be just as dominant, if not greater, depending on the input motion characteristics. Restricting response predictions to modal contributions only will lead to underestimation of storey velocities, accelerations and in turn, storey shear forces in the damped structure as these other frequencies are being neglected.

2. For input motions that do trigger resonance in the damped structures (i.e. ideal base excitations for modal analysis), the RSA procedure does not account for the time-varying stiffening effects that arise in the frame as damper forces and stiffness forces get superimposed over each other during shaking. The net result is an over-estimation of peak storey drifts, velocities, and maximum storey shear forces in structures vibrating close to resonance.

Any simple model for preliminary design would need to deviate away from such linear (i.e. frequency-based) procedures, address nonlinearities of the oil dampers, and more importantly, soil-structure interaction, in the time domain using numerical integration techniques. Chapters 4 and 7 of this study presented lumped parameter models for both, the regular frames and the damped structures, which can be easily coded and solved in any modern mathematical software. For the damped structure, the suggested code permits users to define the desired dashpot force-velocity equations to account for different oil dampers during early stage design. The superstructures were modelled as 2-DOF, linear elastic structures, with masses lumped at the centres of gravity of the floor plates and the foundation. Deformations between the lumped masses were restricted to shear (i.e. assuming columns are axially inextensible). For the case of frames embedded in sand, experimental foundation moment-rotation behaviour was replicated by a nonlinear spring inserted beneath the foundation mass. The spring follows a generalised hyperbolic curve developed by Heron (2013) to mimic rotational stiffness degradation of rafts on dry sand experiencing dynamic moments.

The simplified mathematical models for both, the damped and the bare frames, produced satisfactory predictions for fixed base, and dry sand embedment cases. For the intensity of input motions fired in this investigation, a fixed base assumption for most of the damped structure cases tested in the centrifuge resulted in reasonable response predictions. The case of the tall damped frame with a light foundation, and the squat damped structure fitted with light supplemental damping, were the two examples where a hyperbolic foundation-soil model refined predictions of the damped frame response relative to fixed base.

Based on the findings of this study, an optimal seismic mitigation strategy for a structure would be to rely heavily on supplemental inter-storey oil dampers to satisfy performance objectives for frequent design basis type earthquakes, and then use a combination of both, supplemental oil damping and natural energy dissipation at the foundation-soil interface for stronger maximum-considered earthquake type events. The lumped parameter models discussed earlier, particularly with the hyperbolic foundation-soil model of Heron (2013), allow such assessments to be made early on in the design stage. By numerically approximating the natural rocking isolation effects of SSI on the parent frame, a refined choice on the size of oil dampers needed to satisfy performance objectives can be made, potentially resulting in smaller less expensive devices.

8.3 Recommendations For Further Work

Experimental Parameters

The experimental nature of this investigation may have limited the number of parameters that could be physically varied and tested in the centrifuge. Of particular interest is the ratio of structure-to-soil stiffness. In this investigation, that ratio was restricted to that which could be achieved between flexible structures (to allow sufficiently large damper strokes) and dry sand beds of different densities. Structure-to-soil stiffness ratios can have considerable effects on the intensity of dynamic soil-structure interaction. There is considerable value in conducting further centrifuge tests using the same model structures but embedded in more compliant cohesive soils such as clay, or even testing stiffer model frames embedded in dry sand. The latter should result in interesting observations with regard to oil damper hysteresis, since stiffer structures are more likely to rock rather than deform internally during shaking, making inter-storey oil dampers even less effective.

The frames in this investigation were founded on shallow raft foundations. Such foundations resist seismic overturning moments from the superstructure by adjusting vertical stress distributions beneath their surface, deforming the soil, and forming a rotational pivot point at the soil interface. Moments mobilised by the raft vary considerably during shaking as the pivot point translates, and the contact area of the foundation with the soil changes during rocking. It would be of interest to compare results from this study, particularly for the regular frames, to a case where the structures are founded on isolated spread footings. A stiffer foundation moment-rotation behaviour is expected for such a system, with a well defined peak moment cut-off; the isolated footings mobilise moments by coupling axial loads from each foundation, rather than varying the size of foundation patch in contact with the soil during rotations.

Installation of supplemental oil dampers in this study have considerably reduced the structures' sensitivity to soil-structure interaction effects. Inertial interaction at the foundation-soil interface of the tall damped frame with a light foundation in sand limited peak oil damper forces in the structure, and contributed to energy dissipation in the system that would otherwise be confined to the oil dampers. Testing taller frames with even more degrees of freedom should help amplify these effects even more, and confirm the validity of the mentioned experimental findings.

Rotational Response of Structures with Oil Dampers

Counter-clockwise foundation moment rotation loops were observed in the centrifuge for the structures fitted with oil dampers, implying that rotations lead seismic overturning moments in time. While this is believed to be a consequence of the almost 90 degree phase difference in accelerations between the floors and the foundation of a damped system responding at resonance, further centrifuge testing using high-speed camera tracking of the foundation should provide more definitive explanations for such a response. Experimental imaging of the floors of a damped structure can also help confirm the existence of a flexible to semi-rigid block transition in the rotational response of the structure, as forces in the inter-storey oil dampers build-up and diminish during floor sway.

Miniature Dampers for Centrifuge Testing

This study presented the first attempt at miniaturising oil dampers for use in model structures under the high gravitational field of a geotechnical centrifuge. Whilst successful at dissipating energy during high frequency small stroke excitations, the velocity-dependant oil dampers also exhibited secondary dependencies on stroke, visualised graphically as lag between input velocity and damper output force. Such compliance in the devices is unrealistic, and could be eliminated by using a run-through piston rod design that would replace the volume compensating air bladder in the damping chamber. Development of such devices should result in smoother and more consistent miniature oil damper outputs, approaching that of prototype devices typically deployed in the field.

A more interesting investigation would be examining the effects of dynamic SSI on the performance of displacement-dependant dampers in model structures in the centrifuge; this would require developing miniature Buckling Restrained Braces (BRBs), or metalic yielding braces to provide passive control over floor vibrations. Force output from such devices is in-phase with peak stiffness forces in the frame, which are considerably reduced in the structure when intense SSI is triggered during shaking. For the miniature oil dampers tested in this investigation, velocity proportional oil damper forces peaked ahead of maximum

floor accelerations and storey drifts, the two parameters impacted the most by SSI. The result was mostly modest reductions in oil damping hysteresis, driven mainly by drops in oil damper strokes. On the other hand, inertial-interaction at the foundation-soil interface of a frame fitted with displacement-dependant devices is expected to have a more direct negative influence on both, device input strokes and output forces. The reductions in displacement-dependant damper hysteresis with reducing base fixity conditions are expected to be much greater in comparison to those measured for the oil dampers used in this study.

Numerical Parametric Studies

Experimental data collected from dynamic centrifuge testing in this study constitutes a valuable database against which fully-coupled nonlinear soil-structure finite element models could be calibrated. Through verified computational models, the scope of this study could be expanded to investigate the effects of deeper foundation embedments, or the effects of inserting a basement structure beneath the model frames. The seismic performance of the bare and damped structures could also be compared across different foundation systems; spread foundations and pile foundations are popular options typically employed in relevant damped building prototypes. At the superstructure level, a wider range of structure-to-soil stiffness ratios, oil damper properties, and structural aspect ratios could be investigated in relation to what was tested in the centrifuge. Such a parametric study should provide a wider understanding of how the performance of inter-storey oil dampers is affected by different levels of SSI during shaking.

References

Anastasopoulos, I., Gazetas, G., Loli, M., Apostolou, M., and Gerolymos, N. (2010). Soil failure can be used for seismic protection of structures. *Bulletin of Earthquake Engineering*, 8:309–326.

Anastasopoulos, I., Gelagoti, F., Kourkoulis, R., and Gazetas, G. (2011). Simplified constitutive model for simulation of cyclic response of shallow foundations: validation against laboratory tests. *Journal of Geotechnical and Geoenvironmental Engineering*, 137(12):1154–1168.

ASCE 7-16 (2016). *Minimum design loads and associated criteria for buildings and other structures*. American Society of Civil Engineers, Reston, Virginia.

Ashour, S. and Hanson, R. (1987). *Elastic seismic response of buildings with supplemental damping*. Department of Civil Engineering, University of Michigan, Ann Arbor, Michigan.

Boksmati, J. and Madabhushi, S. (2020). Centrifuge modelling of structures with oil dampers under seismic loading. *Earthquake Engineering and Structural Dynamics*, 49:356–374.

Boksmati, J., Madabhushi, S., and Thusyanthan, N. (2018). Development of model structural dampers for dynamic centrifuge testing. *Proceedings of the 9th International Conference on Physical Modelling in Geotechnics (ICPMG)*, pages 343–348.

Boksmati, J., Madabhushi, S., and Thusyanthan, N. (2019). Effects of dynamic soil structure interaction on the performance of structures equipped with viscous dampers. *Proceedings of the 7th International Conference on Earthquake Geotechnical Engineering (ICEGE)*, pages 1927–1938.

Boksmati, J., Madabhushi, S., and Thusyanthan, N. (2021). Dynamic soil-structure interaction of a shallow founded shear frame and a frame equipped with viscous dampers under seismic loading. *Engineering Structures*, 227.

Bolisetti, C., Whittaker, A., and Coleman, J. (2018). Linear and nonlinear soil-structure interaction analysis of buildings and safety-related nuclear structures. *Soil Dynamics and Earthquake Engineering*, 107:218–233.

Borja, R., Wu, W., Amies, A., and Smith, H. (1994). Nonlinear lateral, rocking, and torsional vibration of rigid foundations. *Journal of Geotechnical Engineering*, 120(3):491–513.

Brennan, A. and Madabhushi, S. (2002). Design and performance of a new deep model container for dynamic centrifuge testing. *Proceedings of the 5th International Conference on Physical Modelling in Geotechnics (ICPMG)*, pages 183–188.

BSI (2005). *Eurocode 8: Design of structures for earthquake resistance - Part 1: General rules, seismic actions and rules for buildings*. British Standards Institution, London, UK.

Caryl, S. (2020). Jan 17, 1995 ce: Kobe earthquake. *National Geographic*. [online] https://www.nationalgeographic.org/thisday/jan17/kobe-earthquake/.

Chang, K., Lin, Y., and Chen, C. (2008). Shaking table study on displacement-based design for seismic retrofit of existing buildings using nonlinear viscous dampers. *Journal of Structural Engineering*, 134(4):671–681.

Chatzigogos, C., Figini, R., Pecker, A., and Salencon, J. (2011). A macroelement formulation for shallow foundations on cohesive and frictional soils. *International Journal For Numerical and Analytical Methods in Geomechanics*, 35:902–931.

Chian, S., Stringer, M., and Madabhushi, S. (2010). Use of automatic sand pourers for loose sand models. *Proceedings of the 7th International Conference on Physical Modelling in Geotechnics (ICPMG)*, 1:117–121.

Chopra, A. (2012). *Dynamics of Structures*. Prentice Hall, fourth edition.

Christopoulos, C. and Filiatrault, A. (2006). *Principles of Passive Supplemental Damping and Seismic Isolation*. IUSS Press, Pavia, Italy.

Chuanromanee, O. (1995). *The influence of soil-structure interaction on the seismic response of structures with high damping*. PhD thesis, The University of Michigan, Department of Civil Engineering.

Chuanromanee, O., Hanson, R., and Woods, R. (1995). The influence of soil-structure interaction on the overall damping of structures with high damping. *Transactions on the Built Environment*, 14.

Coelho, P., Haigh, S., and Madabhushi, S. (2003). Boundary effects in dynamic centrifuge modelling of liquefaction in sand deposits. *16th ASCE Engineering Mechanics Conference*.

Constantinou, M., Soong, T., and Dargush, G. (1998). *Passive Energy Dissipation Systems for Structural Design and Retrofit*. Multidisciplinary Center for Earthquake Engineering Research, Buffalo, NY.

Constantinou, M. and Symans, M. (1992). Experimental and analytical investigation of seismic response of structures with supplemental fluid viscous dampers. *Technical Report MCEER-92-0032*.

Constantinou, M. and Symans, M. (1993). Experimental study of seismic response of buildings with supplemental fluid dampers. *The Structural Design of Tall Buildings*, 2:93–132.

Domenico, D., Ricciardi, G., and Takewaki, I. (2019). Design strategies of viscous dampers for seismic protection of building structures: A review. *Soil Dynamics and Earthquake Engineering*, 118:144–165.

Dong, B., Sause, R., and Ricles, J. (2016). Seismic response and performance of a steel mrf building with nonlinear viscous dampers under dbe and mce. *Journal of Structural Engineering*, 142(6).

Elghazouli, A. (2017). *Seismic design of buildings to eurocode 8*. CRC Press, Taylor and Francis Group, second edition edition.

FEMA-273 (1997). *NEHRP Guidelines for the Seismic Rehabilitation of Buildings*. Federal Emergency Management Agency, Washington, DC.

Flavigny, E., Desrues, J., and Palayer, B. (1990). Le sable d' hostun. *Revue Francaise De Geotechnique*, pages 67–70.

Fu, Y. and Kasai, K. (1998). Comparative study of frames using viscoelastic and viscous dampers. *Journal of Structural Engineering*, 124(5):513–522.

Fuller, T., Singhvi, A., Grondahl, M., and Watkins, D. (2019). Buildings can be designed to withstand earthquakes. *National Geographic*. [online] https://www.nytimes.com/interactive/2019/06/03/us/earthquake-preparedness-usa-japan.html.

Gajan, S. and Kutter, B. (2008). Capacity, settlement, and energy dissipation of shallow footings subjected to rocking. *Journal of Geotechnical and Geoenvironmental Engineering*, 134(8):1129–1141.

Gazetas, G. (1983). Analysis of machine foundation vibrations: state of the art. *Soil Dynamics and Earthquake Engineering*, 2(1).

Gelagoti, F., Kourkoulis, R., Anastasopoulos, I., and Gazetas, G. (2012). Rocking isolation of low-rise frame structures founded on isolated footings. *Earthquake Engineering and Structural Dynamics*, 41:1177–1197.

Grange, S., Kotronis, P., and Mazars, J. (2009). A macro-element to simulate dynamic soil-structure interaction. *Engineering Structures*, 31:3034–3046.

Greco, R. and Marano, G. (2013). Identification of parameters of maxwell and kelvin-voigt generalised models for fluid viscous dampers. *Journal of Vibration and Control*, 21(2):260–274.

Guo, T., Xu, J., Xu, W., and Di, Z. (2015). Seismic upgrade of existing buildings with fluid viscous dampers: Design methodologies and case study. *Journal of Performance of Constructed Facilities*, 29(6).

Hardin, B. and Drnevich, V. (1972). Shear modulus and damping in soils: design equations and curves. *Journal of Soil Mechanincs and Foundations Division, ASCE*, 98(SM7):667–692.

Heron, C. (2013). *The dynamic soil-structure interaction of shallow foundations on dry sand beds*. PhD thesis, University of Cambridge, Department of Civil Engineering.

Heron, C., Haigh, S., and Madabhushi, S. (2015). A new macro-element model encapsulating the dynamic moment-rotation behaviour of raft foundations. *Geotechnique*, 65(5):442–451.

Housner, G., Bergman, A., Caughey, T., Chassiakos, A., Claus, R., Masri, S., Skelton, R., Soong, T., Spencer, B., and Yao, J. (1997). Structural control: Past, present, and future. *Journal of Engineering Mechanics*, 123(9):897–971.

Hwang, J., Lin, W., and Wu, N. (2013). Comparison of distribution methods for viscous damping coefficients to buildings. *Structure and Infrastructure Engineering*, 9:28–41.

Jabary, R. (2016). *Dynamic soil-structure interaction effects on tuned mass dampers*. PhD thesis, University of Cambridge, Department of Civil Engineering.

Jabary, R. and Madabhushi, S. (2015). Tuned mass damper effects on the response of multi-storied structures observed in geotechnical centrifuge tests. *Soil Dynamics and Earthquake Engineering*, 77:373–380.

Jiang, X. and Yan, Z. (1998). Earthquake response analysis of building-foundation-building interaction system. *Journal of Vibration Engineering*, 11(1).

Jozwiak, B., Orczykowska, M., and Dziubinski, M. (2015). Fractional generalizations of maxwell and kelvin-voigt models for biopolymer characterization. *PLoS ONE*, 10(11).

Kasai, K. and Matsuda, K. (2014). Full-scale dynamic testing of response-controlled buildings and their components: concepts, methods and findings. *Earthquake Engineering and Engineering Vibration*, 13:167–181.

Kasai, K., Mita, A., Kitamura, H., Matsuda, K., Morgan, T., Taylor, A., Pu, W., and Wada, A. (2012). Jssi's investigations on recorded performance of seismic protection systems for buildings. *Proceedings of the 15th world conference on earthquake engineering*.

Kim, D., Lee, S., Kim, D., Choo, Y., and Park, H. (2015). Rocking effect of a mat foundation on the earthquake response of structures. *Journal of Geotechnical and Geoenvironmental Engineering*, 141(1).

Kourkoulis, R., Anastasopoulos, I., Gelagoti, F., and Kokkali, P. (2012). Dimensional analysis of sdof systems rocking on inelastic soil. *Journal of Earthquake Engineering*, 16(7):995–1022.

Kramer, S. and Stewart, J. (2004). *Chapter 4: Geotechnical aspects of seismic hazards, Engineering Seismology to Performance-Based Engineering*. CRC Press.

Kutter, B. (1982). *Centrifugal modelling of the response of clay embankments to earthquakes*. PhD thesis, University of Cambridge, Department of Civil Engineering.

Lee, D. and Taylor, D. (2001). Viscous damper development and future trends. *The Structural Design of Tall Buildings*, 10:311–320.

Li, P., Yang, J., and Lu, X. (2015). Study on influence of the vibration reduction effect of viscous dampers considering soil-structure dynamic interaction. *Proc. 6th International Conference on Advances in Experimental Structural Engineering*.

Lin, W. and Chopra, A. (2002). Earthquake response of elastic sdf systems with non-linear fluid viscous dampers. *Earthquake Engineering And Structural Dynamics*, 31:1623–1642.

Liu, W., Tong, M., and Lee, G. (2005). Optimization methodology for damper configuration based on building performance indices. *Journal of Structural Engineering*, 131(11):1746–1756.

Lu, Y. (2016). *Seismic Soil-Structure Interaction In Performance-Based Design*. Department of Civil Engineering, The University of Nottingham, Nottingham, U.K.

Lyamin, A., Salgado, R., Sloan, S., and Prezzi, M. (2007). Two and three dimensional bearing capacity of footings in sand. *Geotechnique*, 57(8):647–662.

Madabhushi, S. (1991). *Response of tower structures to earthquake perturbations*. PhD thesis, University of Cambridge, Department of Civil Engineering.

Madabhushi, S. (2015). *Centrifuge modelling for civil engineers*. Taylor and Francis, Boca Raton, Florida.

Madabhushi, S., Houghton, N., and Haigh, S. (2006). A new automatic sand pourer for model preparation at university of cambridge. *Proceedings of the 6th International Conference on Physical Modelling in Geotechnics (ICPMG)*, pages 217–222.

Madabhushi, S., Schofield, A., and Lesley, S. (1998). A new stored angular momentum (sam) based earthquake actuator. *Centrifuge '98*, pages 111–116.

Makris, N. and Constantinou, M. (1991). Fractional-derivative maxwell model for viscous dampers. *Journal of Structural Engineering*, 117(9):2708–2724.

Mason, H., Trombetta, N., Chen, Z., Bray, J., Hutchinson, T., and Kutter, B. (2013). Seismic soil-foundation-structure interaction observed in geotechnical centrifuge experiments. *Soil Dynamics and Earthquake Engineering*, 48:162–174.

Meek, J. and Veletsos, A. (1974). Simple models for foundations in lateral and rocking motion. *Proc. 5th World Conference on Earthquake Engineering*, 2:2610–2613.

Merritt, R. and Housner, G. (1954). Effect of foundation compliance on earthquake stresses in multistory buildings. *Bulletin of the Seismological Society of America*, 44(4):551–569.

Mitchell, M. (1996). *An introduction to genetic algorithms*. MIT Press, Cambridge, MA.

Mitrani, H. (2006). *Liquefaction remediation techniques for existing buildings*. PhD thesis, University of Cambridge, Department of Civil Engineering.

Morris, D. (1979). *The centrifugal modelling of dynamic soil-structure interaction and earthquake behaviour*. PhD thesis, University of Cambridge, Department of Civil Engineering.

Nakamura, Y. and Okada, K. (2019). Review on seismic isolation and response control methods of buildings in japan. *Geoenvironmental Disasters*, 6:7.

NEHRP - National Earthquake Hazard Reduction Program (1994). *NEHRP Recommended Provisions for Seismic Regulations for New Buildings and Other Structures*. Report No. FEMA 222A, Washington, D.C.

Newmark, N. and Hall, W. (1982). *Earthquake spectra and design*. Monograph Series, Earthquake Engineering Research Institute, Oakland, California.

Novak, M. and Hifnawy, L. E. (1983). Effect of soil structure interaction on damping of structures. *Earthquake Engineering and Structural Dynamics*, 11:595–621.

Osman, A. and Bolton, M. (2005). Simple plasticity-based prediction of the undrained settlement of shallow circular foundations on clay. *Geotechnique*, 55(6):435–447.

Oztoprak, S. and Bolton, M. (2013). Stiffness of sands through a laboratory test database. *Geotechnique*, 63(1):54–70.

Palermo, M., Silvestri, S., Landi, L., Gasparini, G., and Trombetti, T. (2016). Peak velocities estimation for a direct five-step design procedure of inter-storey viscous dampers. *Bulletin of Earthquake Engineering*, 14:599–619.

Palermo, M., Silvestri, S., Landi, L., Gasparini, G., and Trombetti, T. (2018). A direct five-step procedure for the preliminary seismic design of buildings with added viscous dampers. *Engineering Structures*, 173:933–950.

Paolucci, R., Shirato, M., and Yilmaz, M. (2008). Seismic behaviour of shallow foundations: Shaking table experiments vs numerical modelling. *Earthquake Engineering and Structural Dynamics*, 37:577–595.

Pekcan, G., Mander, J., and Chen, S. (1999a). Design and retrofit methodology for building structures with supplemental energy dissipating systems. *Technical Report MCEER-99-0021*.

Pekcan, G., Mander, J., and Chen, S. (1999b). Fundemental considerations for the design of non-linear viscous dampers. *Earthquake Engineering and Structural Dynamics*, 28:1405–1425.

Pelekis, I., Madabhushi, G., and DeJong, M. (2018). Seismic performance of buildings with structural and foundation rocking in centrifuge testing. *Earthquake Engineering and Structural Dynamics*, 47(12):2390–2409.

Pitilakis, D., Lopez-Caballero, F., Modaressi, A., and Clouteau, D. (2006). Soil-structure interaction: linear, equivalent linear and nonlinear approximation for the soil behavior modeling; a comparative study. *Proc. 8th U.S. National Conference on Earthquake Engineering*, 5:2601–2610.

Prevost, J. and Scanlan, R. (1983). Dynamic soil-structure interaction: centrifugal modeling. *Soil Dynamics and Earthquake Engineering*, 2(4):212–221.

Rahimian, A., Mattox, R., Anzola, E., Shleykov, I., Nikolaou, S., and Diaz-Fanas, G. (2019). Structural design challenges for tall buildings in mexico city. *Structural Performance*.

Rahimian, A. and Romero, E. (2003). Standing tall. *Modern Steel Construction*.

Rainer, J. (1975). Damping in dynamic structure-foundation interaction. *Canadian Geotechnical Journal*, 12(1):13–22.

Ramirez, M., Constantinou, M., Kircher, C., Whittaker, A., Johnson, M., Gomez, J., and Chrysostomou, C. (2001). Development and evaluation of simplified procedures for analysis and design of buildings with passive energy dissipation systems. *Technical Report MCEER-00-0010*.

Reinhorn, A., Li, C., and Constantinou, M. (1995). Experimental and analytical investigation of seismic retrofit of structures with supplemental damping, part1: Fluid viscous damping devices. *Technical Report MCEER-95-0001*.

Richart, F. and Whitman, R. (1966). Comparison of footing vibration tests with theory. *Journal of Soil Mechanics and Foundations*, 92(SM6).

Richart, F., Woods, R., and Hall, J. (1970). *Vibrations of Soils and Foundations*. Prentice-Hall.

Sadek, F., Mohraz, B., and Riley, M. (1999). *Linear static and dynamic procedures for structures with velocity-dependent supplemental dampers*. NISTIR 6329, National Institute of Standards and Technology, Gaithersburg, MD.

Salgado, R. (2006). *The Engineering of Foundations*. McGraw-Hill Higher Education, first edition.

Schnabel, P., Lysmer, J., and Seed, H. (1972). A computer program for earthquake response analysis of horizontally layered sites. *A computer program distributed by NISEE/Computer Applications, Berkeley*.

Schofield, A. (1980). Cambridge geotechnical centrifuge operations. *Geotechnique*, 30(3):227–268.

Schofield, A. (1981). Dynamic and earthquake geotechnical centrifuge modelling. *Proceedings of the First International Conference on Recent Advances in Geotechnical Earthquake Engineering and Soil Dynamics*, pages 1081–1100.

Seamer, B. and Wang, D. (2019). Case study 9: Seismic retrofit of the tower of hope - preservation of a masterwork of mid-century modernism. *Taylor Devices Inc.* Fluid Viscous Dampers: General guidelines for engineers including a brief history.

Seleemah, A. and Constantinou, M. (1997). Investigation of seismic response of buildings with linear and nonlinear fluid viscous dampers. *Technical Report MCEER-97-0004*.

Shepley, P. (2013). *Water injection to assist pile jacking*. PhD thesis, University of Cambridge, Department of Civil Engineering.

Shukla, A. and Datta, T. (1999). Optimal use of viscoelastic dampers in building frames for seismic force. *Journal of Structural Engineering*, 125:401–409.

Silverstri, S. and Trombetti, T. (2007). Physical and numerical approaches for the optimal insertion of seismic viscous dampers in shear type structures. *Journal of Earthquake Engineering*, 11(5):787–828.

Silvestri, S., Gasparini, G., and Trombetti, T. (2010). A five-step procedure for the dimensioning of viscous dampers to be inserted in building structures. *Journal of Earthquake Engineering*, 14(3):417–447.

Singh, M. and Moreschi, L. (2002). Optimal placement of dampers for passive response control. *Earthquake Engineering and Structural Dynamics*, 31:955–976.

Singh, P., Verma, N., and Moreschi, L. (2003). Seismic analysis and design with maxwell dampers. *Journal of Engineering Mechanics*, 129(3):273–282.

Soong, T. and Constantinou, M. (1994). *Passive and active structural vibration control in civil engineering*. Springer, Verlag, NY.

Summerson, M. (2017). Local product keeps mexico tower standing, dampers built by taylor devices in nt used in building. *Lockport Journal*. [online] https://www.lockportjournal.com/news/local_news/local-product-keeps-mexico-tower-standing/article_bae3e569-8c76-550b-9cd4-06e6d4699ef9.html.

Symans, M., Charney, F., Whittaker, A., Constantinou, M., Kircher, C., Johnson, M., and McNamara, R. (2008). Energy dissipation systems for seismic applications: current practice and recent developments. *Journal of Structural Engineering*, 134(1).

Symans, M. and Constantinou, M. (1995). Development and experimental study of semi-active fluid damping devices for seismic protection of structures. *Technical Report MCEER-95-0011*.

Symans, M. and Constantinou, M. (1998). Passive fluid viscous damping systems for seismic energy dissipation. *ISET Journal of Earthquake Technology*, 35(4):185–206.

Takewaki, I. (1997). Optimal damper placement for minimum transfer functions. *Earthquake Engineering and Structural Dynamics*, 26:1113–1124.

Takewaki, I. (2009). *Building control with passive dampers*. John Wiley and Sons.

Takewaki, I. and Uetani, K. (1999). Optimal damper placement for building structures including surface ground amplification. *Soil Dynamics and Earthquake Engineering*, 18:363–371.

Taylor, D. (2007). Seismic protection with fluid viscous dampers for the torre mayor, a 57 storey office tower in mexico city. *Taylor Devices Inc*.

Taylor, D. (2010). Smart buildings and viscous dampers - a design engineer's perspective. *The Structural Design of Tall And Special Buildings*, 19:369–372.

Taylor Devices Inc. (2019). *Fluid Viscous Dampers: General Guidelines for Engineers Including a Brief History*. Taylor Devices Inc., North Tonawanda, NY.

Terenzi, G. (1999). Dynamics of sdof systems with nonlinear viscous damping. *Journal of Engineering Mechanics*, 125(8):956–963.

Teymur, B. and Madabhushi, S. (2003). Experimental study of boundary effects in dynamic centrifuge modelling. *Geotechnique*, 53(7):655–663.

Trombetta, N., Mason, H., Chen, Z., Hutchinson, T., Bray, J., and Kutter, B. (2013). Nonlinear dynamic foundation and frame structure response observed in geotechnical centrifuge experiments. *Soil Dynamics and Earthquake Engineering*, 50:117–133.

Trombetti, T. and Silvestri, S. (2006). On the modal damping ratios of shear-type structures equipped with rayleigh damping systems. *Journal of Sound and Vibration*, 292(2):21–58.

Veletsos, A. and Meek, J. (1974). Dynamic behaviour of building-foundation systems. *Earthquake Engineering and Structural Dynamics*, 3:121–138.

Veletsos, A. and Nair, V. (1975). Seismic interaction of structures on hysteretic foundations. *Journal of the Structural Division, ASCE*, 101(ST1):109–129.

Veletsos, A. and Wei, Y. (1971). Lateral rocking vibrations of footings. *Journal of Soil Mechanics and Foundations*, 97:1227–1248.

Weissman, K. and Prevost, J. (1991). Results and analysis of soil-structure interaction experiments performed in the centrifuge. *Earthquake Engineering and Structural Dynamics*, 20:259–274.

Wolf, J. (1985). *Dynamic Soil-Structure Interaction*. Prentice-Hall, Englewood Cliffs, N.J.

Wolf, J. (1988). *Soil-structure-interaction analysis in time domain*. Prentice-Hall, Englewood Cliffs, N.J.

Wu, J. and Hanson, R. (1989). Study of inelastic spectra with high damping. *Journal of Structural Engineering*, 115(6):1412–1431.

Zhang, R. and Soong, T. (1992). Seismic design of viscoelastic dampers for structural applications. *Journal of Structural Engineering*, 118(5):1375–1392.

Zhao, X., Wang, S., Du, D., and Liu, W. (2017). Optimal design of viscoelastic dampers in frame structures considering soil-structure interaction effect. *Shock and Vibration, Hindawi Publishing*.

Zhao, Y., Gafar, K., Elshafie, M., Deeks, A., Knappett, J., and Madabhushi, S. (2006). Use of automatic sand pourers for loose sand models. *Proceedings of the 6th International Conference on Physical Modelling in Geotechnics (ICPMG)*, pages 265–270.

Zhou, Y., Guo, Y., and Zhu, Y. (2012). Influence of soil-structure interaction effects on the performance of viscous energy dissipation systems. *Proc. 15th World Conference on Earthquake Engineering*, 6:4223–4229.